THE UNIVERSITY OF QUEENSLAND

AUSTRALIA

Charge Generation and Transport Phenomena in Disordered Organic Semiconductors and Photovoltaic Diodes

Martin Stolterfoht

M.Sc.

A thesis submitted for the degree of Doctor of Philosophy at

The University of Queensland in 2016

School of Mathematics and Physics

Abstract

Organic semiconductors are of great interest for a broad range of optoelectronic applications due to their solution processability, chemical tunability and mechanical flexibility. In contrast to traditional banded semiconductors, organic semiconductors are intrinsically disordered systems and exhibit therefore much lower charge carrier mobilities. They are also low dielectric constant systems – as such, their photo-excitations are excitonic at room temperature with the electron-hole pair remaining Coulombically-bound. Blending organic semiconductors with differing electron affinities, so-called electron acceptors and donors, creates molecular heterojunctions which deliver the required driving force for exciton separation. These so-called bulk heterojunctions (BHJs) are the dominant architecture for creating organic photovoltaic cells and photodetectors. However, not least because of an incomplete understanding of the underlying physical mechanism that control the conversion of photons to free charges, and the subsequent extraction of these free charges to the electrodes, these organic optoelectronic systems still lag behind their inorganic counterparts.

Motivated by these factors, the work described in this thesis advances the fundamental understanding of the loss mechanisms associated with charge photogeneration and charge transport phenomena in BHJ organic solar cells and photodetectors, and presents new experimental methodologies to study these processes. The transport of photogenerated charge carriers in the percolated donor: acceptor pathways towards the extracting electrodes has been studied in-depth via existing and newly developed transient photovoltage and steady-state characterization techniques. A simple but conclusive understanding has been developed which allows for minimization of the detrimental recombination of free charge carriers for given device parameters such as film thickness, applied voltage and the mobility of the slower carrier type (either electrons or holes). The models' predictions have been experimentally validated for many different (> 25) BHJ solar cell systems. Inspired by the need to selectively optimize the processes which control the photocurrent output of the cell, such a charge photogeneration and extraction, a technique to quantify and disentangle both efficiencies has been developed as a next step. Corroborated by transient absorption spectroscopy, the dynamics of the photocarrier generation process was examined. The results suggest that the so-called charge-transfer state (CTS) separation limits the conversion of photons to free charges and the photocurrent output from short-circuit to the maximum power point, strongly depending on the slower carrier

mobility. These findings were explained by the ability of the slower carriers to leave the donor: acceptor interface *via* 1) a high enough mobility, 2) a sufficiently large domain size, and 3) enough conduction pathways (entropy). This work also shows that the dynamics of charge extraction and CTS dissociation are similar in the sense that both are critically controlled by the slower carrier mobility. As such, the findings underline the importance of optimizing the photocarrier generation quantum yield via a high mobility of both charge carrier types, which simultaneously maximizes the extraction yield as well. Lastly, the large benefit of re-dissociating CTS for all photovoltaic key parameters has been demonstrated for one of the most efficient organic solar cell systems to-date. Overall, the works presented in this thesis form a simple but powerful model to explain the performance of organic solar cells and photodetectors, and offer direct optimization guidelines through a more complete fundamental understanding of charge generation and transport phenomena in these systems.

Declaration by author

This thesis is composed of my original work, and contains no material previously published or written by another person except where due reference has been made in the text. I have clearly stated the contribution by others to jointly-authored works that I have included in my thesis.

I have clearly stated the contribution of others to my thesis as a whole, including statistical assistance, survey design, data analysis, significant technical procedures, professional editorial advice, and any other original research work used or reported in my thesis. The content of my thesis is the result of work I have carried out since the commencement of my research higher degree candidature and does not include a substantial part of work that has been submitted to qualify for the award of any other degree or diploma in any university or other tertiary institution. I have clearly stated which parts of my thesis, if any, have been submitted to qualify for another award.

I acknowledge that an electronic copy of my thesis must be lodged with the University Library and, subject to the policy and procedures of The University of Queensland, the thesis be made available for research and study in accordance with the Copyright Act 1968 unless a period of embargo has been approved by the Dean of the Graduate School.

I acknowledge that copyright of all material contained in my thesis resides with the copyright holder(s) of that material. Where appropriate I have obtained copyright permission from the copyright holder to reproduce material in this thesis.

Publications during candidature

[1] **Stolterfoht, M.**, Philippa, B., Armin, A., Pandey, A. K., White, R. D., Burn, P. L., Meredith, P., and Pivrikas, A. Advantage of suppressed non-langevin recombination in low mobility organic solar cells. *Applied Physics Letters* **105**, 013302 (2014).

[2] Philippa, B., **Stolterfoht, M**., Burn, P. L., Juska, G., Meredith, P., White, R. D., and Pivrikas, A. The impact of hot charge carrier mobility on photocurrent losses in polymer-based solar cells. *Scientific Reports* **4**, 1–8 (2014).

[3] Philippa, B., **Stolterfoht, M**., White, R. D., Velusamy, M., Burn, P. L., Meredith, P., and Pivrikas, A. Molecular weight dependent bimolecular recombination in organic solar cells. *The Journal of Chemical Physics* **141**, 054903 (2014).

[4] Armin, A., Kassal, I., Shaw, P. E., Hambsch, M., **Stolterfoht, M**., Lyons, D. M., Li, J., Shi, Z., Burn, P. L., and Meredith, P. Spectral dependence of the internal quantum efficiency of organic solar cells: Effect of charge generation pathways. *Journal of the American Chemical Society* **136**, 11465–11472 (2014).

[5] Lyons, D. M., Armin, A., **Stolterfoht, M**., Nagiri, R. C., van Vuuren, R. D. J., Pal, B. N., Burn, P. L., Lo, S.-C., and Meredith, P. Narrow band green organic photodiodes for imaging. *Organic Electronics* **15**, 2903 – 2911 (2014).

[6] **Stolterfoht, M.**, Armin, A., Philippa, B., White, R. D., Burn, P. L., Meredith, P., Juska, G., and Pivrikas, A. Photocarrier drift distance in organic solar cells and photodetectors. *Scientific Reports* **5**, 1–7 (2015).

[7] **Stolterfoht, M.**, Philippa, B., Shoaee, S., Jin, H., Jiang, W., White, R. D., Burn, P. L., Meredith, P., and Pivrikas, A. Charge transport without recombination in organic solar cells and photodiodes. *The Journal of Physical Chemistry C* **119**, 26866–26874 (2015).

[8] **Stolterfoht, M.**, Armin, A., Shoaee, S., Kassal, I., Burn, P., and Meredith, P. Slower carriers limit charge generation in organic solar cells. *Nature Communications* ***7***, 11944 (2016).

[9] Armin, A., Subbiah, J., **Stolterfoht, M.**, Shoaee, S., Xiao, Z., Lu, S., Jones, D. J., and Meredith, P. Reduced Recombination in High Efficiency Molecular Nematic Liquid Crystalline: Fullerene Solar Cells, *In Press Advanced Energy Materials* (2016).

Publications included in this thesis

Philippa, B., **Stolterfoht, M**., Burn, P. L., Juska, G., Meredith, P., White, R. D., and Pivrikas, A. The impact of hot charge carrier mobility on photocurrent losses in polymer-based solar cells. *Scientific Reports* **4**, 1–8 (2014). The publication is incorporated in **Section III.1** and accessible online http://dx.doi.org/10.1038/srep05695.

Contributor	**Contribution**
Bronson Philippa	Main idea (33%)
	Performed numerical simulations (100%)
	Result Interpretation (20%)
	Drafted the paper (40%)
	Manuscript editing/optimization (20%)
Martin Stolterfoht	Main idea (33%)
	Performed experiments (100%)
	Fabricated devices (100%)
	Result Interpretation (40%)
	Drafted the paper (20%)
	Manuscript editing/optimization (20%)
Paul Burn	Manuscript editing/optimization (10%)
Gytis Juska	Consultation with A.P. (100%)
Paul Meredith	Manuscript editing/optimization (20%)
Ronald D. White	Manuscript editing/optimization (10%)
Almantas Privrikas	Main idea (33%)
	Result Interpretation (40%)
	Drafted the paper (40%)
	Manuscript editing/optimization (20%)

Stolterfoht, M., Armin, A., Philippa, B., White, R. D., Burn, P. L., Meredith, P., Juska, G., and Pivrikas, A. Photocarrier drift distance in organic solar cells and photodetectors. *Scientific Reports* **5**, 1–7 (2015). The publication is incorporated in **Section IV.1** and accessible online http://dx.doi.org/10.1038/srep09949.

Contributor	**Contribution**
Martin Stolterfoht	Main idea (90%)
	Performed experiments (100%)
	Fabricated Devices (100%)
	Design of IPC measurement setup (25%)
	Result Interpretation (45%)
	Drafted the paper (100%)
	Manuscript editing/optimization (20%)
Ardalan Armin	Design of IPC measurement setup (75%)
	Result Interpretation (15%)
	Manuscript editing/optimization (10%)
Bronson Philippa	Performed numerical simulations (100%)
	Result Interpretation (15%)
	Manuscript editing/optimization (10%)
Ronald D. White	Manuscript editing/optimization (10%)
Paul Burn	Manuscript editing/optimization (10%)
Paul Meredith	Result Interpretation (10%)
	Manuscript editing/optimization (20%)
Gytis Juska	Consultation with A.P. (100%)
Almantas Pivrikas	Main idea (10%)
	Result Interpretation (15%)
	Manuscript editing/optimization (20%)

Stolterfoht, M., Philippa, B., Shoaee, S., Jin, H., Jiang, W., White, R. D., Burn, P. L., Meredith, P., and Pivrikas, A. Charge transport without recombination in organic solar cells and photodiodes. *The Journal of Physical Chemistry C* **119**, 26866–26874 (2015). The publication

is incorporated in **Section IV.2** and accessible online http://dx.doi.org/10.1021/acs.jpcc.5b09058.

Contributor	**Contribution**
Martin Stolterfoht	Main idea (90%)
	Performed experiments (other than TAS) (100%)
	Fabricated Devices (50%)
	Result Interpretation (70%)
	Drafted the paper (100%)
	Manuscript editing/optimization (30%)
Bronson Philippa	Performed Simulations (100%)
	Result Interpretation (10%)
	Manuscript editing/optimization (10%)
Safa Shoaee	Performed TAS experiments (100%)
	Result Interpretation (5%)
	Manuscript editing/optimization (5%)
Hui Jin	Fabricated Devices (50%)
Wei Jiang	Synthesized polymeric donor "WJ1-04" (100%)
Ronald D. White	Supervised the numerical study (100%)
	Manuscript editing/optimization (10%)
Paul Burn	Manuscript editing/optimization (10%)
Paul Meredith	Result Interpretation (5%)
	Manuscript editing/optimization (30%)
Almantas Privrikas	Main idea (10%)
	Result Interpretation (10%)
	Manuscript editing/optimization (10%)

Stolterfoht, M., Armin, A., Shoaee, S., Kassal, I., Burn, P., and Meredith, P. Slower carriers limit charge generation in organic solar cells. *Nature Communications* **7**, 11944 (2016). The

manuscript is incorporated in **Section V.2** and accessible online http://www.nature.com/ncomms/2016/160621/ncomms11944/full/ncomms11944.html.

Contributor	Contribution
Martin Stolterfoht	Main idea (80%)
	Performed experiments (other than TAS) (100%)
	Fabricated Devices (100%)
	Result Interpretation (30%)
	Drafted the paper (100%)
	Manuscript editing/optimization (20%)
Ardalan Armin	Main idea (20%)
	Result Interpretation (20%)
	Manuscript editing/optimization (10%)
Safa Shoaee	Performed TAS experiments (100%)
	Result Interpretation (20%)
	Manuscript editing/optimization (25%)
Ivan Kassal	Result Interpretation (20%)
	Manuscript editing/optimization (25%)
Paul Burn	Manuscript editing/optimization (5%)
Paul Meredith	Result Interpretation (10%)
	Manuscript editing/optimization (15%)

Armin, A., Subbiah, J., **Stolterfoht, M.**, Shoaee, S., Xiao, Z., Lu, S., Jones, D. J., and Meredith, P. Reduced Recombination in High Efficiency Molecular Nematic Liquid Crystalline: Fullerene Solar Cells, *In Press Advanced Energy Materials* (2016). The publication is incorporated in **Section V.3** and accessible online DOI: 10.1002/aenm.201600939.

Contributor	Contribution
Ardalan Armin	Performed Experiments (50%)
	Fabricated Devices (100%)
	Drafted the paper (70%)

	Result Interpretation (40%)
	Manuscript editing/optimization (25%)
Jegadesan Subbiah	Manuscript editing/optimization (5%)
Martin Stolterfoht	Performed Experiments (50%)
	Drafted the paper (30%)
	Result Interpretation (40%)
	Manuscript editing/optimization (20%)
Safa Shoaee	Result Interpretation (10%)
	Manuscript editing/optimization (15%)
Zeyun Xiao	Manuscript editing/optimization (5%)
Shirong Lu	Manuscript editing/optimization (5%)
David Jones	Manuscript editing/optimization (5%)
	Synthesized donor material “BTR” (100%)
Paul Meredith	Result Interpretation (10%)
	Manuscript editing/optimization (20%)

Contributions by others to the thesis

The result provided in this thesis are based on five manuscripts which are published in peer reviewed journals (incorporated in **Sections III.1**, **IV.1**, **IV.2**, **V.2, V.3)** and one manuscript which is currently under review in a peer reviewed journal (incorporated in **Section V.1**). The Supplementary Information is available online https://www.dropbox.com/s/13k55gsglk16rov/Supplementary_Information_efied.docx?dl=0.

Significant contributions of others to **Section V.1** are listed below.

Contributor	**Contribution**
Ardalan Armin	Performed Space Charge Limited Current measurements.
Wei Jiang	Synthesized polymeric donor “WJ1-04” and “WJ1-06”.
Hui Jin	Fabricated WJ1-04:PC70BM and WJ1-06:PC70BM devices.

Statement of parts of the thesis submitted to qualify for the award of another degree

None.

Acknowledgements

Truly, I owe my deepest gratitude to my parents Helmut and Ingrid Stolterfoht for their love and support throughout my whole life. My father, who taught me to live an unmaterialistic life and being environmentally-conscious, which continues to guide me in my life and work. My mother, who always put her family first and dedicated her life to her children. Words are not enough to express my gratitude.

A very affectionate thanks to my partner Isabel for her patience and for putting up with me on daily basis. She has given me the love, kindness, support and encouragement in pretty much everything I did, which has been important for my work too. I would also like to thank my siblings, my friends back home and my new friends I've found here for their strong support.

No doubt, at the beginning of my time at the University of Queensland it was my advisor Almantas Pivrikas, whose enthusiasm and expertise provided me an excellent start into the project. It was also him who has given me the opportunity to work in this fascinating field and taught me the required skills. I have benefited a great deal from his guidance and ideas for the first 2 years until he continued his career at another university. I would like to express my sincere gratitude to my advisor Prof. Paul Meredith for his continuous support throughout my Ph.D research, and for his patience, motivation and wisdom. I greatly appreciated that he has given me a free hand to complete my PhD projects and ideas. He has also been a great example of how to be professional in many ways and his broad knowledge of physics and organic electronics was very influential to my research. I would also like to express my sincere gratitude to the head of the COPE institute, Prof. Paul Burn for his support and quick help when it was needed and when papers were about to be submitted.

I truly enjoy working at UQ in Brisbane - a great city with wonderful people -which made my research much more enjoyable and fun! These include all the physicists/chemists/scientists at COPE: Robert, Pegah, Mujeeb, Khalid, Dani, Paul S., Ebinazar, Bernie, Pascalo, Vincento, Aren, Larry, Ajeesh, Nasim, Hellen, Kinitra, Sarah, Vincent, Margaritha, Ardalan, Ivan, Safa, Ravi, Steve, Mike and more. Many thanks also to our collaborators at the James Cook University, Bronson and Ronald for all your insights from theoretical modelling. And last but not least my gratitude to the administrative managers: Rob Kembery and Murray Kane, and to Sam Zammit for the so-often needed IT support. Thank you guys!

In particular, I would like to give my sincere gratitude to 3 very special colleagues, with whom I spent the most time in the second half of the project. Ardalan Armin has been my closest colleague throughout the whole time. From the very beginning we faced similar scientific

questions/challenges and through many passionate discussions we found many answers beyond our expectations. He also taught me skills and always had a great idea at hand. My sincerest appreciation to Safa Shoaee, who has been very influential to my research and has been always there to lend a helping hand. Lastly, I also wish to thank Ivan Kassal, who's brilliant ideas and sharp thoughts brought our last collaborations significantly forward. Once again, I would like to thank Ardalan, Safa, Ivan and also Robert for proof-reading this thesis and for the great suggestions.

Lastly, I acknowledge that this study wouldn't have been possible without financial support from the University of Queensland International scholarship, and the stipend from the Australian Centre for Advanced Photovoltaics (ACAP).

Keywords

Solar cells, optoelectronics, organic semiconductors, photovoltaics, photodiodes, photophysics, charge transport, charge generation

Australian and New Zealand Standard Research Classifications (ANZSRC)

ANZSRC code: 020504, Photonics, Optoelectronics and Optical Communications, 40%
ANZSRC code: 020401, Condensed Matter Characterisation Technique Development, 30%
ANZSRC code: 100702, Molecular and Organic Electronics, 30%

Fields of Research (FoR) Classification

FoR code: 0205, Optical Physics, 40%
FoR code: 0204, Condensed Matter Physics, 30%
FoR code: 1007, Nanotechnology, 30%

Table of Contents

Chapter I: Introduction

I.1 Organic Photovoltaics and Photodetectors

Sustainable and efficient energy production is one of the biggest challenges mankind has to face in the 21st century. The global energy consumption is ever increasing, along with the increasing population and economic expansion, as well as CO_2 emissions. This, in combination with the limited amount of finite energy resources such as coal, oil, and natural gas poses a serious problem for mankind's energy security and the environment. Nevertheless, renewable resources currently play only a minor role in our energy supply (~19% in 2013 [1]), and the majority of this comes from biomass and hydro energy. Solar photovoltaic and wind energy play an even smaller role providing about 1% of the global energy supply in 2015 [1, 2], despite the sun being by far the most abundant energy resource available. **Figure 1** illustrates that the earth receives an estimated electrical energy of 89000 TWy [3] per year from the sun which greatly exceeds the human energy demand of ~18 TWy (in 2013 [2]). In fact, the annual solar energy incident on earth's land masses greatly exceeds that which will ever be gained from fossil fuels and uranium combined.

The logical conclusion is to direct efforts to reduce our dependence on the finite resource via existing technologies to harvest the sunlight, and to establish ways to do this more effectively at a lower cost. Indeed, considerable endeavour has been dedicated worldwide to a sustainable energy transition. Most notably, Germany is aiming to increase its share of renewable energies for electricity to 80% by 2050 [4], with solar power playing a key role.

.

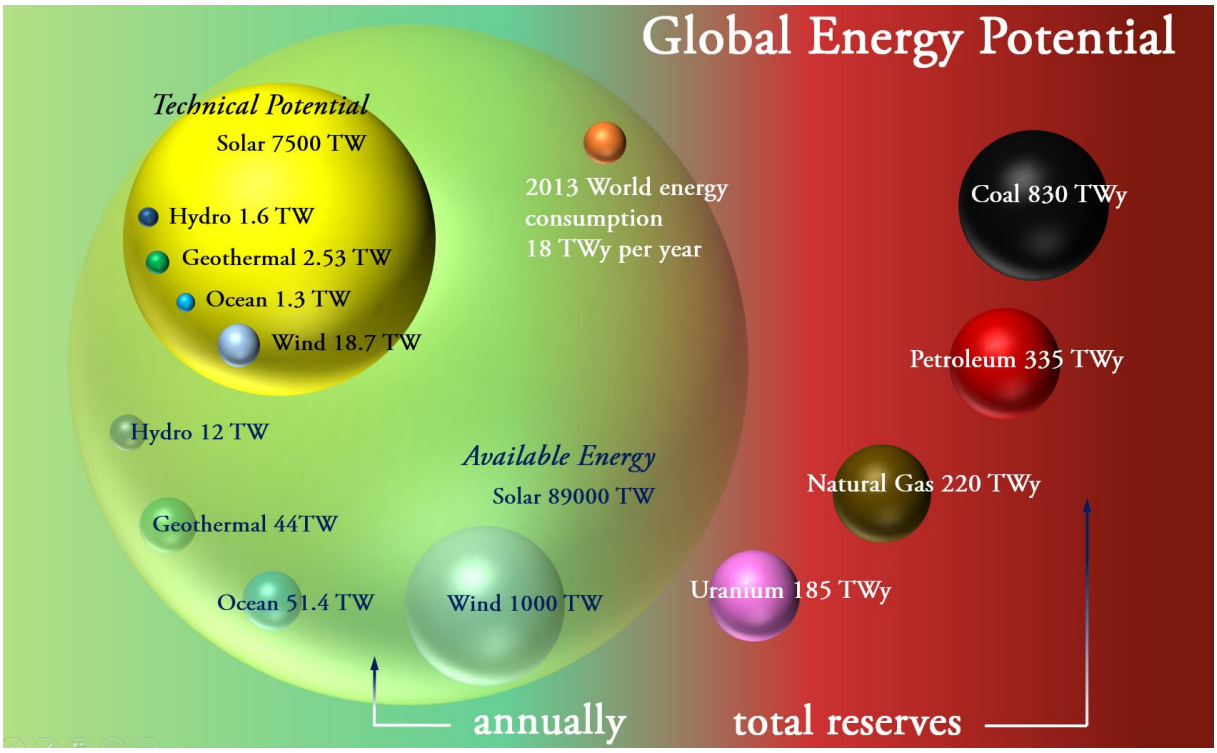

Figure 1. *Orders-of-magnitude estimates of technical/available world potentials of renewable energy resources compared to totally recoverable/finite resources and our energy demand. All resources are represented by the volume of the spheres. The "Technical Potential" means resources that can be extracted and converted into electrical energy given current technologies. For example, assuming a photon-to-electron conversion efficiency of ~30% and harvest only from landmasses that are reasonable accessible. The solar power that strikes earth's landmasses greatly exceeds the sum of all finite proved reserves. Renewable energy data adapted from [3]. Gas, petroleum and coal resources are estimates according to a report of British Petroleum in 2015 [5]. Uranium estimates are taken from [6].*

Photovoltaic (PV) cells that directly convert the sunlight into electricity are one the most promising technologies to utilize solar power. Currently, commercial PV cells use almost entirely crystalline silicon as the active layer material. There are multiple reasons for this, notably, the abundance of silica - the raw material for silicon, as well as widespread usage of silicon in a broad range of electronic elements and therefore the availability of silicon processing techniques. To date, silicon solar cells achieve in laboratories power conversion efficiencies of 25% [7, 8], and the module price industrially is constantly decreasing. Today, the technology is already cost-competitive compared to other power generation technologies based on fossil fuels, and has a large potential to address our future energy needs. For example,

simple calculations show that, in fact, covering only <1% of the earth's surface with silicon cells could theoretically cover the required energy demand [3].

However, the Si PV technology has its limitations. For example, the growth of monocrystalline silicon requires high-temperature processing techniques (~1400 °C [9]). This leads to an energy payback time of a few years [10]. Moreover, the efficiency of silicon cells is fundamentally limited to close to 30% [11, 12]. In the long term, solar cells fabricated from synthesized inexpensive materials could produce electricity at a much lower cost and surpass silicon cells. These facts have triggered significant research into the development of alternative (thin-film) PV technologies in the past decades. Examples include, copper indium gallium selenide, cadmium telluride, quantum dots, copper zinc tin sulphide, organohalide perovskites and organic dyes, polymers and small molecules. While all these types have certain advantages and disadvantages, to date their long term photovoltaic performance remains well below silicon cells [13].

One of the main benefits of organic solar cells (OSCs) fabricated from semiconducting small molecules and polymers is their potential for solution deposition and lightweight active layers. Therefore, cheap fabrication techniques such as spin coating, inkjet printing or roll-to-roll printing are applicable to ideally print the whole PV module in a single step. Early research efforts into single layers of organic semiconductors sandwiched between electrodes provided efficiencies of below 1%. The invention of the so-called "bulk heterojunction" (BHJ) cell in the early 90s [14] has significantly accelerated the research activities into organic solar cells and record efficiencies of 11.5% [15] have been achieved for single and small area junctions in laboratories. However, to date several problems render this technology not competitive compared to other photovoltaic technologies. These problems include the relatively low power conversion efficiencies, degradation problems, difficulties in scaling the device area for large area applications without further efficiency losses; and last but not least an incomplete understanding of the underlying physical mechanism that control the photon energy conversion.

In parallel to the development of organic semiconductors for photovoltaic applications, these materials have received enormous attention for application in other optoelectronic systems, due to their low fabrication costs, chemical tunability and mechanical flexibility. Examples of these electronic devices include organic light emitting diodes (OLED), flexible transistors for

bioelectronics applications (OFETs), or photodetectors for light detection (OPDs). The simultaneous developments in these fields have coined the term organic electronics. Like solar cells, photodetectors are light harvesting diodes, however, light detection applications require the optimization of different figures of merit [16]. Photodetectors are essential for a large number of systems, for example cameras, fibre-optic communication, biological sensing or spectroscopy [17]. In this field, organic semiconductors are of great practical interest as they exhibit unique properties that inorganic semiconductors do not possess. Most notably, organic semiconductors provide tunable energy levels and thereby tunable absorption spectra. This opens up new possibilities for wavelength selective colour discrimination. On the other hand, inorganic semiconductors exhibit broadband spectral responses and dichroic prism or optical filters are used for wavelength selective light detection, which increases the complexity of the pixel and limits the quality of sensing. The properties of organic semiconductors are particularly desirable for infrared vision, narrow band colour sensors, machine vision, advanced surveillance, or infrared blind cameras. However, OPDs are also often limited by the physical mechanisms that control the photon energy conversion.

I.2 Aims and Structure of the Thesis

The work described in this thesis aims to advance the fundamental understanding of organic semiconductor physics primarily for solar energy applications and secondly for photodetectors. The objectives of this work are as follows:

I: The first objective of this thesis is the development of new experimental techniques to surpass the limitations of existing methodologies in order to more reliably study charge transport and recombination of disordered semiconductors and associated photovoltaic diodes. This objective includes the development of a theoretical/experimental framework to measure the charge carrier mobilities of electrons and holes as they move towards the extracting electrodes, as well as their recombination rates. The methodologies should be applicable to relevant devices under close-to-operational conditions, in order to correlate the charge transport parameters to the performance of the device under test.

II: The second objective is to understand the impact of the charge transport on the photovoltaic performance of organic photocells; and to establish generally valid design principles to

minimize the detrimental charge recombination losses in devices with varying nano-morphology, percolation pathways etc. This goal requires the development of an experimental technique to reliably measure the charge transport efficiency, as well as a deep understanding of the interplay between film thickness, driving voltage, charge carrier mobilities recombination coefficients, charge trapping and recombination dynamics. Subsequently, the impact of these parameters on the charge extraction efficiency needs to be addressed.

III: The third objective of this thesis lies in the investigation of the photocarrier generation mechanism; to understand its impact on the device performance, and to establish ways to optimize the charge generation yield. Despite 25 years of tremendous research efforts, the process by which charge carriers are formed is still not fundamentally understood, and remains heavily debated. This thesis focuses in particular on the relationship between the donor: acceptor percolation pathways, the donor: acceptor blend ratio, charge carrier mobilities, electric field - and the impact of these variables on the exciton and charge-transfer state splitting efficiency. This goal requires the development of a new methodology to quantify the overall generation yield, corroborated by exiting spectroscopic tools to probe the dynamics of charge generation phenomena on very short timescales (fs-to-ns).

Chapter I contains an introduction to the research topic, and **Chapter II** the theoretical and experimental background as well as a literature review of recently debated topics in this field. The sections thereafter are based upon submitted and published works by the author in the peer reviewed literature. These works are grouped into three main parts: Methodology Development (**Chapter III**), Advances in Fundamental Understanding of Charge Transport (**Chapter IV**), Advances in Fundamental Understanding of Charge Generation (**Chapter V**). The published and submitted works are converted to the general format of the thesis. (**Chapter VI**) presents the conclusions of this thesis.

Chapter II: Theoretical and Experimental Framework

In this second chapter, the basic experimental and theoretical constructs relevant for the work described in this thesis are detailed. In particular, the basic physics of organic semiconductors will be exemplified and key differences between organic and inorganic semiconductors highlighted. Concepts such as charge generation, transport and recombination as they pertain to excitonic, disordered semiconductors will be covered and contextualised with respect to light harvesting diode architectures such as the bulk heterojunction. In addition, the electro-optics of thin film, low finesse semiconductor cavities will be described alongside the basic operating performance parameters of solar cells. Once these fundamental precepts have been established, conventional experimental methodologies used to characterise both materials and devices will be discussed. Lastly, "hot topics" in the field are outlined and strategies to improve the photovoltaic performance of organic light harvesting systems identified.

II.1 Organic Semiconductors/Insulators compared to Inorganic Semiconductors

Inorganic semiconductors, such as silicon or germanium form a periodic crystal structure. Each atom is covalently bonded by sharing one of its 4 valence electrons with one neighbouring atom. Bringing together a large number of atoms and electrons creates a quasi-continuum of possible

electron energy levels – an energy band. At finite temperatures, electrons are able to leave the localized bonds and become free and delocalized across the whole crystal. The energy band corresponding to the free electrons is called the conduction band, while electrons remaining in the covalent bonds from the valence band. In semiconductors, these bands do not cover the whole energy range and a gap exists between the valance and the conduction band which is not accessible by electrons. In the conduction band, one can think of electrons as an ideal gas, which is in a first approximation only perturbed by the potential of the lattice atoms. Mathematically these electrons can be described as Bloch electrons, which are the solutions to the single electron Schrödinger equations that describes the system.

As opposed to inorganic semiconductors, the conducting properties of organic semiconductors arise from their backbones of contiguous sp^2 hybridized carbon atoms and their perpendicular oriented p_z orbitals. The coupling of p_z orbitals of adjacent carbon atoms leads to delocalized electron and hole densities across the molecule. According to molecular orbital theory, the sp^2 orbitals form sigma molecular orbitals (*i.e.* rotationally symmetric bonds with respect to the bond's axis) which are either bonding (σ) or and anti-bonding (σ^*). Likewise, the p_z orbitals form bonding and antibonding molecular π orbitals. The bonding (π) and antibonding (π^*) orbitals are usually the molecule's Highest Occupied Molecular Orbital (HOMO) and the Lowest Unoccupied Molecular Orbital (LUMO), respectively. Solids of organic semiconductors exhibit only weak intermolecular interactions of the van der Waal type. These interactions are a result of the fully occupied π orbitals and prevent electron delocalization and the formation of banded states across the whole solid. Due to the weak intermolecular interactions, the mechanical and electronic properties of these materials differ substantially from inorganic materials. It is noteworthy that the HOMO and LUMO terminology is misleading to describe the relevant energy levels in organic solids, albeit their omnipresence in the literature. The charge transport relevant energy levels are better described by a (Gaussian) distribution of delocalized and localized states, or simply by the ionization potential (IP) and electron affinity (EA) of the material.

II.1.1 Electrical Conductivity and Mobility

The electrical conductivity of any conductor is defined as

$$\sigma = en\mu\,, \tag{1}$$

where e is the elementary charge, n the carrier density and μ the carrier mobility. In addition, n and μ are dependent on various parameters such as light intensity, temperature and the band gap in a semiconductor. The conductivity can be precisely controlled by introducing n- or p-type dopants (e.g. phosphorous or gallium in inorganic silicon-based semiconductors), which allow an increase of the carrier density by several orders of magnitude. The mobility is a measure of how fast charge carriers drift in the presence of an external field. As a result of the weak long range intermolecular electronic coupling, the charge transport in disordered organic semiconductors is usually limited by a hopping mechanism, leading to typically low mobilities. Typical mobilities values of organic semiconductors sandwiched between 2 electrodes, range between 10^{-6} $cm^2/V^{-1}s^{-1}$ and 10^{-3} $cm^2/V^{-1}s^{-1}$, while the electron mobility in silicon is around 1400 $cm^2/V^{-1}s^{-1}$ [18]. It is also important to mention that the mobility in organic solids is often dispersive, leading to a mobility distribution.

II.2 Working Mechanism of an Organic Solar Cells

The key steps of the photocurrent generation process in an organic photocell is schematically illustrated in **Figure 2** and explained below:

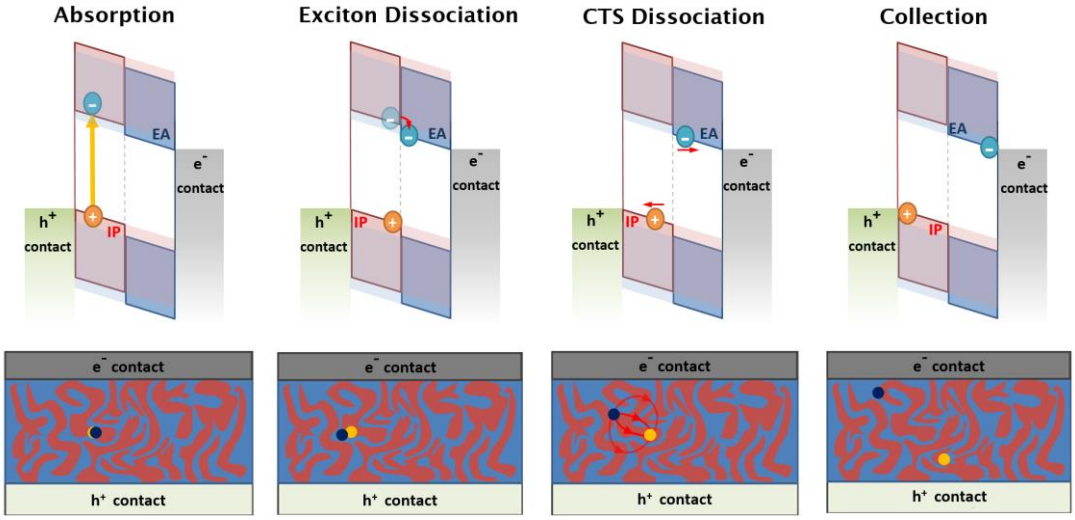

Figure 2*. The 4-step photocurrent generation process in organic photocells. (i) Absorption, (ii) exciton diffusion and dissociation, (iii) charge-transfer state dissociation, and (iv) charge collection.*

I - Absorption (η_{ABS}): The first step is to absorb a photon in the photoactive layer of the cell. The photon energy is thereby transferred to an electron promoting it from the IP (HOMO) to the EA (LUMO), creating an exciton formally defined as a Coulombically bound electron-hole pair pseudo-particle.

II - Exciton diffusion and dissociation (η_{EX}): After exciton generation, the exciton needs to dissociate into its constituent charges if the solar cell is to produce a photocurrent. As a consequence of the low dielectric constant in organic semiconductors (ε_r ~ 3-5), the exciton is strongly Coulombically-bound with binding energies of several hundred meV [19]. This in combination with the low mobilities prevents a direct electron-hole dissociation as found in their high dielectric inorganic counterparts (Si, ε_r ~ 12) [20]. Current strategies to facilitate the exciton dissociation rely upon a finely mixed donor: acceptor network ("bulk heterojunction", BHJ) in order to allow the exciton to reach the interface within the typical exciton diffusion length of ~10 nm [21].

In the case the photon was absorbed by the donor material, the electron will be transferred from the EA of the donor to the EA of the acceptor, provided that the energy level offset is sufficiently large; usually > 0.3eV [21, 22]. The mirror process where the hole is transferred from the acceptor IP to the donor IP is equally possible, depending on which material was excited. The photoinduced electron transfer is also known as *Channel I*, while the photoinduced hole transfer is known as *Channel II [23]*.

III - Charge-transfer state dissociation (η_{CT}): The electron (transferred from the donor to the acceptor) and the remaining hole form the so-called charge-transfer state (CTS). The CTS is still Coulombically-bound (by several hundred meV [19]) and can either dissociate into free charges or recombine geminately.

IV - Charge collection (η_{COLL}): In this last step the free charge carriers must be transported *via* drift within the internal built-in electric field to the respective electrodes with a minimum of recombination losses. Percolated pathways of the donor and acceptor phases to the electrodes are required to achieve this. Charge collection is efficient if the charge carrier transit (extraction)

time t_{tr} is shorter than the charge lifetime τ. This restricts the maximum active layer thickness (d, typically on the order of 100 nm [24, 25, 26]), above which the transit time is too long to guarantee efficient carrier collection. On the other hand, it is desirable to increase the film thickness to facilitate an increase in light absorption. Both, η_{ABS} and η_{COLL} therefore form a trade-off depending on the BHJ thickness.

The efficiency, comprising these 4 processes, is expressed as the external quantum efficiency

$$\mathrm{EQE} = \eta_{\mathrm{ABS}}\,\eta_{\mathrm{EX}}\,\eta_{\mathrm{CT}}\,\eta_{\mathrm{COLL}} = \eta_{\mathrm{ABS}}\,\mathrm{IQE}\,, \tag{2}$$

which gives the number of collected charges per incident photon, while the internal quantum efficiency (IQE) gives the number of collected charges per absorbed photon. The product of the exciton (η_{EX} and η_{CT}) is defined in this work as the generation yield η_{GEN}. The EQE determines the photocurrent at a given irradiation intensity and spectrum

$$J_{\mathrm{SC}} = e\int_0^{\infty} \mathrm{EQE}(\lambda) \times \varphi(\lambda)\, d\lambda\,, \tag{3}$$

where e is the elementary charge and $\varphi(\lambda)$ the air mass 1.5 global (AM1.5G) solar spectrum with 100 mW/cm^2. The EQE can be measured experimentally and the IQE can be obtained upon knowing the active layer absorption spectrum.

II.3 Power Conversion Efficiency

In order to generate electrical power the cell must also generate voltage. The maximum voltage a solar cell can produce is known as the open-circuit voltage V_{OC}. For a BHJ organic solar cell (OSC) the V_{OC} is limited by the energy levels of the IP of the donor and EA of the acceptor material

$$eV_{\mathrm{OC(max)}} < \mathrm{IP_D} - \mathrm{EA_A} \tag{4}$$

The contact electrodes impose a secondary limitation along with the CTS energy and other chemical potential losses. If the solar cell is biased either with a voltage or load resistance, the photocurrent and voltage will change. The condition under which the photocurrent-voltage product is at maximum defines the maximum power voltage V_{MP}. The solar cell's performance is defined as the power conversion efficiency (PCE), which represents the ability of the cell to convert optical power (P_{light}) into electrical power (P_{SC}).

$$\mathrm{PCE} = \frac{P_{\mathrm{SC}}}{P_{\mathrm{light}}} = \frac{Isc * V_{\mathrm{OC}} * \mathrm{FF}}{P_{\mathrm{light}}}, \tag{5}$$

Here, I_{SC} is the short-circuit current and FF denotes the fill factor, defined as the ratio of the maximum achievable power $I_{\mathrm{MP}}V_{\mathrm{MP}}$ (*i.e.* the current-voltage product at the maximum power point) and the product of $I_{\mathrm{SC}}V_{\mathrm{OC}}$. **Figure 3** shows a typical current-density versus voltage (JV) curve and the key parameters that define the PCE.

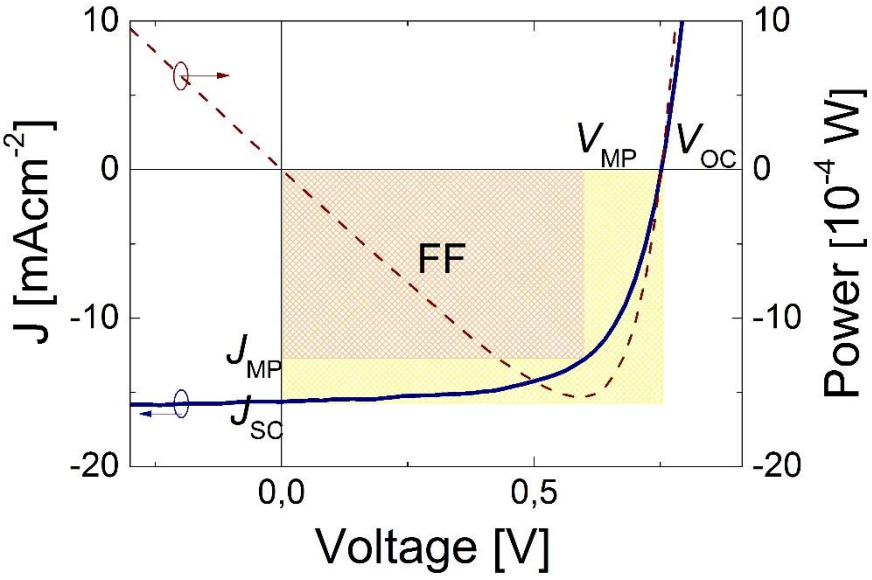

***Figure 3**. Current-density vs. voltage characteristics. The key photovoltaic parameters are marked such as the short circuit current density* (J_{SC})*, open-circuit* voltage (V_{OC})*, current density* (J_{MP}), and *voltage at maximum power* point (V_{MP}) *and fill factor (FF).*

II.3.1 Theoretical Efficiency Limiting Processes

In 1961, William Shockley and Hans Queisser calculated the possible efficiency of single junction solar cells based on the fundamental thermodynamic physics [27]. An upper limit of ≈30% was specified as the detailed balance efficiency (Shockley-Queisser) limit (although this value has been later slightly corrected to ≈33% [28, 29]). **Figure 4** presents a breakdown of the inevitable energy losses in single junction solar cells, which are discussed below.

I - Spectral Losses: The trade-off between absorption losses of photons with higher energy than the optical gap, and the relaxation of carriers to the band edge imposes an upper efficiency limit to the cell (which is 48% for Si [28]). Only photons with energy > optical gap can be converted to electrons. In a Si p-n junction with a bandgap of 1.1 eV this amounts to 19% of the incoming sunlight [28]. Lowering the bandgap, however, increases the losses due to relaxation of carriers to the band edge. In a silicon p-n junction, for instance, a large portion of the energy of a blue photon (*e.g.* 2.75 eV) is lost due to thermal relaxation (approximately 33% of the incoming energy).

II - Radiative recombination: The opposite process to photon absorption, where the electron and hole recombine with the emission of a photon, is an inevitable loss mechanism according to the principles of detail balance. The radiative recombination losses increase with applied forward voltage [28, 29], which increases the concentration of electrons and holes in the conduction and valence bands, respectively. Even in the dark without external voltage applied, the cell will emit blackbody electromagnetic radiation at a finite temperatures, which limits the maximum V_{OC} below the bandgap.

Even for silicon cells, there are some other loss mechanisms leading to a maximum achievable efficiency, somewhat below the detailed balance limit of close to 30% [11, 12]. These include non-radiative (*e.g.* Auger) recombination losses and optical absorption losses due to light reflection. These losses present also for a BHJ OSCs, the fundamental barrier, however, for this type of solar cell, many other factors need to be considered:

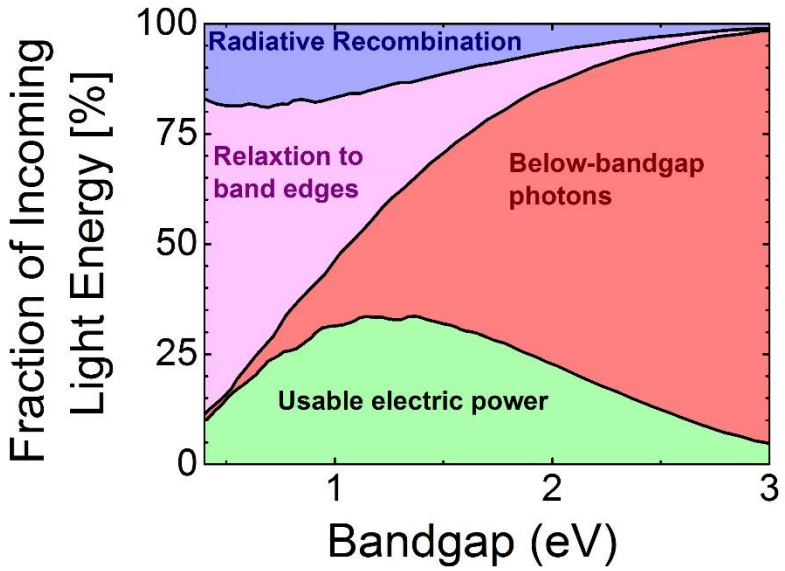

Figure 4*. The maximum efficiency according to the Shockley-Queisser model as a function of the junction bandgap. Breakdown of the photon energy losses: spectral losses due to photons below the bandgap and the relaxation of photogenerated charges to the band edges, as well as radiative recombination mainly due to the black body radiation limiting the open-circuit voltage. The maximum efficiency is achieved for junctions with a bandgap between 1.1 eV and 1.4 eV. Data adapted from [28, 29].*

Energy Level Offset (δ_{EA}): One of the biggest disadvantages of OSCs compared to their inorganic counterparts are the low dielectric constants of their active layer materials. This imposes the need for a large energy level offset between the donor EA and acceptor EA in order to overcome both the exciton binding energy and the reorganization energy (see **Section II.6.2**). The offset means a reduction of the maximum achievable V_{OC} due to the lower energy of free carriers (**Figure 5**). If the V_{OC} is optimized via tuning the blend's optical gap, then the absorption of the cell is compromised by a gap that is larger than optimal. It follows easily that a reduction of the energy level offset is the most promising strategy to minimize the wasted energy and optimize the photovoltaic performance.

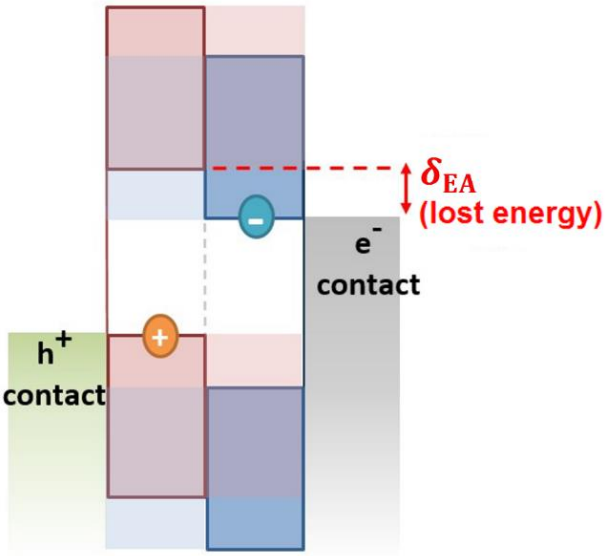

Figure 5*. Schematic representation of the donor: acceptor energy levels at open-circuit conditions highlighting the lost energy as a result of the requirement to split the strongly bound exciton.*

II.3.2 Current Challenges

Despite the inherent limitations of the BHJ architecture, the efficiencies of BHJ OSCs remain far below their optimum [22]. Current challenges are discussed below.

Losses in the Short-Circuit Current: A major limitation is the non-optimal optical gap of the active layer components. The highest performing donor and acceptors materials exhibit an optical gap of around ~1.8 eV [30], which is far below the optimal regime in the Shockley-Queisser model (~1.1 eV to 1.4 eV). This limits the absorption of the individual components and this is borne out by the low short-circuit current density (~15 mA cm^{-2}, compared to that of a silicon solar cell of ~40 mA cm^{-2}). Koster *et al.* [22] showed that efficiencies of ~20% are feasible for optimized donor (acceptor) gaps of ~ 1.4 eV, even with an energy level offset of ~200 meV. However, to date, the adjustment of the donor/acceptor energy levels is somewhat restricted to the use of [6,6]-phenyl-C_{70}-butyric acid methyl ester (PC70BM) as a common acceptor, which provides by far the highest efficiencies.

Additional Losses in the Open Circuit Voltage: The V_{OC} is usually several hundred meV below the blend optical gap due to various reasons [31], such as interfacial disorder (broadening

of the energy levels), the short CTS lifetimes (several hundred ps), and large binding energies (~200 meV) [19].

FF losses: While charge generation η_{GEN} and transport η_{COLL} are often quite efficient under short-circuit conditions, the photocurrent in forward bias is often poor. Therefore, the FF of many OSCs is usually significantly lower compared to their inorganic counterparts.

Other losses: From a device engineering perspective, parasitic absorption processes in non-active layers often reduce the device's absorption efficiency. Non-ideal electrodes can cause charge injection barriers to the donor's IP, and acceptor's EA, and minority surface recombination at the contacts can further reduce the V_{OC} and photocurrent [32, 33].

II.4 Light Absorption in Optical Cavities

The strong light absorption in organic semiconductors is one of their biggest advantages compared to inorganic semiconductors. **Figure 6** shows the absorption coefficient α of a model organic semiconductor blend comprising of poly[*N*-9"-heptadecanyl-2,7-carbazole-*alt*-5,5-(4',7'-di-2-thienyl-2',1',3'-benzothiadiazole (PCDTBT) and $PC_{70}BM$, compared to α for monocrystalline silicon and gallium arsenide.

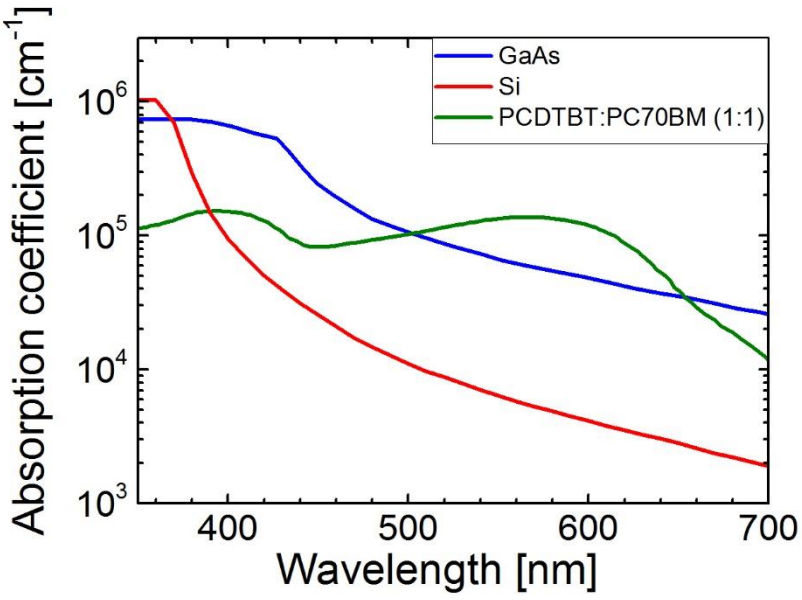

***Figure 6**. The absorption coefficient of a typical organic semiconductor blend (PCDTBT:PC70BM, blended 1:1 by weight) used for OSCs, compared to the absorption coefficient of silicon (Si) and gallium arsenide (GaAs). Si and GaAs data reproduced from [34].*

In an OSC, light absorption can occur in the donor as well as in acceptor material if the photon energy exceeds the optical gap. It is important to note that the optical gap ($E_{\mathrm{gap}}^{\mathrm{optical}}$) is lower than the electrical gap E_{gap} in inorganic semiconductors due to the large binding energy of the exciton ($E_{\mathrm{b}}^{\mathrm{EX}}$),

$$E_{\mathrm{gap}}^{\mathrm{optical}} = E_{\mathrm{gap}} - E_{\mathrm{b}}^{\mathrm{EX}}. \tag{6}$$

The strong light absorption allows employing very thin active layers (e.g. between 50 – 500 nm), which are orders of magnitude thinner than used for Si or other thin-film solar cells (with active layers exceeding several μm).

In order to calculate the light absorption efficiency, the cell needs to be considered as a thin film, low finesse optical cavity. Optical effects such as light reflections, light interference and parasitic absorptions in non-active layers need to be taken into account. **Figure 7** illustrates the light absorption in a photovoltaic diode in comparison to the film absorption on a glass slide.

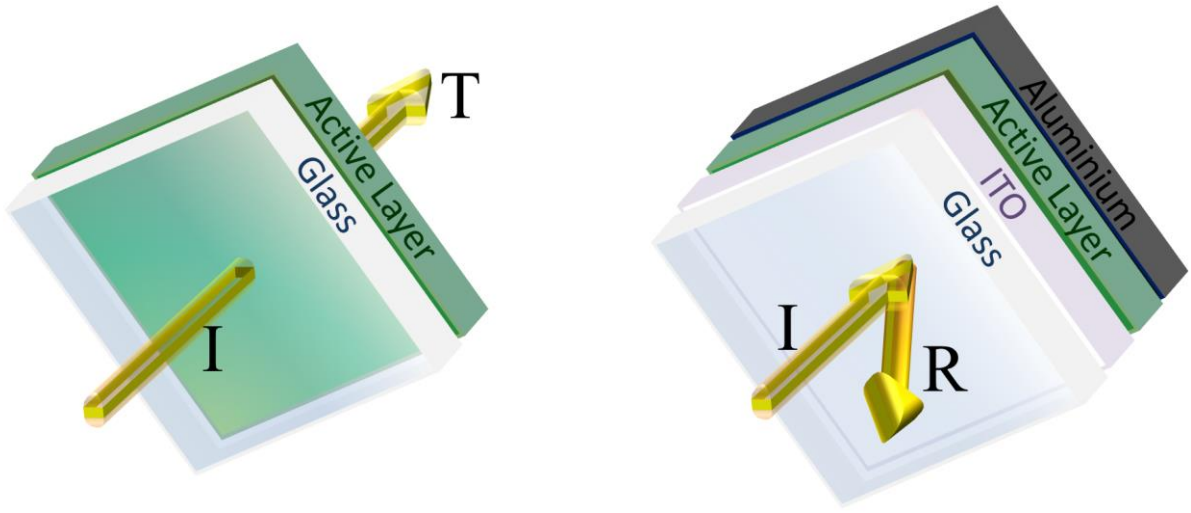

Figure 7*. The active layer absorption of a film on a glass slide (left) is different to the active layer absorption of the same film sandwiched between two electrodes (right) due to the back reflection of the light and optical cavity effects.*

According to Armin *et al.* [35] the most suitable strategy to obtain the desired active layer absorption is a multistep approach: First, the device reflectance spectra $R(\lambda)$ needs to be measured. As the back electrode is non-transparent, the device absorption spectra $A(\lambda)$ can be obtained *via* 1 - $R(\lambda)$. Second, the parasitic absorption in non-active layers such as the electrodes and electron/hole transport layers needs to be subtracted from $A(\lambda)$. The parasitic absorption can be estimated by simulating the optical field distribution and absorptions in all stack layers, using transfer matrix calculations [36]. This requires the knowledge of the spectral dependence of the refractive index n_{r} and the absorption coefficient k for all layers, which can be experimentally measured using spectroscopic ellipsometry.

II.5 Charge Transport and Recombination

Charge transport in low mobility organic semiconductors (< 1cm^2 V^{-1}s^{-1}) can be understood as polarons hopping from molecule site to molecule site towards the extracting electrodes in the presence of the built-in field. A simple intuitive approach to calculate the hopping rate is given by Miller-Abraham theory [37, 38], which describes the charge transport via a combination of phonon-assisted tunnelling from hopping site *i* to *j*, and thermal activation. The hopping rate in the Miller-Abraham formalism is given by

$$k_{ij} = v_0 \, exp^{-\gamma r_{ij}} \begin{cases} exp^{-\frac{\epsilon_j - \epsilon_i}{k_{\mathrm{B}} T}}, & if\ \epsilon_j > \epsilon_i \\ 1 & if\ \epsilon_j < \epsilon_i \end{cases}, \tag{7}$$

where, v_0 is the phonon vibration frequency or the jump-attempt rate; γ the inverse localization radius describing how well charges can tunnel from site *i* to *j*; r_{ij} is the distance between the sites with energy $\epsilon_{i\,(j)}$; k_{B} is the Boltzmann constant and *T* the temperature. The hopping velocity is

$$v_{ij} = r_{ij}/t_{ij} = r_{ij}\, k_{ij}\,, \tag{8}$$

where t_{ij} is the time needed for a single hop. The hopping rate is, therefore, proportional to the mobility *via*

$$\mu = < r_{ij} k_{ij} > E \,, \tag{9}$$

where E the electric field, and $< \cdots >$ denotes the spatial average. The mobility defines the time it takes charge carrier to transit from one device electrode to the other electrode, i.e. the transit (or extraction) time

$$t_{\mathrm{tr}} = d^2/\mu U \,, \tag{10}$$

where U is the effective driving voltage of the cell.

In order to understand the transport of the charge carriers to the extracting electrodes, one needs to consider the recombination rate of free polarons [39, 40, 41], and their lifetime τ. The recombination rate follows from simple considerations. The recombination process involves always the annihilation of one electron and one hole (a "bimolecular" processes) or multiple particles at the same time. Because the latter case occurs only at very high intensities it be will excluded in the following considerations. The recombination rate R ($cm^{-3}s^{-1}$) is therefore given by product of the electron density n and the hole density p in the device,

$$R = k_{\mathrm{bulk}} np \tag{11}$$

Where k_{bulk} is the bimolecular recombiantion rate coefficient (cm^3s^{-1}). The electron and hole lifetimes are related to the recombination coefficient *via*

$$\tau_{\mathrm{e}} = \frac{1}{k_{\mathrm{bulk}} p} \qquad \text{and} \qquad \tau_{\mathrm{h}} = \frac{1}{k_{\mathrm{bulk}} n} \tag{12}$$

i.e. the liftime decreases with increasing carrier concentration p (or n). A simple conclusion is that charge extraction will be efficient if

$$t_{\mathrm{tr}} < \min(\tau_{\mathrm{e}}, \tau_{\mathrm{h}}) \,. \tag{13}$$

To estimate k_{bulk}, one needs to consider the mean free path of charge carriers in relation to the Coulomb capture radius. In most organic semiconductors with mobility <1 $cm^2V^{-1}s^{-1}$, the charge carriers are scattered at almost every molecule site. The mean free path can, therefore, be approximated by the lattice constant. The Coulomb capture radius is defined as the distance at which the Coulombic attractive potential energy

$$E_{\mathrm{C}} = \frac{e^2}{4\pi\epsilon_{\mathrm{r}}\epsilon_0 r}, \tag{14}$$

equals the kinetic thermal energy of the carrier

$$E_{kin,thermal} = k_{\mathrm{B}}T\,. \tag{15}$$

The Coulomb capture radius (also known as Onsager radius [42]) is therefore

$$r_{\mathrm{c}} = \frac{e^2}{4\pi\epsilon\epsilon_0 k_{\mathrm{B}}T}. \tag{16}$$

At room temperature and typical relative dielectric constant of ~4, the Coulomb radius is ~15 nm, which is much larger than the scattering length. In this simple picture, charges are doomed to recombine as soon as they come within their Coulomb capture radius. The recombination coefficient of charges that feel their mutual Coulomb attraction can be described using Langevin's theory from 1903 [43]. Langevin calculated the recombination rate coefficient of cations and anions in a gas from the time it takes the ions to drift towards each other within their Coulomb field under the assumption that the subsequent ion bond formation is instantaneous. Generally, the recombination rate coefficient is expressed by the product of charge carrier velocity and the recombination cross section σ_{r}

$$k_{\mathrm{bulk}} = v\sigma_{\mathrm{r}}\,. \tag{17}$$

Under the assumption that the electric field of an opposite point charge extends to infinity, the drift velocity within the Coulomb field E_{C} of the opposite charge is

$$v = \mu E_{\mathrm{C}} = \mu \frac{e}{4\pi\varepsilon_{\mathrm{r}}\varepsilon_0 r^2} \,. \tag{18}$$

The recombination cross section of the moving carrier is

$$\sigma_r = 4\pi r^2 \,. \tag{19}$$

The resulting Langevin recombination coefficient is consequently

$$k_{\mathrm{L}} = \frac{e(\mu_e + \mu_h)}{\epsilon_r \epsilon_0}, \tag{20}$$

assuming that the opposite charge carrier also moves with a certain mobility. As carriers recombine with the speed they can possibly approach each other k_{L} represents an upper limit of the recombination coefficient.

It is noteworthy to mention that the same recombination coefficient applies to diffusing polarons outside the Coulomb radius, which can be shown using the Debye-Smoluchowski formalism [44, 45, 46, 47] for ions in solution in the limit of small ion encounter radii - where bond formation occurs.

Langevin recombination has been observed in many organic solids [48, 49, 50, 51], although exceptions apply. Especially, many efficient organic semiconductors blends [52] exhibit “Non-Langevin“ recombination dynamics, where the recombination rate is substantially lower than predicted by Langevin [49, 53, 54]. In these cases, the recombination rate coeffienct k_{bulk} is surpressed relative to the Langevin rate coefficient k_{L}. The surpression is specified by the reduction factor

$$\gamma_{\mathrm{L}} = \frac{k_{\mathrm{L}}}{k_{\mathrm{bulk}}} \,. \tag{21}$$

Non-Langvin materials posses the advantage that they can sustain higher carrier densities, above which bimolecular recombination occurs. A well-known example is regio-regular-

Poly(3-hexylthiophene-2,5-diyl (rr-P3HT):PCBM, where the recombination coefficients can be as low as $\sim k_{\mathrm{L}}/10^4$ were observed [53].

Although, several factors could potentially influence k_{bulk}, such as the charge transport dimension [55], and weak the external electric field [56]; commonly there are two accepted mechanism, which lead to a recombination rate coefficient below Langevin's coefficient: (i) encounter limited recombination as discussed in the following, and (ii) CTS re-dissociation controlled recombination, as discussed in **Section II.9.5**.

II.5.1 Encounter Limited Recombination

Langevin recombination can only apply to a single phase. Encounter limited (reduced) recombination applies to BHJs where charge carriers are confined to different phases and recombination only occurs at the donor: acceptor interface. In a BHJ, the carrier that reaches the interface first has to wait for the slower carrier in order for a recombination event to occur. Koster et al. [57] therefore proposed an amendment to the bimolecular recombination rate - the slower carrier limited recombination rate coefficient [58].

$$k_{\mathrm{slower}} = \frac{e\,\mu_{\mathrm{s}}}{\epsilon_{\mathrm{r}}\epsilon_0}. \tag{22}$$

This rate can be, however, only correct in a bilayer, and only when the faster carrier reaches the interface first, as illustrated in **Figure *8*** .

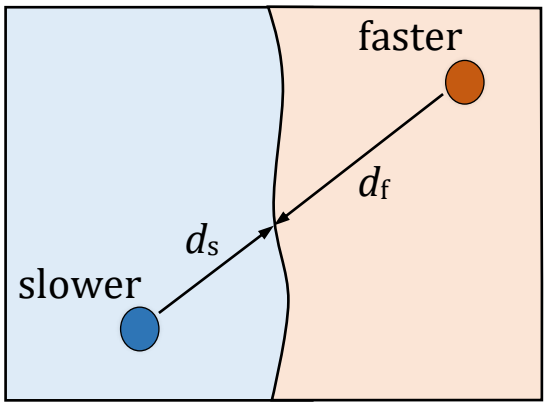

***Figure 8**. Illustration showing the recombination of an electron and hole in a bilayer, where carriers are confined to different phases. In such a system, the faster carrier has to wait at the interface for the slower carrier in case imbalanced carrier mobilities.*

Even in a bilayer there are configurations where the faster carrier is much further away from the interface compared to the slower ($d_\mathrm{f}/d_\mathrm{s} > \mu_\mathrm{f}/\mu_\mathrm{s}$). In these configurations the arrival of the faster carrier is the rate limiting step for the recombination rate.

In a BHJ with multiple interconnected donor: acceptor phases in the nanometre regime, one needs to consider the domain size in relation to the Coulomb capture radius. Intuitively, one might expect that the recombination rate in a BHJ is somewhere in between the Blom-Koster slower carrier limited rate and the Langevin rate, which applies in the limit of infinitely small donor: acceptor phases. This was confirmed in 2008, by Groves and Greenham using Monte-Carlo (MC) simulations. Very recently, Heiber et al. [59] have further shown that the origin of the strongly reduced recombination is not necessarily an inherent property of BHJs due to the spatial separation of electrons and holes within different phases. This new study shows that encounter-limited recombination can only result in relatively small reduction factors ~10 for typical domain sizes of BHJs (~5 – 50 nm) and reasonable faster to slower mobility ratios (~1-1000). Therefore, it is most likely that the reason behind the often observed strong suppression of the Langevin rate coefficient in BHJ systems lies elsewhere, which will be explained in **Section II.9.5**.

II.6 Charge Generation

Charge generation in excitonic low dielectric organic materials is a heavily debated issue and the process by which charge carriers are formed is still not fundamentally understood. However, there are many suggested theories in the literature which aim to understand this mechanism. As described in **Section II.2**, charge generation is in this work defined as the combined process of multiple mechanisms occurring from the photoexcitation, to free charge carriers. This section will discuss the critical steps and **Section II.9** recent developments in this area.

II.6.1 Excitons

Following photon absorption, an electrically neutral quasiparticle called an exciton, is formed. Excitons are classified according to their radius, as defined by the average separation of the electron from its corresponding hole: (i) The Frenkel exciton located on a single molecular site with a radius comparable to the distance of separation of the molecules (lattice constant). (ii) The Wannier-Mott exciton, with radius more than 1 order of magnitude larger than the intermolecular separation (lattice spacing). The Wannier-Mott exciton is mainly found in inorganic semiconductors, and the excitation in organic semiconductors is typically of the Frenkel-type with strong Coulomb binding between charges of opposite polarities.

Conventionally it is thought that exciton dissociation occurs at the donor:acceptor interface, whereby either the electron or the hole transfers to a molecule across the interface, leaving a charge of the opposite polarity on the other side. As such the diffusion length of excitons can be important which is given by

$$L_{\mathrm{D}} = \sqrt{D/k_{\mathrm{diff(EX)}}}\,, \tag{23}$$

where D is the Einstein diffusion coefficient and $k_{\mathrm{diff(EX)}}$ the diffusion rate constant. The diffusion length is usually on the order of ~10 nm in conjugated polymers [19]. If the exciton does not reach an interface it will alternatively get trapped due interactions with lattice phonons and relaxes back to ground state. It is expected that exciton diffusion plays a significant role for charge generation in BHJs with interconnected mixed and neat phases in the nanometre regime. However, the often observed "ultrafast" (<100 fs) charge transfer suggests that at least a fraction of excitons are immediately dissociated. This results in a Coulombically bound geminate pair – the CTS; or directly in free charges [60].

II.6.2 Marcus-Hush Theory

A well-established model to describe charge transfer processes was established by Marcus in 1956 [61] and Hush [62] and has been developed ever since, resulting in the Nobel price for Marcus in chemistry in 1992 [63]. Marcus-Hush theory is an intuitive, (semi-)classical approach

to describe electron transfer reactions for a broad range of chemical and biological reactions [63]. In Marcus-Hush theory, the exciton dissociation rate depends on (i) the driving force for dissociation - the change in the Gibbs free energy ΔG, and (ii) on the reorganization energy λ - the energy needed to transfer the equilibrium configuration of the excited donor:acceptor (D*A) state (reactant) into the equilibrium position of the final charge transferred state (D^+A^-) (product). Therefore, λ takes into account the polaronic nature of charge carriers to distort the surrounding molecules during charge transfer. Together, ΔG and λ define the Gibbs energy barrier for dissociation that defines the dissociation rate k_{d} via Boltzmann statistics

$$k_{\mathrm{d}} = A\, exp^{-\Delta G_{\mathrm{B}}/k_{\mathrm{B}}T}\,, \tag{24}$$

where A is a prefactor that depends on the reaction type, solvent and exponentially on the distance between the molecules. In order to estimate the energy barrier, the movement of the atomic nuclei involved in the charge transfer process is described by harmonic oscillations around the equilibrium positions of the initial and final state. The harmonic oscillators are represented by energy parabolas in the configuration space and are sketched in **Figure 9** (**a**) for the initial (D*A) and final state (D^+D^-) as a function of a generalized reaction coordinate.

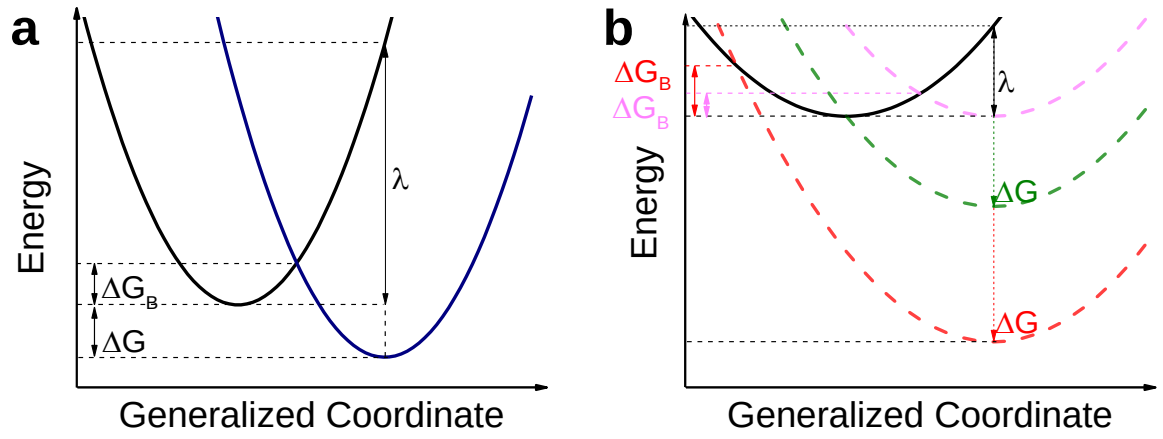

***Figure 9**. (**a**) Energy parabolas of the excited donor:acceptor (D*A) state and the charge transferred state (D^+A^-). The energy barrier for dissociation (ΔG_B) is given by the energy difference between the initial state and the energy at the intersection of the 2 parabola. ΔG_B can be estimated from geometrical considerations considering the change in the Gibbs free energy for dissociation ΔG and the reorganization energy λ. (**b**) Energy parabolas with*

different energetic driving forces ΔG and identical λ. The dissociation rate is a maximum if ΔG equals λ, but decreases for driving forces larger or lower than the reorganization energy.

If one takes the coordinates (0,0) for the equilibrium position of the left parabola and (a,b) for the final state, as well as the functional dependence $y \sim x^2$ of both curves, one can calculate the activation energy for the charge transfer process from the intersection of the 2 parabolas and the charge transfer rate

$$\Delta G_B = (\Delta G + \lambda)^2 / 4\lambda \,, \tag{25}$$

$$k_{\mathrm{d}} = a\, exp^{-\beta r} exp^{-\frac{(\Delta G+\lambda)^2}{4\lambda k_{\mathrm{B}} T}} \,. \tag{26}$$

Equation 26 displays a quadratic (Gaussian) dependence of k_{d} on ΔG. The theory predicts a peak of the dissociation rate at $\Delta G \sim \lambda$, but also a reduction in the transfer rate for too large driving forces $\Delta G > \lambda$ (Markus-Hush inverted region), as illustrated in **Figure 9** (**b**).

The applicability of Marcus-Hush theory to describe photoinduced charge transfer processes in OSCs has been demonstrated by Coffey et al. [64]. In this work, BHJs with very imbalanced donor:acceptor concentrations were studied, where the dilute phase was directly excited in order to overcome limitations imposed by the limited exciton diffusion length. However, Marcus-Hush theory does not consider the exciton binding energy, as well as quantum mechanical effects such as charge carrier delocalization and coherent electron transfer [60]. Instead, the theory rather underlines the importance of the reorganization energy as an additional energy barrier for dissociation. It is also likely that other processes than the actual charge transfer step limit the overall charge generation yield, such as exciton diffusion or the CTS dissociation, which will be detailed in the next section.

II.6.3 Charge-Transfer States

It is clear from basic calculations (**Equation 14**) that the Coulomb binding energy between the electron and hole residing on adjacent molecules, with typical separation of ~1.5 nm [65] greatly exceeds the thermal kinetic energy (320 meV vs. 26 meV, respectively). This renders

the mechanism by which the CTS separates, and how this occurs hotly contested, and quite possibly different in different OSC systems. Recent findings in this context will be discussed in **Section II.9**, after introducing a model to describe the dynamics and yield of CTS dissociation, and experimental techniques.

II.6.4 Onsager-Braun Theory

Braun's model [66], based on Onsager's theory of ionic dissociation [42], is a standard model to describe charge transfer separation in donor:acceptor solids. The model is based on the kinetic competition between the dissociation (k_d) and recombination (k_f) rate constants of the CTS, but does not consider charge extraction. The dissociation yield of a CTS is given by the branching ratio

$$\eta_\mathrm{CT} = \frac{k_\mathrm{d}(E)}{k_\mathrm{d}(E) + k_f}, \tag{27}$$

where the dissociation rate depends on the electric field E. The recombination from the charge-separated (CS) state back to the CT-state with rate constant k_r is assumed to be described by Langevin theory [43, 51] (see **Section II.5**). Note, k_r and k_L from **Equation 20** are identical, except that k_r refers to a geminate recombination rate coefficient in contrast to the bimolecular recombination coefficient k_L. A key assumption of the Braun model is that dissociation and recombination are related by detailed balance, which implies that the CT and CS state populations (n_CT and n_CS, respectively) come into equilibrium after a photoexcitation. In equilibrium, the rate $R_\mathrm{CT-CS}$ from CT to CS is equal to the rate $R_\mathrm{CS-CT}$ from CS to CT

$$R_\mathrm{CT-CS} = R_\mathrm{CS-CT} \rightarrow k_\mathrm{d} n_\mathrm{CT} = k_\mathrm{r} n_\mathrm{CS}\,. \tag{28}$$

This means the ratio $k_\mathrm{d}/k_\mathrm{r}$ defines the ratio $n_\mathrm{CS}/n_\mathrm{CT}$, which is not dependent on the kinetic parameters. In this case, $k_\mathrm{d}/k_\mathrm{r}$ equals the equilibrium constant for charge separation K. Therefore, Braun concluded that k_d must also be proportional to $\mu_\mathrm{e} + \mu_\mathrm{h}$. Whether the condition of an equilibium between CT and CS (considering only geminate dissociation and recombination) is justified, is non-trivial, although it was recently proposed that an equilibrium

occurs in the case of a moderately reduced Langevin recombination coefficient $\gamma_{\mathrm{L}} \sim > 10$ [31]. Regardless if the equilibrium (or detailed balance) condition holds, if the charge carriers can move away from the interface as quickly as they can return, k_{d} and k_{r} depend, in the same way, on the kinetic parameters.

Braun also investigated the interaction of the CTS dipole with the local electric field and calculated that the equilibrium constant is proportional to the field

$$k_{\mathrm{d}} = k_{\mathrm{r}} K = \frac{e(\mu_{\mathrm{f}} + \mu_{\mathrm{s}})}{\epsilon_{\mathrm{r}} \epsilon_0} \left(\frac{3}{4\pi r^3} exp^{-\frac{\Delta E_{\mathrm{C}}}{k_{\mathrm{B}} T}} \right) * \left(1 + b + \frac{b^2}{3} + \frac{b^3}{18} + \cdots \right), \tag{29}$$

where ΔE_{C} is the Coulomb binding energy as given by **Equation 14** and b is proportional to the electric field $b = e^3 E / 8\pi \epsilon_{\mathrm{r}} \epsilon_0 k_{\mathrm{B}}^2 T^2 \sim E$.

A problem of the Braun model, is the use of the Langevin recombination rate which can differ in BHJs with varying domain sizes (as discussed **Section II.5.1**). Moreover, spectroscopic measurements often show that the dissociation (and recombination) happens on very short timescales (carriers may be formed within fs-to-ns [60, 67]). Therefore, for Braun's model to be accurate, initial (or "local") mobilities significantly larger than the measured bulk mobilities need to be assumed. For example, initial mobilities 1 ps after generation, close to ~ 0.1 $cm^2 V^{-1} s^{-1}$ were found in P3HT:PC70BM blends using Electric Field-Induced Second Harmonic measurements [68]. Similarly, the mobilities on a nm length scale obtained from Transient Microwave Conductivity measurements is typically 1, 2 orders of magnitude higher than the bulk mobility [69]. Possible reasons are that charges have to cross less or no domain boundaries in the nm regime, or charge delocalization over the polymer chain or several molecules.

II.7 Standard Techniques to Study Charge Transport and Recombination

The following 2 sections exemplify common experimental methodologies to measure the charge transport, recombination and charge generation (**Section II.8**) in organic semiconductor photovoltaic diodes, which were used in the work described in this thesis. Among the myriad

of methodologies to study the charge transport in organic semiconductors, the most intuitive approach is to measure the transit time of carriers from one electrode to the other side (**Equation 10**). Due to the often large mobility distribution and associated uncertainty of the average mobility value, at least 2 different techniques should be applied to more reliably specify the mobility. It is interesting to note that charge carrier mobilities measured using OFETs are often orders of magnitude larger compared to values obtained in diode configuration (which will be discussed in more detail in **Section II.9.6**).

II.7.1 Space Charge Limited Current

In diodes, carrier mobilities are most often obtained from the dark current density-voltage characteristic according to the widely used space charge limited current (SCLC) model [71, 72, 73]. According to the Mott-Gurney law, the photocurrent reaches the SCLC value at high enough effective voltages U [74, 75].

$$J_{\mathrm{SCL}} = \frac{9}{8}\mu\epsilon_r\epsilon_0 U^2/d^3 \,. \tag{30}$$

Apart from the factor 9/8, **Equation 30** basically predicts that the injection current is limited to the injection of the electrode charge CU per transit time (where C is the device capacitance). For BHJ OSCs, were both electrons and holes are injected from the electrodes, the SCLC is predicted to be proportional to the sum of the pure electron and hole SCLCs in the case of Langevin recombination [52, 75]. However, for operational OSCs this dependence is experimentally often not observed, possibly due to the presence of non-Langevin recombination, substantial charge carrier trapping, or large contact/series resistances cases [54]. In order to simplify the analysis, the methodology is usually applied to unipolar donor- (or acceptor-) only diodes, as well as unipolar BHJs where the injection of one carrier type is blocked (hole- or electron-only devices) [71, 73, 76].

For SCLC measurements on unipolar BHJ diodes, symmetric electrodes should be chosen to minimize complications due to a built-in voltage. After measurement of the dark JV-curve, the functional dependence between the current density and the voltage needs to be analysed:
I: J goes as U^2, then **Equation 30** can be applied.

II: $J \sim U^{<2}$ then contact or series resistance are limiting the injection.

III: $J \sim U^{>2}$ indicates trapped carriers that are de-trapped as the voltage and electric field increases [76]. This increases the effective carrier mobility according to the Poole-Frenkel effect [77]. A simple approach to deal with significant carrier trapping is to fit the JV-curve with the Poole-Frenkel modification of the Mott-Gurney law [76].

$$J_{\mathrm{SCL(PF)}} \sim \frac{9}{8}\mu_0 \epsilon_\mathrm{r} \epsilon_0 \frac{U^2}{d^3} \exp\left(0.89\, \gamma_{\mathrm{PF}} \sqrt{\frac{U}{d}}\right), \tag{31}$$

where γ_{PF} describes the electric-field dependence of the zero-field mobility μ_0. A typical dark JV-curve, fitted to the Poole-Frenkel modification of the SCLC law is shown in **Figure 10**.

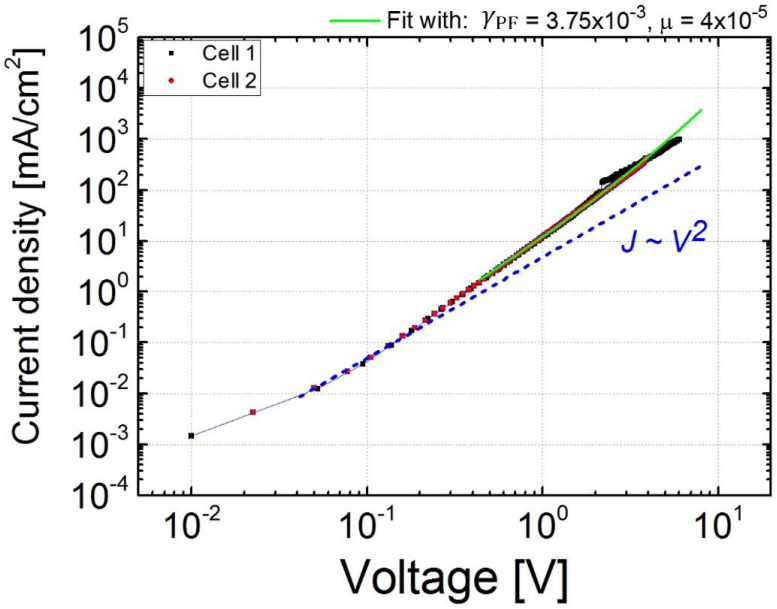

***Figure 10**. The Space Charge Limited Current (SCLC) of a typical BHJ with electrodes chosen to inject only holes. The SCLC is fitted to the Pole-Frenkel modification of the Mott-Gurney law to describe the electric field dependence of trapped charges and the with field increasing effective mobility (specified in $cm^2\ V^{-1}\ s^{-1}$).*

II.7.2 Time of Flight

In this transient experiment, a square voltage pulse is applied in reverse bias to extract the charge carriers [78, 79]. A short laser pulse in the middle of the square pulse generates the

charge carriers. Conventionally, Time of Flight (ToF) is typically applied to several μm thick organic semiconductor films to ensure surface photo-generation at the transparent (indium tin oxide, ITO) electrode. After generation a "sheet" of carriers travels through the device and a drop in the photocurrent transient indicates the arrival of the carriers, which allows one to estimate the transit time (**Equation 10**). Strongly dispersive transport, where the mobility is subject to a distribution (which is more pronounced in thick films), smears out the carrier arrival kink and complicates its identification. Moreover, the morphology and the mobility dependence on the film thickness [80, 81, 82] limits the usability of ToF [83].

II.7.3 Charge Extraction using Linearly Increasing Voltage

In this transient experiment, a triangular voltage pulse is applied in reverse bias to extract the charge carriers [70, 83]. A short laser pulse is used in Photogenerated Charge Extraction using Linearly Increasing Voltage (photo-CELIV) at the beginning of the voltage pulse to generate the carriers. As the extracting voltage increases the carriers are accelerated while moving towards the opposite electrode. A peak in the photocurrent transient signal marks the extraction maximum at t_{max}, which is proportional to the faster carrier transit time, allowing one to evaluate the faster carrier mobility. Also, the reduction factor γ_L of the Langevin rate coefficient can be conveniently measured from the ratio of the maximum extraction current and the dark displacement current step [83, 84].

Problems of the technique are that the extraction maximum can be obscured or confused with the premature extraction of charge carriers by the U_{BI}, especially in thin and/or high mobility devices. A voltage offset can be applied to cancel the U_{BI}, however, the pre-extraction of charge can often not be prevented. This often hinders the estimation of the faster carrier mobility as well as γ_L. Photo-CELIV also suffers from the technical difficulty of generating short triangle-shaped voltage pulses shorter than 1 μs. This limits the time-resolution of the experimental setup and renders the technique inapplicable for measuring charge carrier mobility and recombination in typical thin (~ 100 nm) polymer:fullerene blends with > ~10^{-4} $cm^2V^{-1}s^{-1}$.

II.8 Standard Techniques to Study Charge Generation

Photoinduced charge transfer happens on very short timescales of the order of femtoseconds to nanoseconds, therefore, a direct measurement of charge transport phenomena is experimentally very challenging. Similar to charge transport measurements, there are steady state and transient methods. While steady state measurements may allow quantification of the overall efficiency of a studied process, transit experiments further enable one to study the dynamics of the process. The combination of pulsed laser and high-performance multichannel detection devices allows the effective formation and detection of transient species. Complimentary techniques such as: (i) emission spectroscopy, (ii) absorption spectroscopy, and (iii) microwave conductivity are often used to generate a photophysical profile of charge generation. These techniques have also a wide range of time-resolutions, from femtosecond to millisecond and offer flexible and tunable light source. In the following, these 3 standard techniques are introduced.

II.8.1 Photo- and Electroluminescence

Photoluminescence (PL) (or fluorescence spectroscopy) is a powerful spectroscopic tool to measure the radiative recombination event from excited states, upon a laser excitation in transient or steady state mode. The contribution of the CTS to the PL spectrum is usually weaker because the recombination is dominated by non-radiative transitions. A standard application of PL is the analysis of the exciton emission intensity of a donor:acceptor blend compared to that of the neat films of either component. Usually, it is found that the steady-state PL of organic semiconductor blends is very efficiently quenched (~99%) compared to the PL spectrum of the neat materials, as illustrated in **Figure 11** (**a**) for the PCDTBT:PC60BM model system. Such results confirm efficient exciton dissociation in many BHJs [60]. In blends, the photoluminescence is also found to be redshifted due to the significant contribution from interfacial CTS [60], as illustrated for different PCDTBT:PCBM blends in **Figure 11** (**b**). However, it is difficult to disentangle the contribution from the CTS from singlet emission alone.

In contrast, Electroluminescence (EL) allows the presence of the CTS to be directly probed as well as its energy via charge carrier injection in forward bias. The principle behind this is based on the bimolecular recombination of the injected charge carriers which occurs necessarily via

the CTS (as explained in the Braun model **Section II.6.4**). It is also expected that the first state that allows for recombination is the lowest energetic state, i.e. the (relaxed) CTS. **Figure 11** (**c**) illustrate the EL spectra of Poly[2-methoxy-5-(3′,7′-dimethyloctyloxy)-1,4-phenylenevinylene] (MDMO-PPV) blended with PC60BM 1:4 by weight, and the constituent neat materials. The strongly redshifted PL spectrum is direct evidence for radiative CTS recombination that occurs only in the blend. The position of the peak allows one to further calculate the energy of the relaxed CTS. EL signals can be further analysed at varying bias voltages to study the electric field dependence of geminate recombination; and other groups have applied EL to study surface minority recombination [32, 33].

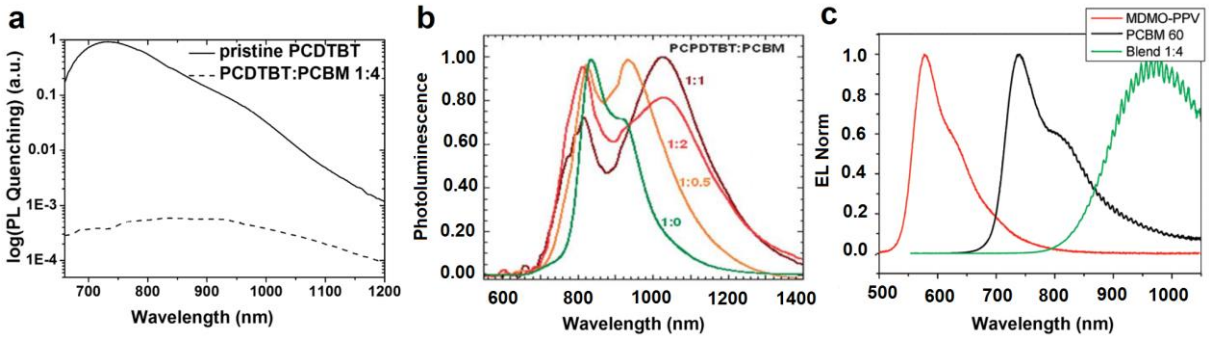

Figure 11. *(**a**) The photoluminescence (PL) spectrum of the PCDTBT:PCBM (1:4) blend is significantly quenched compared the emission spectrum of the neat PCDTBT. (**b**) Normalized PL spectra of different PCDTBT:PCBM blends demonstrating the redshift due to the contributions from the CTS in efficient blends. (**c**) The electroluminescence (EL) spectrum of MDMO:PPV (1:4) blend is not a superposition of the EL of the neat material, which shows that the bimolecular recombination in the blends proceeds via the (radiative) charge transfer state. (**a**) Reprinted with permission from ([85]). Copyright (2016) American Chemical Society. (**b**) Reproduced from [86] with permission of The Royal Society of Chemistry. (**c**) Adapted with permission from [87]. Copyright (2016) American Chemical Society.*

II.8.2 Transient Absorption Spectroscopy

One of the most common and powerful techniques used to for charge generation studies in organic semiconductors is transient absorption spectroscopy (TAS). TAS is an all-optical pump-probe technique used to probe excited state dynamics within films or multi-layer devices by the measurement of changes in the absorption of the sample. In a typical transient absorption

experiment, two laser pulses (typically around 150 fs) are incident on a sample in which they spatially overlap. The intense laser pulse excites the sample and the induced optical changes are monitored as a function of time by the absorption measurement of the weaker, broadband probe pulse, as sketched in **Figure 12** (**a**). Spectral changes in absorption of the sample due to different excited species such as singlet excitons, triplet excitons, bound and free charges are detected with a spectrometer. A two-dimensional recording of transient absorption as a function of wavelength and time is thus obtained. Varying the delay time between pump and probe allows for the study of the dynamics and lifetime of these species. A TAS absorption spectrum, as shown in **Figure** 12 (**b**) consists typically of 3 distinctive features: *ground state bleaching*, *stimulated emission*, and *photon induced absorption*.

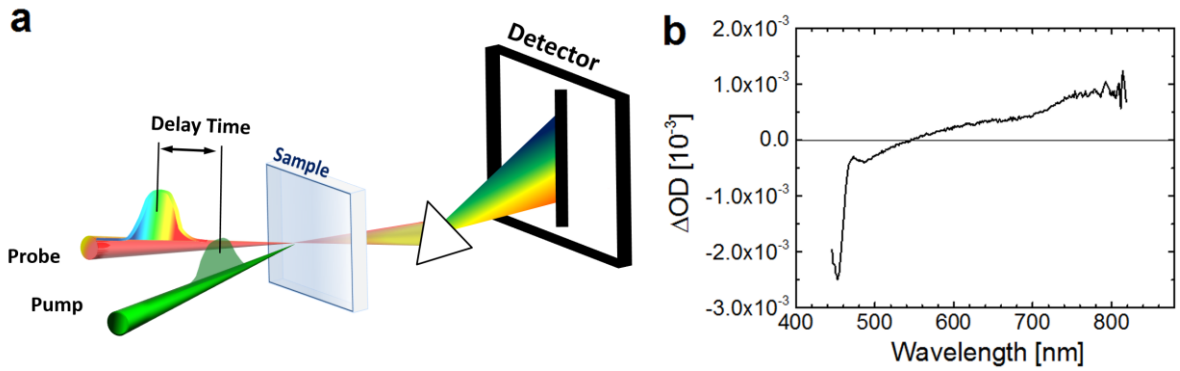

Figure 12. ***(a)*** *Schematic experimental setup of transient absorption spectroscopy highlighting the pump-probe procedure: The pump beam excites the system and the probe beam allows one to specify the excited species and their dynamics.* ***(b)*** *Example of a transient absorption spectra measured on an organic semiconductor blend. The change in the optical absorption ΔOD is plotted as a function of wavelength at a delay time of 10 ps after excitation at 600 nm. The ground state bleaching and stimulated emission overlap and cause a decrease in the sample absorption, while photoinduced absorption increases the sample absorption in the near infrared regime.*

Ground state bleaching happens if the ground state becomes depleted. After a fraction of the molecules has been promoted to the excited state with the aid of pump pulse, probing in this wavelength regime causes a decrease in the sample absorption. *Stimulated emission* is typically observed in the emissive region of the spectrum (i.e., it is Stokes shifted with respect to the ground-state bleach) where charges recombine radiatively to the ground state. Upon population

of the excited state, stimulated emission to the ground state will occur when the probe pulse passes through the excited volume. Since stimulated emission is a radiative recombination, it results in an increase of light intensity on the detector, corresponding to a negative signal. The third feature, the *photoinduced absorption* is most critical for the scope of this work since it is caused by excitons, bound or free charge populations. Upon excitation with the pump beam, optically allowed transitions from the excited states exist in certain wavelength regions, and absorption of the probe pulse at these wavelengths will occur. Consequently, a positive signal in the spectrum is observed in the wavelength region of excited-state absorption. Therefore, a TAS measurement in this regime allows to quantify the populations of these species and to study their decay dynamics. To identify whether the excited species are excitons or dissociated charges, the decay dynamics of blends can be compared to that of the neat material. Neat materials exhibit a characteristic exciton feature that decrease exponentially with time due to a first order recombination kinetics. The excitons are also present in blends, however, in efficient systems, they are typically rapidly quenched and transferred to bound or free carriers. Probing at very short timescales allows the visualisation of the transition from excitons to the CTS.

II.8.3 Transient Microwave Conductivity

Transient Microwave Conductivity (TRMC) is also a pump-probe experiment, where the pump is an optical excitation and the probe a microwave radiation with GHz frequency. Analogous to TAS, the photoexcitation creates free polarons that absorb the power of the subsequent microwave pulse. The change in the absorption of the microwave power ΔP is monitored at certain delay times and is related to the photoconductivity via

$$\frac{\Delta P}{P} = c\,\Delta\sigma \ , \tag{32}$$

where c is a cavity and device geometry dependent perfector. The photoconductivity is given - similar to **Equation** 1 - by

$$\sigma = en \sum (\mu_{\mathrm{h}} + \mu_{\mathrm{e}}) \, . \tag{33}$$

where the carrier density n is proportional to the generation yield η_{GEN} in the absence of carrier recombination. Therefore, the change in the microwave power as measured in TRMC is proportional to the yield-mobility-sum product

$$\frac{\Delta P}{P} \sim \eta_{\mathrm{GEN}} \sum \mu \tag{34}$$

in the absence of non-geminate recombination. The dependence on the mobility is explained by the mobility (velocity) dependent recombination coefficient of (bound or free) charge carriers interacting with the microwave (**Equation 17**).

II.9 Hot Topics

This section presents several examples of currently heavily debated topics in the field of organic solar cells and photodetectors. The presented topics revolve about the mechanism and understanding of charge generation as well as strategies to improve the photovoltaic performance. This section also establishes a more advanced theoretical framework on which the experimental results in **Chapter V** are based.

II.9.1 Dissociation via Relaxed or Hot Charge-Transfer States

One of the most interesting but also disputed questions is whether the excess energy (> blend optical gap) effectively contributes to the dissociation or charges, or if the excess energy is lost in a thermalization process prior to dissociation. Several experimental studies indicate either the first or the second possibility.

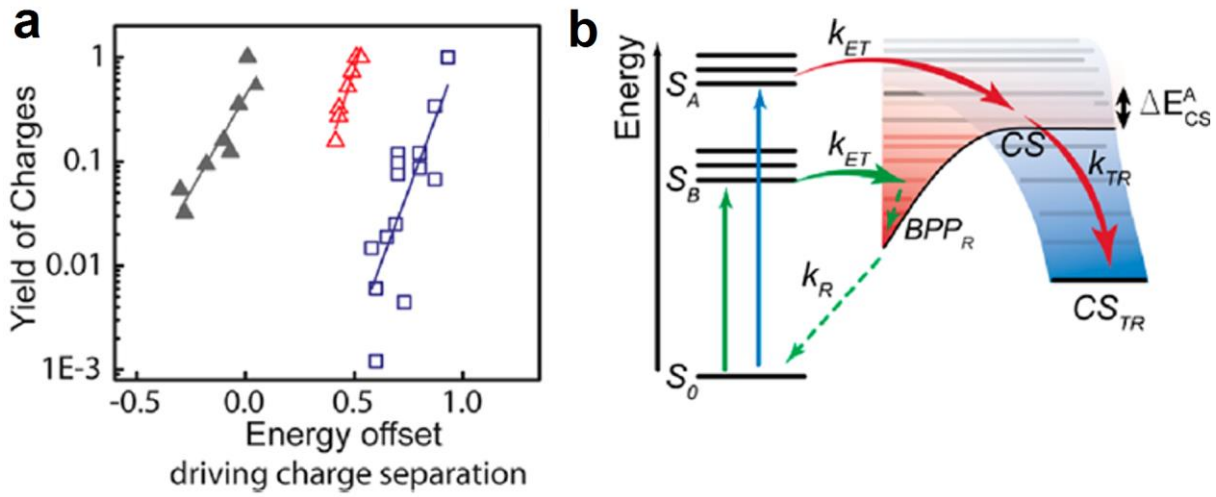

Figure 13. *(**a**) Charge generation yield versus energy offset ($\Delta E^{\mathrm{A}}_{\mathrm{CS}}$) for different classes of polymers blended with fullerenes. (black triangles) diketopyrrolopyrrole (DPP) based copolymers blended with PC70BM 1:2 by weight; (red triangles) thiazolothiazole-based polymers blended with PCBM and PCBM derivates; (blue squares) polythiophene-based polymers (such as P3HT) blended with PCBM 1:1 by weight. (**b**) Illustration of the dissociation pathway via hot CTS because the energy difference ($\Delta E^{\mathrm{A}}_{\mathrm{CS}}$) between the singlet polymer (S_{A}, S_{B}) exciton and the charge separated state ($E^{\mathrm{A}}_{\mathrm{CS}}$) defines the charge generation yield. A donor:acceptor combination where the dissociation proceeds via the red path is expected to be more efficient compared to a donor:acceptor combination where dissociation proceeds via the green path. Adapted with permission from [88]. Copyright (2016) American Chemical Society.*

For example Durrant et al. [88] tested over 300 different BHJ systems and observed a strong correlation between the donor:acceptor energy levels and the generation efficiency, a strong indication for a pathway facilitated by excess energy. The main results of ref. [88] are presented in **Figure 13** (**a**). The figure shows that the charge generation yield depends on the "energetic driving force" ($\Delta E^{\mathrm{A}}_{\mathrm{CS}} = S_1 - E^{\mathrm{A}}_{\mathrm{CS}}$), where S_1 is the lowest lying singlet polymer exciton and ($E^{\mathrm{A}}_{\mathrm{CS}}$) the energy of the charge separated state. The latter is given by the blend optical gap (**Equation 4)**. Therefore, $\Delta E^{\mathrm{A}}_{\mathrm{CS}}$ equates to the offset of the donor/acceptor EAs (δ_{EA}) less the exciton binding energy, i.e. $\Delta E^{A}_{CS} = \delta_{\mathrm{EA}} - E^{\mathrm{EX}}_{\mathrm{b}}$. **Figure 13** (**b**) underlines that charge generation proceeds *via* the hot CTS pathway, because a larger energetic offset is more efficient for charge generation (red arrows) compared to a low energetic offset (green arrows).

It appears that the conclusions of Durrant et al. (and many others [64]) disagree with several studies of Vandewal et al. [89], who demonstrated for a series of BHJs that the relaxed (lowest lying) CTS dissociates as efficiently as a CTS originating from a higher photon energy excitation. Vandewal et al. measured the spectral dependence of the IQE. **Figure 14** (**a**) presents the EQE, IQE, device absorption spectra as well as the CTS emission (EL) spectra $N(E)$ of MEH-PPV:PC61BM devices - all as a function of the photon energy. The absorption spectrum was determined by electroluminescence and photothermal deflection spectroscopy (PDS), which measures the change in refractive index due to heating of the surrounding medium upon the light absorption. The peak of the CTS emission spectrum corresponds to the relaxed CTS (CT_1 as marked), because the radiative decay from the CTS manifold is dominated by the CT_1 to ground state transitions. The graph demonstrates that the relaxed CTS dissociates as efficiently as higher-energy excitations, which was also confirmed for many other BHJ OSCs. The results indicates a thermal relaxation rate that is much faster compared to the CTS dissociation rate. **Figure 14** (**b**) illustrates the proposed model of charge generation via the lowest lying CTS [90]. The results of Vandewal et al. could indicate that the (lowest-lying) CTS dissociates thermally or assisted by the internal electric field.

Overall, the results of these two research groups highlight that more research is required to understand the role of the energy levels and charge thermalization on the charge generation yield.

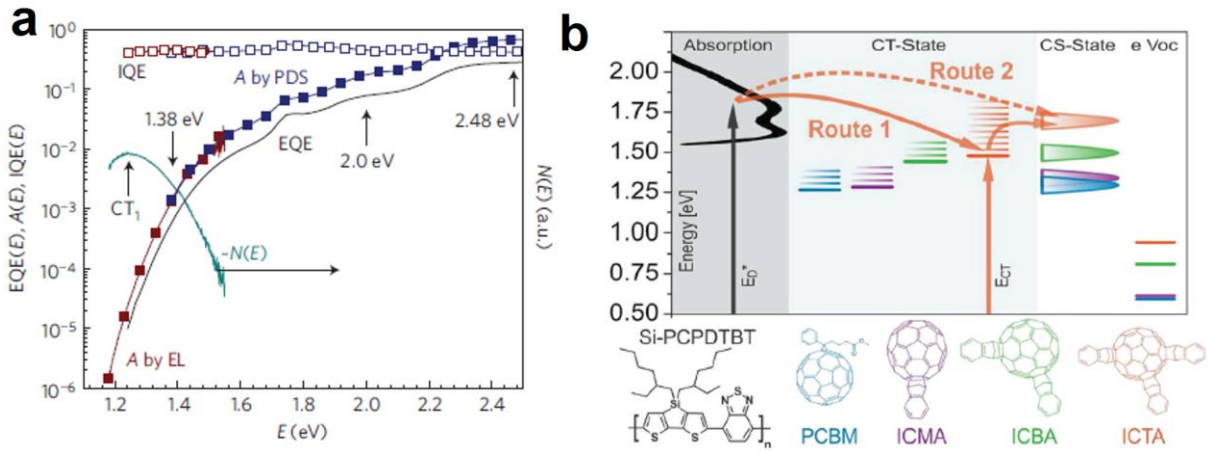

Figure 14. *(**a**) External/Internal Quantum Efficiencies (EQE/IQE), as well as light absorption $A(E)$ and charge-transfer state (CTS) emission spectra $N(E)$ for MEH-PPV:PC61BM devices. $N(E)$ was determined from electroluminescence measurements. The light absorption spectrum*

*was obtained from photo thermal deflection and electroluminescence. The IQE of the lowest lying CTS is identical to the IQE from higher energy excitations. (**b**) Proposed model of charge generation via the lowest lying CTS (route 1) rather than via a hot CTS (route 2) because thermal relaxation is substantially faster than the CTS dissociation. (**a**) Reprinted by permission from Macmillan Publishers Ltd: Nature Materials [89], copyright (2016). (**b**) Data reproduced with permission from John Wiley and Sons [90], copyright (2016).*

II.9.2 Electric Field Dependence of Charge Dissociation

Whether or not the dissociation of the CTS is dependent on the external/internal electric field is another controversial topic and of particular importance to understand the fill factor of organic solar cells. As described in the previous section, the Onsager-Braun model postulates the electric-field (*E*) dependence of the CTS dissociation yield due to dependence of the equilibrium constant *K* on *E* (**Equation 29**). For BHJ OSCs, there are, however, several points that render the field dependence of the dissociation rate constant non-trivial:

(i) The donor-acceptor interfaces may be randomly orientated with respect to the direction of *E* [60]. This would suggest that the initial separation of the interfacial bound-state is independent of *E* since some CTS will be pushed towards the interface and others away from it.

(ii) Comparing the field between charges that form the CTS (e.g. ~ 1.5×10^6 V/cm assuming an initial separation of 1.5 nm [65]) with the external electric field (e.g. ~ 7×10^4 V/cm, assuming 0.7 V built-in voltage and an active layer thickness of 100 nm) may suggest a negligible impact of *E* on the dissociation efficiency.

(iii) Morphological and energetic aspects or charge delocalization effects may outweigh the impact of the external electric field.

Many experimental studies, e.g. time-delayed-collection field (TDCF) experiments [91, 92, 93] or ultrafast spectroscopic measurements [60, 94] suggest an electric-field-independent CTS dissociation in relatively efficient blends. This thesis presents in **Chapter V** a study of the electric field dependence of the CTS dissociation.

II.9.3 Charge Delocalization

An emerging theory to explain the efficient charge separation in organic solar cells is based on the delocalization of the CTS [60, 95, 96, 97]. For example, Gélinas et al. [60] showed that efficient dissociation is achieved *via* "ultrafast" (~ 40 fs) long range (~4–5 nm) charge separation of delocalized π-electron states in ordered fullerene aggregates. Gelinas et al. tracked the electric field E that is generated as the charges separate using electro-absorption measurements. The electric field during separation changes the energy levels of neighbouring molecules, which leads to a change in their electronic transitions and optical absorptions. The electro-absorption signal can be measured with a fs time resolution using transient absorption spectroscopy. The electro-absorption amplitude (E_{A}) is defined as the energy that is stored in the electric field

$$E_{\mathrm{A}} \sim \int |E(t)^2| dV \tag{35}$$

which is as a function of time t. The E_{A} equals the Coulombic attractive potential energy from **Equation 14**, which allows one to measure the electron-hole separation (independent on the dipole orientation).

A main result of this work is the measurement of the temporal evolution of the singlet exciton and hole absorption signals, as well as the EA for different PCDTBT:PC60BM blend ratios, which are reproduced in **Figure 15** (**a**). Neat PCDTBT exhibits only the polymer's singlet exciton, which decays with time. The relatively inefficient 4:1 PCDTBT:PC60BM blend shows only the quenching of the singlet exciton and a signal of the photoinduced absorption of the polymer's cation (hole). The efficient 1:4 PCDTBT:PC60BM blend with high fullerene loading shows a similar feature as the 4:1 blend in terms of singlet exciton quenching and photoinduced absorption of the hole. However, in contrast to the 4:1 blend, the 1:4 blend shows an EA signal at timescales as early as 30 fs after excitation. The appearance of the EA signal implies the build-up of an electric field as the electron and hole separate. The absence of the EA in the 4:1 blend but presence of the hole absorption signal suggests the presence of a bound CTS that does not separate.

Figure 15 (**b**) presents the main conclusions that separation is achieved either *via*: (i) a single incoherent transition from localized donor states to delocalized acceptor eigenstates as described by Fermi's golden rule (as shown by the yellow curves for different coupling and disorder energies); (ii) or, *via* a phase-coherent superposition of acceptor eigenstates that propagates across the Coulomb quantum well (as shown by the red curves for different coupling and disorder energies). In this case, the charge separates 3-5 nm within ~300 fs. According to Gélinas et al., both mechanism can explain the observed separation on early timescales in contrast to fully localized electron transitions in the framework of Marcus-Hush theory. However, a study of the generation yield in devices with varying composition ratios, as shown in **Chapter V** of this thesis, suggests that electron delocalization is not enough for efficient CTS dissociation.

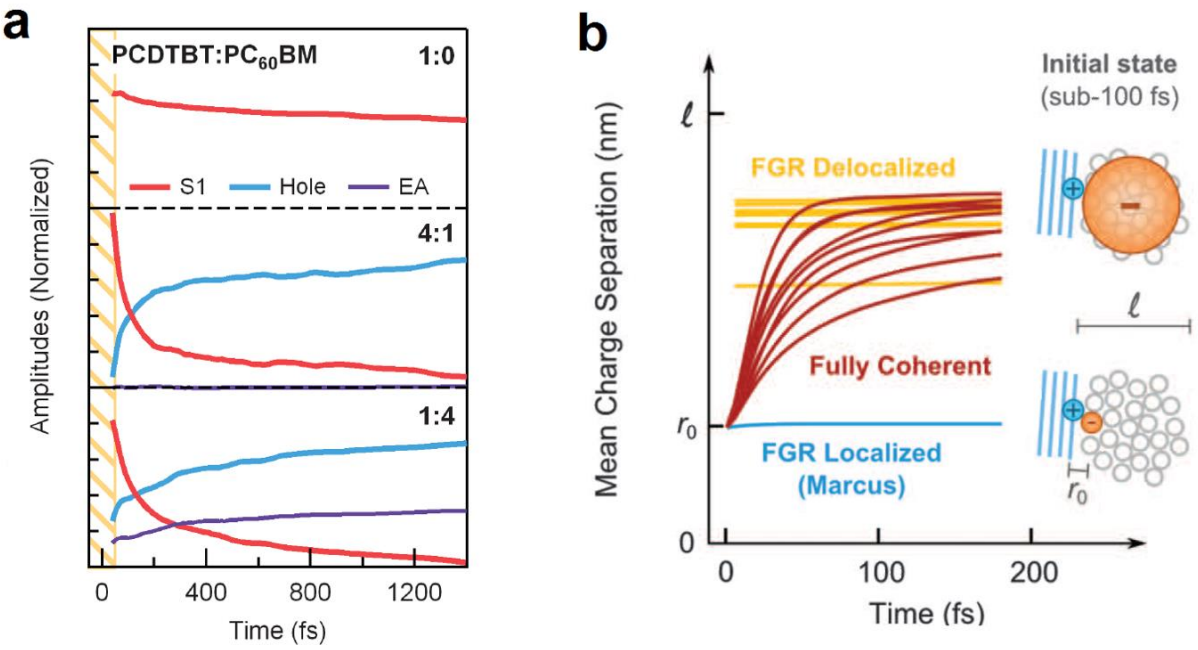

Figure 15. *(**a**) Transient absorption signals in PCDTBT:PCBM blends with varying blend ratio composition. The neat polymer shows the transient absorption of the singlet. The optimal 1:4 blend shows a significant electro absorption signal (E_A), which is absent in the inefficient 4:1 blend, which exhibits only a hole signal. The presence of the electro-absorption signal implies electron-hole separation on the measured time scales. (**b**) Schematic conclusion that charge separation proceeds either via (i) tunnelling from localized donor states to delocalized acceptor states according to Fermi's golden rule (yellow lines) or (ii) via the propagation of a phase-coherent wave packet (red lines). Electron tunnelling into localized states according to Marcus-*

Hush theory cannot explain the results (blue curve). From [60]. Reprinted with permission from AAAS.

II.9.4 Entropy

Recent studies suggest that entropy can contribute to charge dissociation due to a vast expansion of the number of available states as the carriers diffuse away from the interface [68, 98, 99, 100]. The entropy is a part of the Gibbs free energy (G) that defines the free energy barrier (ΔG_{B}) and the dissociation rate constant via the Arrhenius equation.

$$k_{\mathrm{d}} \sim \exp\left(-\frac{\Delta G_{\mathrm{B}}}{k_{\mathrm{B}}T}\right) , \tag{36}$$

$$G(r) = H(r) - T\Delta S = E(r) - k_{\mathrm{B}}T\ln\big(\Omega(r)\big) , \tag{37}$$

Where $H(r)$ is the enthalpy or the Coulomb binding energy, and $\Omega(r)$ the number of possible electron-hole configurations gained during charge separation. **Equation 37** shows that the separation r reduces the Coulomb barrier because the number of electron-hole configurations $\Omega(r)$ increases with increasing separation distance. To understand the impact of entropy on charge separation one needs to understand the functional form of $\Omega(r)$. The effect of entropy was first investigated by Clarke et al. [100] who showed that the magnitude of the entropy term is comparable to the Coulomb binding energy. Subsequently, Gregg [98] investigated the impact of the molecule dimension on the entropy. According to Gregg, fullerenes are 3 dimensional molecules since they can conduct equally well in all dimensions, while P3HT was used as an example of a 2D object as it conducts along the $\pi - \pi$ stacking direction as well as along the π conjugated backbone. For a 3D object, Gregg assumed that $\Omega(r)$ should scale with the surface area and not with the volume because for a given electron-hole separation r, the electron can occupy sites on a spherical surface centred around the hole, which gives

$$\Omega(r) = 4\pi\left(\frac{r}{a}\right)^2 , \tag{38}$$

where a is the lattice constant. However, Gregg modelled the entropy gain in a neat material, as opposed to a CTS at the interface. The main results of Gregg are reproduced in **Figure 16**, which shows the free-energy barrier as a function of the electron-hole separation in a single phase composed of molecules with different dimensions. Zinc octakis (B—octyloxyethyl) porphyrin (ZnOOEP) conducts only along the π-stacking direction, while P3HT and PCBM exhibit higher dimensional charge transport. The conclusions of this work are that the entropy is a key attribute for efficient charge separation and that higher-dimensional semiconductors provide inherent advantages for charge separation. The latter argument might explain why fullerenes - the only known true 3D organic semiconductors - play such an important role for BHJ OSCs.

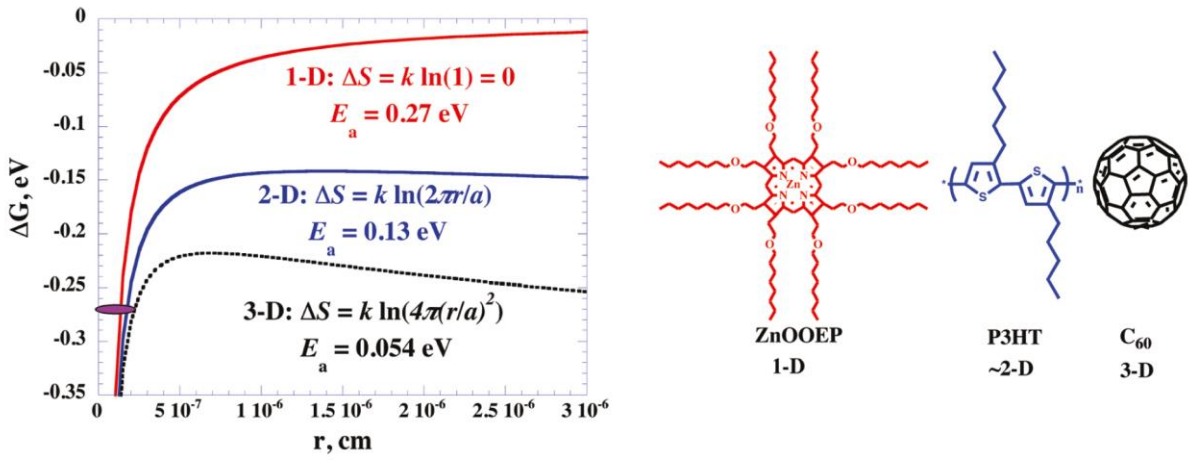

Figure 16. *The Gibbs free energy barrier G as a function of the separation distance (r) in single phase films composed of molecules with different dimensions for charge carrier conduction. Higher dimensional materials that conduct electricity in all 3 dimensions are beneficial for charge separation as the number of electron-hole configurations increases with the square of r. Adapted with permission from [98]. Copyright (2016) American Chemical Society.*

Overall, the entropic contribution to charge separation may give rise to efficient dissociation of the relaxed CTS [89]. Nevertheless, a quantitative model to describe $\Omega(r)$ for BHJs with disordered interfaces, varying domain sizes and composition ratios remains elusive. Moreover, direct experimental evidence of the entropy gain during separation is challenging, although first attempts were undertaken [99]. The effect of the entropy in devices with varying blend ratio compositions is further discussed in **Chapter V**.

II.9.5 Non–Encounter Limited Recombination

The Langevin model describes a recombination process where carriers immediately recombine once they find each other and form a CTS. The recombination rate in this picture is entirely controlled by the meeting probability of free carriers, and the finite re-dissociation probability of the CTS is not considered. As explained in **Section II.5.1**, an increasing body of work suggests that the strongly reduced recombination in many BHJs is related to the re-emission probably of the CTS. To calculate the expected Langevin reduction factor (γ_{L}) from macroscopic recombination measurements by considering the finite CT lifetime, the simple kinetic scheme from Braun's model can be used, which is shown in **Figure 17**.

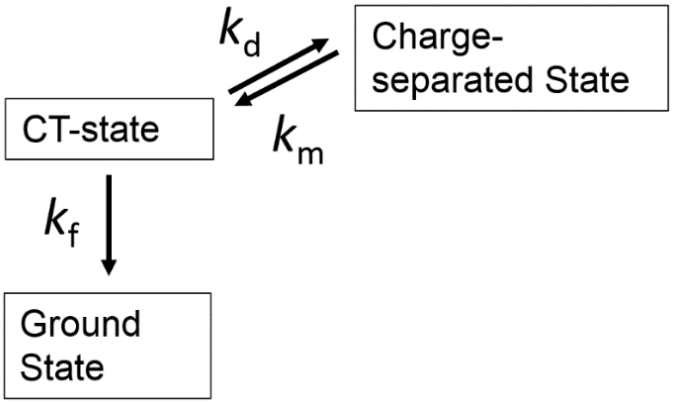

Figure 17*. The kinetic scheme of the Braun model shows that charge recombination is a 2 step process given by the encounter rate k_m of free charges times the recombination probability of the charge-transfer state $k_{\mathrm{f}}/(k_{\mathrm{f}}+k_{\mathrm{d}})$.*

The overall bulk recombination coefficient k_{bulk} is a 2 step process and given by the free carrier encounter rate coefficient k_{m} forming the CTS times the CTS recombination probability [31]. The latter is given by the branching ratio $k_{\mathrm{f}}/(k_{\mathrm{f}}+k_{\mathrm{d}})$. Therefore, we can write for the bulk recombination coefficient

$$k_{\mathrm{bulk}} = \frac{k_{\mathrm{L}}}{\gamma_{\mathrm{L}}} = \frac{k_{\mathrm{f}}}{k_{\mathrm{d}}+k_{\mathrm{f}}}k_{\mathrm{m}} = \frac{k_{\mathrm{f}}}{k_{\mathrm{d}}+k_{\mathrm{f}}}\frac{k_{\mathrm{L}}}{\gamma_{\mathrm{enc}}} = \frac{k_{\mathrm{L}}}{\gamma_{\mathrm{CT}}\gamma_{\mathrm{enc}}}, \tag{39}$$

where γ_{CT} and γ_{enc} are the reduction factors associated with the encounter limited recombination rate coefficient and the CTS recombination probability. The results presented in

Chapter V, show the implications of a high CTS re-dissociation probability (and γ_{CT}) on the overall photovoltaic performance.

II.9.6 Strategies for Improvements

Besides the sub-optimal energy levels of today's active layer components, the relatively low efficiencies can be traced back to 3 parameters, which are: (i) the dielectric constant ϵ_{r}; (ii) the charge carrier mobilities (μ); and (iii) the CTS recombination rate coefficient k_{f}. Importantly, each parameter (ϵ_r, μ and k_{f}) can simultaneously increase both η_{COLL} and η_{GEN}, and in turn all key photovoltaic parameters (J_{SC}, FF, V_{OC}). Ultimately, tuning the 3 parameters (μ, ϵ_{r}, k_{f}) could fully bridge the gap between present organic and inorganic solar cell materials. Recent strategies are summarised below.

Dielectric constant: A moderate increase of ϵ_{r} (2-3 times) allows for the reduction of the detrimental but necessary energy level offset δ_{EA} (as discussed in **Section II.3.2**) *via* lowering the binding and reorganization energies. *Ab initio* calculations show that the exciton binding energy depends on the dielectric constant [22, 101] *via*

$$E_{\mathrm{b}}^{\mathrm{EX}} \sim c/\epsilon_{\mathrm{r}}^2 \,, \tag{40}$$

where c is a constant. Koster et al. expected [22] that $E_{\mathrm{b}}^{\mathrm{EX}}$ decreases to a value below the thermal energy for high dielectric materials with $\epsilon_{\mathrm{r}} > 9$. Also, the reorganization energy (usually on the order of several hundred meV for currently used organic semiconductors) is expected to be significantly lower in high dielectric materials [22]. Overall, the detrimental energy level offset may be completely omitted - and in fact the BHJ concept - by using high dielectric materials. Although efforts to create purely organic semiconductors with high ϵ_{r} approaching that of inorganic semiconductors are still in their infancy, recent results demonstrate that a static dielectric constant of ~10 can be achieved by replacing the alkyl side chains by short ethylene glycol chains [102].

Carrier Mobility: A high mobility increases the charge collection η_{COLL} (**Section II.5**), but also the CTS dissociation rate constant k_{d} (**Equation 29**). A high mobility also allows δ_{EA} to be reduced because carriers can escape the Coulomb barrier more easily if the mobilities

approach those of inorganic semiconductors. It is interesting to note that the mobilities of organic semiconductors in OFET structures are already comparable to polycrystalline silicon with recently achieved mobilities approaching ~ 10 $cm^2V^{-1}s^{-1}$ [103]. However, to the author's knowledge, the mobilities have never been observed to be higher than ~ 10^{-2} to 10^{-1} $cm^2V^{-1}s^{-1}$ in diode configuration, with the electron mobility of PC70BM [104] and the hole mobility of diketopyrrolo-pyrrole-dithiophene-thienothiophene (DPP-DTT) being closest to that limit (μ_h ~ 0.1 $cm^2V^{-1}s^{-1}$ [105]). The differences between OFETs and diodes could be related to the different charge transport directions, the specific nature of the semiconductor/insulator interface of the OFET channel [71, 82, 106], as well as the different operating modes (charge injection, vs. photocurrent extraction). Given the importance of the charge carrier mobility on the photovoltaic performance, future research is required to better understand the mobility mismatch in diode and OFET configuration.

CTS recombination coefficient: Lowering the CTS recombination rate coefficient k_f could reduce both non-geminate and geminate recombination losses (**Equation 39**). However, to date, specific design principles to control k_f remain poorly understood. This thesis presents in **Chapter V** a detailed study of a BHJ OSCs with one of the highest reported photovoltaic performances. A strongly reduced bulk recombination coefficient was observed in this system due to a relatively low k_f (compared to k_d). The study may provide a unique opportunity to establish design principles to control the CTS recombination coefficient.

II.10 Chapter Summary

This chapter presented combined basic theoretical and experimental concepts relevant for the following results chapters. Consistent with the main focus of this work, theories and experimental techniques to understand the charge-transfer state dynamics, as well as the physics of charge transport and recombination were prominent. Disputed research topics in the field were discussed, along with strategies to improve the photovoltaic performance of organic light harvesting diodes.

The following chapters are based upon submitted and published works by the author in the peer reviewed literature. These works are grouped into three main parts: Methodology Development

(**Chapter III**), Advances in Fundamental Understanding of Charge Transport (**Chapter IV**) and Advances in Fundamental Understanding of Charge Generation (**Chapter V**).

Chapter III: Methodology Development

Charge transport and recombination in organic semiconductors and associated photovoltaic diodes has been intensively studied using a considerable number of experimental techniques – some of them adapted from inorganic semiconductor solid state physics. Although these methodologies can each deliver very useful information about organic semiconductors as disordered systems, there are still several limitations associated with the applicability of the obtained results to operational solar cells and photodiodes. For example, these methodologies often require active layers that are significantly thicker than optimum (e.g. conventional ToF) and/or measurement conditions or device configurations not relevant to operational photocells (as OFETs, SCLC, photo-CELIV, see **Section II.7**). This motivated us to investigate ways to overcome the limitations of the commonly used techniques by approaching operational conditions when measuring the electro-optical properties of organic semiconductors.

In this chapter a transient photovoltage technique, that we term "resistance dependent photovoltage (RPV)" will be presented. RPV essentially extends the applicability of the previously established TOF methodology by combining the differential and integral operational modes. It allows one to obtain key charge transport parameters on operational organic solar cells, such as the mobilities of both electrons and holes, deeply trapped charges, and the bimolecular recombination coefficient in operational devices. This chapter consists of one

published paper, which exemplifies the application of RPV for mobility and trapping measurements. In addition, RPV can be used at high laser fluences (termed “HI-RPV”) to estimate the bimolecular recombination rate coefficient. The corresponding publication [49] is not presented in this thesis, although a brief description of HI-RPV is included in **Section V.3**.

III.1 RPV for Measurement of Charge Transport Parameters

In this section it will be shown that RPV provides key advantages over other charge mobility measurement techniques, notably: (a) it is applicable to thin films relevant to optoelectronic devices with diode-like geometries; (b) it is robust against optical interference effects; (c) both carrier types can be simultaneously measured in operational devices if the electron and hole mobilities are imbalanced; (d) deeply trapped charge carrier can be disentangled from mobile (or shallow-trapped) charge carriers; and (e) RPV is not as sensitive to the series resistance (mainly sheet resistance) as other techniques. However, there are also disadvantages and opportunities for further improvements, notably: RPV is not inherently selective to electrons and holes and the transport of both is superimposed and hard to disentangle in the case of moderately imbalanced mobilities (< ~ 10 times). The pulse duration of our laser (~5 ns) and the circuit response limits the time-resolution of our experimental setup to ~ 25 ns. Also, the assignment of the mean mobility value, in case of dispersive transport where the mobility is subject to a distribution, remains an approximation. The technique was used throughout the work described in this thesis and the obtained parameters are consistent with those obtained from other experimental techniques (e.g. SCLC, metal-insulator-semiconductor-CELIV [107] and intensity dependent photocurrent).

The supplementary information for this paper can be accessed online at (http://dx.doi.org/10.1038/srep05695).

The impact of hot charge carrier mobility on photocurrent losses in polymer-based solar cells

Abstract

A typical signature of charge extraction in disordered organic systems is dispersive transport, which implies a distribution of charge carrier mobilities that negatively impact on device performance. Dispersive transport has been commonly understood to originate from a time-dependent mobility of hot charge carriers that reduces as excess energy is lost during relaxation in the density of states. In contrast, we show via photon energy, electric field and film thickness independence of carrier mobilities that the dispersive photocurrent in organic solar cells originates not from the loss of excess energy during hot carrier thermalization, but rather from the loss of carrier density to trap states during transport. Our results emphasize that further efforts should be directed to minimizing the density of trap states, rather than controlling energetic relaxation of hot carriers within the density of states.

Introduction

While natural photosynthesis transfers electrons through a cascade of energy states, artificial photovoltaic systems must extract photogenerated charges to the electrodes, and despite recent performance gains [26], fundamental questions about this charge extraction still remain unanswered. There has been intense scrutiny of the mechanisms of charge generation and the impact of above-bandgap photon energy [65, 108, 109], however, this level of attention has not extended to studies of the *extraction* of such 'hot' charge carriers, despite the fact that efficient charge extraction is crucial for device performance [110].

The most characteristic feature of charge transport in disordered systems is the dispersion of the charge carrier movement velocities [38]. Dispersive transport harms device performance because the slowest carriers bring down the average mobility [111], and consequently, the vast majority of novel organic semiconductors remain inapplicable for efficient devices. Moreover, the detrimental effects of dispersion are exacerbated by the inhomogeneities in film thicknesses caused by the targeted low cost deposition methodologies, because the transit time distributions become dramatically longer and more dispersed in regions of increased thickness.

Dispersive transport in organic semiconductors is usually thought to be caused by the energetic relaxation of hot charge carriers within their density of states [112]. Spectroscopic measurements and Monte Carlo simulations have revealed energetic relaxation extending even to the microsecond timescales, where it could be relevant to bulk charge transport [113, 114]. Even if the bulk of the energetic relaxation were to occur on very fast timescales, there is still the question of whether residual thermalization might continue to long, microsecond timescales. This energetic relaxation is often understood to cause a time-dependent mobility and therefore explain dispersive current transients [115, 116], yet we will show here that this commonly-used model is inconsistent with our observations in high efficiency organic solar cell materials. Instead, there is an alternative mechanism for the creation of a distribution of carrier velocities, namely, via trapping. This observation has a very direct impact on the numerous models, theories and experimental results describing dispersive charge transport in disordered organic semiconductors. Furthermore, it points to a new strategy for improving charge transport "management" in devices such as organic solar cells.

The classic signature of dispersive transport is a time-of-flight photocurrent signal that decays with time even before the carriers have transited through the film [117]. This decay in photocurrent can occur due to two mechanisms, a reduction in carrier mobility, and/or a reduction in the number (or concentration) of moving carriers. The former, a time-dependent hot carrier mobility, is presently commonly believed to be the cause of dispersion in organic semiconductors [112, 115, 116] and it is usually understood to originate from a loss of energy as carriers thermalize within their density of states [118, 119, 120]. Higher energy carriers are expected to have a higher hopping probability, and hence a higher velocity [121, 122, 123], so the thermalization within the density of states causes the carrier mobility to decline. Recent studies [Melinana et al, Howard et al.] have reported mobility thermalization times on the order of microseconds. However, an alternative explanation for the decaying transient photocurrent, which is less commonly accepted in organic semiconductors, is a time dependent *concentration* that can arise if carriers are gradually lost to traps [124, 125, 126]. The photocurrent signal will continue to reduce as long as the net concentration of moving carriers continues to decrease. If that physical process prevails, there can be decaying photocurrent despite the moving carriers having a constant drift velocity. Additionally, if the cause of dispersion is trapping, then it will influence all devices, even those which operate in the dark [127, 128].

In this article, we demonstrate that a time-dependent hot carrier mobility cannot explain the dispersive transport in two well-known bulk heterojunction solar cells comprised of poly[*N*-9''-hepta-decanyl-2,7-carbazole-*alt*-5,5-(4',7'-di-2-thienyl-2',1',3'-benzothiadiazole)] (PCDTBT) [129] and [6,6]-phenyl-C_{70}-butyric acid methyl ester ($PC_{71}BM$) in an optimized blend ratio of 1:4 by weight [130]; as well as poly[[4,8-bis[(2-ethylhexyl)oxy]benzo[1,2-b:4,5-b']dithiophene-2,6-diyl] [3-fluoro-2-[(2-ethylhexyl)carbonyl]thieno[3,4-b]thiophenediyl]] (PTB7):$PC_{71}BM$ blends [131], the results of which are shown in the Supplementary Information. Both blends have been also extensively studied [54, 107, 132, 133] and are known to have quite different charge transport properties (PTB7:PC70BM being superior). In order to elucidate the cause for dispersive transport we performed transient photoconductivity experiments in which we vary the transit time by changing the electric field and/or device thickness. The expectation is that if the dominant cause of dispersive transport is mobility relaxation, then the average mobility and the amount of dispersion should vary with the electric field and/or film thickness, because longer transit times will allow for more relaxation to occur. Conversely, if the dominant effect is trapping, then it is the concentration of carriers which is changing in time rather than their mobility, and consequently, the average mobility and the dispersion range should not vary with film thickness or electric field. This transit time dependence allows these two dispersive mechanisms to be experimentally distinguished.

Results

Numerical Simulations of Resistance dependent PhotoVoltage (RPV) measurements

Our experiments were made possible by the development of a new transient photoconductivity technique that we call Resistance dependent PhotoVoltage (RPV), which is described here and in the Methods section. The experimental measurement circuit for RPV is shown in **Figure 1**. This setup is similar to time-of-flight, where charge carriers are photogenerated by a short low-intensity laser pulse. A low light intensity is necessary so that the electric field inside the device is undisturbed. The transient photosignal is determined by the competition between two simultaneous processes: the transport of charge carriers inside the film, and the response of the external RC circuit. Unique to the RPV approach, and in contrast with time-of-flight, the entire measurement is repeated at many different load resistances spanning the range from differential mode (small R) to integral mode (large R). The resistance is varied for two reasons: firstly, to

visualize the transit times, as will be shown below; and secondly, to reveal the slower carrier mobility by amplifying the slower carrier's conduction current. The slower carriers produce a much smaller current than the faster carriers, and their transit would be buried in the noise at resistances that are optimized for the faster carriers. Slower carriers have much longer transit times, allowing the use of larger resistances, and consequently allowing for their weaker electrical signal to be amplified. In this way, RPV bridges the gap between differential mode and integral mode time-of-flight, and allows measurement of the transport of both types of charge carriers.

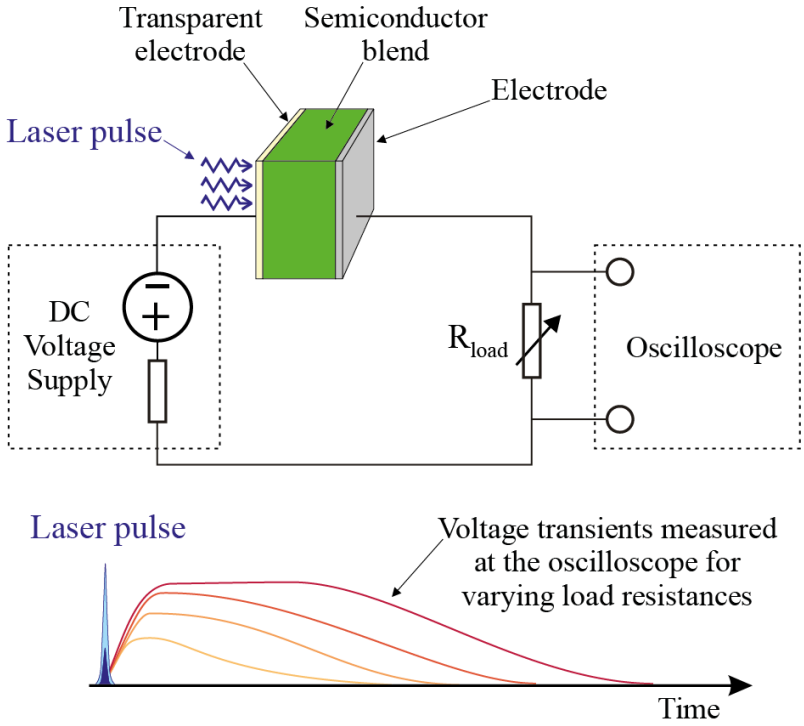

Figure 1. *Resistance dependent PhotoVoltage (RPV) measurement circuit (**top**) and timing diagram (**bottom**). A low light intensity nanosecond laser pulse is used to photogenerate charge carriers inside (for example) the semiconductor junction of an organic solar cell. Low light intensity is critical in the RPV experiment to ensure operation within the "small charge extraction mode" where the internal electric field distribution in the film is not altered by transported charges. After photogeneration, the charge carrier transport through the film is driven by the built-in or the applied external electric field, and the resulting transient photosignal is recorded by an oscilloscope. The transient photosignals are measured at various load resistances* R_{load}.

The combination of the *RC* circuit dynamics, dispersive transport, and optical interference effects prevent analytic analysis of the transients. To study highly dispersive systems, such as organic solar cells, the simultaneous impact of all these effects must be understood. We applied numerical simulations to develop this understanding. The simulations are described in the Methods section and in the Supplementary Information. Typical simulated transients for an organic solar cell with dispersive transport are shown in **Figure 2 (a)**. The transients show two distinct extraction "shoulders," as indicated by the arrows. The transients at different resistances assist in visually identifying the location of these "shoulders." The positions of these arrows correspond to the mean transit times required for the faster and slower carriers to cross the entire thickness of the film. In this simulation, carriers are repeatedly trapped and de-trapped, creating dispersion because the total time spent in traps is different for different carriers. The resulting distribution of transit times is shown at the top of **Figure 2** (**a**), and its approximate width is indicated by the shaded background. It can be seen that the RPV technique allows the mean charge carrier mobility to be obtained even in the presence of strong dispersion. In addition to shallow traps that cause dispersion, we also considered deep traps that immobilize carriers for times much longer than the transit time of either carrier. Long lived trapping is typical in disordered organic semiconductors [126, 134], because many organic materials behave as unipolar conductors, and solar cells often have strongly imbalanced mobilities [107]. In these cases, repeated photogeneration adds more trapped charge in the form of the immobilized charge carriers, which might accumulate with every repetitive laser shot, redistributing the electric field and distorting the measurement. **Figure 2 (b)** shows simulations of this film charging for the case of fast Langevin-type recombination under repeated laser shots, as would arise from the presence of deep trap states far inside the forbidden energy gap [75]. These are large resistance transients, in other words, the measurement circuit has integrated the photocurrent such that the peak voltage is proportional to the extracted charge. If the extracted charge is decreasing and the extraction time remains constant, then carriers must be lost to recombination and not due to field screening, and hence we conclude that the trapped charges act as recombination sites for the mobile carriers. However, the mobility of the charge carriers can be determined independently of the trapping effects, because the rapid Langevin recombination prevents the build-up of large amounts of trapped charge that would disturb the transit time.

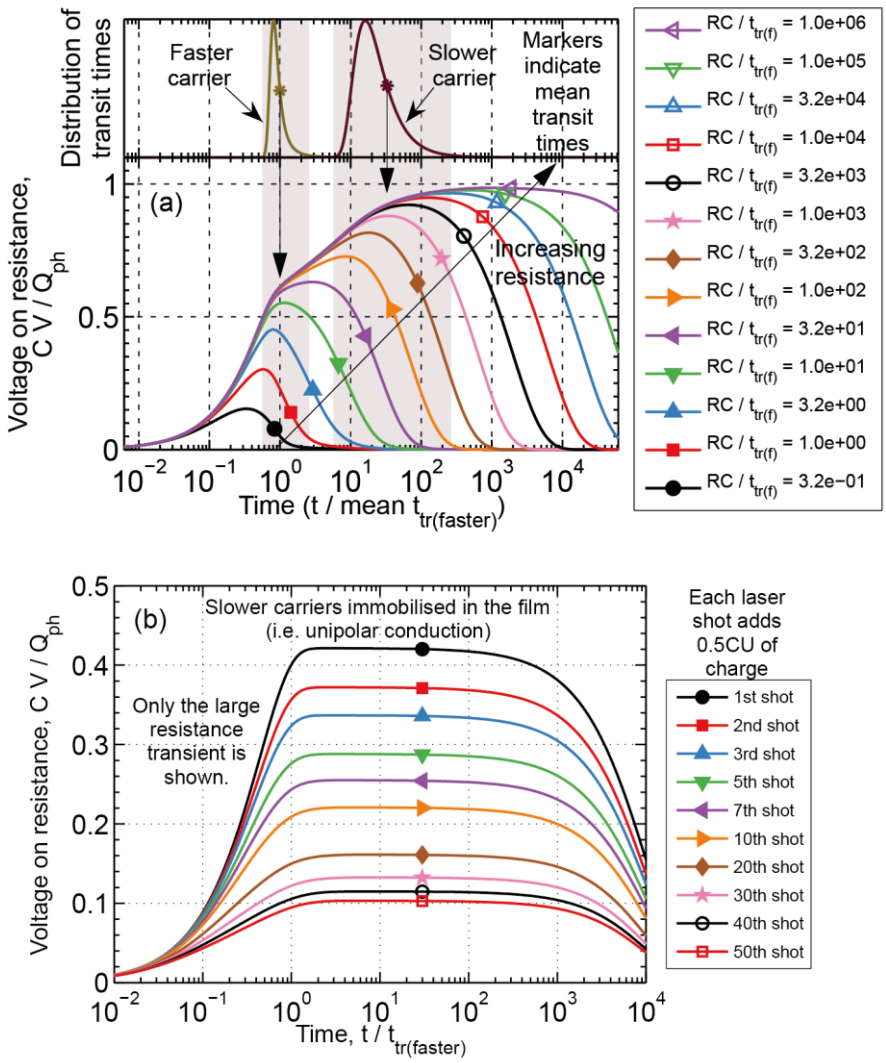

Figure 2. *Numerically simulated RPV transients in the case of* ***(a)*** *dispersive transport caused by shallow traps, and* ***(b)*** *film charging caused by deep traps.* ***(a)*** *In the case of dispersive transport, the extraction "shoulders" approximately correspond to the mean charge carrier mobility.* ***(b)*** *In the case of deep traps, the film becomes charged and the magnitude of the RPV transient is reduced in subsequent shots of the laser, but the transit "shoulder" remains unhindered which allows for reliable charge carrier mobility estimation.*

Figure 3 shows the recorded RPV transient signals for a PCDTBT:$PC_{71}BM$ solar cell. All transients were recorded at near to short-circuit conditions. This remains true even at large resistances, because the maximum photovoltage occurring during the transient is substantially less than the built-in voltage. The first shoulder marks the arrival time of faster carriers (27 ns), which is attributed to electron transport since the time scale is similar to that measured for

$PC_{71}BM$ (please refer to the Supplementary Information for measurements on $PC_{71}BM$). The second shoulder is less well defined due to the strongly dispersive nature of hole transport in this system, but marks the arrival of the slower carriers (2.59 µs). The mean electron and hole mobilities were determined from the intersections of tangents (dotted lines) fitted to the photovoltage rise corresponding to the movement of faster and slower carriers, as indicated by arrows in **Figure 3**. The approximate spread of arrival times is indicated by the shaded boxes (corresponding to the regions where the photovoltage transients deviate and saturate to the dotted lines). The edges of these shaded boxes give the "fastest" and "slowest" case transit times, from which we obtained the dispersion range in the mobilities for each species. This range is an essential feature of the dispersive transport exhibited by this system, because a single mobility value does not correctly quantify the transport when the system is dispersive. We measured the mean electron mobility to be 2.9×10^{-3} cm^2 V^{-1} s^{-1} with a dispersion range from 1.1×10^{-3} cm^2 V^{-1} s^{-1} to 4.5×10^{-3} cm^2 V^{-1} s^{-1} and the mean hole mobility to be 3×10^{-5} cm^2 V^{-1} s^{-1} with a dispersion range from 9.2×10^{-6} cm^2 V^{-1} s^{-1} to 7.4×10^{-5} cm^2 V^{-1} s^{-1}. Despite the high level of dispersion observed here (the hole dispersion range covers nearly an order of magnitude), the OPV device still maintains good performance. However, further work is necessary to identify the impact of the dispersion range on the performance of solar cells.

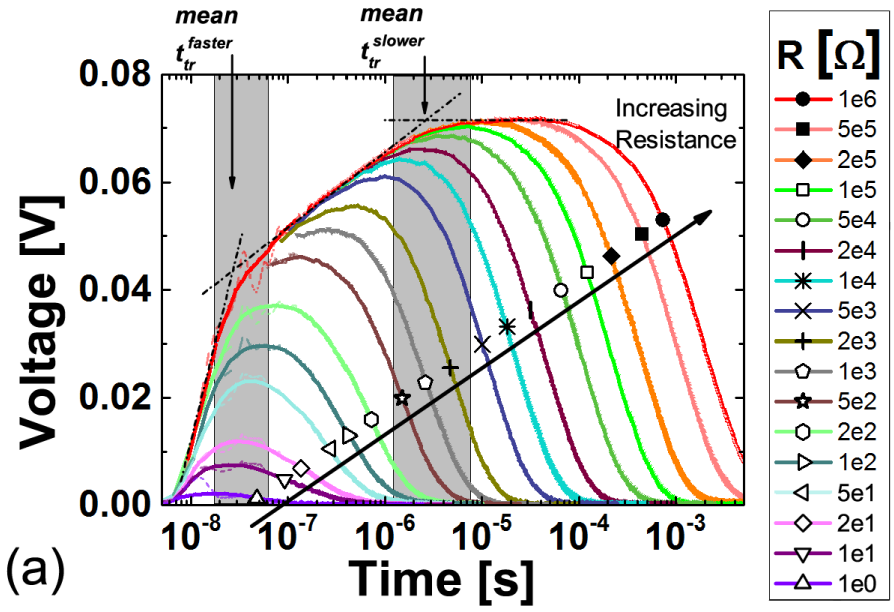

***Figure 3**. Experimentally measured RPV transient photo-signals in an optimized PCDTBT:$PC_{71}BM$ solar cell. Mean electron (faster) and hole (slower) transit times are marked, from which the respective mean mobilities are estimated. The dispersive nature of charge*

transport in the studied solar cells is highlighted by shaded boxes marking the range of carrier arrival times. Thin curves show recorded data, while bold lines show data smoothed by adjacent averaging. The short timescales for large resistances were omitted for clarity.

Next, we studied the impact of photon energy on the hot charge carrier transport, because any relaxation effects are likely to be dependent upon the initial energy. This is important because of recent suggestions that excess above-bandgap energy may assist excitonic dissociation [109], although the methodology of that observation has been challenged [135]. We note that quantum yields have been shown to be independent of the energy level of the excited state, suggesting that hot excitons are indeed not beneficial for exciton separation [89]. Nevertheless, hot *charge carriers* – rather than excitons – might also possess excess energy and shape the internal quantum efficiency spectra; therefore, it is important to clarify these effects, aiming for improvement in the charge extraction of typical low mobility organic materials. In the past the absence of hot charge carrier effects has been observed indirectly [136]. Numerical simulations predict that RPV is independent of optical interference effects (Supplementary **Figures 2** and **3**), allowing direct and unambiguous measurement of any hot charge carrier effects that may be present. RPV transients were measured at two different photon energies, 3.49 eV (355 nm) and 2.33 eV (532 nm). The results are plotted in **Figure 4**, showing nearly identical transients resulting from laser excitation at the two different wavelengths. The photon energy independent mobility suggests that excess energy plays a minimal role in dispersive transport, since carrier thermalization (if it is present) must happen in time scales much shorter than the transit time.

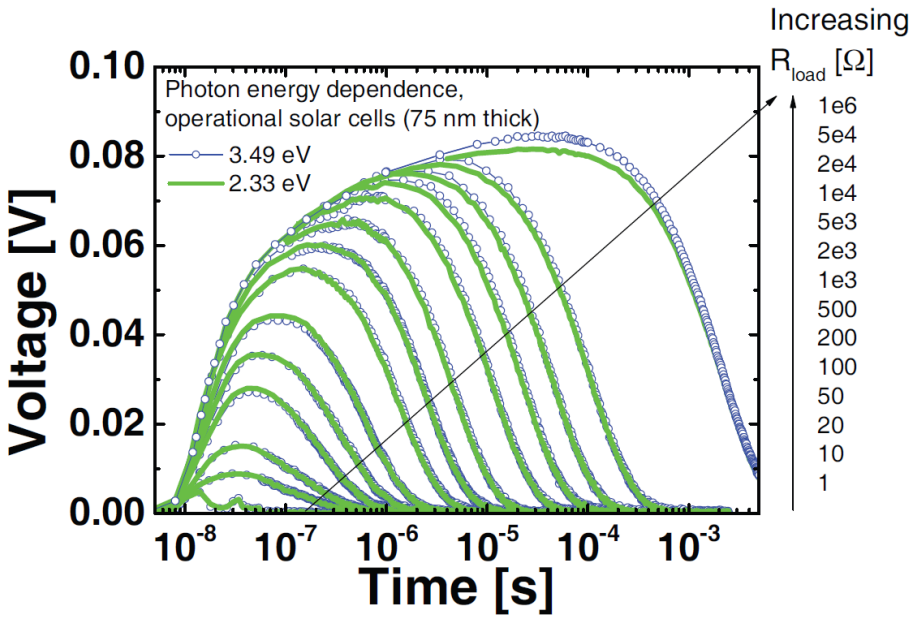

Figure 4. *RPV transients measured on a 75 nm PCDTBT:$PC_{71}BM$ solar cell using two different laser wavelengths: 355 nm (3.49 eV) and 532 nm (2.33 eV). The nearly identical transient responses directly demonstrate the absence of hot carrier effects in this system.*

To further confirm that the dispersion in hot carrier mobilities is not caused by the thermalization of carriers, we studied the electric field and film thickness dependence. Longer transit times should allow more time for thermalization, thus influencing the result if the dispersion is due to carrier relaxation. The results are shown in **Figure 5**; the Supplementary Information includes a selection of the transients from which these mobilities were estimated.

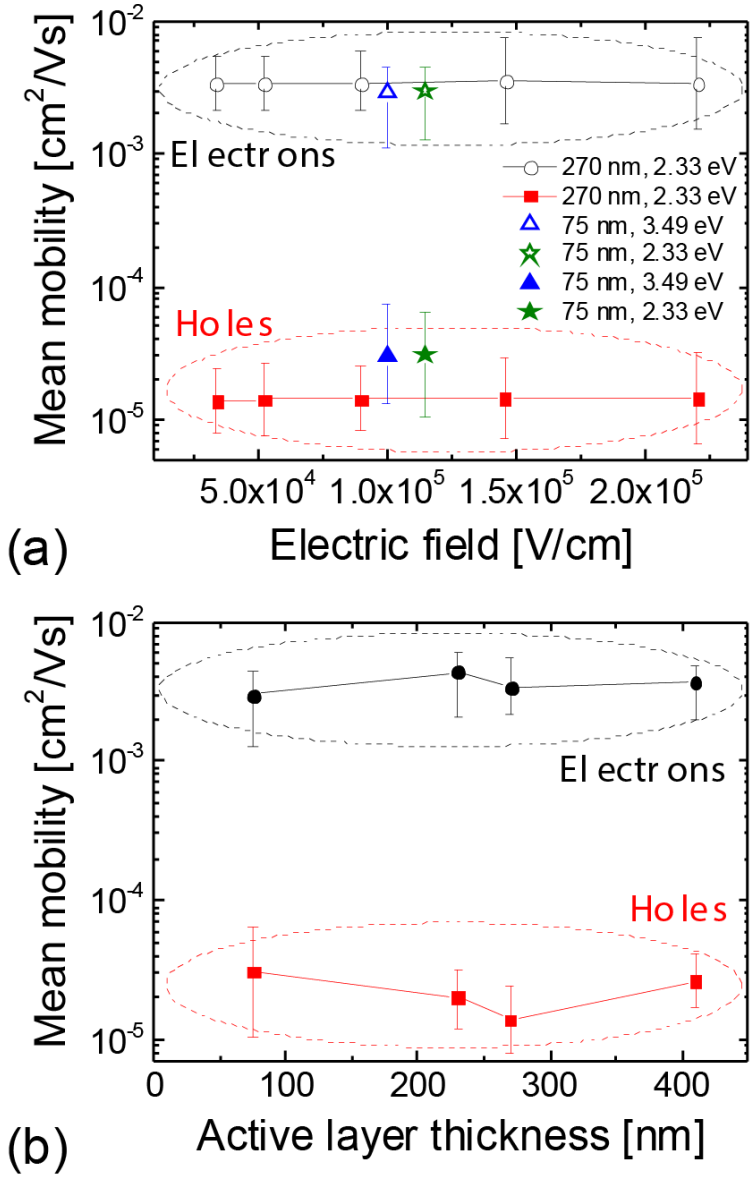

Figure 5. *Electron and hole mobilities measured in PCDTBT:$PC_{71}BM$ solar cells. The error bars show the dispersion ranges. Carrier mobilities and dispersion ranges are independent of electric field and photon energy [panel **(a)**], and nearly independent of film thickness [panel **(b)**], demonstrating that carrier thermalization cannot account for the dispersive transport in this system. Consequently, dispersion is caused by trapping.*

The mobilities and dispersion ranges are completely independent of electric field and photon energy [**Figure 5** (**a**)], suggesting that trapping mechanisms are more significant than relaxation mechanisms. The lack of electric field dependence is in contrast with the Poole-Frenkel dependence reported in pristine PCDTBT [137]. This is an unexpected result, because in disordered organic systems significant electric field dependence is typically observed, even at relatively low values of electric fields [137], which is thought to originate from hopping-type charge transport. Further studies of the temperature dependence, and measurements on other systems, have to be performed in order to clarify the origin of this observation. Additionally, we observe that the mean mobilities and dispersion ranges are nearly independent of the film thickness [**Figure 5** (**b**)]. We attribute the small changes in mobility to device-to-device variations that result from the fabrication process. The thickness independence of the mean mobilities and dispersion ranges further support the claim that the dispersion is caused by traps instead of relaxation. A charge carrier density dependence in the mobility even at low concentrations has been observed in P3HT:PCBM blends [128], and we note that a concentration dependence might cause dispersion as carriers gradually become trapped and the density decreases. We do not exclude the possibility of a density dependence here. However, in our measurements, increasing thickness corresponds to lower densities because the amount of photogenerated charge was always less than *CU*, which is inversely proportional to thickness. Consequently, the thickness independence in the mobility implies that there is negligible density dependence at the concentrations probed here.

Further measurements were also performed on solar cells made with PTB7 blends. The results show the same conclusions as the PCDTBT blends: the mean mobility and dispersion ranges are independent of film thickness, applied electric field, and photon energy (Supplementary **Figures 8**, **10**, and **11**). The results reported here appear to be generally applicable and are certainly not specific to PCDTBT blends.

Discussion

Charge transport in the studied operational OPV blends is strongly dispersive, as demonstrated by the decaying time-of-flight photocurrent transients in thick devices (**Supplementary Figure 6**). These time-of-flight transients were recorded in a regime where drift dominates over diffusion, so the current density is described by $j = eE\,(n\mu_n + p\mu_n)$, where e is the charge of an electron, μ_n and μ_p are the electron and hole mobilities, n and p are the carrier concentrations, and E is the electric field. The observation of a decaying photocurrent density j can be explained by two mechanisms: thermalization (a time dependent mobility, μ), and/or trapping (a time dependent concentration of moving charge carriers, n). These mechanisms are schematically illustrated in **Figure 6**, from which it can be seen that either model would result in dispersive photocurrent transients. We found no evidence of thermalization-type effects on the timescales comparable with those involved in charge transport. **Figure 4** directly demonstrates that that excess energy of hot carriers has essentially no contribution to mobility or dispersion. In **Figure 5**, we demonstrate that the dispersion range is independent of the applied electric field and changes very little with thickness. If thermalization on transport time scales [120] were the cause of the dispersion, then modifications to the transit time should change the mean mobility and/or dispersion range by varying the time available for relaxation. Such a variation was not observed, and hence we exclude thermalization as the mechanism of the dispersive transport. Any relaxation processes must be much faster than charge transport, so that the distance covered by charges as they relax is insignificant compared with the film thickness, and hence the relaxation has negligible contribution to the overall dispersion. With relaxation excluded, the only remaining mechanism is a reduction in the concentration of moving carriers, therefore, we conclude that *trapping* is the primary cause of the dispersion in these systems. This challenges the widely-used model of hot carrier relaxation within the density of states. Consequently, dispersive transport potentially impacts on the many different devices that employ films made from disordered semiconductors, including those that operate in the dark or at steady-state conditions.

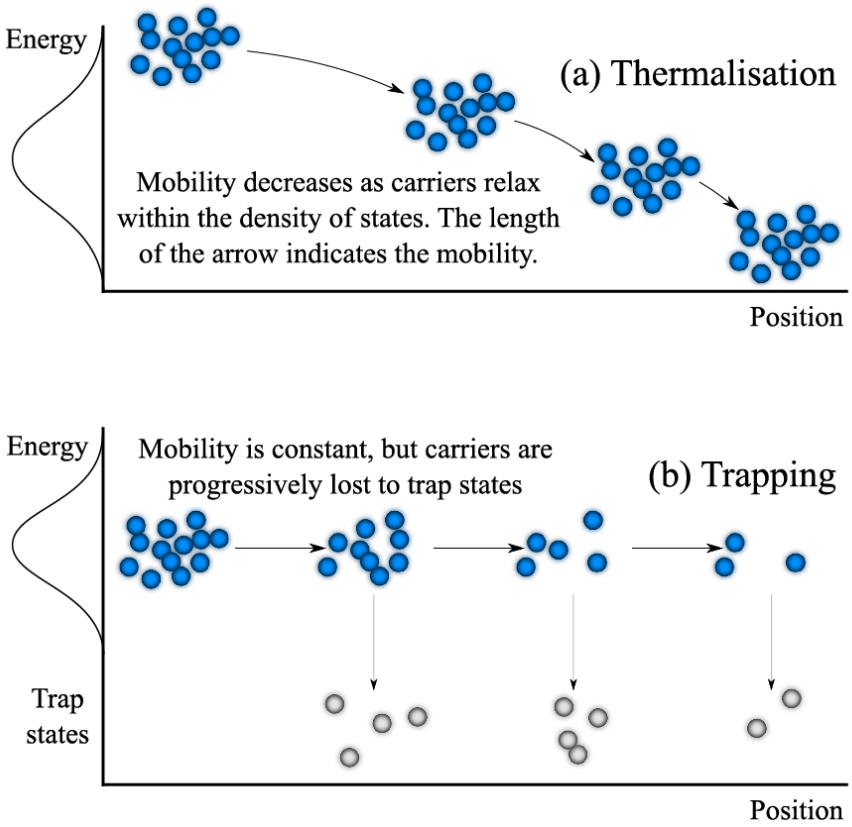

Figure 6. *Schematic illustration of the two pathways to dispersive transport.* ***(a)*** *Thermalisation causes the mobility to decrease with time, whereas* ***(b)*** *trapping causes the loss of carrier density. We have shown here that the latter case (trapping) is the dominant effect in the studied solar cells.*

Conclusion

In conclusion, electron and hole mobilities and their dispersion ranges were measured simultaneously using the RPV technique in a high efficiency narrow optical gap polymer/fullerene system (PCDTBT:$PC_{71}BM$). We found that the transport of electrons and holes are both strongly dispersive in these thin, efficient solar cells. We introduced the dispersion range as a parameter to quantify charge transport, since a single mobility value is insufficient to properly characterize a dispersive material. We directly observed the absence of "hot carrier" effects on time scales relevant to charge extraction, and furthermore found that the dispersion is caused by trapping rather than thermal relaxation. We have found that the widely-used model of hot carrier relaxation within a density of states is not the dominant process causing the dispersion in the studied solar cells. Furthermore, in contrast with the Poole-Frenkel dependence previously reported in pristine PCDTBT and other disordered systems, the studied

solar cell blends exhibit an unexpected negligible electric field dependence. While further work is needed to clarify this observation, electric field independence may assist in maintaining a good fill factor by keeping the mobility higher near the maximum power point. The absence of hot carrier effects and an electric field independent mobility were also observed in PTB7:$PC_{71}BM$ solar cells, suggesting that these conclusions may be more generally applicable. This work signifies the importance of localized trap states as opposed to thermalization and hot carrier effects in efficient polymer-based solar cells. Since dispersion arises from trapping, it is also important for other types of devices, such as organic field effect transistors and diodes. Trap states are relevant whether the carriers were injected or photogenerated, and whether the device is in transient or equilibrium conditions. Our results suggest that further scientific research should be directed towards reducing the density of trap states rather that utilizing above-bandgap energy for improving electronic device performance.

Methods

Numerical simulations*:* The simulations are based on a standard one-dimensional drift-diffusion-recombination solver [138, 139] assuming a negligible amount of equilibrium carriers, which is typically the case in organic semiconductors [52] as well as in the studied devices. For simulations of dispersive transport, we implemented a multiple trapping and release model [124, 125, 140] with an exponential density of localized states. The full list of equations are given in the Supplementary Information.

Solar cell fabrication: 15 Ω/sq. Indium tin oxide (80 nm thick, purchased from Kintec) coated glass substrates were cleaned in a 100 ºC water bath with alconox (detergent), followed by sonicating in sequence with de-ionized water, acetone and 2-propanol for 6 minutes each. Next, a 30 nm layer of poly(3,4-ethylenedioxythiophene):poly(styrenesulfonate) (PEDOT:PSS) was spin-coated at 5000 rpm for 60 sec onto the cleaned substrates, which were then annealed at 170 ºC for a few minutes in air. For PCDTBT devices, a solution of PCDTBT (purchased from SJPC Group) and $PC_{71}BM$ (purchased from Nano-C) was prepared by using a 1:4 blend ratio by weight and a total concentration of 25 mg/cm^3 in dichlorobenzene (DCB). Solar cells with four active layer thicknesses, 75 nm, 230 nm, 270 nm and 410 nm (measured by a DekTek profilometer), were fabricated by spin coating. The chosen PCDTBT:PC70BM system is suitable for this study because its amorphous nature [141] allows to minimize the impact of the film thickness on the morphology. The thin film (active layer thickness of 75 nm) PCDTBT:$PC_{71}BM$ solar cell exhibited a power conversion efficiency of 6.3% under standard AM1.5G illumination, while the PTB7:$PC_{71}BM$ blends reached 7.7%. Current-voltage curves for both devices are shown in **Supplementary Figure 5**. None of the optimized PCDTBT or PTB7 based devices demonstrated any significant film morphology inconsistencies in the range of studied film thickness. (See the Methods section for the details of the fabrication and the

Supplementary Information for characterization of photovoltaic performance). The presence of dispersive transport was confirmed by time-of-flight experiments on thick films (**Supplementary Figure 6**). No photocurrent plateaus were observed; the transients decrease with time as is typical of dispersive systems. For PTB7 devices, the active layer of PTB7 (1-Material, Mw = 97.5 kDa, PDI = 2.1) and $PC_{71}BM$ (ADS) was prepared as previously described [26] resulting in 100 nm, 150 nm, 230 nm, and 700 nm thick films. To complete the solar cells 1.2 nm of samarium and 75 nm of aluminium were deposited under a 10^{-6} mbar vacuum by thermal evaporation. The device areas were 0.2 cm^2 for current density versus voltage (*J-V*) measurements and 3.5 mm^2 for charge transport measurements. *J-V* characteristics were obtained in a 4-wire source sense configuration and an illumination mask was used to prevent photocurrent collection from outside of the active area. An Abet solar simulator was used as the illumination source and provided ~ 100 mW/cm^2 AM1.5G light.

RPV measurements: A delay/trigger generator (Stanford Research Systems DG535) was used to trigger the laser and function generator (Agilent 33250A) pulses for timing control. A pulsed Nd:Yag laser (Brio Quantel) with a pulse length of 5 ns, frequency of 2 Hz and output energy of ~ 50 mJ was used to generate the carriers. Neutral density filters (in this particular case optical density 7) were used to reduce the laser intensity for the RPV measurements such that the resulting photovoltage at a load resistance of 1 MΩ (~100 mV) remains significantly below the built-in voltage. This ensures that the measurement is performed under quasi short-circuit conditions. A function generator was used to apply external voltage pulses for electric field dependent mobility measurements. RPV photovoltage signals were recorded with an oscilloscope (WaveRunner 6200A) at various external load resistances. RPV transients were smoothed with an adjacent averaging function to neutralize the electromagnetic wave oscillations in the measurement circuit. In agreement with previous studies done by Clarke *et al.* [78], dark-CELIV transient responses showed no equilibrium carrier extraction, justifying the application of RPV to the studied devices. Optical interference simulations were performed using the transfer matrix approach [142] with typical optical constants of PCDTBT/PCBM blends [143].

Chapter IV: Advances in Fundamental Understanding of Charge Transport

It is well known that the low mobility and the fast recombination dynamics of the Langevin-type in disordered organic semiconductors negatively impacts the charge collection efficiency of organic photovoltaic diodes. Therefore, a detailed knowledge of the conditions under which the extraction of charge carriers is not affected by the detrimental recombination of free charges would be desirable to optimize the photovoltaic performance. The previous chapter presented a photovoltage transient technique (RPV) to estimate the charge transport parameters in operational OSCs, however, knowing these parameters in isolation is still insufficient to gain a conclusive understanding of the charge collection efficiency. This inspired us to investigate in a next step techniques to assess the charge carrier collection efficiency (η_{COLL}) and in particular to understand how the charge transport parameters is correlated with η_{COLL}.

The two published works in this chapter present an improved methodology to understand and quantify η_{COLL}. The results provide a simple recipe for avoiding non-geminate recombination in thin-film organic photovoltaic diodes in which charge photogeneration occurs in the volume of the active layer (< ≈500nm). As such, the two works provide a conclusive understanding of the overall charge collection efficiency in organic photovoltaic diodes. The experiments

explained in this chapter also indicate that charge transport is not a major limit factor of typical OSCs at short-circuit conditions with relatively thin active layers on the order of 100 nm.

IV.1 Conditions to Avoid Bimolecular Recombination Losses

In this section the bimolecular recombination of opposite charge carriers during charge extraction is discussed. We extended the applicability of the existing intensity dependent photocurrent (iPC) methodology experimentally and theoretically. Experimentally the iPC was measured over several decades of light intensity – to the author's knowledge – with a higher precision than in any previous study. The iPC measurements allows one to identify the light intensity at which the bimolecular recombination rate affects photocurrent extraction rate. The results demonstrate that bimolecular recombination losses emerge if the photocurrent hits approximately the space charge (or transport) limited photocurrent, which further reveals how the charge transport parameters control these recombination losses. Thereby, this work presents a simple set of design rules to manufacture organic photodiodes that are not limited by bimolecular recombination; this can be done through both device and material engineering. The results were verified in different photovoltaic diodes with varying active layer thicknesses, at different applied voltages and excitation wavelengths, and backed up by numerical simulations. Notably, the main results have been further confirmed for many (~20) other OSCs (**Section V.1** and **Section V.3**) and also for OSCs with varying blend ratios (**Section V.2**).

The supplementary information of this paper can be accessed online at (http://dx.doi.org/10.1038/srep09949)

Photocarrier drift distance in organic solar cells and photodetectors

Abstract

Light harvesting systems based upon disordered materials are not only widespread in nature, but are also increasingly prevalent in solar cells and photodetectors. Examples include organic semiconductors, which typically possess low charge carrier mobilities and Langevin-type recombination dynamics – both of which negatively impact device performance. It is accepted wisdom that the "drift distance" (i.e., the distance a photocarrier drifts before recombination) is defined by the mobility-lifetime product in solar cells. We demonstrate that this traditional figure of merit is inadequate for describing the charge transport physics of organic light harvesting systems. It is experimentally shown that the onset of the photocarrier recombination is determined by the electrode charge and we propose the mobility-recombination coefficient product as an alternative figure of merit. The implications of these findings are relevant to a wide range of light harvesting systems and will necessitate a rethink of the critical parameters of charge transport.

Introduction

Light harvesting devices fabricated using non-single-crystal films such as polymers, organic molecules, dye-sensitized structures, nanoparticles as well as perovskites offer the potential for low cost and large area fabrication. All these systems lack long-range electronic order and have a common feature, i.e., their electrical conduction is inferior to highly-crystalline inorganic semiconductors such as silicon. The relatively poor electrical conduction arises because of their orders of magnitude lower electron and hole mobilities, and the low density of intrinsic charge carriers. Low photocarrier mobility causes charge transport losses, and limits the performance of optoelectronic devices, and in particular those designed to harvest or detect photons.

Charge transport losses are typically described by the average distance that a photocarrier travels prior to its recombination event. The critical requirement for lossless charge transport is that the drift or diffusion distance (L_D) must be longer than the active layer thickness (d). For inorganic crystalline semiconductors this distance is classically defined by the product of the charge carrier mobility and lifetime ($\mu\tau$) regardless whether the photocarrier driving force is the electric field (drift) or concentration gradient (diffusion) [144]. In strongly non-Langevin

materials such as silicon and other inorganic crystalline semiconductors (where the recombination coefficient is typically $>10^5$ times lower compared to Langevin systems [145]), the photogenerated charges can pass each other at distances closer than Coulomb radius without recombination during transport. The reason is that the carrier mean free carrier path (the average distance between carrier collisions during random thermal motion) of ~100 nm is much larger than the Coulomb radius (the distance at which the thermal energy equals the Coulomb energy) of ~5 nm [20]. This implies that the mutual Coulombic attraction between positive and negative charges does not significantly affect the travel trajectory and the photocarrier lifetime represents the true nature of recombination. Therefore, the mobility-lifetime product can adequately describe the distance charges travel prior to recombination in these crystalline non-Langevin systems.

In contrast, in disordered organic semiconductors (an archetypal Langevin-system) the mean free path is defined by the carrier hopping distance (~1 nm), which is substantially shorter than the Coulomb radius (~20 nm) [51]. Hence, when the charge carrier density is such that the average separation distance between charges is comparable to the Coulomb radius, charge carriers have a high probability of recombination because positive and negative charges are not able to escape the Coulomb attraction. The recombination dynamics is then defined by the Langevin rate. The photocarrier lifetime under these conditions is strongly dependent upon the physical separation of negative and positive charges, which is determined by the carrier density, distribution, and, for example, on the formation of space charge regions. Therefore, a single carrier lifetime cannot adequately characterize the entire device. In contrast the recombination coefficient is a material property, which is unaffected by the distribution of charge carriers. Furthermore, the lifetime also depends on the photocarrier mobility [146], which dictates the average velocity with which charges of opposite signs move with respect to each other. Given this dual dependency and the arguments above, the mobility-lifetime product (and hence L_D) is clearly unsuitable as a universal "figure of merit" for the transport physics of organic semiconductors which are Langevin-type, as most are [51].

Despite these considerations, the mobility-lifetime product is widely used as an appropriate predictive metric by which to assess and explain the performance of organic solar cell materials and architectures, and indeed more broadly photon-harvesting or detecting devices [127, 147, 148, 149, 150, 151]. In this work, we address the fundamental processes determining the

photoconductivity and charge transport losses in low mobility disordered films of organic semiconductors. We demonstrate that the classical mobility-lifetime approach is not a convenient parameter to describe the charge transport in these light harvesting systems. We independently measure the relevant charge transport parameters in operational devices, and directly relate these basic properties to the bimolecular recombination losses. The results show that the critical carrier density that triggers the onset of the recombination losses is determined by the charge density on the device electrodes. Based upon this physics we propose an alternative figure of merit allowing the minimization of charge transport losses in undoped disordered systems, where charge trapping does not dictate the photovoltaic performance. To this end, we employ intensity dependent PhotoCurrent (iPC) and Resistance dependent PhotoVoltage (RPV) measurements in two high efficiency organic solar cell (OSC) systems – each with quite different transport physics.

Results

Photovoltaic performance of solar cells

The most efficient single junction organic solar cell architecture currently employed is the so-called bulk heterojunction (BHJ). This architecture has an active layer containing a blend of organic semiconductors with electron acceptor and electron donor characteristics. In our study we employed two high efficiency blends namely: poly[(4,8-bis{2-ethylhexyloxy}benzo[1,2-b:4,5-b']dithiophene-2,6-diyl)(3-fluoro-2-{[2-ethylhexyl]carbonyl}thieno[3,4-b]thiophenediyl)]:[6,6]-phenyl-C_{70}-butyric acid methyl ester (PTB7:PC70BM) [131] and poly[*N*-9''-heptadecanyl-2,7-carbazole-*alt*-5,5-(4',7'-di-2-thienyl-2',1',3'-benzothiadiazole)] (PCDTBT):PC70BM [152]. The structures of the two different polymers are provided **Figure 1.** These systems have been extensively studied [54, 104, 107, 132, 133] and are known to have quite different charge transport properties (PTB7:PC70BM being superior). In this work we varied the junction thickness as an experimental parameter so as to access a range of key charge transport properties (recombination and mobility) in a systematic manner and study their impact upon device performance.

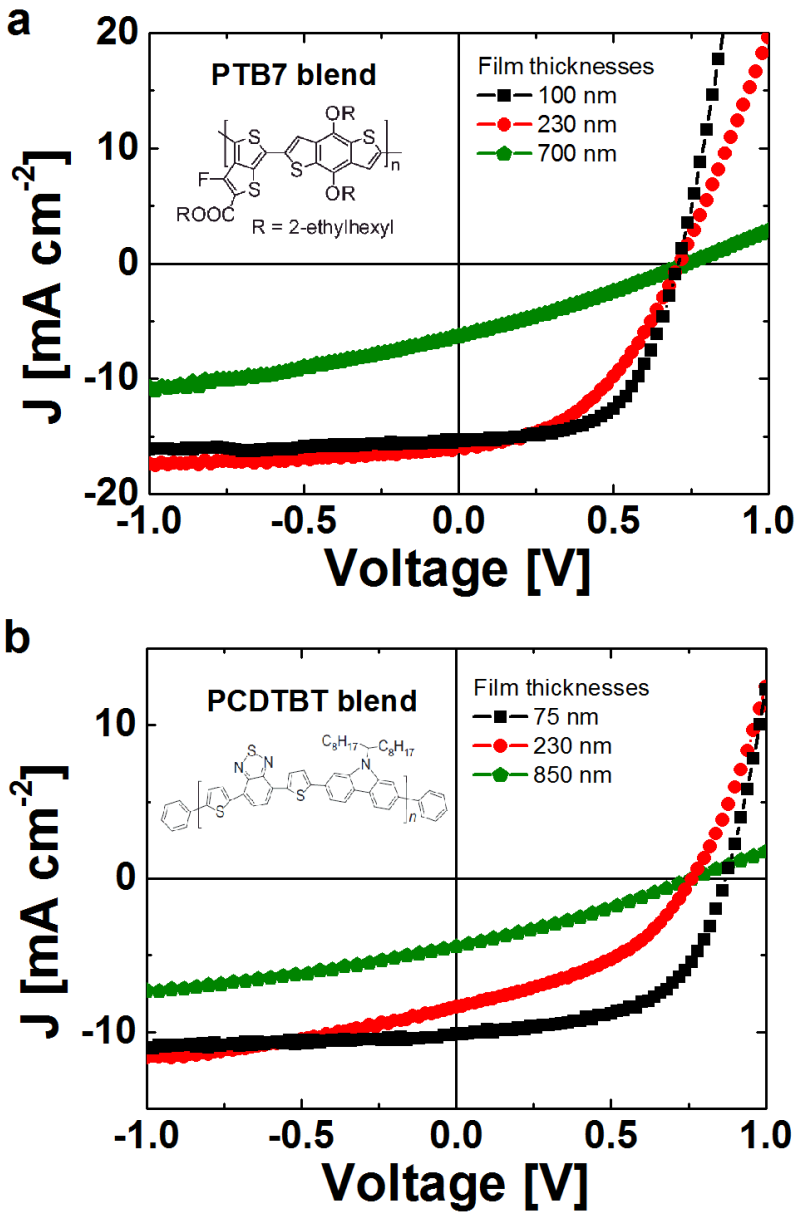

Figure 1. *Average Current density-voltage (JV) characteristics under standard AM 1.5G illumination of organic solar cells fabricated from* ***(a)*** *PTB7:PC70BM blends with 100 nm, 230 nm and 700 nm thick active layers and* ***(b)*** *PCDTBT:PC70BM blends with 75 nm, 230 nm and 850 nm thick junctions. The photovoltaic performance of the PCDTBT:PC70BM blends is much more susceptible to the film thickness of the active layer compared to PTB7:PC70BM.*

Figure 1 shows white light current density versus voltage (*JV*) plots obtained under standard AM 1.5G illumination for each polymer:PC70BM blend as a function of junction thickness. The plots are representative of fabrication batches containing multiple devices (see **Methods**). For PTB7:PC70BM solar cells shown in **Figure 1 (a)**, the optimal junction thickness is 100 nm, and hence 230 nm and 700 nm are essentially sub-optimal and this is borne out by the *JV* curves.

Similarly, **Figure 1 (b)** shows representative white light *JV* characteristics for the PCDTBT:PC70BM system. In this case the optimal junction thickness is 75 nm – 230 nm and 850 nm being sub-optimal. The performance metrics including relevant statistics are summarized in **Table 1**. It has previously been demonstrated that the Fill Factor (FF) and PCE fall off rapidly for junctions > 80 nm for PCDTBT:PC70BM [133], and we also observe the same trend. This has been attributed to poor charge transport in this blend, in particular low hole mobilities which leads to significant bimolecular recombination under 1 sun operating conditions. The PTB7:PC70BM cells have considerably better charge transport and the PCE is maintained past 100 nm – although it does fall off for thicker junctions. Loss of FF still limits the optimal junction thickness to 100 nm – 150 nm: increasing the thickness to 230 nm delivers higher short circuit current but FF losses lead to reduced PCE of 5.1%. These observations are in-line with expectations.

Photovoltaic performance parameters

Polymer blended with PC70BM and junction thickness	PTB7 100 nm	PTB7 230 nm	PTB7 700 nm	PCDTBT 75 nm	PCDTBT 230 nm	PCDTBT 850 nm
J_{SC} [mA/cm^2]	**15.3** (± 0.3)	**16.0** (± 0.4)	**6.3** (± 1.7)	**10.3** (± 0.3)	**8.3** (± 0.8)	**4.4** (± 1.2)
V_{OC} [V]	0.7	0.71	0.72	0.84	0.75	0.76
FF [%]	59	45	28	56	42	33
PCE [%]	**6.3** (± 0.1)	**5.1** (± 0.2)	**1.3** (± 0.4)	**4.8** (± 0.1)	**2.6** (± 0.2)	**1.1** (± 0.3)

Table 1. *Device performance parameters including standard errors of the studied PTB7:PC70BM and PCDTBT:PC70BM devices.*

Photocarrier recombination losses

To quantify these transport losses and relate the observed losses in the photovoltaic performance in the non-optimal, thick active layer junctions to the losses in charge transport, we employed two techniques: iPC and RPV measurements. The iPC method has been extensively used to assess bimolecular losses in organic solar cells [128, 132, 153, 154, 155,

156] and relies upon the accurate measurement of photocurrent as a function of the input light intensity (typically from 1 to 100 mW cm^{-2}). A linear fit to the photocurrent-intensity in a log-log plot is used (where the slope is often marked as α) to determine whether the device performance is limited by bimolecular recombination or not. Deviation from slope 1 shows the presence of significant bimolecular recombination. However, fitting a line to the photocurrent data over a narrow range of intensities near this transition between the linear and the sub-linear regimes [73, 154, 157] can result in an arbitrary slope and is prone to error. Furthermore, iPC measurements over a large range of light intensities are also crucial for characterizing organic photodiodes (OPDs) since the point of deviation determines the Linear Dynamic Range (LDR) - an important figure of merit in all photodetectors. Once again LDR measurements are often not performed over a sufficiently broad intensity range to accurately determine the deviation point [158, 159].

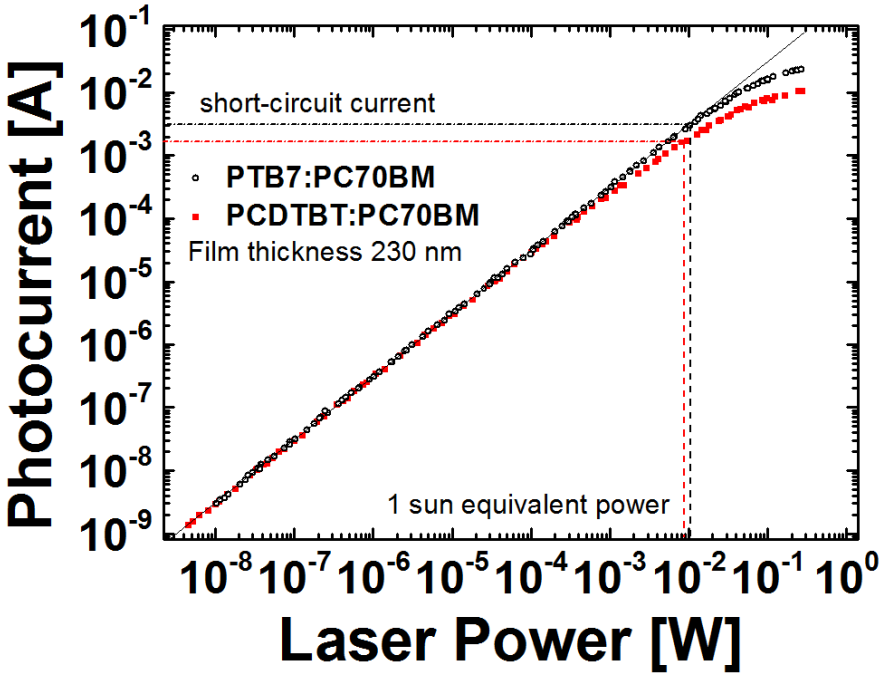

Figure 2. *iPC results: the photocurrent measured as a function of the incident laser power varied by orders of magnitude in PTB7:PC70BM blends and PCDTBT:PC70BM blends with junction thickness of ~230 nm. The 1 sun equivalent laser power is marked by the dashed lines. The onset of the bimolecular recombination losses appear at the highest laser powers when the photocurrent becomes non-linear.*

With these considerations in mind, we have extended the measurement range by many orders of magnitude. **Figure 2** shows extended range iPC results for both polymer blends with

photocurrent measured between ~ $3x10^{-9}$ W and ~ $3x10^{-1}$ W of laser power (note, the illuminated device area is 0.2 cm^2). The junctions in both cases were ~230 nm thick and the iPC measurements on other junction thicknesses are provided in the **Supplementary Information** for completeness (see **Supplementary Fig. 1**). We observe that the photocurrent increases linearly at low light intensities until a critical current that we call the deviation current is reached. Beyond the deviation current, the bimolecular recombination rate becomes comparable with the extraction rate and causes the photocurrent to deviate from linearity. In the linear regime the photocurrent is only affected by first order losses (i.e., those with a rate proportional to the first power of the illumination power). The origin of the first order losses has been attributed to a number of photophysical processes including incomplete absorption and geminate recombination [153, 155]. Note, that a linear scaling of the photocurrent with the laser power does not guarantee the absence of photocarrier recombination in cases where there are a large amount of long-lived trap states or strong doping [40, 132, 160, 161]. It has been, however, previously argued that first order photocarrier recombination (or trap-assisted recombination) is not relevant in optimized and efficient OSCs [40, 162]. In particular, dominant second order recombination dynamics have been observed in optimized polymer:PC70BM blends [93, 163]. In this work we have also experimentally confirmed the absence of long-lived trap-induced recombination losses by repetitive RPV shots in the optimized and the 230 nm thick junctions (**Supplementary Note 1** and **Supplementary Fig. 2**), while dark-CELIV transients prove the absence of doping induced charges (**Supplementary Fig. 3**). Since first-order non-geminate recombination is not significant at short-circuit in the polymer- fullerene combinations of this work, we focus on the impact of the charge transport parameters on the transition from the linear to the nonlinear iPC regime, which corresponds to the onset of substantial bimolecular recombination losses with a non-linear recombination order.

In order to better visualize the onset of photocarrier (bimolecular) recombination, in **Figure 3 (a)** and **(b)** we have re-plotted the iPC data as External Quantum Efficiency (EQE – the ratio of the photocurrent with input light intensity at short circuit) *versus* input light power. This process creates a non-logarithmic y-axis to visualize and compare more accurately the deviation points for all the junction thicknesses in both systems. We have also normalized the x-and-y-axes respectively to 1 sun equivalent power (i.e., the laser power at the short-circuit current) and the EQE in the constant regime to 100%.

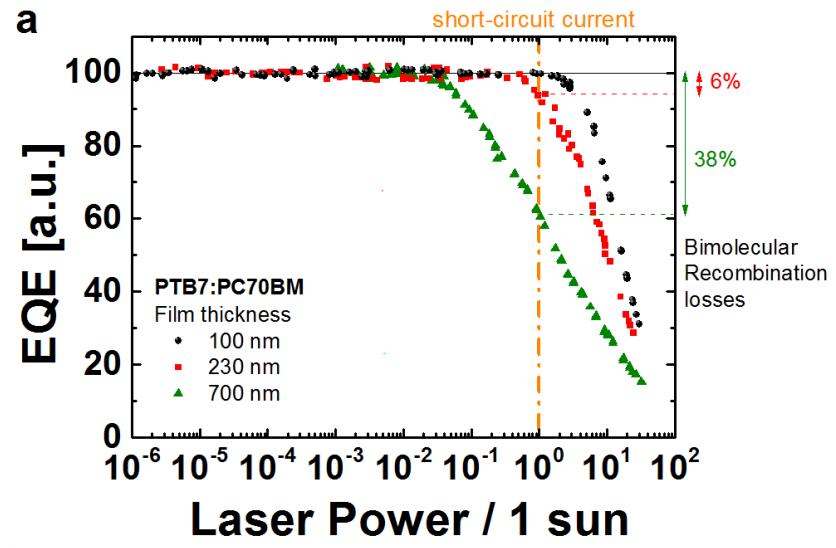
a
short-circuit current
EQE [a.u.]
100
80
60
40
20
0
6%
38%
Bimolecular
Recombination
losses
PTB7:PC70BM
Film thickness
100 nm
230 nm
700 nm
10-6 10-5 10-4 10-3 10-2 10-1 100 101 102
Laser Power / 1 sun

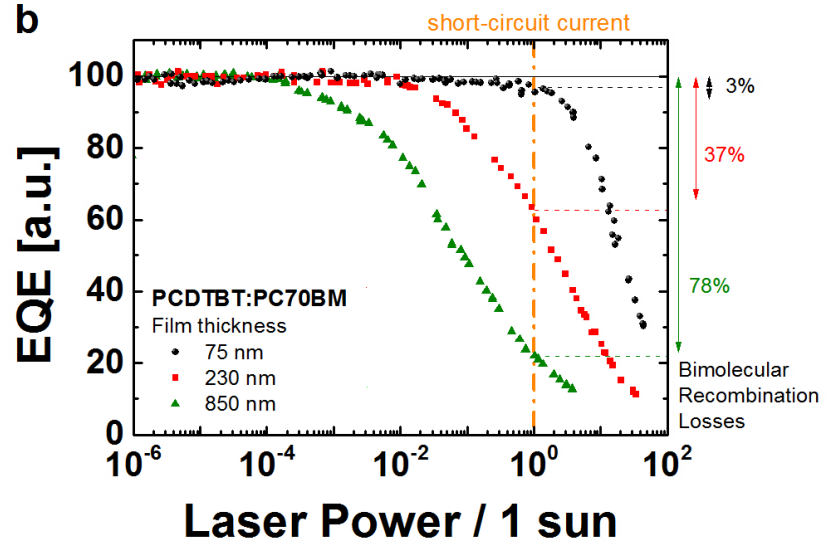
b
short-circuit current
EQE [a.u.]
100
80
60
40
20
0
3%
37%
78%
Bimolecular
Recombination
Losses
PCDTBT:PC70BM
Film thickness
75 nm
230 nm
850 nm
10-6 10-4 10-2 100 102
Laser Power / 1 sun

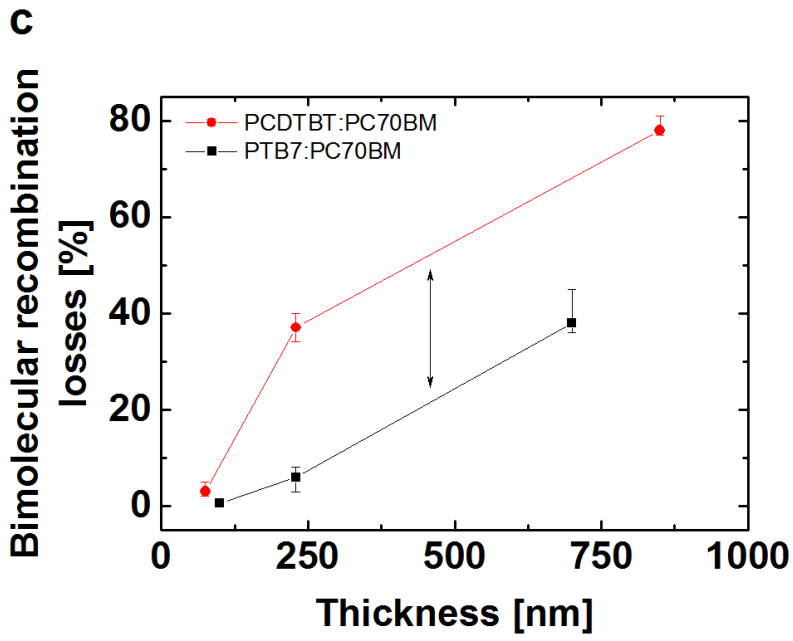
c
Bimolecular recombination
losses [%]
80
60
40
20
0
PCDTBT:PC70BM
PTB7:PC70BM
0 250 500 750 1000
Thickness [nm]

Figure 3. *External Quantum Efficiencies (EQEs) (re-plotted from representations such as* ***Figure 2****) shown as a function of the incident laser power in the studied active layer thicknesses of* ***(a)*** *PTB7:PC70BM and* ***(b)*** *PCDTBT:PC70BM blends. The EQEs were normalized to 100% and the laser power to the 1 sun equivalent power to visualize the bimolecular recombination losses at the short-circuit conditions. This methodology allows one to quantify the photocarrier bimolecular recombination losses in actual solar cells under close-to-operational conditions. Figure* ***(c)*** *shows the recombination losses estimated from the Figures* ***(a)*** *and* ***(b)*** *and plotted as a function of the active layer thickness.*

Note, this normalization sets the absorption and generation efficiency of the EQE to 100%. Therefore losses in the normalized EQE directly show losses in the transport (collection) efficiency. **Figure 3 (a)** shows the PTB7:PC70BM data and one observes that there are minimal recombination losses for the 100 nm and 230 nm thick junction solar cells up to 1 sun equivalent power (<1% and ~6% loss, respectively). However, in the 700 nm junction device, significant recombination losses are observed (~38%). For the PCDTBT:PC70BM devices, shown in **Figure 3 (b)**, again only minor losses were observed in the highest efficiency, 75 nm thick junction cell. In contrast to the PTB7:PC70BM system, the 230 nm device displays considerable 1 sun recombination losses (transport efficiency reduced by ~ 37%). As the active layer is further increased to 850 nm, recombination decreases the transport efficiency substantially by ~78%. The recombination losses for all devices are summarized in **Figure 3 (c)**. In both blend systems, the recombination losses are observed to follow the same trend as the solar cell performance metrics. It is worth noting that the trends in the two systems are similar, but with the effect of the recombination losses in the PTB7:PC70BM blends being shifted to thicker junctions.

Origin of photocarrier bimolecular recombination losses

To further understand the losses in charge transport, we have measured the charge carrier mobilities and recombination coefficients in the studied devices. It should be noted that it was essential for this work to compare the mobility values (or transit times) with the recombination onset on the same devices. The well-known SCLC measurement technique was not applicable because the $J \sim U^2$ dependence of the Mott-Gurney law cannot be observed for the operational devices [54] and mobilities obtained on pristine films are usually not the same as in blends of two organic semiconductors [107]. Therefore, we have used the RPV [54, 104] and High

Intensity Resistance dependent PhotoVoltage (HI-RPV) [49, 54] techniques to determine the mobility of both electrons and holes as well as the bimolecular recombination coefficient ratio β_L/β (where β is the actual and β_L the Langevin recombination coefficient) (**Supplementary Fig. 4** to **Supplementary Fig. 7**). We found thickness independent dispersive carrier mobilities and bimolecular reduction factors: $\mu_{electron}$ ~ $3x10^{-3}$ cm^2 $V^{-1}s^{-1}$, μ_{hole} ~ $3x10^{-4}$ cm^2 $V^{-1}s^{-1}$ and β_L/β ~ 50 in PTB7:PC70BM devices. The mobility of holes is ~10 times lower and the bimolecular recombination coefficient ratio is ~2 times lower in the PCDTBT:PC70BM devices, while a similar electron mobility was observed in both blends. An interesting observation is that the measured charge carrier mobility and β_L/β are almost the same in all studied film thicknesses for each polymer:PC70BM blend (**Supplementary Fig. 5** and **Supplementary Fig. 7**). This suggests that well controlled device preparation conditions did not result in any significant change in film structure that may have affected the charge transport.

Figure 3 also illustrates that the substantial bimolecular recombination losses appear at different photocarrier densities, which are dependent upon the junction thickness and blend system. Similarly, the space charge limited current (I_{SCLC}) is determined by the density of space charge [164]. The I_{SCLC} has been shown to follow a square root dependence on the bimolecular recombination coefficient ratio $(\beta_L/\beta)^{1/2}$ [52]. It has also been previously demonstrated that the space charge limited photocurrent is proportional to the extraction rate of the slower charge carriers because they create a "bottleneck" for charge transport forming the space charge and causing the bimolecular recombination losses [155, 165]. Therefore, the following expression can then be generalized:

$$I_{\mathrm{SCLC}} \sim CU/t_{\mathrm{tr}}^{\mathrm{slower}}\ (\beta_{\mathrm{L}}/\beta)^{1/2} \qquad (1)$$

where C is the device capacitance, U is the effective voltage (superposition of built-in and external) and t_{tr}^{slower} is the transit time of slower charge carrier species.

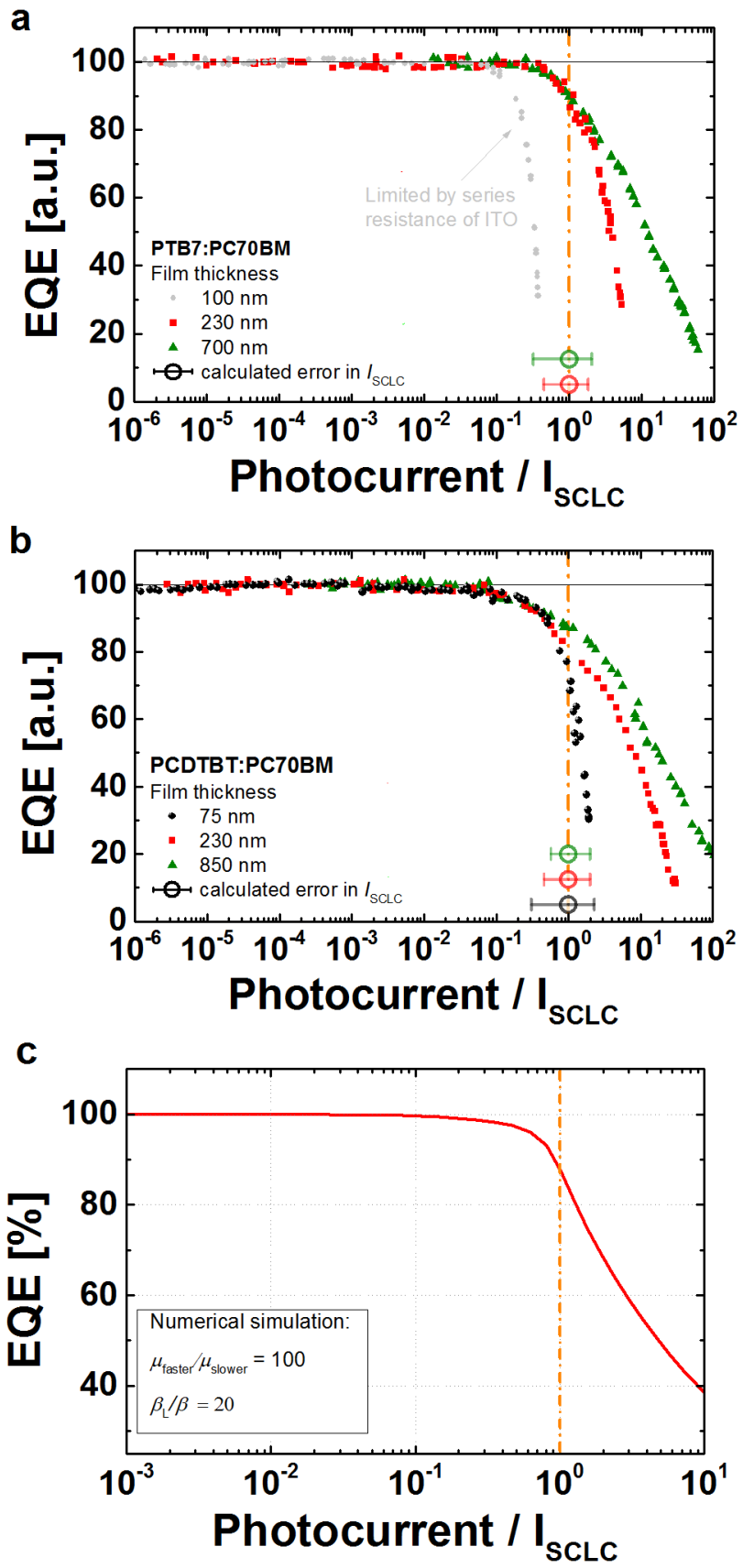

Figure 4. *Normalized External Quantum Efficiencies (EQEs) shown as a function of the measured photocurrent in the studied active layer thicknesses of* ***(a)*** *PTB7:PC70BM blends and*

(b) *PCDTBT:PC70BM blends. The photocurrent is normalized to the space charge limited current (ISCLC), which is calculated from the measured charge transport parameters using* ***Equation 1****. When the actual measured photocurrent approaches the space charge limited current, substantial recombination losses manifest implying that the electrode defined space charge controls the drift distance of photocarriers.* ***(c)*** *Numerically simulated EQEs as a function of the photocurrent confirm that the deviation is caused by the* I_{SCLC}*, where the appearance of the first recombination losses can occur at a slightly lower photocurrent compared to* I_{SCLC}*.*

Using the measured slower carrier mobilities/transit times and recombination coefficients we can calculate the I_{SCLC} for each device (see **Methods**) and replot the previous EQEs (**Figure 3**) as a function of the photocurrent normalized to the I_{SCLC} for the PTB7:PC70BM and PCDTBT:PC70BM blends in **Figure 4 (a)** and **(b)** respectively. Note, that the calculated I_{SCLC} values vary over many orders of magnitude mainly because of differences in the slower carrier transit times due to the different junction thicknesses. The key observation from **Figure 4** is that the bimolecular recombination losses start when the photocurrent reaches approximately the I_{SCLC} value, regardless of the active layer thickness. This implies that the critical charge carrier density that causes significant bimolecular recombination (compared to the extraction rate) is approximately equal to the surface charge density stored on the electrodes (*CU*), while the recombination coefficient ratio allows this critical density to be larger. The results are also confirmed in photodetectors with the same device architectures using applied external voltages to facilitate the charge transport and extraction. The bimolecular recombination losses are typically smaller at higher applied reverse biases, because the applied voltage increases the charge carrier drift velocity and the value of *CU* (**Supplementary Figure 8** (**a**)). Nevertheless, even as the applied bias voltage is varied, the onset of substantial losses continues to coincide with the I_{SCLC} (**Supplementary Figure 8** (**b**)). When a forward bias is applied (relevant to solar cells at operational conditions) the recombination losses increase (**Supplementary Fig. 9**).

Numerical simulations of the EQEs, shown in **Figure 4 (c)** for a mobility ratio of 100 and a recombination coefficient ratio of 20 further confirm the validity of **Equation 1**, the role of the $\mu_s(\beta_L/\beta)^{1/2}$ product and the space charge current limit. Moreover, these simulations can be used to predict the onset of bimolecular recombination losses as a function of experimental conditions such as the impact of the mobility ratio, recombination coefficient, the series

resistance and the light absorption profile (see **Supplementary Note 2** and **3; Supplementary Fig. 10** to **Supplementary Fig. 12**).

Discussion

Space charge determined photocarrier drift distance

Drawing these experimental results together demonstrates that significant bimolecular recombination losses appear at very specific light intensities, junction thicknesses and applied voltages, depending upon the materials system in question. The experimental results suggest, that when the photocurrent matches the space charge limited current (i.e., when the photocarrier density is close to the *CU* space charge defined by the electrodes in Langevin-type systems), then the photocarrier drift distance becomes comparable to the junction thickness ($L_D \sim d$) and substantial recombination losses emerge. Referring back to the Introduction, in which we compared the charge carrier drift distances in two classes of materials, non-Langevin and Langevin, we reiterate that in the latter the critical photocarrier lifetime and drift distance are dependent upon carrier density. This is defined by a number of material and device related parameters such as the light intensity, optical cavity effects, quantum efficiency of charge generation, film thickness, the photocarrier mobility, and others. This, in addition to the observed space charge dependent drift distance, clarifies that the $\mu\tau$ product (and therefore the drift distance itself) is not an independent intrinsic parameter that can be conveniently used as a comparative figure of merit to understand the charge transport physics. Importantly, the $\mu\tau$ product can also not be used to determine the critical active layer thickness to minimize the bimolecular recombination losses. These concepts and results are visualized in **Figure 5**. Based upon this considerations we propose the product of the materials parameters $\mu_s (\beta_L/\beta)^{1/2}$ from **Equation 1** as a comparative transport figure of merit because it determines the decisive I_{SCLC}. It is important to note, however, that this figure of merit alone is not sufficient for describing the performance of the actual devices, because the recombination losses are governed by additional device related parameters, such as the film thickness, dielectric constant (both are defining the device capacitance) and effective voltage. **Figure 4** shows that significant bimolecular recombination losses can be avoided only when the I_{SCLC} is greater than the actual photocurrent produced by the solar cell (see SI **Supplementary Fig. 13** for the minimum $\mu_s (\beta_L/\beta)^{1/2}$ required to minimize the bimolecular recombination for a given active layer thickness and achievable photocurrent).

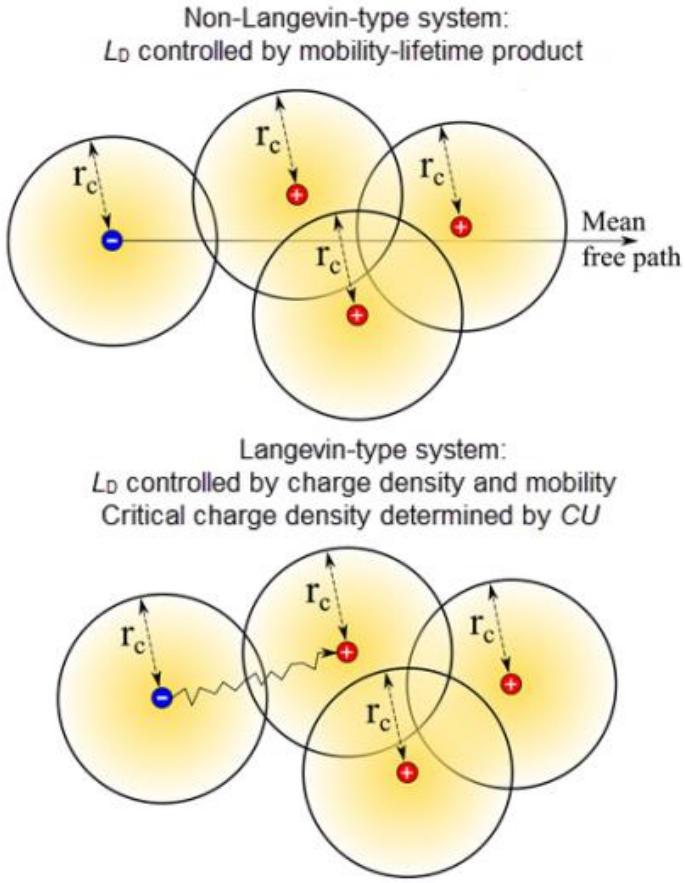

Figure 5. *Schematic drawing showing the nature of charge carrier transport in non-Langevin (a) and Langevin-type systems (b). The photocarrier drift distance (L_D) in non-Langevin systems is adequately described by the mobility-lifetime product because in these typically highly ordered systems the photocarrier mean free path is much larger that the Coulomb radius (r_c). The photocarrier drift distance in Langevin-type systems is determined by the physical separation between the charges and their mobility. The critical charge density that triggers significant recombination (compared to the extraction rate) is determined by the electrode defined space charge density CU. This situation is relevant to disordered structures where the photocarrier hopping distance is much smaller that the Coulomb radius (localized charge transport).*

Finally, we note the influence of the transport and recombination dynamics in our two studied systems: the observed differences in the junction thickness dependent recombination losses are explained by the 10 times higher value of the slower carrier mobility and the ~2 times higher bimolecular recombination reduction factor in the PTB7 blends as compared to the PCDTBT blends. This allows the PTB7 devices to work efficiently in slightly thicker junction devices (~ 230 nm). Our results also demonstrate the performance benefit due to the suppressed non-

Langevin bimolecular recombination rate in all our devices (~50 times in PTB7 blends and ~ 25 times in PCDTBT blends) (see **Supplementary Fig. 14**). Therefore, improving the carrier mobility is not the only transport strategy to deliver higher overall organic solar cell PCEs. In summary, increasing the $\mu_s (\beta_L/\beta)^{1/2}$ product allows: (a) the device to operate efficiently at a higher maximum power point V_{mp} (increasing the FF), because a lower effective voltage is sufficient to extract the carriers without significant recombination losses; (b) the short-circuit current density (J_{SC}) to be increased if the system is limited by bimolecular recombination at the short-circuit condition; and (c) an increase of V_{oc} *via* an enhanced carrier concentration [41, 166]. This means that thicker junctions can be used to improve the efficiency of light harvesting systems.

Conclusion

We have clarified that the conventional figure of merit (the $\mu\tau$ product or the drift distance L_D) is not appropriate for a comparative analysis of charge transport losses in organic solar cells due to the photocarrier mobility and density dependent lifetime. It is argued that this is generally the case for a broad range of high performance light harvesting systems made of disordered low mobility and undoped materials. We found that the electrode charge density marks the onset of significant bimolecular recombination losses and therefore controls the critical photocarrier drift distance ($L_D \sim d$). Based upon this physics we propose a new figure of merit for material and device characterization – the critical mobility-recombination-coefficient product $\mu_s (\beta_L/\beta)^{1/2}$. This parameter allows to minimize photocarrier recombination losses and to maximize the photovoltaic performance of organic solar cells and photodetectors. We verify this analysis in our model systems and find that the PTB7:PC70BM blends are superior compared to PCDTBT:PC70BM blends from a charge transport perspective because of the higher hole mobility and stronger suppressed recombination. Our work establishes a set of design rules to allow thicker junctions in organic solar cells whilst maintaining a high fill factor and power conversion efficiency. This is advantageous from a manufacturing perspective and offers an approach to improve the light harvesting efficiency of photovoltaic and photodetecting devices fabricated from low mobility materials.

Methods

Device preparation: The substrates (PEDOT:PSS/ITO/glass) were prepared as described in [48] and the active layer (junction) solution of PTB7 (purchased from 1-Material, M_w = 97.5 kDa, PDI = 2.1) and PC70BM (American Dye Source, Inc., Canada) was fabricated by using a 1:1.5 blend ratio by weight in chlorobenzene (CB) with 3% 1,8-diiodoctane (DIO) by volume.

Solar cells with three different junction thicknesses were prepared by using a total concentration of 31 mg/cm^3 for the 100 nm and 230 nm thick blends respectively, while a concentration of 45 mg/cm^3 was used to fabricate the 700 nm thick blend. The solutions were spun cast at 2200 rpm, 400 rpm and 600 rpm for 120 s, respectively. The films were subsequently dried at 70 °C. The active layer solution of PCDTBT (SJPC, Canada, Mw = 122 200 g/mol, PDI=5.4) and PC70BM was prepared by using a 1:4 blend ratio by weight in 1,2-dichlorobenzene (DCB) following the procedure described in [167]. Solar cells with three active layer thicknesses, 75 nm, 230 nm and 850 nm were fabricated by using a total concentration 25 mg/cm^3 for the 100 nm and 230 nm thick blends respectively, while a concentration of 40 mg/cm^3 was used to fabricate the 850 nm thick film. The solutions were spun cast at 2000 rpm, 500 rpm and 500 rpm for 90 s, respectively. The active layer thicknesses were measured with a DekTak 150 profilometer. All devices were completed by vacuum evaporation of 1.2 nm of samarium followed by 75 nm of aluminum under a 10^{-6} mbar vacuum. The device area was 0.2 cm^2 for *JV*, iPC and EQE measurements and 3.5 mm^2 for RPV measurements, respectively. The laser beam was expanded to cover the whole electrode. Note, we found the RPV measurement results were independent of the area of the pixel. All device fabrication took place within a glove box with < 1ppm O_2 and H_2O and *JV* and EQE measurements were also performed inside a glove box. Subsequently the devices were encapsulated for the iPC measurements.

Current density-voltage characteristics: *JV* curves were obtained in a 2-wire source sense configuration and an illumination mask was used to prevent photocurrent collection from outside of the active area. The presented PCEs correspond to average values of 6 pixels after several *JV*-measurements and represent the efficiencies of the devices directly before the iPC measurements were conducted. An Abet Class AAA solar simulator was used as the illumination source providing ~ 100 mW cm^{-2} of AM1.5G light. The exact illumination intensity was used for efficiency calculations and the simulator was calibrated with a standards traceable NREL photodiode.

Light intensity dependent measurements: iPC measurements were performed with a 532 nm continuous wave laser (Ningbo Lasever Inc.) providing a power of 1 W. Optical filters (ThorLabs) were used to attenuate the laser power and the photocurrent transients were recorded with an Agilent semiconductor device analyser (B1500A). Each measured data point corresponded to a steady state photocurrent measurement of the OSC at the respective incident laser power, which was simultaneously measured with a Silicon photodetector to improve the accuracy of the measurement. The error bars in Figure 3 (c) were estimated from the spread of the EQE values at the 1 sun equivalent power and the uncertainty in the short-circuit current. The error analysis for the calculated I_{SCLC} was conducted as follows: The circles in Figure 4 represent the calculated I_{SCLC} from the actual measured charge transport parameters on duplicate devices. In particular, the mean slower carrier transit time (Supplementary Figure 4) was used and the built-in voltage (U_{BI}) approximated by V_{oc}. The values of the I_{SCLC} are 78.3 mA, 4.4 mA, 0.17 mA for the 100 nm, 230 nm and the 700 nm thick PTB7:PC70BM junctions, and 15.1 mA, 0.34 mA, 0.01 mA for the 75 nm, 230 nm and the 850 nm thick PCDTBT:PC70BM junctions. For the upper error bar a 10% thicker active layer was assumed,

a 0.05V U_{BI} higher than V_{oc}, $\beta_L/\beta = \beta_L/\beta + 5$, and for t_{tr}^{slower} the lower limit of the dispersive slower carrier transit time range (Supplementary Figure 4) was taken. For the lower error bar a 10% thinner active layer was assumed, V_{oc} as the built-in voltage, $\beta_L/\beta = \beta_L/\beta - 5$ and the transit time of the slowest carriers in the device. Note, that the range of the error bar is mainly determined by the measured dispersive slower carrier mobility range, while the upper error bar represents a rather unrealistic case for the I_{SCLC}, because that would imply that the fastest of the slower carriers determine the onset of the bimolecular recombination losses.

Mobility, Recombination Coefficient, Trapping and dark-Celiv Measurements: RPV transients for mobility, β_L/β and charge trapping measurements were recorded with an oscilloscope (LeCroy WaveRunner 6200A) with different external load resistances (R_{Load}), while a delay generator (Stanford Research Systems DG535) was used to trigger a function generator (Agilent 33250A) and a pulsed Nd:Yag laser (Brio Quantel) with a pulse length of 10 ns. An excitation wavelength of 532 nm was used to generate the charge carriers, while neutral optical density (OD) filters were used to attenuate the ~ 50 mJ energy output. The RPV transients were measured under various applied biases. Low laser pulse intensities (~ OD 7) were used for the RPV mobility measurements to avoid space charge effects [104]. In contrast a high laser intensity (OD 3.5) was used to measure the bimolecular recombination coefficient on the same films. Celiv transients were recorded in the dark with the same experimental setup.

Numerical Simulations: The numerical simulations implement the key processes that occur in organic solar cells, such as carrier drift, diffusion, trapping, non-geminate recombination and space charge effects by taking into account the circuit resistance and the influence of the light absorption profile. Details of this model can be found in the Supplementary Information Methods

IV.2 Absence of First-Order Trap-Assisted Recombination

In order to be able to distinguish non-geminate recombination of free charges and geminate recombination of bound states and selectively quantify them under operational conditions and relevant devices, we first investigate whether or not non-geminate bulk recombination (known to be a non-linear process) may exhibit a linear recombination order with respect to the light intensity. This would render this loss mechanism indistinguishable from geminate recombination. In particular, we studied the impact of trap-assisted (and equilibrium charge assisted) recombination on the quantum efficiency. This work demonstrates that the recombination of free charges with traps is bimolecular in nature and is as such distinct in an iPC experiment for typical organic solar cells. The results implicate that charge transport free of non-geminate recombination can be realized at sufficiently low light intensities and this enables us to decouple geminate (first order) and non-geminate (second order) losses.

The supplementary information of this paper can be accessed online at (http://dx.doi.org/10.1021/acs.jpcc.5b09058).

Charge Transport without Recombination in Organic Solar Cells and Photodiodes

Abstract

Decoupling charge generation and extraction is critical to understanding loss mechanisms in polymer: fullerene organic solar cells and photodiodes, but has thus far proven to be a challenging task. Using steady state and time-resolved light intensity dependent photocurrent (iPC) measurements in combination with transient photovoltage, we estimate the total charge inside a typical device during steady state photoconduction, which is defined by the trapped, doping-induced and mobile charge populations. Our results show that non-geminate recombination of any order can be avoided as long as this charge is much less than capable of being stored on the electrodes – a criterion that is typically met in the linear iPC regime in donor:fullerene systems even with low, imbalanced mobilities. Knowing the conditions under which non-geminate recombination is essentially absent is an important device and materials design consideration. Our work also demonstrates that the technique of iPC is not only useful to assess the charge extraction efficiency, but can also be used to estimate the efficiency of free carrier generation in fully operational devices.

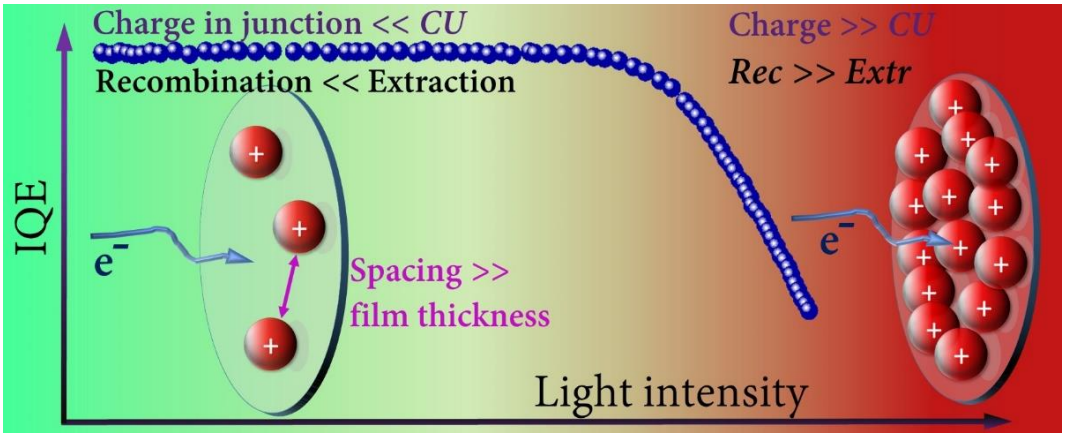

Introduction

The past decade has seen significant progress in improving the power conversion efficiencies of organic solar cells. This progress has been underpinned by the development of numerous donor and acceptor organic semiconductors, both polymeric and non-polymeric molecules [168]. The so-called thin film bulk heterojunction (BHJ) architecture has emerged as the preferred device platform, and blends of semiconducting donor polymers in combination with

fullerene acceptors are the main materials used in solution processed organic solar cells [169]. However, amongst the myriad of material systems and combinations reported in the literature, there are relatively few that yield truly high performance of order 10% in single junctions [26, 170, 171]. There are many reasons for this relative scarcity of efficient systems, not least of which is an incomplete understanding of the fundamental processes which define charge generation and extraction – and in particular the underlying loss mechanisms [60, 107, 172]. Most previous studies in this regard have focused on either charge generation or transport, but rarely simultaneously and in devices under relevant operational conditions [90, 173, 174]. This limitation can be attributed to an absence of appropriate experimental techniques that can clearly disentangle the two phenomena.

Charge generation is often studied using transient absorption spectroscopy (TAS) [174], transient microwave conductivity (TRMC) [69] or with the relatively new Time-Delayed Collection Field (TDCF) technique [90, 91]. TAS allows the assessment and quantification of the initial population of exciton and charge transfer states prior to recombination of free carriers and TRMC measures the product of the generation yield and the sum of the "local" charge carrier mobilities. TDCF essentially uses the (bias dependent) extracted charge after a short laser excitation as a measure of the charge generation yield by excluding non-geminate recombination. However, these techniques are typically not applied to operational solar cells and/or under relevant conditions. For example TAS requires often orders of magnitude higher illumination irradiances than delivered under 1 Sun conditions, TRMC is a very local probe of nm-scale generation and transport, and TDCF is a transient experiment that does not allow examination of steady-state charge carrier populations. That is not to say that these techniques have not delivered valuable insights, however one must always consider these results in the context of the experimental conditions under which they were obtained.

Electro-optical measurements of the external and internal quantum efficiency (EQE / IQE) are used to quantify the combined efficiencies of carrier photogeneration and extraction [23, 35, 109, 135]. However, charge generation and charge extraction losses cannot be differentiated through such an approach. There are several reasons for this, notably the impact of pseudo-first order non-geminate recombination (the process by which an electron and hole not originating from the same photoexcitation recombine) on the EQE. First order processes are often termed, sometimes incorrectly, monomolecular and are linearly dependent on the input light intensity.

Various studies have concluded that first order, non-geminate recombination strongly determines the overall solar cell performance in BHJ systems [40, 132, 160, 161], and substantial work has been conducted to identify the importance of trap states in the bulk and at the electrode contacts on the prevailing recombination order [33, 40]. Conversely, others have apparently demonstrated that bimolecular photocarrier recombination (which is non-linear with respect to the incident light intensity) is the efficiency limiting processs [93, 151, 156, 162, 172]. The order and nature of the dominant recombination and its impact upon device performance is therefore a matter of active scientific interest.

Recently, we employed steady-state intensity dependent photocurrent (iPC) measurements to quantify and understand the non-linear recombination losses in organic solar cells under relevant operational conditions [172]. In this current work, and motivated by the need to clarify the first order recombination losses, we study the linear iPC regime with similar steady state measurements in two donor:fullerene blend systems in a full BHJ architecture. Further, we extend the methodology by measuring the iPC in a time-resolved mode (similar to previous works [132, 175, 176, 177, 178]) in combination with transient photovoltage [54, 104]. In so doing, we are able to estimate the amount of charge present during steady state photoconduction at short-circuit conditions which allows us to arrive at consistent conclusions regarding the origin of non-geminate recombination. We find that if the amount of photogenerated charge is significantly less than that capable of being stored on the electrodes (where C is the capacitance and U the effective voltage which equals to the built-in voltage at short-circuit conditions) then the transport of already-dissociated charge carriers is apparently free of non-geminate recombination. This is even the case in situations where the hole mobility is low and the electron-hole mobilities are imbalanced, i.e., where we would normally expect significant hole trapping even at low light intensities. Understanding the conditions under which non-geminate recombination is minimised or even eliminated is the key to disentangle the charge generation and extraction efficiencies for solar cells under normal operating conditions.

Results

Device details and performance metrics: We studied two donor:acceptor blend systems namely: poly[*N*-9''-heptadecanyl-2,7-carbazole-*alt*-5,5-(4',7'-di-2-thienyl-2',1',3'-benzothiadiazole)]:[6,6]-phenyl-C_{70}-butyric acid methyl ester (PCDTBT:PC70BM) [152]; and N^1,N^3,N^5-tris(4-methoxyphenyl)-N^1,N^3,N^5-triphenylbenzene-1,3,5-triamine (WJ1-

04):PC70BM. WJ1-04 is a non-polymeric electron donor with the molecular structure, energy levels, solid state absorption, and preparation procedure provided in the Supplementary Information (SI, **Figure S1** and **Supplementary Note 1**). PCDTBT:PC70BM blends have been extensively studied [54, 104, 107, 133, 175] and are known to deliver an IQE of close to 100% in optimized device structures using a 1:4 ratio of polymer to fullerene. This is despite the blend possessing electron and hole mobilities that are ~100 times imbalanced: ~$2.5x10^{-3}$ cm^2 V^{-1} s^{-1} for electrons and ~$2.5x10^{-5}$ cm^2 V^{-1} s^{-1} for holes. The mobility values were determined using Resistance dependent Photovoltage (RPV) measurements (**Figure S2a** and **Methods**) for the BHJ structure following the previously described methodology [54, 104]. We note RPV mobilities have been successfully used to explain the charge collection efficiency of different polymer:fullerene cells with varying active layer thicknesses [172], and are similar to those reported using more conventional transport techniques [78, 107]. The optimal WJ1-04:PC70BM blend (1:10 by weight) has a much lower hole mobility ($6x10^{-7}$ cm^2 V^{-1} s^{-1} also **Figure S2b**) than the PCDTBT blend although the electron mobilities are similar and slightly lower than those reported for neat PC70BM diodes [104]. The WJ1-04:PC70BM blend represents an extreme example of mobility imbalance, which nevertheless delivers a significant photovoltaic response. Therefore, WJ1-04:PC70BM is an ideal system to study the impact of charge trapping (manifesting in a low effective mobility) on the non-geminate recombination mechanism. For both systems, the active layer thickness was optimized to deliver the highest power conversion efficiency (PCE), resulting in active layers of ~75 nm for PCDTBT:PC70BM and ~50 nm for WJ1-04:PC70BM. Nevertheless, the measured PCEs differ considerably: ~4.5±0.1% for the PCDTBT:PC70BM and 0.8±0.1% for the WJ1-04:PC70BM devices. Average white light current density versus voltage (*JV*) characteristics obtained under standard AM 1.5G illumination for each donor:PC70BM blend are provided in Supplementary **Figure 3** and **Supplementary Table 1**. Although our devices were optimized by blend ratio and active layer thickness, we note that the methodologies and concepts that are introduced in this work are not limited in any way by the need for fully optimized devices.

Non-geminate photocarrier recombination losses (steady state and time-resolved iPC)

Figure 1 (**a**, **b**) illustrate the protocols used for the steady state and time-resolved iPC measurements (Optical Input and Electrical Output). Note, all experimental details are described in Methods. **Figure 1a** shows the temporal profile of the application of incident light from a laser or light emitting diode (LED) of different intensities. **Figure 1b** illustrates how the

short-circuit photocurrent changes upon application of the light from the steady state through to the transient decay as the light is turned off. The shaded area in the transient region represents the extracted charge (Q_{ext}) which is obtained by integrating the photocurrent decay as a function of time. We note that, our method to measure Q_{ext} is essentially identical to the technique known as "Charge Ectraction (CE)", a well-known characterization tool to estimate the charge carrier density either at short-circuit conditions [132, 175, 176], or open circuit conditions [177, 178]. **Figure 1c** illustrates the results of such an experiment for an optimised PCDTBT:PC70BM device at short-circuit conditions. The steady state photocurrent as a function of incident light power is shown as a black dotted line (obtained from conventional steady state iPC with a laser source) and the estimated total charge present in the active layer (or junction) during steady state conditions (Q) is plotted with red data points. Q was obtained from the integrated photocurrent (Q_{ext}, refer to Methods for the differences between Q and Q_{ext}) using time-resolved iPC with an LED source and is normalized to CU, where U is the built-in voltage. The capacitance was determined using the dark-CELIV technique (Charge Extraction under Linearly Increasing Voltage – **Figure S4**) and the error bars are determined from the uncertainty in Q and CU in combination, as well as with the normal variance seen for multiple iPC measurements (see Methods). Equivalent measurements on WJ1-04:PC70BM solar cells are shown in **Figure S5**, and **Figure S6** summarises the measured transients and the extracted charge as a function of time for the studied systems. We note in both cases that the steady state photocurrent was found to be linear as a function of light intensity up to approximately 1 Sun (indicated by arrows in **Figure 1c** and **Figure S5**). Q appears to follow a sublinear trend, which is however, affected by a relatively large measurement error. Note, a linear steady state photocurrent does not imply a linear Q since, for instance, trapped charge carriers may be present in steady-state conditions that do not contribute to the photocurrent.

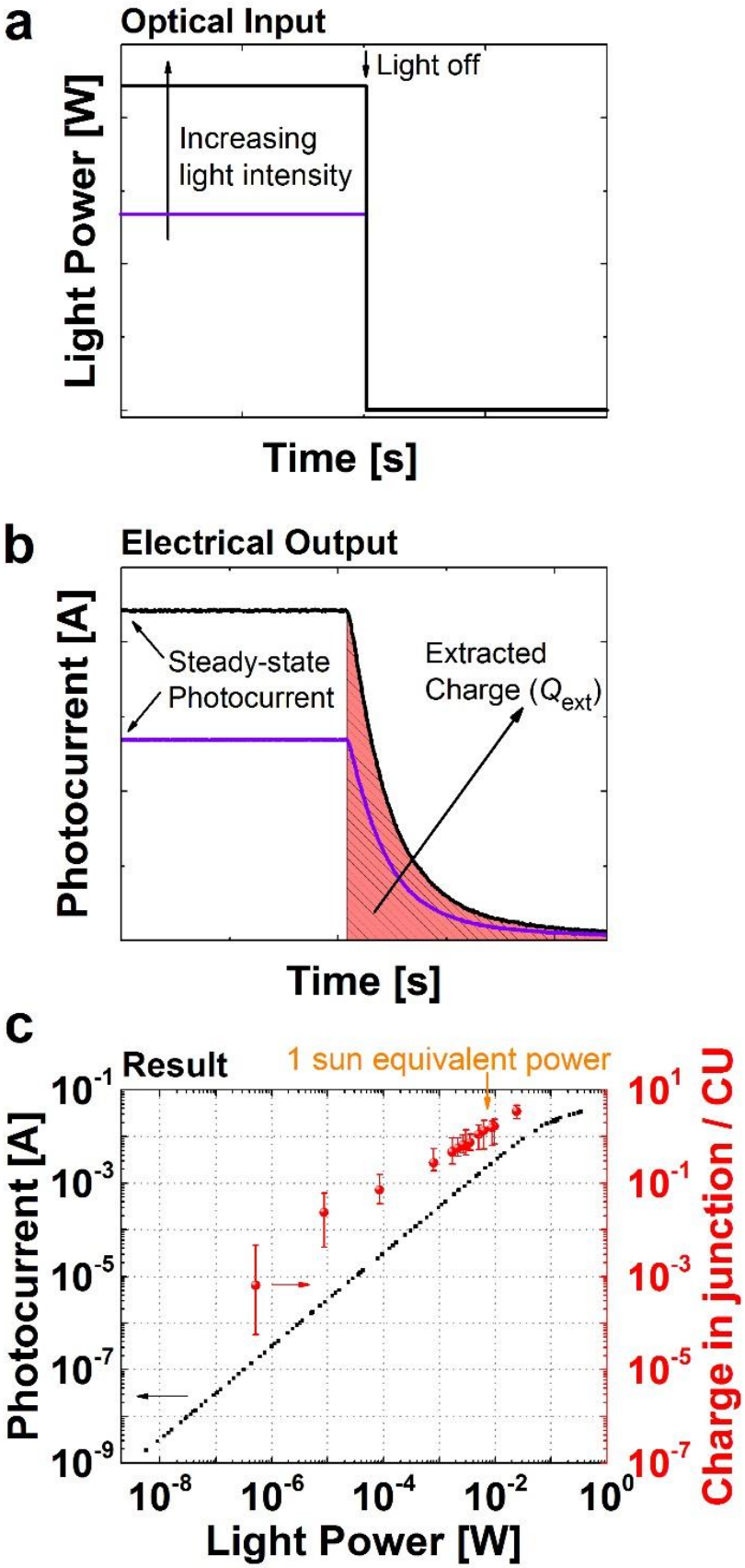
a
Optical Input
Light off
Increasing
light intensity
Light Power [W]
Time [s]
b
Electrical Output
Steady-state
Photocurrent
Extracted
Charge (Q_{ext})
Photocurrent [A]
Time [s]
c
Result
1 sun equivalent power
Photocurrent [A]
Charge in junction / CU
Light Power [W]

Figure 1. *Steady state and time-resolved photocurrent measurements. (**a**) Optical Input - Incident light with varying power is applied to the operational solar cell and then removed after some steady state period. (**b**) Electrical Output - The resultant steady state and transient photocurrent is measured as a function of incident light power. The extracted charge (Q_{ext}) is determined from the integrated decaying transient signal (shaded area). **(c)** Typical steady state photocurrent (black dotted line) and the actual amount of charge present in the junction (active layer) during steady state photoconduction (Q) normalized to the electrode charge (CU) (red dots) as a function of the incident light power. Q was estimated from Q_{ext} and can be further used to estimate the average lateral separation distance between the charges.*

As we have previously shown [172], the logarithmic scale of the conventional iPC plot of **Figure 1c** makes it difficult to analyse bimolecular recombination losses of small magnitude and makes the deviation from linearity hard to determine. Therefore, and in line with [172], we also present in **Figure 2**, the steady state iPC data from **Figure 1c** (**Figure S5**) replotted to represent the EQE (short circuit photocurrent divided by light power) as a function of input light power. The non-logarithmic EQE on the y-axis emphasizes the deviation from the linear iPC behaviour. Losses in the charge extraction efficiency due to bimolecular recombination can then be estimated from the deviation of the EQE at 1 Sun equivalent power [172], although other processes may also exhibit a non-linear recombination dynamic such as exciton-exciton annihilation or geminate recombination of CT states which could be affected by the reorganization of the electric field in the space charge limited current regime. We note the following: i) there are minimal 1 Sun bimolecular recombination losses in the optimized PCDTBT:PC70BM system; ii) WJ1-04:PC70BM suffers from (not unexpectedly) relatively larger 1 Sun bimolecular recombination losses (~10% of the collection efficiency) despite the junction being extremely thin (~50 nm); and iii) first (or pseudo-first) order losses dominate at 1 Sun for both systems (~25% and 78% of the EQE for PCDTBT:PC70BM and WJ1-04:PC70BM, respectively). These first order losses include: wasted light, non-optimal exciton and charge-transfer state (CT) dissociation, minority surface recombination losses of photogenerated charges or CT states that diffuse into the “wrong” electrode [32, 33], and potentially first order non-geminate recombination.

Estimation of the total charge in the active layer during steady state photoconduction

Extracted charge Q_{ext} measurements (as shown in **Figure 1b**) have been often used as tool for device performance analyisis [132, 175, 176, 177, 178]. However, there are a number of important experimental considerations, that must be accounted for in order to be able draw a correlation between Q_{ext} and the actual charge in the active layer (Q), namely: i) the extracted charge must become saturated as a function of time (right column **Figure S6**); ii) the charge accumulated on the electrodes during steady state illumination must be accounted for to calculate the extraction from the film $Q_{ext(film)}$ (see Methods); iii) care must be exercised with respect to the oscilloscope sensitivity limit which can be checked by measuring the extracted charge as a function of measurement load resistance (**Figure S7**); iv) the non-uniformity of the carrier distribution profile must be considered. Briefly, numerical simulations show that $Q_{ext(film)}$ underestimates Q by roughly a factor of 3 for the devices studied here (see Methods, **Figure S8** and explanatory figure caption); v) the possible presence of doping-induced equilibrium charge carriers which significantly influence the electric field and charge carrier distribution inside the film (**Figure S4** and attendant figure caption).; and vi) probably most importantly, long-lived, deeply trapped charges present in the film, i.e., those trapped and de-trapped on timescales much longer than accessible by the extraction measurement (>50 ms in our case) will not be recorded within Q_{ext}.

In our extracted charge calculations we carefully assessed and arranged the experimental details to account for considerations i) to v). In addition, to check for the presence of long-lived deeply trapped charges in our two blend systems, we employed the repetitive photovoltage technique ([104], see Methods). In this experiment we recorded the photovoltage transient generated by a single laser pulse on the device previously kept in the dark (the "first transient" in **Figure S9**). Thereafter, we recorded the same transients after many laser pulses with a repetition rate of 20 Hz (the "saturated transient" in **Figure S9**). The difference between the first and the saturated transient reveals if recombination losses are present due to these long-lived trapped charges (>50 ms). Identical first and saturated RPV transients were observed for both blends showing that charges that live longer than accessible by the Q_{ext} measurement do not cause recombination losses and those that may be present can thus be discounted in the analysis. The red dots in **Figure 2a** and **b** represent the calculated total charge in the junction (Q) normalized to CU. The errors bars were again determined as outlined in Methods from multiple

measurements, the uncertainty in *CU*, and the uncertainty of the correction factor that relates $Q_{ext(film)}$ to Q.

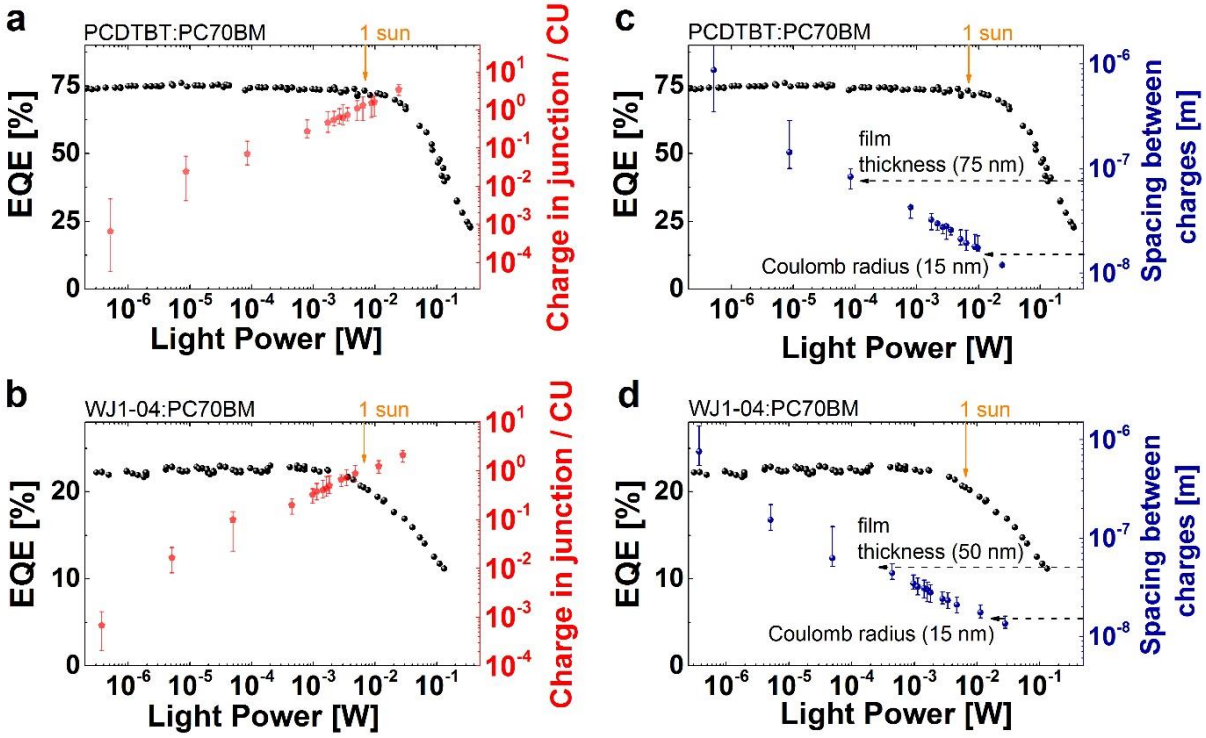

Figure 2. *Results obtained using the steady state and time-resolved iPC approach outlined in* ***Figure 1*** *for PCDTBT:PC70BM (a, c) and WJ1-04:PC70BM (b, d) blends. We plot the external quantum efficiency (EQE) as a function of the incident light power (black dots). (a) and (b) also present the total charge in the junction (active layer) normalized to the charge on the electrodes CU (red dots) as a function of input light intensity. (c) and (d) also show the average lateral spacing between charges (blue dots) calculated from the total charge in the junction. The equivalent 1 Sun intensities are marked by arrows and the Coulomb radius and junction (film) thicknesses are also noted. At the lowest accessible light intensities we observe in both blends an average lateral spacing between charges of ~1 μm. This indicates that free and shallow trapped carriers are extracted with a statistically negligible probability of meeting a non-geminate carrier. Significant bimolecular (non-linear and non-geminate) recombination losses emerge at lateral charge-to-charge spacings approximately equal to the Coulomb radius for PCDTBT:PC70BM blends, and this also corresponds to ~1 CU of charge in the device. In the WJ01-04:PC70BM system these losses persist at slightly greater charge spacings and lower charge carrier densities compared to PCDTBT:PC70BM. Note, the total charge does not*

saturate to a constant value at low light powers. That indicates the absence of a significant amount of equilibrium carriers or trap states that are filled, independent on the light intensity – a requirement for pseudo-first order non-geminate recombination.

Charge carrier spacing during steady state photoconduction

From the above estimation of the total charge in the junction, the carrier density can also be determined and hence the average spacing between the carriers in the film at all measured incident light powers (assuming a uniform distribution of carriers in the bulk). To interpret the spacing between carriers, we visualize their trajectories as the volume swept by a sphere during extraction. Considering the huge electrode area (compared to the film thickness) the resultant tubes lie, on average, mostly perpendicular to the electrodes. Consequently, the vertical distance between charge carriers is of little importance when aiming to assess the likelihood of a non-geminate recombination event. Therefore, we define the separation distance as the average lateral spacing between carriers, which was obtained by projecting all carriers onto the electrode area, assuming each carrier occupies a surface area of πr^2. The 2 dimensional lateral separation distance is then determined by 2 times r as shown in **Figure 2c** and **d** for the PCDTBT:PC70BM and WJ1-04:PC70BM blends, respectively. At the lowest accessible light powers in our experiment, the average lateral spacing between the charges is ~1 μm, which is much larger than the film thickness. Hence, under these conditions and post CT state separation, photogenerated free and shallow trapped carriers should from the statistical perspective be transported to the electrodes with negligible probability of meeting a non-geminate charge of the opposite polarity. At increasing incident light powers and thus carrier densities, the average charge-to-charge lateral distance reduces to a value at which the force of Coulombic attraction becomes larger than the force that drives the charge carriers towards the electrodes (the external electric field). Statistically therefore, charges of opposite polarity have a higher recombination probability. For the PCDTBT:PC70BM system at separation distances of ~10–20 nm the EQE begins to decrease as bimolecular recombination losses become significant. This separation distance is similar to the Coulomb radius (~15 nm), which is the critical distance that charge carriers can approach each other with a low recombination probability in the absence of an external electric field [51]. For the WJ01-04:PC70BM blend the bimolecular recombination losses appear to emerge at an average lateral charge-to-charge spacing slightly greater than the Coulomb radius, which is, however, not further analysed due to the uncertainty in the measurement.

Figure 2a and **b** also reveal that the non-geminate recombination losses emerge when the charge in the active layer approaches the electrode charge *CU*. Therefore, in order to avoid non-geminate recombination of any order in (near-to) Langevin systems, the amount of charge carriers in the film must be significantly below the *CU* value. As previously shown, that condition can be fulfilled by sufficiently high (slower carrier) mobilities [172], small amounts of trap states, and low doping-induced charge carrier densities. A reduced bimolecular recombination coefficient β (compared to the Langevin coefficient β_L) allows, however, an increase in the critical carrier density beyond the *CU* charge [172]. Indeed we observe that the charge in the junction is slightly higher than the *CU* value in the PCDTBT:PC70BM system (**Figure 2a**) because of its non-Langevin-type behaviour (β_L/β ~25) [172]. In contrast, drift-diffusion simulations indicate that WJ1-04:PC70BM behaves (**Figure S8**) like a Langevin system with very imbalanced mobilities. The non-geminate recombination onset is predicted to occur in such a system at lower photogenerated charge concentrations of between ~1/10 to 1/2 of *CU*.

Estimation of the Generation Efficiency

To summarise the discussion thus far, we demonstrate for the lowest experimentally accessible light intensities: (i) charge carriers that are extracted or detrapped on a timescale <50 ms (i.e., those accessible in our Q_{ext} experiment) are transported to the electrodes with negligible probability of meeting and recombining with a non-geminate charge of the opposite polarity; and (ii) charge carriers that are deeply trapped on longer timescales (>50 ms) do not cause recombination. This implies the absence of non-geminate recombination of any order at the lowest light intensities, or in other words the recombination rate is negligible compared to the extraction rate. This conclusion must remain equally valid as long as the iPC is linear (or the EQE constant). Although our experimental results do show that the transport of charges towards the extracting electrodes is essentially free of non-geminate recombination in the linear iPC regime, it is important to note that photogenerated charges as well as CT states and/or excitons may diffuse to the reverse electrode. The recombination of charges at the reverse electrode interface is also called *minority surface recombination* and is considered a first order recombination loss. Recent studies have shown its impact on the photovoltaic performance of devices with non-ideal electrodes [32, 33]. In general, choosing the correct contacts means back diffusion can be minimized. In this current work we use molybdenum oxide (MoO_3) as hole

contact for WJ1-04:PC70BM devices, which blocks the extraction of electrons at the hole contact due to the large energetic barrier [32, 179]. For PCDTBT:PC70BM cells in the standard architecture employed here, a high electroluminescence intensity at a forward current density of 50 mA cm^{-2} has been found, which is a signature for selective contacts and low minority surface recombination [32]. Even if the loss due to reverse diffusion is significant its impact will be likely on the dissociation of CT states, which we define as Coulombically bound charges that originate from the same photoexcitation rather than free carriers (charge collection). The effect on free carriers is smaller because the reverse diffusion length of the charges is expected to be limited to a few nm [68, 180].

Hence, if we consider back diffusion to be a minimal loss in the charge collection step, we can estimate the charge generation efficiency in fully operational devices under relevant operating conditions from our iPC data. By measuring the light absorption losses in operational devices upon spectroscopic reflectometry and simulating the parasitic absorptions in the non-active layers [36, 135], we determined the photocarrier generation efficiency to be approximately 91% (PCDTBT:PC70BM blend) and 53% (WJ1-04:PC70BM blend) at short-circuit conditions and an incident wavelength of 532 nm (**Supplementary Figure 10**). **Figure 3** summarises the relevant loss pathways, including optical and parasitic losses (EQE divided by IQE), as well as generation and transport losses at a 1 sun equivalent power at short-circuit conditions for PCDTBT:PC70BM devices (**Figure 3a**) and WJ1-04:PC70BM device (**Figure 3b**) .

Finally, as a further corroboration of our approach, we used transient absorption spectroscopy (TAS) to monitor the transient absorption (ΔOD) of photogenerated bound and free charge carriers following low-intensity laser excitation and the results are shown in **Figure 3c.** We found that the signals exhibit intensity-independent exponential decay dynamics, indicating first-order losses in the bound-charge (or CT) states [67]. After the exponential decay stops, the total dissociation yield of CT states can be estimated from the fraction of free charges remaining at longer times. Comparing the overall generation yield obtained from the iPC method with the CT dissociation yield from TAS we see good agreement (91% versus 86% for PCDTBT:PC70BM; and 53% versus 48% for WJ1-04:PC70BM, respectively). These results further support our fundamental assertion that the charge transport is free of non-geminate recombination in the linear iPC or constant IQE regime.

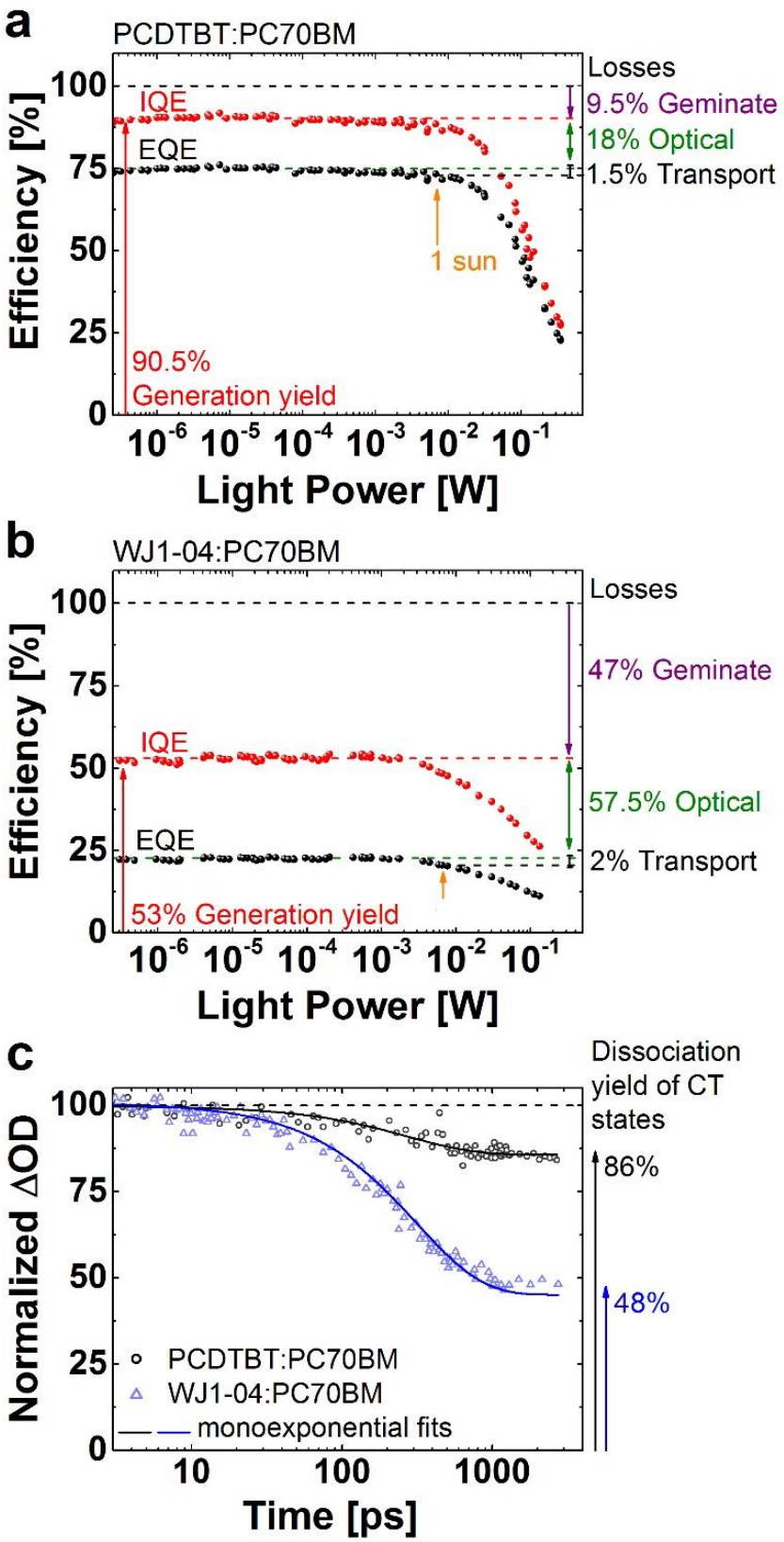

Figure 3. *External Quantum efficiency (EQE, black dots) and Internal Quantum efficiency (IQE, red dots) as a function of the incident light power for PCDTBT:PC70BM (a) and WJ1-*

04:PC70BM (b) blends. The lost incoming photon energy is decoupled into optical losses (i.e., lost light absorption in the active layer plus parasitic light absorption in non-active layers), geminate recombination and non-geminate recombination (charge transport) losses at short-circuit and 1 sun equivalent conditions for both blends. The remaining photon energy is converted into photocurrent. (c) Normalized transient absorption of the two blend systems at 1000 nm, following excitation at 560 nm measured at a low laser fluence of 500 nJ cm^{-2}. The experiment monitors the decay dynamics of ultrafast generated (<1 ps) charge transfer (i.e. bound) and free charges, which absorb at 1000 nm. The solid lines are exponential fits, indicating the geminate recombination of the bound states. The CT dissociation yield is given by the fraction of charge remaining at long times, and similar to the constant IQE value for both blends. This work demonstrates that (non-geminate) charge recombination is absent in the constant IQE regime and hence suggests that the charge generation yield can be estimated from the constant IQE value, which is further supported by the transient absorption data.

Conclusion

In summary, we have applied steady state and time-resolved intensity dependent photocurrent in combination with repetitive photovoltage to estimate the total charge inside an organic solar cell during steady state photoconduction. We have demonstrated that non-geminate recombination losses of any order are minimal in organic solar cells that are intrinsically undoped under operational conditions in a regime where the total photogenerated charge is significantly less than the charge stored on the electrodes (*CU*). This manifests as a linear intensity dependent photocurrent regime. The condition for remaining below the *CU* limit can be fulfilled by sufficiently high mobilities, small amounts of trap states and low doping-induced charge carrier densities. This work suggests that pseudo-first order non-geminate trap-assisted recombination does not limit the photovoltaic performance of organic solar cells. We believe that this finding should be generic for organic light harvesting systems since the absence of non-geminate recombination in the linear iPC regime is clear, even in blends with low carrier mobilities (~6x10^{-7} cm^2 V^{-1}s^{-1}), which is often a signature of significant trapping. Furthermore, this work shows that iPC is a suitable tool to disentangle the efficiencies for generation and extraction and in our case we have confirmed these findings using TAS as an independent measure at low light intensities. The ability to quantify both the generation efficiency and transport losses, and to understand the order of the dominant recombination mechanism is

important to systematically design organic solar cells and photodetectors with improved performance.

Methods

Device preparation: The substrates were cleaned by sonicating in sequence with Alconox, deionized water, acetone, and 2-propanol for 5 min, respectively. Subsequently, 15 nm of MoO_3 was deposited onto the cleaned indium tin oxide (ITO) substrates by thermal evaporation for the WJ104:PC70BM devices, while the substrates used for the PCDTBT:PC70BM devices were coated with 30 nm poly(3,4-ethylenedioxythiophene):poly(styrene sulfonate) (PEDOT:PSS; Baytron P VPAl4083). The active layer (junction) solution of PCDTBT (SJPC, Canada, Mw = 122 200 g/mol, PDI=5.4) and PC70BM was prepared by using a 1:4 blend ratio by weight in 1,2-dichlorobenzene (DCB). This blend ratio has previously been determined to be optimum [133]. An active layer thickness of 75 nm was obtained by using a total concentration of 25 mg/cm^3 and spin-coating at 2000 rpm for 90 s. PCDTBT:PC70BM solar cells operate most effectively for junction thicknesses <100 nm after which they suffer well documented losses of fill factor [133]. The active layer solution of WJ1-04:PC70BM was prepared by using an optimized blend ratio of 1:10 by weight in chloroform. The optimized active layer thickness of 50 nm was obtained using a WJ1-04:PC70BM concentration of 7.5 mg/cm^3 and spin-coating at 1000 rpm for 40 s. The active layer thicknesses were measured with a DekTak 150 profilometer. PCDTBT: PC70BM (WJ1-04:PC70BM) devices were completed by vacuum evaporation of 1.2 nm of samarium (15 nm of calcium) followed by 75 nm of aluminium under a 10^{-6} mbar vacuum. The device area was 0.2 cm^2. All device fabrication took place within a glove box with < 1ppm O_2 and H_2O and *JV* and EQE measurements were also performed inside a glove box. Subsequently the devices were encapsulated for the *JV*, iPC, RPV and dark-CELIV measurements.

Current density-voltage characteristics: *JV* curves were obtained in a 2-wire source-sense configuration and an illumination mask was used to prevent photocurrent collection from outside of the active area. The presented PCEs correspond to average values of 6 pixels after several *JV*-measurements and represent the efficiencies of the devices directly before the iPC measurements were conducted. An Abet Class AAA solar simulator was used as the illumination source providing ~100 mW cm^{-2} of AM1.5G light. The exact illumination intensity was used for efficiency calculations, and the simulator was calibrated with a standards traceable NREL photodiode.

Light intensity dependent measurements: Steady state iPC measurements were performed with a 532 nm continuous wave laser (Ningbo Lasever Inc.) providing a power of 1 W. Optical filters (ThorLabs) were used to attenuate the laser power and the photocurrent transients were recorded with an Agilent semiconductor device analyser (B1500A). Each measured data point corresponded to a steady state photocurrent measurement at the respective incident laser power, which was simultaneously measured with a Silicon photodetector to improve the accuracy of the measurement.

Time resolved (transient) iPC measurements require a light source with a fast switch-on/off time which prevented the use of the laser. We chose instead a green light emitting diode (LED) (Epistar) with light emission from 520 to 530 nm and a switch on/off time <50 ns. The same optical filters (ThorLabs) were used to attenuate the light power and the transients were recorded with a Tektronix oscilloscope (DPO 7354C). Two types of Q_{ext} measurements were performed: (i) using a constant load resistance (R_{Load}) of 50 Ω to record the transients at different light intensities (top 4 panels **Supplementary Figure 6**), (ii) R_{Load} was varied from 50 to 50000 Ω depending on the light power (bottom 4 panels **Supplementary Figure 6**). The latter experiment allows the measurement of lower extracted charge values, since a high R_{Load} allows for the amplification of the signal at low light powers. R_{Load} was subsequently reduced at higher incident powers such that the resulting photovoltage did not exceed 100 mV to ensure that conditions close to short-circuit were always maintained. Q_{ext} as measured at the load resistance constitutes both the charge that moves in the film ($Q_{ext(film)}$) and the charge that accumulated on the electrodes during steady state conditions. To obtain $Q_{ext(film)}$ it is necessary to subtract the electrode charge from Q_{ext}. The electrode charge in the steady state conditions equals C times the sum of the voltage drop on the circuit resistance ($R_{circuit}$) and the load resistance U_{load} (at steady state conditions). The extracted charge from the film is consequently $Q_{ext(film)} = Q_{ext} - C (I R_{Series} + I R_{Load})$, where I is the measured photocurrent at the load during steady state conditions. The values for the circuit resistance (originating mainly from the ITO electrode) were obtained from the extrapolated saturated photocurrents in the iPC measurements (~30 Ω for both studied systems). Next, the actual charge in the active layer Q is estimated from $Q_{ext(film)}$: under operational conditions the charge density is non-uniform, with the highest densities nearest to the electrodes (**Supplementary Figure 8d**). Consequently, the average carrier will travel less than half the thickness of the film during the turn-off transient, and so $Q_{ext(film)}$ as obtained from the integral of the transient decay will underestimate the true charge density that was originally present. To estimate the error introduced by these non-uniform charge densities, we applied numerical simulations (**Supplementary Figure 8**) and concluded that $Q_{ext(film)}$ underestimates the charge present in the active layer by approximately a factor of 3 for the devices studied here. This correction factor was applied in our analysis, however, it should be mentioned this factor is an estimation only. It will be sensitive to the nature of the semiconductor-metal interface, and we did not consider non-ideal interfaces in our simulations. The light power of the laser and the LED were calculated from the measured (average) EQE (**Figure S10**) at the emission maximum (which is at 532 nm for the laser and between 520 nm and 530 nm for the LED).

The error bars in **Figure 1** and **Figure 2** were estimated from the spread of the data in multiple measurements as well as from the uncertainty in the extracted charge and the CU values from dark-CELIV measurements (see below). For the upper error bar a 5% lower C value than that obtained from the dark-CELIV measurements (**Figure S4)** and V_{oc} was assumed for the built-in-voltage U. For the lower error bar a 5% higher C value and a 10% higher built-in voltage than V_{oc} were used. Moreover, we accounted for the uncertainty in the correction factor that

relates $Q_{ext(film)}$ and Q. For the lower error bar a correction factor of 2.5 was used and for the upper error bar the factor was 3.5.

Repetitive and Resistance dependent PhotoVoltage and dark-Celiv measurements: RPV transients for mobility and charge trapping measurements were recorded with an oscilloscope (LeCroy WaveRunner 6200A) with different external load resistances (R_{Load}), while a delay generator (Stanford Research Systems DG535) was used to trigger a function generator (Agilent 33250A) and a pulsed Nd:Yag laser (Brio Quantel) with a pulse length of 10 ns. An excitation wavelength of 532 nm was used to generate the charge carriers, while neutral optical density (OD) filters were used to attenuate the ~50 mJ energy output. The RPV transients were measured under various applied biases. Low laser pulse intensities (resulting in a photovoltage close to 100 mV at a load resistance of 1 MΩ) were used for the RPV mobility measurements to avoid space charge effects [104], while the absence of long-lived trap-induced recombination was checked at a load resistance of 1 MΩ and at different laser powers (from low powers resulting in a photovoltage of ~30 mV up to high powers that saturate the photovoltage). Dark-CELIV measurements were recorded with the same experimental setup, without the use of a laser. A capacitance value of 10.45 nF was obtained for the PCDTBT:PC70BM and C = 15.1 nF for the WJ1-04:PC70BM films. A summary of these measurement techniques and how they are used to estimate the mobility, trapping and the capacitance are provided in the SI within the figure captions of **Figure S2**, **Figure S9** and **Figure S4**, respectively.

Transient Absorption Spectroscopy (TAS) measurements: Femtosecond TAS was carried out using a commercially available transient absorption spectrometer, HELIOS (Ultrafast systems). Samples were excited with a pulse train generated by an optical parametric amplifier, TOPAS (Light conversion). Both, the spectrometer and the parametric amplifier were seeded with an 800 nm, <100 femtosecond pulses at 1 KHz generated by a Solstice Ti:Sapphire regenerative amplifier (Newport Ltd). Changes in the optical density of the films induced by the laser excitation were followed with a second broadband pulse (830–1450 nm) generated in a sapphire crystal. The HELIOS transient absorption spectrometer was used for recording the dynamics of the transient absorption spectra up to 2.7 ns with an average 200 fs instrument response function. Measurements were performed on the same devices as the rest of the study. Samples were excited at 560 nm, 500 nJ cm^{-2}. The low fluence ensures absence of second order recombination processes. The decay dynamics were analysed at 1000 nm, corresponding to the polymer positive polaron (cation) absorption. Global analyses of the data were carried out using the data analysis package Igor.

Numerical Simulations: The numerical simulations implement the key processes that occur in organic solar cells, such as carrier drift, diffusion, trapping, non-geminate recombination and space charge effects by taking into account the circuit resistance and the influence of the light absorption profile. Geminate recombination is not considered in the simulations. Details of this model can be found in the Supplementary Information Methods.

Chapter V: Advances in Fundamental Understanding of Charge Generation

The results described in the previous **Chapter IV** demonstrated that the charge transport issues are relatively small under short-circuit and 1-sun equivalent illumination for typical OSCs, and that these losses can be essentially avoided by adjusting the active layer thickness. Instead, photocurrent lossless at short-circuit conditions lie often in the charge generation quantum yield, and in particular in the dissociation of the CTS. Establishing design rules to precisely control the CTS dissociation can, therefore, not only increase the generation quantum yield of current light harvesting diodes, but could also enable a greater freedom to tune the blend band gap and the energy level offsets of the donor and acceptor components. Ultimately this could close the gap to inorganic solar cells.

In this chapter results are described which extend our analysis using the iPC methodology in order to advance the understanding of charge generation and the CTS dissociation. In particular we focus on the relationship between the donor:acceptor percolation pathways, donor:acceptor blend ratio, charge carrier mobilities, electric field - and the impact of these variables on the exciton and charge transfer splitting efficiency. Moreover, we show how the interplay between CTS recombination and dissociation influences the overall recombination rate of free charges. This chapter consists of two published papers and one that is currently under review.

V.1 Recombination Losses at Operational Bias

This section presents a detailed study of the electric-field dependence of charge generation. The results suggest that the geminate recombination is susceptible to changes in the driving electric field depending on the slower carrier of the system. In contrast to the common understanding, geminate recombination is a significant limiting factor of the photocurrent in forward bias, which negatively impacts the fill factor of organic photovoltaic diodes. The results also suggest that both the generation and the collection efficiency depend critically on the slower carrier mobility and, thus, indicate why it has been previously difficult to distinguish both losses in the power generating regime of organic solar cells.

The manuscript incorporated below is currently under consideration in *Advanced Energy Materials*. The supplementary information of this paper can be accessed online at (https://www.dropbox.com/s/13k55gsglk16rov/Supplementary_Information_efied.docx?dl=0)
.

Electric-Field Dependent Geminate Recombination Losses in Organic Solar Cells *via* the Poole-Frenkel Effect

Abstract

Charge photogeneration in bulk-heterojunction organic solar cells (OSCs) involves charge-transfer state (CTS) dissociation into free charges. The dependence of this process on electric field is complex due to the strong Coulomb-interaction of the charges within the CTS. We have studied the recombination dynamics in bulk-heterojunction OSCs with different hole mobilities from short-circuit to maximum power point. We show that in this regime, in contrast to previous studies, geminate recombination is at least as significant as bimolecular recombination of photo-generated charge carriers. We demonstrate that the geminate losses increase with decreasing slower carrier mobility, and attribute the field-assisted CTS dissociation to either mobilization of charges trapped at the donor:acceptor interface through the Poole-Frenkel effect, and a reduced Coulomb barrier for dissociation. The dependence of both charge extraction and generation on the slower carrier mobility explains why the field dependence of organic solar cell efficiencies have historically been attributed to charge-extraction losses.

Introduction

Bulk-heterojunction (BHJ) organic solar cells (OSCs) comprising blends of electron donating:accepting organic semiconductors continue to improve as a result of optimizations in molecular design, device engineering, and an increased understanding of how they work. A promising feature of BHJ solar cells is their high internal quantum efficiency (IQE) – the product of the charge generation (η_{GEN}) and collection (η_{COLL}) efficiency, which in the best systems, are close to 100% under short-circuit conditions [89, 129]. However, at the maximum power voltage (V_{MP}), OSCs often exhibit significant losses in the photocurrent, lowering the fill factor (FF) and the photovoltaic performance. Despite attempts to understand these losses under operational biasing, their origin remains unclear [181].

In addressing this critical question, it is important to distinguish the different processes that can lead to photocurrent losses in forward bias: the most fundamental distinction being whether the charge recombination is non-geminate or geminate. Recombination is non-geminate if the two charges in the encounter originated from different photoexcitations, and is the most common explanation for photocurrent losses under operational bias [91, 92, 162, 182, 183]. In forward bias, the driving field for extraction decreases, which leads to a build-up of electron (*n*) and

hole (p) density in the bulk of the heterojunction. Hence, the bimolecular recombination rate scales as $R \sim np$. As both n and p depend on the incident light intensity (I), the recombination losses are non-linear with respect to I.

That said, certain non-geminate recombination processes could conceivably lead to losses that are linear with I [40, 132, 160, 161]. In particular, the recombination of mobile carriers with trapped charges may be linear if one carrier type is trapped independent of the light intensity such that $R \sim N_{\mathrm{trap}} p$. Similarly, photogenerated charges can recombine with a large excess of injected charges from the electrodes [184], or equilibrium charges (due to unintentional doping). Finally, non-geminate recombination can occur not only within the bulk of the heterojunction, but also at the 'wrong' electrode due to diffusion [32, 33, 184]. The losses associated with these mechanisms increase with the applied voltage in forward bias; both because charge injection increases, and because charge diffusion becomes more dominant as the driving field diminishes.

In contrast, geminate recombination occurs if the two charges originate from the same photoexcitation. In both geminate and non-geminate cases recombination occurs *via* a charge transfer state (CTS). The CTS consists of two separate charges, which can interact with a local or applied electric field (E). The E-field dependence of the CTS dissociation rate constant $k_{\mathrm{d}} \sim (1 + E + E^2/3 + \cdots)$ is described in the Braun model [66]. However, assuming an initial charge separation of 1.5 nm [65], the Columbic field between charges forming the CTS is >10 stronger than a typical built-in electric field in a BHJ, which suggests the electric field should only have a small impact. This hypothesis is consistent with the majority of transient photocurrent measurements on efficient blends, and some absorption spectroscopy studies [89, 92, 91, 94, 183]. Nevertheless, other studies have shown field dependent charge generation by measuring the CTS emission intensity, lifetime and transient absorption, or using steady-state photocurrent measurements [173, 185, 186, 187, 188], with the results often quantitatively explained with the Braun model. In addition to the field dependence of k_{d}, the Braun model suggests that k_{d} scales with the sum of the faster and slower carrier mobilities, $\mu_{\mathrm{f}} + \mu_{\mathrm{s}}$. Due to the electronically disordered nature of organic semiconductors, the mobility depends on temperature and often on the electric field, as shown by the Poole-Frenkel relation [77]. Thus, apart from the interaction of the field with the CTS dipole, the field-dependence of k_{d} can also originate from a field-dependent mobility, i.e., $k_{\mathrm{d}} \sim \mu(E)$.

Motivated by these considerations, we investigate the photocurrent losses from short-circuit to V_{MP}, and in particular, the dependence of the recombination losses on the light-intensity, electric field, and mobility. We report on five organic semiconductor blends with very different hole mobilities, but similar electron mobilities. Light intensity-dependent photocurrent measurements show that for these materials combinations, the majority of the photocurrent losses from short-circuit to operational bias scale with the first-order of the light intensity. Furthermore, these first-order losses increase with decreasing slower-carrier mobility. Our experiments indicate that the first-order losses are, in this bias regime, less affected by non-geminate recombination due to trapped, injected or equilibrium charges with pseudo-first-order dynamics, or non-geminate recombination at the electrodes. We attribute them to an electric-field-dependent mobilization of trapped (slower) charges and/or a reduced Coulomb barrier for dissociation, which is counter to the conventional view that photocurrent losses are predominantly bimolecular.

Results and Discussion

Materials

We studied bulk heterojunction OSCs fabricated from 5 different donor: acceptor blends. **Figure 1** (**a**) shows the molecular structures and energy levels of each donor material with [6,6]-phenyl-C_{70}-butyric acid methyl ester (PC70BM) - the acceptor. The optimized blends for device performance have been previously reported and are:

(i) poly(2,5-(2-octyldodecyl)-3,6-diketopyrrolopyrrole-alt-5,5-(2 ,5-di(thien-2-yl)thieno[3,2-b]thiophene) (DPP-DTT):PC70BM [103, 189].

(ii) poly[(4,8-bis{2-ethylhexyloxy}benzo[1,2-b:4,5-b']dithiophene-2,6-diyl)(3-fluoro-2-{[2-ethylhexyl]carbonyl}thieno[3,4-b]thiophenediyl)] (PTB7):PC70BM [131].

(iii) (poly[*N*-9"-heptadecanyl-2,7-carbazole-*alt*-5,5-(4',7'-di-2-thienyl-2',1',3'-benzothiadiazole) (PCDTBT):PC70BM [152].

(iv): N^1,N^1,N^3,N^3,N^5,N^5-hexakis(4-methoxyphenyl)benzene-1,3,5-triamine (WJ1-06):PC70BM [190, 191].

(v): N^1,N^3,N^5-tris(4-methoxyphenyl)-N^1,N^3,N^5-triphenylbenzene-1,3,5-triamine (WJ1-04):PC70BM [192].

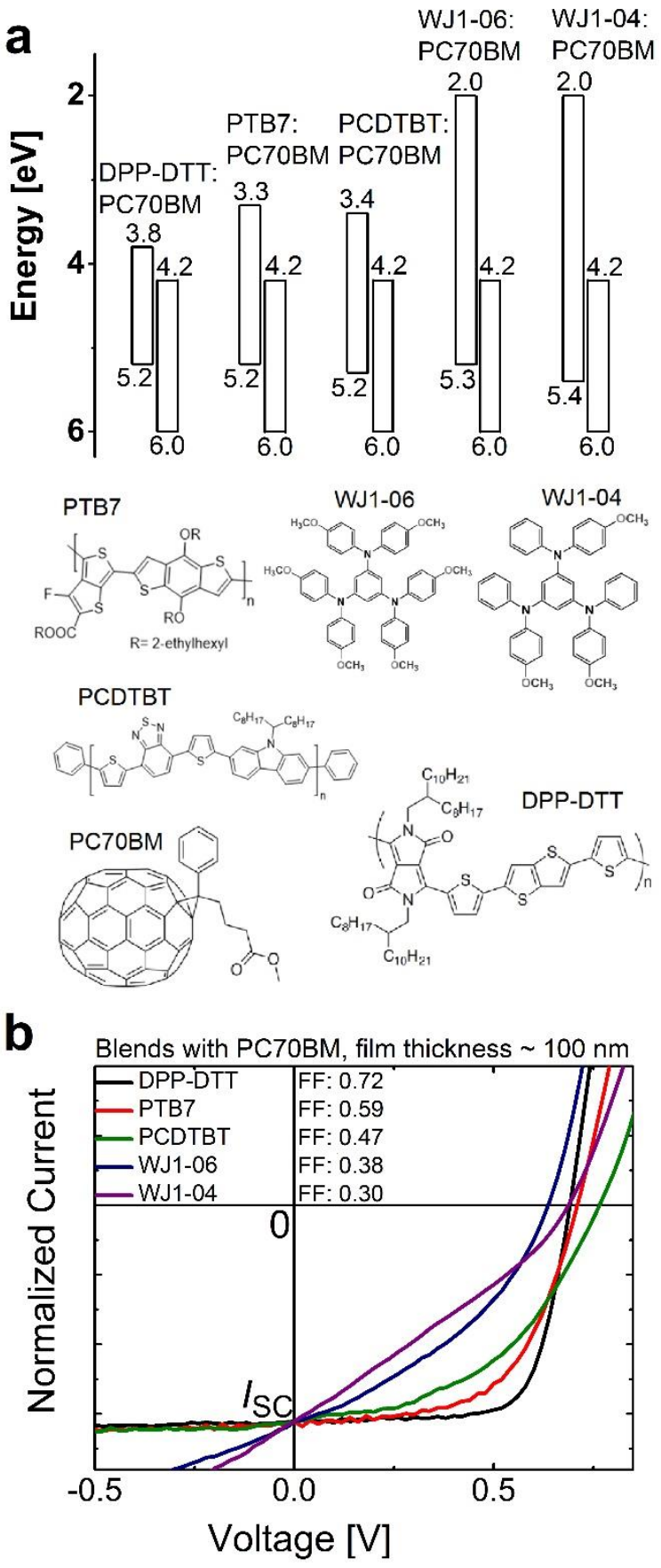
a
Energy [eV]
2
4
6
DPP-DTT: PC70BM
PTB7: PC70BM
PCDTBT: PC70BM
WJ1-06: PC70BM
WJ1-04: PC70BM
3.8
4.2
5.2
6.0
3.3
4.2
5.2
6.0
3.4
4.2
5.2
6.0
2.0
4.2
5.3
6.0
2.0
4.2
5.4
6.0
PTB7
R= 2-ethylhexyl
WJ1-06
WJ1-04
PCDTBT
PC70BM
DPP-DTT
b
Blends with PC70BM, film thickness ~ 100 nm
DPP-DTT
PTB7
PCDTBT
WJ1-06
WJ1-04
FF: 0.72
FF: 0.59
FF: 0.47
FF: 0.38
FF: 0.30
0
I_{SC}
Normalized Current
-0.5
0.0
0.5
Voltage [V]

Figure 1. *(**a**) The chemical structures and energy levels of the materials that were studied in this work. Ionization potentials were measured by photoelectron spectroscopy in air, and the spectroscopically measured optical gaps were used to determine the electron affinities. (**b**) Normalized and averaged photocurrent density versus voltage characteristics measured under standard AM 1.5G illumination highlighting the large differences for each blend in the device forward bias fill factors.*

WJ1-04 and WJ1-06 are non-polymeric ('small molecule') organic semiconducting donors, which were synthesized in house [190, 191, 192]. WJ1-06 differs from WJ1-04 in terms of the number of alkoxy substituents on the surface phenyl rings. The active layer thickness of all of the BHJ OSCs was 100 nm, which is a typical thickness used for high efficiency thin-film OSCs. However, we note that the key findings of this work are largely independent of the chosen active layer thickness. The devices were fabricated in the conventional architecture (see Experimental Section).

The material systems were chosen based on the large differences in their slower-carrier mobilities (ranging from ~$1x10^{-3}$ $cm^2V^{-1}s^{-1}$ to ~$6x10^{-7}$ $cm^2V^{-1}s^{-1}$ as measured by Resistance dependent Photovoltage). This delivers a large variation in the forward-bias photocurrent losses and FFs. **Figure 1** (**b**) shows representative white-light current-voltage (*J-V)* performance curves obtained under standard AM 1.5G illumination. We note that multiple devices were fabricated and tested for each blend combination to confirm the reproducibility of the results. The *J-V* curves are normalized to their short-circuit current to highlight the differences in photocurrent losses in the power-generating regime of the cells. The original *JV* curves and the key photovoltaic parameters are provided in the Supplementary Information (S.I.), **Figure S1** and **Table S1**, respectively.

Light-intensity dependence of photocurrent losses from short-circuit to the maximum-power point

In order to disentangle first-order and higher-order photocurrent losses under operational solar cell conditions, we performed intensity dependent photocurrent (IPC) measurements at an excitation wavelength of 532 nm. From the IPC measurements we calculated the EQE and examined it as a function of the photocurrent, which increases with the applied laser intensity. Details of this methodology are given in the literature [172, 192]. First, we measured IPC at

short-circuit (0 V) and then subsequently at the maximum power point under 1-sun equivalent conditions (V_{MP} applied). The results of these IPC measurements are presented for WJ1-04:PC70BM in **Figure 2** (**a**), while the results for the other blends are shown in **Figure S2**. **Figure 2** (**a**) presents the EQE of WJ1-04:PC70BM device as a function of the photocurrent at 0 V (black data points) and at V_{MP} (red data points). The EQE was normalized to 100% at 0 V, which eliminates losses in the generation efficiency and the absorption efficiency at short-circuit from the analysis. The following analysis is, however, not limited in any way by this normalization but does allow for direct and convenient comparison of first and second order losses. The 1-sun short-circuit current (I_{SC}) and maximum power point current (I_{MP}) are marked by circles. The plot shows that the WJ1-04:PC70BM blend is strongly limited by bimolecular recombination under 1-sun conditions, as seen by the decrease of the EQE at relatively low photocurrents < ~10^{-5} A) [172]. The reason for this behaviour is the relatively low slower carrier mobility in this blend (6×10^{-7} $cm^2V^{-1}s^{-1}$), which creates a strong mobility imbalance, a build-up of slower carriers in the junction, and subsequent high encounter probability of non-geminate charge carriers [172].

The EQE under forward bias has two characteristic features. First, we observe that the constant EQE value (prior to deviation) is less compared to the EQE at 0 V, which we define as a first-order recombination loss (more clearly observable in the original IPC plot in **Figure S3** (**a**). The magnitude of these first-order losses strongly depends on the effective driving voltage V (built-in minus the applied voltage, **Figure S3** (**b**). Second, the deviation from constant EQE occurs at lower photocurrents, indicating increased bimolecular recombination losses. Qualitatively we can therefore say that both first and second order losses are increased under forward bias in this blend. In order to estimate the increased recombination at V_{MP}, we normalized the EQE at 0 V to the EQE at V_{MP} in the constant EQE regime, as illustrated by the blue dotted line in **Figure 2** (**a**). This allows the first-order recombination losses to be calculated from the difference between the EQE value at I_{SC} (black circle) and the normalized EQE^* at I_{SC} (blue circles), i.e., $\mathrm{EQE}(I_{\mathrm{SC}}) - \mathrm{EQE}^*(I_{\mathrm{SC}})$. Similarly, the increased bimolecular recombination losses can be obtained from $\mathrm{EQE}^*(I_{\mathrm{SC}}) - \mathrm{EQE}(I_{\mathrm{MP}})$.

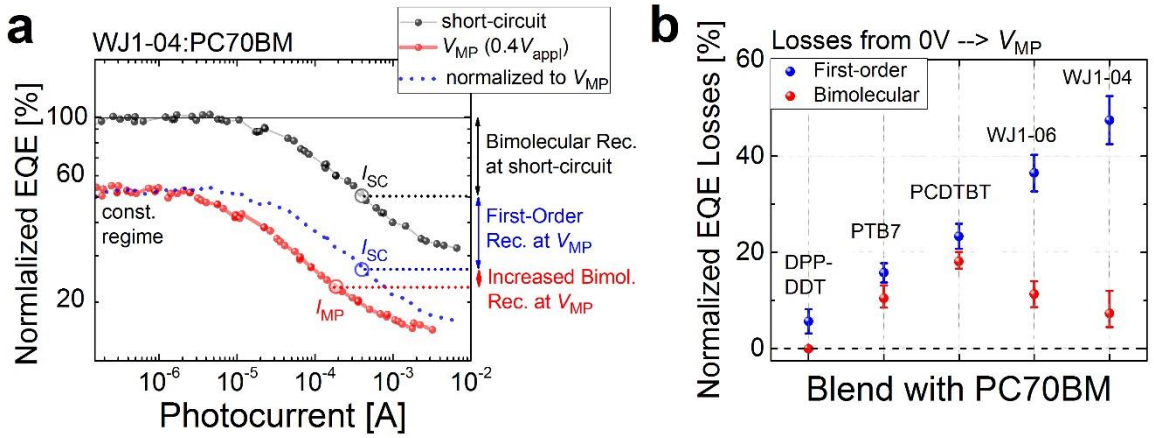

Figure 2. *(**a**) Photocurrent dependent external quantum efficiencies (EQEs) measured on the WJ1-04:PC70BM blend at 0 V applied (black data points) and the maximum power voltage (V_{MP}) (red data points). The 1-sun short-circuit current (I_{SC}) is marked by the black circle and the photocurrent at V_{MP} by the red circle (I_{MP}). The dotted blue line (denoted as EQE^*) represents the EQE at 0 V normalized (parallel shifted) to the EQE at V_{MP}. This procedure allows estimaion of the first-order losses from $EQE(I_{SC}) - EQE^*(I_{SC})$ and bimolecular recombination losses from $EQE^*(I_{SC}) - EQE(I_{MP})$. (**b**) The first-order and bimolecular recombination losses of the blends from short-circuit to V_{MP}. The actual photocurrent losses at V_{MP} can be obtained by multiplying the I_{SC} by the plotted first-order and bimolecular recombination losses. The error bars of the first-order losses were estimated from the standard deviations of the constant EQE regimes at 0 V and V_{MP}, considering also an uncertainty of 40 mV in the V_{MP} and expected shifts of the constant EQE values due to this uncertainty. The error bars of the bimolecular losses were estimated from the standard deviations of the EQEs at 0 V and V_{MP}, including a 10% uncertainty in both I_{SC} and I_{MP}.*

Figure 2 (**b**) summarises the increase in first-order and bimolecular recombination losses from short-circuit to V_{MP} for each of the blends (again noting the EQE(I_{SC}) is normalized to 100%). The graph demonstrates that the increase in first-order losses are higher for each blend. In addition, it is interesting to note that the gap between the first-order and second-order recombination losses is larger in blends that are already strongly limited by bimolecular recombination at short-circuit (WJ1-06:PC70BM and more pronounced in WJ1-04:PC70BM). On the other hand, the DPP-DTT blend, which is not limited by bimolecular recombination at short-circuit nor at V_{MP}, exhibits only small first-order recombination at V_{MP}. OSCs that are at the boundary of being limited by bimolecular recombination at 1-sun under short-circuit conditions, such as PCDTBT:PC70BM and PTB7:PC70BM, exhibit similar losses in first-order

and bimolecular recombination, with the former being slightly higher (outside experimental error). We further confirmed this observation for the same blends with different active layer thicknesses (**Figure S4**). While the generality of these observations, and the exact trends over the whole power generating regime cannot be simply implied, the important conclusion is that first-order recombination plays an important role for the JV-curve, particularly at V_{MP} in OSCs.

Mobility dependence of the first-order photocurrent losses

To elucidate the origin of the first-order losses, we compared the charge carrier mobilities with the first-order losses at a fixed reduction of the driving field. The charge transport parameters were studied using a transient photovoltage technique [54, 104]. The left column of **Figure 3** shows the transient photovoltage responses for each blend (see **Figure** 1) after a short (~5 ns) laser exaction at 532 nm at different load resistances. The technique allows visualization of the arrival of charge carriers at the electrodes after transiting the whole active layer thickness from the shoulders in the photovoltage transient signal. The data shows that the carrier arrival times, as marked by the arrows, differ by many orders of magnitude (i.e., $1x10^{-7}$s to $2x10^{-4}$s). Accordingly, the slower carrier mobility varies from ~$1x10^{-3}$ $cm^2V^{-1}s^{-1}$ in the DPP-DTT:PC70BM blend to $6x10^{-7}$ $cm^2V^{-1}s^{-1}$ in the WJ1-04:PC70BM blend. The other blends lie between these two limiting cases. In blends with significantly imbalanced mobilities (> ~10 times imbalanced) the faster and slower carrier transit time can be identified unambiguously. The arrival of faster carriers can be observed from the first shoulder in the photovoltage signal. The faster carrier can be assigned to electrons in PCDTBT:PC70BM, WJ1-06:PC70BM and WJ1-04:PC70BM [104, 192]. In PTB7:PC70BM and DPP-DTT:PC70BM devices however, the electron and hole mobilities are superimposed. Nevertheless, it can be seen that the electron mobility is very similar in each blend (varying between $2x10^{-3}$ $cm^2V^{-1}s^{-1}$ and $3x10^{-4}$ $cm^2V^{-1}s^{-1}$), in contrast to the hole mobility.

The right column of **Figure 3** presents EQEs as a function of the measured photocurrent for each blends at short-circuit (black data points) and under forward bias (blue data points). For a fair comparison between the blends with different built-in voltages (U_{BI}), the applied voltage was chosen to decrease the built-in field by roughly 3.5 times (the applied voltage varied between 480 mV to 550 mV, which is similar or slightly above the V_{MP} of each device).

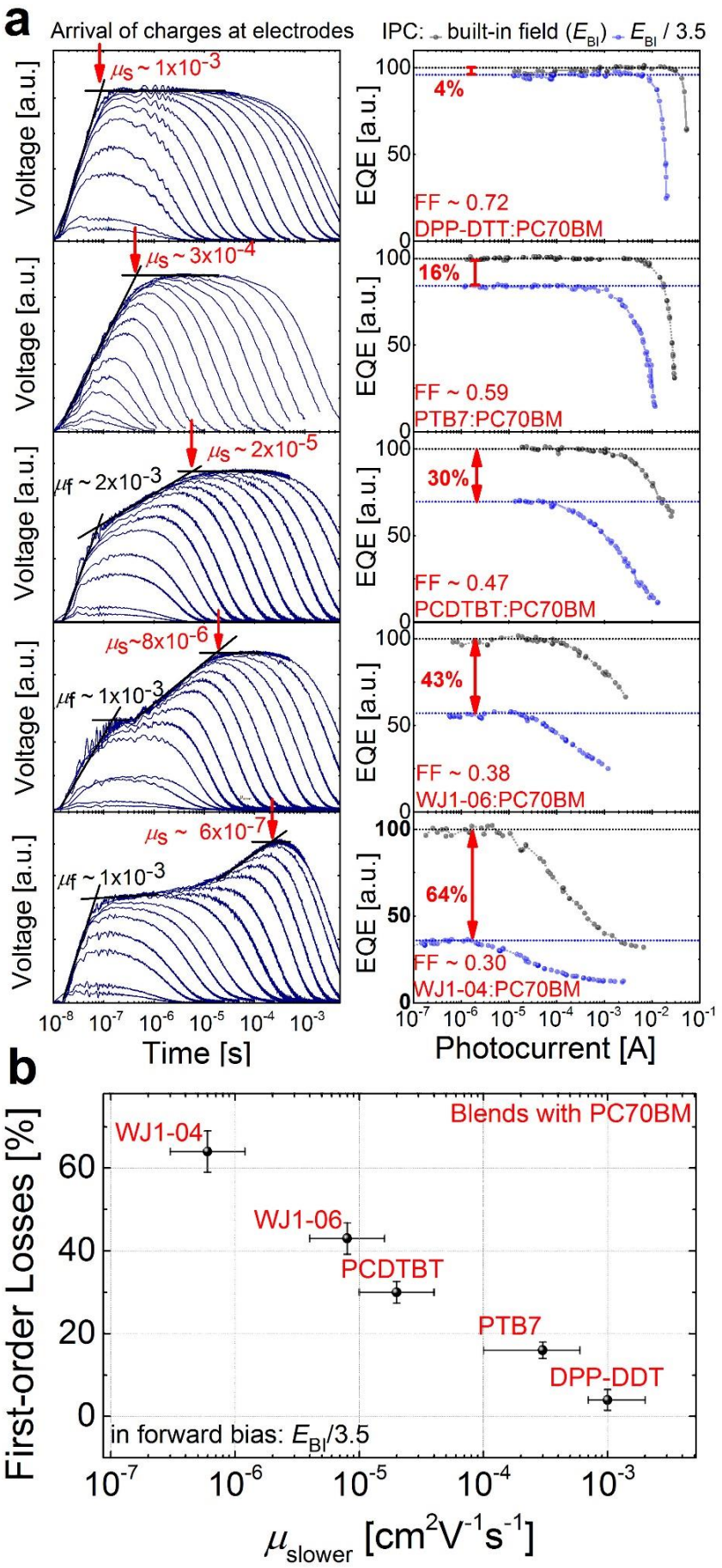
a
Arrival of charges at electrodes
IPC: built-in field (E_{BI}) E_{BI} / 3.5
Voltage [a.u.]
μ_s ~ 1x10^{-3}
μ_s ~ 3x10^{-4}
μ_s ~ 2x10^{-5}
μ_f ~ 2x10^{-3}
μ_s~8x10^{-6}
μ_f ~ 1x10^{-3}
μ_s ~ 6x10^{-7}
μ_f ~ 1x10^{-3}
Time [s]
EQE [a.u.]
4%
FF ~ 0.72
DPP-DTT:PC70BM
16%
FF ~ 0.59
PTB7:PC70BM
30%
FF ~ 0.47
PCDTBT:PC70BM
43%
FF ~ 0.38
WJ1-06:PC70BM
64%
FF ~ 0.30
WJ1-04:PC70BM
Photocurrent [A]
b
Blends with PC70BM
WJ1-04
WJ1-06
PCDTBT
PTB7
DPP-DDT
in forward bias: E_{BI}/3.5
First-order Losses [%]
μ_{slower} [cm^{2}V^{-1}s^{-1}]

Figure 3. (a, left column) *Resistance dependent photovoltage (RPV) transient signals for each blend revealing the arrival of charge carriers at the device electrodes. The magnitude of the transients increase (progressive photovoltage traces) with the load resistance, which was varied from 1 Ω to 1 MΩ. The slower carrier mobility/transit time, as indicated by the red arrows, varies by four orders of magnitude from DPP-DTT:PC70BM (top) to WJ1-04:PC70BM (bottom). The faster carrier mobility (electrons), as observed from the first shoulder in the transient responses, is similar among all devices. The mobility values are specified in* $cm^2V^{-1}s^{-1}$*.* ***(a, right column)*** *The photocurrent dependent EQEs of the blends measured at short-circuit and in forward bias corresponding to a ~3.5 times reduction of the internal driving field. The first-order photocurrent losses in forward bias, are observed from the shift of the constant EQE value and are marked by the arrows.* ***(b)*** *The first-order losses in forward bias as a function of the slower carrier mobility in the blends. The losses decrease with increasing slower carrier mobility from 64% in films of WJ1-04:PC70BM to 4% in DPP-DTT:PC70BM, which suggests the importance of the slower carrier mobility on these losses. The x-error bars were estimated from the uncertainty of the carrier arrival times as observed in RPV (see Methods). The y-error bars of the first-order losses were estimated from the standard deviations of the constant EQE regimes at short-circuit and in forward bias, considering also an uncertainty of 40 mV in the* V_{MP} *and expected shifts of the constant EQE values due to this uncertainty.*

This factor was chosen based on a trade-off between a large as possible reduction of the driving field, while maintaining a small injection current (the highest injection current was observed for the PTB7:PC70BM blend with ~8 µA, **Figure S5**). The first-order losses in forward bias are plotted in **Figure 3** (**b**) as a function of the slower carrier mobility. The losses in forward bias increase from 4% in the DPP-DTT:PC70BM blend, which has the highest slower carrier mobility and highest FF (0.72), to 64% in WJ1-04:PC70BM films, which has the lowest slower carrier mobility and FF (of 0.3). Again, all other systems lie between these two extreme cases.

Impact of non-geminate recombination on the first-order photocurrent losses

The experimental results show the critical impact of the first-order photocurrent losses depending on the slower carrier mobility of the BHJ blend, while bimolecular recombination plays a minor role, at least between 0 V and V_{MP}. Referring back to the Introduction, Street et al. [160] (and others [161]) have assigned the first-order photocurrent losses in forward bias to a non-geminate recombination process of free charges with (light-intensity independent) trap

states. In contrast, our results show that trapped charges are not present independent of the light-intensity (**Figure 6S**). The effect of charge-carrier-trapping will be to lower the effective slower carrier mobility, which in turn leads to increased bimolecular recombination losses at lower photocurrents. This is clearly seen in **Figure 3** (**a**) from the downward deviation of the EQE, which occurs when the bimolecular recombination rate becomes comparable to the extraction rate. As we have previously shown [172], this happens when the photocurrent reaches the space charge (and transport) limited photocurrent (I_{SCLC}), which is mainly defined by the active layer thickness, effective driving voltage and slower carrier mobility. This was also confirmed for the blends studied in this work (**Figure S7**).

Similarly, Dibb et al. [184] pointed out that non-geminate recombination will exhibit first-order dynamics if the amount of injected charges greatly exceeds the amount of photogenerated charges. While this is correct in principal, we note that our previous study demonstrated that this first-order recombination rate will be negligible compared to the extraction rate as long as the amount of charges - which are present independent of the light-intensity - remains significantly below 1 CV (where C is the device capacitance) [192]. Our experiments indicate that recombination induced by injected charges will be minor due to the fact that the injection current at V_{MP} is roughly 2-3 orders of magnitude lower than the magnitude of the first-order photocurrent losses, and because of the opposite trend between the injection current and the first-order losses (**Figure S5**). Lastly, we note that the observed first-order losses are also independent of the excitation wavelength (**Figure S8**) and corresponding photocarrier generation profiles [193], which indicates that losses due to reverse diffusion of charges plays a minor role.

Our observations lead us to conclude that the first-order recombination losses are mostly geminate in nature and originate from CTS-to-ground-state transitions. The electric-field dependence of the CTS separation can originate from two different mechanisms as discussed in the Introduction: i) either the field can affect the Coulomb barrier to dissociation (Braun model); or ii) it can perturb the mobility (Poole-Frenkel effect), which is itself important to dissociation. We will now briefly discuss these two effects.

Electric-field dependent CTS dissociation via a lowered Coulomb barrier

If the Coulomb barrier is substantially lower than expected from the simple calculation presented in the Introduction, then the contribution of the internal electric field could make the decisive difference to a successful CTS dissociation event. Indeed, there are several processes that could lower the Coulomb barrier for dissociation, for example entropic effects [68, 98, 99, 100]. However, the observed differences in the geminate recombination losses upon a constant reduction of the electric field (~3.5x), which also depend on the slower carrier mobility of the system, render this argument incomplete or questionable.

Electric-field dependent CTS dissociation through the Poole-Frenkel effect

As previously discussed, the Poole-Frenkel mechanism describes the electric-field dependence of the CTS-dissociation rate k_{d} through the field dependence of the charge carrier mobility $k_{\mathrm{d}} \sim \mu(E)$ [77]. The effective mobility increases with increasing electric field due to an activation of trapped charges. Thus, the primary role of the internal electric field could be to mobilize trapped charges, especially the slowest charge carriers; and enable them to leave the donor:acceptor interface.

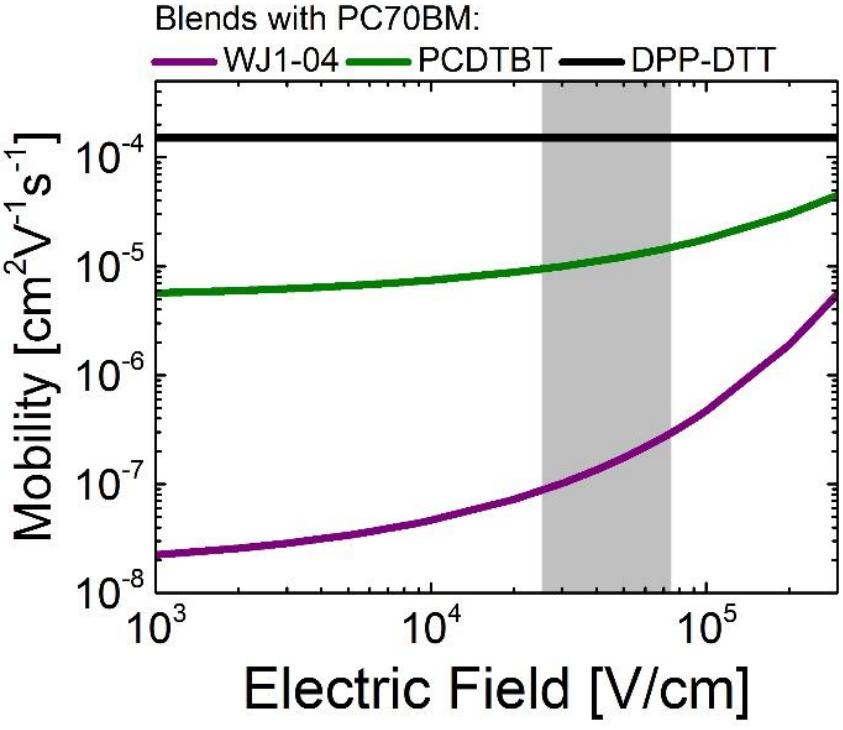

Figure 4. *Slower carrier mobility vs. electric field as obtained from space charge limited current (SCLC) measurements for DPP-DTT:PC70BM, PCDTBT:PC70BM and WJ1-04:PC70BM highlighting the stronger field dependence of low mobility blends. The grey area*

*corresponds to the mobility and field of the measurement conditions from **Figure 3** (i.e., the short-circuit and forward bias conditions).*

To test the dependence of the mobility on the field, we performed additional one-carrier *J-V* measurements on the DTT:PC70BM, PCDTBT:PC70BM and WJ1-04:PC70BM blends to identify the electric field dependence of the slower carrier mobility (**Figure S9**), following to the methodology presented in reference [194]. The results confirm a stronger field dependence of the mobility in blends with low mobilities (WJ1-04:PC70BM and to a lesser extent, PCDTBT:PC70BM) due to significant charge carrier trapping. Therefore, the Poole-Frenkel assisted mechanism could also explain the larger field dependent geminate recombination losses in blends with low slower-carrier mobilities. This is also consistent with a previous study that demonstrated the importance of the ability of the slower carrier to escape the donor:acceptor interface for efficient CTS separation [194]. Lastly, we note that the SCLC electron mobility of the DPP-DTT:PC70BM blend is somewhat lower than that obtained from transient photovoltage measurements (**Figure 3**), which is likely due to injection barriers.

Conclusion

We have studied the electric field, light intensity and mobility dependence of the carrier recombination dynamics in BHJ OSCs from short-circuit to operational biasing conditions. We observe significant first-order photocurrent losses, which increase with applied forward bias. This leads to the conclusion that significant photocurrent losses at V_{MP} do not originate from the competition between charge extraction and recombination of free charge carriers. Instead, substantial photocurrent losses at operational bias originate from an electric field dependent CTS dissociation mechanism. We further find that the CTS dissociation is more susceptible to the compensation of the built-in electric field in systems with low slower carrier mobilities, which contributes to the typically poor fill factor in such devices. Our results are consistent with an electric field assisted mobilization of interfacial trapped charges as described by the Poole-Frenkel effect. The electric field enables the slowest, trapped charges to leave the donor:acceptor interface, which increases the likelihood of a successful dissociation event. The Poole-Frenkel assisted CTS dissociation mechanism is also consistent with SCLC measurements, which demonstrate a strong field dependent mobility in low mobility systems. Our results highlight that charge collection and generation are similar in the sense that both are limited by the slower carrier mobility. This could explain the difficulty in understanding the

losses associated with free carrier extraction and CTS dissociation in the power generating quadrant of the *JV* curve. Our results underline the importance of optimization of CTS dissociation via increasing the mobility of both charge carriers to maximize the generation yield and the fill factor in polymer:fullerene organic solar cells.

Experimental Section

Device preparation: Substrates with an ~80 nm indium tin oxide (ITO) layer (purchased from Kintec) were cleaned by sonicating in sequence with Alconox, deionized water, acetone, and 2-propanol for 5 min, respectively. Subsequently, the substrates were coated with 30 nm poly(3,4-ethylenedioxythiophene):poly(styrene sulfonate) (PEDOT:PSS; Baytron P VPAl4083) for the DPP-DTT, PTB7 and PCDTBT composite devices, and with 15 nm thermal vacuum deposited MoO_3 for the WJ1-04 and WJ1-06 composite devices. The PEDOT:PSS coated substrates were dried at 170 ºC for 10 minutes.

DPP-DTT:PC70BM blends: Blend films of DPP-DTT ($\bar{M}w$ = 350 kDa and PDI = 2.8, synthesized as described in reference [103]) and PC70BM (American Dye Source, Inc., Canada, $\bar{M}w$ = 1032 g/mol) were prepared from a chloroform solution using a total concentration of 24 mg cm^{-3}. The optimized blend ratio by weight of 1 to 3 was used.

PTB7:PC70BM blends: Blends of PTB7 (1-Material, $\bar{M}w$ = 97.5 kDa, PDI = 2.1) and PC70BM were prepared from a 1,2-dichlorobenzene (DCB) with 3% 1,8-diodooctane solution using a total concentration of 31 mg cm^{-3}. The optimized blend ratio by weight of 1 to 1.5 was used.

PCDTBT:PC70BM blends: PCDTBT (SJPC, Canada, $\bar{M}w$ = 122.2 kDa, PDI = 5.4) and PC70BM active layer blends were prepared from a DCB solution using a total concentration of 30 mg cm^{-3}. The optimized blend ratio by weight of 1 to 4 was used.

WJ1-06:PC70BM blends: WJ1-06 ($\bar{M}w$ = 760 g/mol) was synthesized in house following the procedure described in references [190, 191]. WJ1-06 was dissolved along with PC70BM in chloroform using a total concentration of 20 mg cm^{-3}. An optimized blend ratio of 1:1 by weight was used.

WJ1-04:PC70BM blends: WJ1-04 ($\bar{M}W$ = 670 g/mol) was synthesized in house as described in reference [192]. WJ1-04 was dissolved with PC70BM in chloroform using a total concentration of 20 mg cm^{-3}. An optimized blend ratio of 1:10 by weight was used.

In all cases, the solutions were spin-coated onto the substrates, with the spin speed varied to achieve a target active layer thickness of ~100 nm. The active layer thicknesses were measured with a DekTak 150 profilometer. The DPP-DTT, PTB7 and PCDTBT, and (WJ1-04 and WJ1-06) composite devices were completed by vacuum evaporation of 1.2 nm of samarium (15 nm of calcium) followed by 75 nm of aluminium under a 10^{-6} mbar vacuum. The device area was 0.2 cm^2. All device fabrication took place within a glove box with <1ppm O_2 and H_2O and *J-V* and EQE measurements were also performed inside a glove box. Subsequently the devices were encapsulated for the IPC and RPV measurements.

Current density-voltage characteristics: *J-V* curves were obtained in a 2-wire source-sense configuration and an illumination mask was used to prevent photocurrent collection from outside of the active area. An Abet Class AAA solar simulator was used as the illumination source providing ~100 mW cm^{-2} of AM1.5G light. The exact illumination intensity was used for efficiency calculations, and the simulator was calibrated with a standards traceable NREL photodiode. The AM1.5G short-circuit current of devices, which were not limited by bimolecular recombination under 1-sun equivalent conditions, matched the integrated product of the EQE spectrum (as measured using a PV Measurements Inc. QEX7 system) as a further check of our characterisation.

Light intensity dependent measurements: Steady-state intensity dependent photocurrent measurements were obtained with a 532 nm continuous wave laser (Ningbo Lasever Inc.) providing a power of 1 W. Optical filters (ThorLabs) were used to attenuate the laser power and the photocurrent transients were recorded with an Agilent semiconductor device analyzer (B1500A). The IPC responses in forward bias were corrected by subtracting the dark (injection) current. Each measured data point corresponded to a steady-state photocurrent measurement at the respective incident laser power, which was simultaneously measured with a Silicon photodetector to improve the accuracy of the measurement. The EQE was obtained from the ratio of the photocurrent and the laser power.

Transient PhotoVoltage: Photovoltage transients for mobility measurements were recorded with an oscilloscope (LeCroy WaveRunner 6200A) at different external load resistances (R_{Load}) ranging from 1 Ω to 1 MΩ. A pulsed Nd:Yag laser (Brio Quantel) with a pulse length of 5 ns and excitation wavelength of 532 nm was used to generate the charge carriers, while neutral optical density (OD) filters were used to attenuate the ~50 mJ energy output. Low laser pulse intensities (resulting in a photovoltage close to 100 mV at an R_{Load} of 1 MΩ) were applied to avoid space charge effects and to maintain quasi short-circuit conditions during extraction [104]. R_{Load} was varied in order to check the saturation of the maximum photovoltage with increasing load resistance [104]. All transients exhibit a saturated maximum photovoltage at 1 MΩ, which is a requirement to correctly estimate the mobility. The error bars in the mobility values as measured by RPV indicate the uncertainty of the carrier transit times. The uncertainty of the transit time was approximated from the range over which the photovoltage signals deviate and saturate to tangents fitted to the rise and plateau regions of the photovoltage transients.

Space Charge Limited Current: SCLC measurements on WJ1-04:PC70BM and PCDTBT:PC70BM were performed using a hole-only architecture with ITO/MoO_3 as the anode electrode and MoO_3/Silver as the top cathode. SCLC measurements on DPP-DTT were performed using an electron-only device structure, using ITO/Al as the anode and Al as the cathode. The active layer thicknesses were chosen around 250 nm.

Photoelectron Spectroscopy in Air: PESA measurements were performed using a Riken Kekei AC-2 spectrometer. For all samples a power intensity of 5 nW was used. The data were fitted as the square root of the electron count versus energy.

V.2 Slower Carriers Limit Charge Generation Yield

This section describes a further investigation of the mobility dependence of the CTS dissociation yield within the framework of the Onsager-Braun model in devices with varying donor:acceptor blend ratios and electron and hole mobilities. The results show that the CTS separation dynamics is strongly dependent on the ability of the slower charge carrier to leave the donor:acceptor interface. The results suggest that only the joint separation of electron and holes will lead to a successful CTS dissociation in current organic solar cells, and underline the importance of a high carrier mobility to achieve a high generation yield.

The supplementary information of this paper can be accessed online at (http://www.nature.com/ncomms/2016/160621/ncomms11944/full/ncomms11944.html).

Slower carriers limit charge generation in organic semiconductor light harvesting systems

Abstract

Blends of electron donating and accepting organic semiconductors are widely used as photoactive materials in next generation solar cells and photodetectors. The yield of free charges in these systems is often determined by the separation of interfacial electron-hole pairs, which is expected to depend on the ability of the faster carrier to escape the Coulomb potential. Here we show, by measuring geminate and non-geminate losses and key transport parameters in a series of bulk-heterojunction solar cells, that the charge-generation yield increases with increasing slower carrier mobility. This is in direct contrast with the well-established Braun model where the dissociation rate is proportional to the mobility sum, and recent models that underscore the importance of fullerene aggregation for coherent electron propagation. The behavior is attributed to the restriction of opposite charges to different phases, and to an entropic contribution that favors the joint separation of both charge carriers.

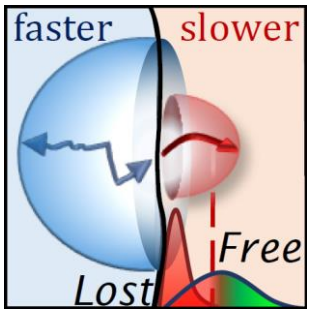

Introduction

Charge generation in electron donor:acceptor blends of excitonic organic semiconductors is complex and still not fully understood [19, 195]. The blends form molecular heterojunctions, and the so-called bulk-heterojunction (BHJ) where the organic semiconductors form nanoscale interconnected neat and mixed phases [196], is the preferred and dominant architecture in organic solar cells and photodiodes. Although a complete understanding of the critical mechanisms and pathways from the photoexcitation to free charges remains elusive, an increasing body of evidence suggests that it is the dissociation of charge-transfer (CT) states that defines the generation efficiency and overall performance of organic solar cells [89, 90, 95, 197, 198]. In order to establish strategies to optimize the dissociation of CT-states it is of particular importance to understand how the carrier mobilities affect the separation dynamics.

Braun's model [66], based on Onsager's theory of ionic dissociation [42], describes charge generation in donor:acceptor solids as depending on the kinetic competition between the dissociation (k_d) and recombination (k_f) rates of charge-transfer (CT) states. The recombination from the charge-separated (CS) state back to the CT-state with rate k_r is assumed to be described by Langevin theory [43, 51], which, in a single material phase, predicts that k_r should be proportional to the sum $\mu_\mathrm{e} + \mu_\mathrm{h}$ of electron and hole mobilities because both carriers drift toward each other due to their electric fields. Another key assumption of the Braun model is that dissociation and recombination are related by detailed balance. Since detailed balance requires that the ratio $k_\mathrm{d}/k_\mathrm{r}$ equals the equilibrium constant K for charge separation, Braun concluded that k_d must also be proportional to $\mu_\mathrm{e} + \mu_\mathrm{h}$. If the charge carriers can move away from the interface as quickly as they can return, k_d and the (geminate) k_r depend, in the same way, on the kinetic parameters. The situation is more complicated in a BHJ. Since recombination in a BHJ occurs at the donor:acceptor interface, the faster carrier (*f*) has to wait at the interface for the slower carrier (*s*) before recombination is possible. As a result, Blom and Koster proposed that the arrival of the slower carrier should be the recombination rate-limiting step, giving $k_\mathrm{r} \propto \mu_\mathrm{s}$, the mobility of the slower carriers [58, 199, 200]. Following Braun's thesis that dissociation and recombination are opposite processes, this reasoning would suggest that CT-state dissociation yield in BHJs should also depend on the slower-carrier mobility. However, Blom and Koster's premise does not consider the influence of the domain size on the recombination rate, and this has been investigated recently by Heiber et al. [59] who showed that the Langevin and Blom-Koster rates are relevant in the limits of very small and very large domains, respectively. Despite the importance of these kinetic considerations on the charge carrier separation, most studies have focused on the impact of the donor and acceptor energy levels [23, 64, 201] and nanoscale morphology [60, 202, 203, 204, 205, 206]. For example, Gélinas et al. [60] have shown that a high fullerene loading is crucial for fullerene aggregation, which assists ultrafast charge separation by enabling electron delocalization. Fullerenes are the dominant n-type organic semiconductor and present particularly intriguing challenges in understanding their basic physics because of their size and symmetry. Gélinas et al. [60] concluded—as have others [95, 96, 97]—that the faster electrons determine the charge generation yield, arguing that they can escape via delocalization, leaving the slower hole unbound and free to diffuse away at its own pace. This prediction is consistent with Braun's assertion of k_d determined by $\mu_\mathrm{f} + \mu_\mathrm{s}$, provided that $\mu_\mathrm{f} \gg \mu_\mathrm{s}$, as is often the case.

Here, we experimentally explore the correlation between the generation yield of free charges and their mobilities, similar to a previous study [207], and thereby test Braun's model in BHJ solar cells with varying blend compositions. We do so by decoupling geminate and non-geminate recombination using recently introduced experimental methods applied to operational devices [104, 172, 192]. Our results show that the dissociation efficiency of CT-states is not dependent on $\mu_e + \mu_h$, as predicted by Braun's theory, but is instead governed by the slower carriers, whether they are the electrons or the holes. We describe the local dynamics of separating CT-states by taking into account the interface that breaks the translational symmetry, changes in the donor:acceptor domain size, and entropic effects that favor the movement of both carriers away from the interface, and not just the escape of the faster carrier.

Results

Studied Systems

We studied two archetypal BHJ organic solar cells using a polymeric donor with a fullerene acceptor, [(poly[*N*-9"-heptadecanyl-2,7-carbazole-*alt*-5,5-(4',7'-di-2-thienyl-2',1',3'-benzothiadiazole)]:[6,6]-phenyl-C_{70}-butyric acid methyl ester (PCDTBT:PC70BM) [152] and poly[(4,8-bis{2-ethylhexyloxy}benzo[1,2-b:4,5-b']dithiophene-2,6-diyl)(3-fluoro-2-{[2-ethylhexyl]carbonyl}thieno[3,4-b]thiophenediyl)] (PTB7):PC70BM [131]. The solar cell fabrication details are provided in **Methods**. The results for PCDTBT:PC70BM are shown below. For PCDTBT:PC70BM blends we varied the composition ratio from 0.1 wt% to 95 wt% PCDTBT in PC70BM and for PTB7:PC70BM blends we used 10 wt% to 95 wt% PTB7 in PC70BM. Varying the blend ratio allows one to tune the efficiencies of charge generation and collection in a systematic way. Average current density versus voltage (JV) scans were obtained under standard AM 1.5G illumination and are provided in **Supplementary Figures 1** and **2** and **Supplementary Tables 1** and **2** for PCDTBT:PC70BM and PTB7:PC70BM blends, respectively. As the composition ratio varies, the power conversion efficiency (PCE) is predominantly determined by differences in the short-circuit current density (J_{SC}).

Photogeneration Yields of all Blend Compositions

To study the relation between charge generation and the carrier mobilities we performed intensity dependent internal quantum efficiency (IQE) measurements. In **Figure 1** (**a**) we plot the IQE as calculated from the intensity-dependent photocurrent (iPC) (**Supplementary Figure 3)** and the actual photojunction absorptions in operational devices (**Supplementary**

Figure 4) versus the photocurrent at an excitation wavelength of 532 nm. The results for PTB7:PC70BM are shown in **Supplementary Figure 5**. These measurements have allowed us to quantify the combined efficiencies of carrier photogeneration and extraction and to decouple first- and higher-order photocurrent losses with respect to the incident light intensity. By increasing the light intensity, the photocurrent can reach the slower-carrier space-charge-limited photocurrent (I_{SCLC}), where bimolecular (non-geminate) recombination of oppositely charged carriers starts to strongly influence the charge extraction efficiency [172]. This is seen as an IQE that decreases at higher light intensities (or photocurrents). We note that the recombination of free charges with trapped charge is bimolecular in nature and is thus distinct in the iPC measurements [192]. Moreover, the equilibrium charge-carrier density is low in all studied devices (much less than CU_{BI}, where C is the device capacitace and U_{BI} the built-in voltage), preventing significant pseudo-first-order recombination between free and equilibrium carriers. Therefore, charge extraction free of non-geminate losses in the bulk can be realized if the light intensity is sufficiently low to guarantee a photocurrent lower than the I_{SCLC}. If geminate recombination losses of free carriers or losses due to back diffusion into the reverse electrode [32, 33] are considered to be minimal, then the charge generation can be readily quantified from the constant IQE value [192].

To corroborate the electrical measurements of the charge generation efficiency, we employed transient absorption spectroscopy (TAS) to monitor the populations of photogenerated bound and free charge carriers following low-intensity laser excitation, as shown in **Figure 1** (**b**). At low intensities, the signals exhibit intensity-independent exponential decay dynamics, indicating first-order losses in the bound-charge states, which is consistent with a previous report [67]. The dissociation yield of the CT-states is obtained from the fraction of free charges remaining at long times (see **Methods** and **Supplementary Figure 6** for further details). The estimated photocarrier generation yields from iPC are in good agreement with the CT dissociation yields from TAS as shown in **Figure 1** (**c**). Furthermore, all the blends studied by TAS showed similar spectra but very short exciton lifetimes compared to neat PCDTBT, suggesting efficient exciton dissociation (see **Supplementary Table 3**). Therefore, the geminate recombination losses obtained by iPC can be largely attributed to CT-state recombination losses [155], as opposed to exciton losses. In line with previous studies [129] and our *JV* measurements, we observe that geminate recombination losses are minimized at a polymer loading of 20 wt%.

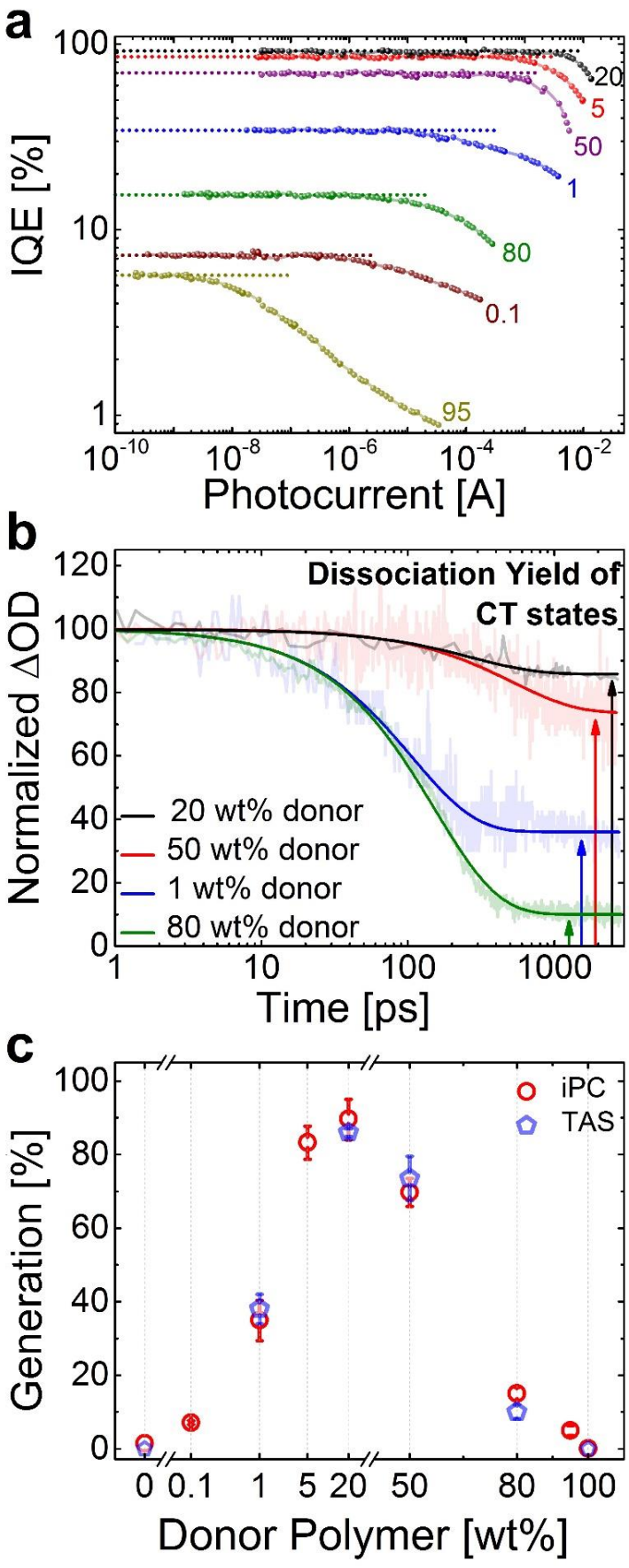
a
100
10
1
IQE [%]
20
5
50
1
80
0.1
95
10^-10
10^-8
10^-6
10^-4
10^-2
Photocurrent [A]
b
120
100
80
60
40
20
0
Normalized ΔOD
Dissociation Yield of
CT states
20 wt% donor
50 wt% donor
1 wt% donor
80 wt% donor
1
10
100
1000
Time [ps]
c
100
80
60
40
20
0
Generation [%]
iPC
TAS
0
0.1
1
5
20
50
80
100
Donor Polymer [wt%]

Figure 1*. Charge generation yields from intensity dependent photocurrent (iPC) and transient absorption spectroscopy (TAS). (a)** *Internal quantum efficiencies (IQEs) as a function of the photocurrent of PCDTBT:PC70BM devices with different donor fractions (wt%, marked by the numbers). The constant IQE at low photocurrents (as marked by the dahed lines) before non-geminate recombination causes the downward deviation is an estimate of the charge generation yield.* ***(b) *Normalized transient absorption spectra of the blends monitoring the polymer's cations, following excitation at 560 nm at a fluence of 500 nJ cm^{-2}. Solid lines are exponential fits, indicating a geminate decay of bound and free charges which absorb at 1000 nm. The dissociation yield of the CT-states is given by the fraction of charges remaining at long times (as marked by the arrows).* ***(c)*** *The generation efficiency of free charges determined from (**a**) and (**b**) as a function of the donor fraction. iPC error bars are determined from the first standard deviation (s.d.) of the constant IQE regime considering 2 measurements on different pixels and a relative variation of 5% of the active layer absorption. TAS error bars represent the first s.d. of the plateau regime of the transient absorption signals.*

Carrier Mobilities of all Blend Compositions

To correlate the generation efficiency with charge-carrier mobilities, we determined the mobilities using two independent methods: first, Resistance-dependent photovoltage (RPV), which allows direct monitoring of the arrival of extracted charge on the device electrodes [104] (see **Methods**, **Supplementary Figures 7** and **8**); and second, iPC to estimate the charge-extraction-limiting slower-carrier mobility. **Figure 1** (**a**) shows that I_{SCLC} varies from 10^{-8} A to almost 10^{-2} A in the 95 wt% and the 20 wt% PCDTBT blends, respectively. The I_{SCLC} is proportional to the product of the slower carrier mobility and the square root of the reduction factor of the Langevin recombination coefficient ($\mu_s \gamma^{1/2}$) [172]. RPV measurements at high laser intensities [49] reveal Langevin recombination in blends with imbalanced donor:acceptor concentrations ($\gamma \sim 1$) and non-Langevin recombination in efficient blends ($\gamma \sim 25$ to 33, **Supplementary Figure 9**). **Figure 2** shows good agreement between the mobilities obtained by the two techniques. Increasing the donor content from 0.1% to 20% considerably increases the slower carrier (hole) mobility, where we also observe a peak in the charge collection efficiency (**Supplementary Figure 10**). Further increasing the donor fraction, decreases the electron mobility and electrons become the slower carriers, similar to previous findings [107]. Therefore, we observe a switch between electrons and holes as the slower carrier between 20 wt% to 50 wt% of donor polymer. Across all blend ratios, the slower carrier mobility changes

by more than five orders of magnitude from approximately $1 \cdot 10^{-10}$ cm^2 V^{-1} s^{-1} to approximately $3 \cdot 10^{-5}$ cm^2 V^{-1} s^{-1} in the 95 wt% and the 20 wt% donor devices, respectively. In contrast, the faster-carrier mobility is relatively constant (around $1 \cdot 10^{-4}$ cm^2 V^{-1} s^{-1} to $2 \cdot 10^{-3}$ cm^2) and controlled by the majority phase, that is PCDTBT (PC70BM) for high (low) donor blends, respectively.

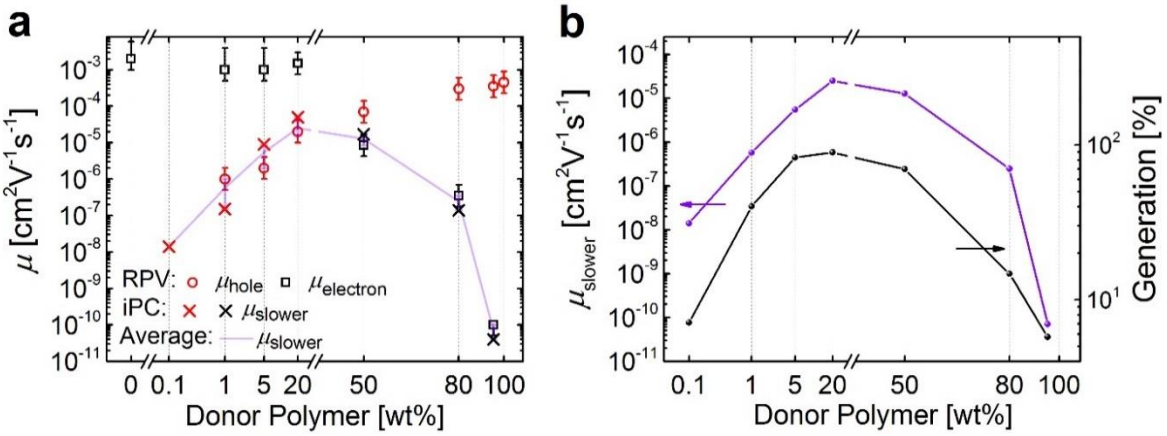

Figure 2. Carrier mobilities and photogeneration yields of PCDTBT:PC70BM blends. (a) *Electron/hole mobilities for different donor (PCDTBT) fractions as obtained from two different techniques; resistance dependent photovoltage (RPV) and intensity dependent photocurrent (iPC). Low-donor blends exhibit high electron and low hole mobilities, while low-acceptor blends exhibit high hole and low electron mobilities. Error bars are determined from the uncertainty in the carrier arrival at the electrodes (see* ***Methods****).* ***(b)*** *The slower carrier mobility and generation yield follow a similar trend as function of the blend ratio composition.*

Figure 2 also shows that the slower carrier mobility and the generation efficiency follow a similar trend as a function of the blend ratio composition, which indicates that the generation efficiency does not depend on the faster carrier as predicted by Braun's theory. The results for PTB7:PC70BM are shown in **Supplementary Figure 11** and confirm this critical observation.

Discussion

These experimental results indicate an important and counter-conventional view: slower carriers—and not the faster ones—play the decisive role in the dissociation of CT-states. To gain further insights into the underlying mechanism we plot in **Figure 3** (**a**) the measured generation efficiencies against the slower carrier mobilities and compare the observed trend with the CT-state dissociation efficiency from Braun's model (dashed line) $\eta_{CT} =$

$k_d/(k_d + k_f)$, but where the dissociation rate k_d is assumed proportional to μ_s, and not $\mu_f + \mu_s$. The CT-state decay rate k_f is fitted to the data assuming it to be independent of the charge carrier mobilities [66], which is also consistent with the roughly constant decay times observed in the TA signals shown in **Figure 1** (**b**). The match highlights the dominant role of the slower carriers on the dissociation of CT-states. We now examine the potential physical mechanisms underlying this important correspondence.

Higher mobility allows the slower carrier to leave the interface and escape recombination: We consider a system with very imbalanced charge transport where the electron and hole are also separated by an interface between different domains, as illustrated in **Figure 3** (**b**, **c**). Because the faster carrier can escape but also return to the interface substantially quicker than the slower carrier, the motion of the slower carrier cannot be neglected. If the slower carrier is so slow as to be effectively immobile, it remains at the interface and is liable to recombine with the faster carrier in **Figure 3** (**c**), whose random walk will be biased towards the slower carrier by their Coulomb attraction. In contrast, if the slower carrier is mobile, it will be able to leave the interface, even if only by a few hops (**Figure 3** (**b**)). Doing so can temporarily protect the CT-state from recombination because the faster carrier cannot enter the slower-carrier phase. This increases the likelihood of escape for the faster carrier. It is important to note that the faster carrier can still escape even if the slower carrier is immobile. Pure faster-carrier escape can explain why the generation does not decrease to zero at very low slower-carrier mobilities, but reaches a plateau of 5% in PCDTBT:PC70BM (**Figure 3** (**a**)) and 14% in PTB7:PC70BM blends (**Supplementary Figure 11** (**b**)). We note, that the local mobility in a nm regime (roughly 5-10 nm, which is relevant for CT-state separation) might differ from the measured bulk mobility, however, if both mobilities scale in the same way with the blend ratio composition, this mechanism offers a possible explanation of our experimental results.

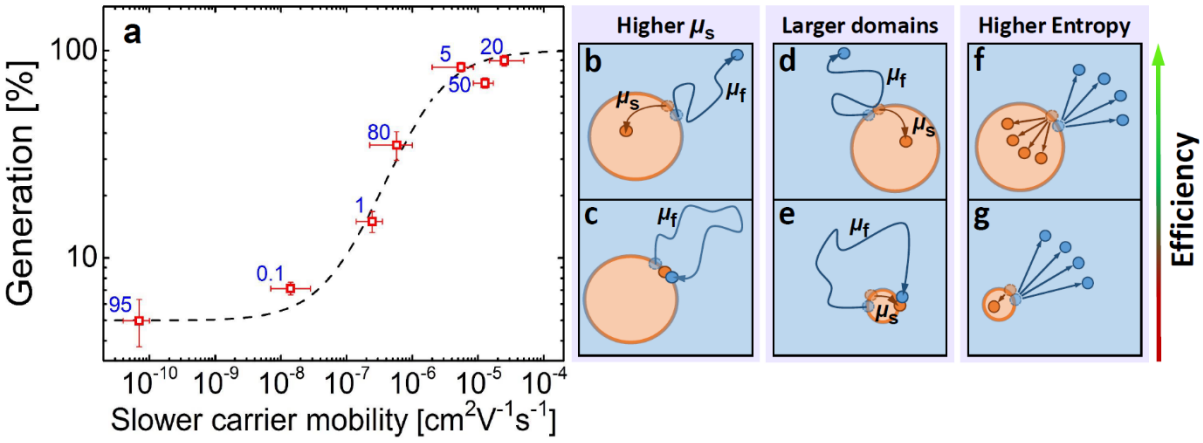

Figure 3. Slower carriers limit charge transfer state splitting and plausible explanations. (a) *Generation yields versus slower carrier mobility - either holes or electrons depending on the donor content (as marked by the numbers). The dashed line is the prediction of Braun's theory assuming an offset in the generation yield at low mobilities and that the CT-state dissociation rate is determined by the slower carrier mobility and NOT the sum of both mobilities. The x-error is the range of the slower carrier mobility as obtained from two independent techniques, and the y-error bar is the first s.d. of the constant internal quantum efficiency regime (as described in* ***Figure 1****).* ***(b, c)*** *Increasing the mobility of the slower carrier (orange dot in the dilute phase) enables it to leave the interface, which temporally protects the CT-state from recombination and allows the faster carrier (blue dot in the majority phase) to escape.* ***(d, e)*** *Larger domains of the dilute phase allow the slower carriers to travel further away from the interface also protecting the CT-state from recombination.* ***(f, g)*** *The entropic contribution to dissociation is maximized in systems where both carriers are mobile because the density of states of two separated charges is vastly larger than the density of states where only one charge is mobile.*

Larger domains allow the slower carrier to leave the interface - protecting the CT from recombination: As the fraction of the dilute phase is increased, its domains grow. Larger domains will decrease the recombination rate and thereby increase the dissociation probability of CT-states as shown in [206] and illustrated in **Figure 3** (**d**). Using Monte Carlo simulations [59], it has recently been shown that in the limiting case of very small domain sizes, the recombination rate will be dependent on the faster carrier (Langevin, **Figure 3** (**e**)), while the Blom-Koster rate is applicable in the limiting case of a bilayer (if the faster carrier reaches the interface first). The transition to a Langevin system occurs if the domain size approaches approximately 5 nm. These theoretical predictions can qualitatively explain our recombination

rate measurements, where we find that k_r scales, in both systems, with the sum of the mobilities ($\gamma \sim 1$) in low donor and acceptor blends and becomes most "non-Langevin" in the most efficient blends ($\gamma \sim 25$ to 33, **Supplementary Figure 9**). It is interesting to note that, in addition to encounter limited recombination, a recent study also suggests that a large CT-state *re*-dissociation rate after free carrier encounters (relative to k_f) could contribute to the suppression of the Langevin recombination coefficient in efficient devices [31]. Although both properties, a high slower carrier mobility and a sufficiently large domain size, are expected to increase the ability of the slower carrier to leave the interface, their relative contribution to the likelihood of a successful separation event may not follow the same trend as a function of blend ratio composition. For example, in PTB7:PC70BM blends with 10 wt%, 25 wt% and 45 wt% PTB7 we find a relatively constant high slower-carrier mobility, while the generation efficiency decreases as the PTB7 concentration is reduced below 45 wt% (**Supplementary Figures 5** and **11**). Our recombination coefficient measurements (**Supplementary Figure 9**) suggest that CT-states in low donor PTB7:PC70BM blends are less protected from recombination, which could explain the observed drop in the generation efficiency. However, further work is required to disentangle the effect of the domain size and slower carrier mobility.

Entropy favors the simultaneous dissociation of both carriers: Lastly, changes in the donor and acceptor domain sizes will also change the entropic contribution to the dissociation as illustrated in **Figure 3** (**f**, **g**). A growing body of evidence suggests that the entropy facilitates charge separation due to the expansion of the number of available states as the carriers diffuse away from the interface [68, 98, 99, 100]. The free energy of dissociation is given by

$$\Delta G = E - T\Delta S = E - k_B T \, ln \frac{\Omega_{CS}}{\Omega_{CT}} \, , \tag{1}$$

where Ω_{CS} and Ω_{CT} are the numbers of accessible charge-separated and charge-transfer states; E is the CT-state binding energy, k_B the Boltzmann constant, and T the temperature. In the extreme case of very imbalanced donor:acceptor concentrations, where only the faster carrier has ways to escape, Ω_{CS} would equal the number Ω_f of states accessible to the faster carrier (**Figure 3** (**g**)). By contrast in balanced donor:acceptor systems, where also the slower carrier is able to leave the interface, the factor Ω_{CS} will be proportional to $\Omega_f \Omega_s$, which greatly increases the entropic contribution to charge separation (**Figure 3** (**f**)). This means that the entropic drive

is stronger in blends where both carriers are mobile and able to leave the interface, reducing the free-energy barrier for dissociation. The entropic contribution to the dissociation rate thereby further supports our fundamental assertion that the dissociation is largely dependent on the slower carrier.

Conclusion

In conclusion, we have experimentally studied the impact of the charge carrier mobilities on the dissociation yield of CT-states in organic semiconductor blends using the archetypal bulk heterojunction organic solar cell architecture. Our electrical transport results which are supported by independent transient absorption spectroscopy measurements do not agree with the common view that charge separation occurs when the faster carrier makes a rapid escape and underscore the failure of a simple Braun model, which is based on the dissociation rate being proportional to the sum of the mobilities. Our data strongly suggests that it is largely the ability of the slower charge carriers to leave the donor:acceptor interface that dictates the efficiency of CT-state dissociation. Possible mechanisms that enable the slower carriers to leave the interface are: a high enough mobility, a sufficiently large domain size, and enough conduction pathways which lower the Coulomb barrier for dissociation due to entropic effects. Our findings are important as they shed new insight into the fundamental physics of organic semiconductors, and also provide new structure-property strategies for optimizing charge generation in excitonic light harvesting systems. Namely, they underscore the need for high mobilities to maximize not only charge collection but also charge generation, and further demonstrate the role of a balanced donor:acceptor blend ratio to maintain the mobility and domain size of slower carriers and a high system entropy.

Methods

Device preparation: Glass substrates with an 80 nm indium tin oxide (ITO, purchased from Kintec) layer were cleaned by sonicating in sequence with Alconox, deionized water, acetone, and 2-propanol for 5 min, respectively. Subsequently, the substrates were coated with 30 nm of poly(3,4-ethylenedioxythiophene):poly(styrene sulfonate) (PEDOT:PSS; Baytron P VPAl4083). PCDTBT (SJPC, Canada, $\bar{M}w$=122200 g/mol, PDI=5.4) and PC70BM (American Dye Source, Inc., Canada, $\bar{M}w$=1032 g/mol) active layer blends were fabricated by first preparing solutions of PCDTBT (30 mg) in 1,2-dichlorobenzene (DCB, 5 mL), and PC70BM (120 mg) in chlorobenzene (CB, 5 mL). The solutions were then mixed in an appropriate ratio to obtain the specified blend ratio compositions. The solutions were spin-coated onto the substrates for 90 s, while the spin speed was varied to achieve the same target active layer thickness (75 nm) for each blend. Blends of PTB7 (1-Material, $\bar{M}w$=97.5 kDa, PDI=2.1) and

PC70BM were prepared by first separately dissolving PTB7 (90 mg) and PC70BM (120 mg) in a mixture of DCB and CB (50%:50%, 5 mL). The solutions were again spin-coated onto the substrates for 90 s, while the spin speed was varied to achieve a similar target active layer thickness (125–150 nm) for each blend. The active layer thicknesses were measured with a DekTak 150 profilometer. All devices were completed by vacuum evaporation of 1.2 nm of samarium followed by 75 nm of aluminium under a 10^{-6} mbar vacuum. The device area was 0.2 cm^2. The device fabrication took place within a glove box with < 1ppm O_2 and H_2O and *JV* and EQE measurements were also performed inside a glove box. Subsequently the devices were encapsulated for the iPC, TAS, RPV and dark-CELIV measurements. Reflectometry for calculating the IQE was measured on duplicate devices with a device area of 6.25 cm^2.

Current density-voltage characteristics: *JV* curves were obtained in a 2-wire source-sense configuration and an illumination mask was used to prevent photocurrent collection from outside of the active area. An Abet Class AAA solar simulator was used as the illumination source providing 100 mW cm^{-2} of AM1.5G light. The exact illumination intensity was used for efficiency calculations, and the simulator was calibrated with a standards traceable NREL photodiode.

Light intensity dependent measurements: Steady state intensity dependent photocurrent measurements were performed with a 532 nm continuous wave laser (Ningbo Lasever Inc.) providing a power of 1 W. Optical filters (ThorLabs) were used to attenuate the laser power and the photocurrent transients were recorded with an Agilent semiconductor device analyser (B1500A). Each measured data point corresponded to a steady state photocurrent measurement at the respective incident laser power, which was simultaneously measured with a Silicon photodetector to improve the accuracy of the measurement. iPC was repeated on several pixels for each blend composition. The EQE was obtained from the ratio of the photocurrent and the laser power. The EQE values obtained from the iPC measurement were compared to the EQE spectra that were measured using a PV Measurements Inc. QEX7 system. The IQE was subsequently calculated from the ratio of the EQE and the active layer absorption. The latter was obtained from specular reflectance spectra (using a universal reflectance attachment on a Perkin-Elmer Lambda 950 spectrophotometer accurately baselined with a reference glass slab) and simulated absorption in non-active layers using a code developed by van de Lagemaat et al. from the National Renewable Energy Laboratory. More details on how the active layer absorptions are obtained are provided in **Supplementary Figure 4.**

Repetitive and Resistance dependent PhotoVoltage: Resistance dependent photovoltage (RPV) for mobility, recombination coefficient and trapping measurements were recorded with an oscilloscope (LeCroy WaveRunner 6200A) with different external load resistances (R_{Load}), while a delay generator (Stanford Research Systems DG535) was used to trigger a function generator (Agilent 33250A) and a pulsed Nd:Yag laser (Brio Quantel) with a pulse length of 10 ns. An excitation wavelength of 532 nm was used to generate the charge carriers, while neutral optical density (OD) filters were used to attenuate the approximately 50 mJ energy output. For the RPV mobility measurements, low laser pulse intensities (resulting in a

photovoltage close to 100 mV at a load resistance R_{Load} of 1 MΩ) were used to avoid space charge effects and to maintain quasi short-circuit conditions [104]. However, the transients were also measured under various applied biases. To estimate the recombination coefficients, the extracted charge (Q_{ext}) is calculated at different load resistances by integrating the photovoltage transients measured at highest pulse intensities that saturate the photovoltage. Repetitive photovoltage transients for charge trapping measurements and very low mobility detection (on the order of 10^{-10} $cm^2\,V^{-1}\,s^{-1}$) were recorded at R_{Load} = 1 MΩ and different laser repetition rates (2 – 20 Hz). Summaries of these measurement techniques are provided in the figure captions of **Supplementary Figure 7**, **Supplementary Figure 8** and **Supplementary Figure 9**, respectively. The error bars in the mobility values as measured by RPV indicate the uncertainty of the carrier transit times. The uncertainty of the transit time was approximated from the range at which the photovoltage signals deviate and saturate to tangents fitted to the rise and plateau regions of the photovoltage transients (as plotted in **Supplementary Figure 7** and **8**).

Transient Absorption Spectroscopy (TAS): Femtosecond TAS was carried out using a commercially available transient absorption spectrometer, HELIOS (Ultrafast systems). Samples were excited with a pulse train generated by an optical parametric amplifier, TOPAS (Light conversion). Both the spectrometer and the parametric amplifier were seeded with an 800 nm, <100 femtosecond pulses at 1 KHz generated by a Solstice Ti:Sapphire regenerative amplifier (Newport Ltd). Changes in the optical density of the films induced by the laser excitation were followed with a second broadband pulse (830–1450 nm) generated in a sapphire crystal. The HELIOS transient absorption spectrometer was used for recording the dynamics of the transient absorption spectra up to 2.7 ns with an average 200 fs instrument response function. Measurements were performed on the active layer next to the top electrode of the same devices as used for the electrical measurements (structure: glass/ITO/PEDOT:PSS/Active Layer). Samples were excited at 560 nm with a fluence of 500 nJ cm^{-2}. The low fluence ensures absence of second order recombination processes in our devises. The decay dynamics were analyzed corresponding to the polymer exciton (1300 nm) and positive polaron (cation) absorption (1000 nm). Global analyses of the data were carried out using the program OriginLab. TAS signals have been averaged 10 times and repeated twice.

V.3 High Performance due to Re-Dissociating Charge-Transfer States

This section presents a study on one of the best performing OSCs to date. The results show that the omnipresent Non-Langevin recombination in efficient OSCs can be explained by the finite CTS lifetime and high probability of CTS re-dissociation after free carrier encounter. It is demonstrated that Non-Langevin recombination due to re-dissociating bound states is highly beneficial, not only to maximize the charge collection, but also the charge generation yield, and in fact all photovoltaic key parameters. The unique properties of the studied donor material may provide an opportunity to establish design principles to control the electronic overlap between the CTS and the ground state and the interplay between CTS dissociation and recombination.

Reduced Recombination in High Efficiency Molecular Nematic Liquid Crystalline: Fullerene Solar Cells

Abstract

Bimolecular recombination in bulk heterojunction organic solar cells is the process by which non-geminate photogenerated free carriers encounter each other, combine to form a charge transfer (CT) state which subsequently relaxes to the ground state. It is governed by the diffusion of the slower and faster carriers towards the electron donor: acceptor interface. In an increasing number of systems, the recombination rate constant is measured to be lower than that predicted by Langevin's model for relative Brownian motion and the capture of opposite charges. Herein, we investigate the dynamics of charge generation, transport and recombination in a nematic liquid crystalline donor: fullerene acceptor system that gives solar cells with initial power conversion efficiencies of >9.5%. Unusually, and advantageously from a manufacturing perspective, these efficiencies are maintained in junctions thicker than 300 nm. Despite finding imbalanced and moderate carrier mobilities in this blend, we observe strongly suppressed bimolecular recombination, which is ~150 times less than predicted by Langevin theory, or indeed, more recent and advanced models that take into account the domain size and the spatial separation of electrons and holes. The suppressed bimolecular recombination arises from the fact that ground-state decay of the CT state is significantly slower than dissociation.

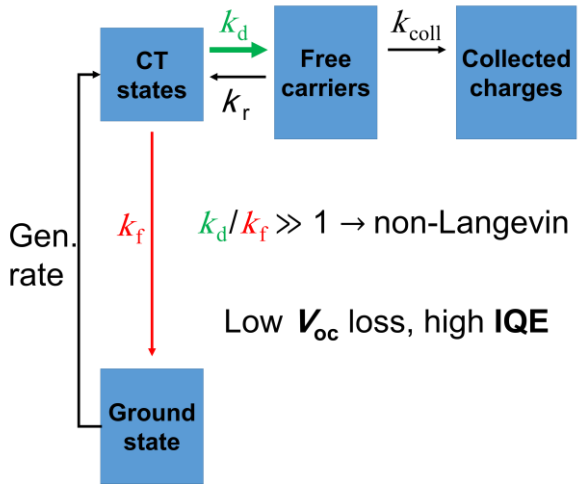

Introduction

Despite considerable activity directed towards materials development over the past two decades, there are still only a handful of organic semiconductor systems that deliver power conversion efficiencies (PCEs) >10% in single junction organic solar cells [170]. The so-called

bulk heterojunction (BHJ) containing a blend of electron donor and acceptor organic semiconductors is the only architecture so far capable of delivering these single junction PCEs, and the electron acceptor is normally a fullerene such as $PC_{71}BM$ ([6,6]-phenyl-C71-butyric acid methyl ester). High efficiency donor materials are often polymers although there are a few notable exceptions [208]. One of the more interesting of these exceptions was recently reported by Sun et al. – a molecular nematic liquid crystalline donor with a benzo[1,2-*b*:4,5-*b*']dithiophene (BDT) centre and rhodamine end groups referred to as 'BTR' [209]. When combined with $PC_{71}BM$ in an optimised architecture, this material delivers an exceptionally high Fill Factor (FF ~ 0.75) and open circuit voltage (V_{OC} ~ 0.95) even when the heterojunction is 310 nm thick. This is unusual and important since 'thick junctions' (>200 nm) are advantageous from multiple perspectives for viable manufacturing of large area organic solar cells.

Electron and hole mobilities in non-crystalline organic semiconductors tend to be <0.1 cm^2/Vs and often imbalanced by several orders of magnitude [107]. There has been significant effort towards understanding the impact of the efficiency with which photogenerated carriers are generated and extracted on the performance of thin and thick junction organic solar cells [52, 59, 182]. For example, Bartesaghi et al. showed how the FF of numerous organic donor:acceptor solar cell systems could be explained by only considering extraction (recombination) losses [182]. Armin et al. recently explained how inverting the junction electrical architecture can be used to compensate for imbalanced mobilities in thick junction devices containing new high mobility donor polymers [210]. Further, Jin et al. demonstrated the direct relevance of suppressing recombination in large area organic solar cells to minimize the impact of thickness inhomogeneities [211].There is also the question of how charge transfer state dissociation efficiency is related to the relative mobilities of the carriers [192].

In general, increasing either the electron and hole mobilities or reducing the bimolecular recombination rate is a means to improving extraction efficiency – particularly in thick junctions. The disordered nature of BHJ films means that the former option is challenging, and been shown to not always deliver the expected benefits [210]. One is therefore led to consider as to how the latter could be achieved. In this regard, and noting the relatively disordered nature of organic semiconductors, the bulk bimolecular recombination rate constant of free charges, k_{bulk}, is traditionally considered to be dependent predominantly upon the time it takes for the

carriers to diffuse close enough to each other to interact within their Coulomb radius. This leads to a diffusion-controlled recombination rate constant, k_{L} –

$$k_{\mathrm{L}} = (\mu_n + \mu_p)e/\epsilon\epsilon_0 \quad (1)$$

where $\mu_{\mathrm{n(p)}}$ is the electron (hole) mobility, e unit charge, ϵ the dielectric constant and ϵ_0 the vacuum permittivity. This construct was originally proposed for the recombination of ions by Langevin [43], and has subsequently been widely used to describe the recombination of charges in disordered materials including dielectrics [212], amorphous silicon [213], small molecule organic semiconductors [214], and polymers [215]. However, more than two decades ago it was shown by Arkhipov and Tyutnev et al. [216, 217] that in some semiconducting polymers, the experimental data for k_{bulk} does not agree with the predicted values of the Langevin rate, k_{L}. The origin of this anomaly was thought to be related to spatial separation of the potential landscapes that electrons and holes experience even in blends, *i.e.*, an effective phase separation of the two charge types [218]. A classic example of this phenomenon is the case of thermally annealed regioregular poly(3-hexylthiophene):[6,6]-phenyl-C_{61}-butyric acid methyl ester (P3HT:$PC_{61}BM$) BHJs. Despite the P3HT:$PC_{61}BM$ system only delivering PCEs of 3-5% (due to the relatively wide optical gap of P3HT), it has become an archetypal example of non-Langevin recombination. This system exhibits reduced bimolecular recombination rate ~100 times less than the Langevin rate [219], thus allowing the FF and PCE to be maintained at optimal values for heterojunctions three times thicker than for most other systems [211]. The reduction factor relative to the Langevin rate can be defined from **Equation 1** as follows:

$$\gamma_{\mathrm{L}} = \frac{k_{\mathrm{L}}}{k_{\mathrm{bulk}}} = \frac{(\mu_n + \mu_p)e}{\epsilon\epsilon_0 k_{\mathrm{bulk}}} \quad (2)$$

Whilst the benefits of reduced bimolecular recombination are now clear – and combining this feature with optimal light harvesting is an important strategy for increasing efficiencies in organic solar cells – the exact origins of non-Langevin recombination are widely debated, with only a few models proposed to explain the behaviour. For example, Tachiya et al. suggested that as free charges can recombine within their Coulomb radius [220], the Langevin model which assumes that recombination occurs at a zero distance, is not a valid description in disordered semiconductors. Koster and Blom [58] postulated that the Langevin rate is not

necessarily valid in the context of BHJs (which are multi-phase systems) since the faster carriers must wait for the arrival of the slower ones at the interface in order for recombination to occur. In such a scenario, the recombination rate constant can be reduced with respect to the Langevin rate when the electron/hole mobilities are strongly imbalanced. Counter to **Equation 1**, Groves et al. [221] used Monte-Carlo simulations, to show that the recombination rate in phase-separated systems is defined by the geometric mean of the electron and hole mobilities. Finally, and most recently, Heiber et al. [59] suggested that the origin of strongly reduced recombination is not necessarily an inherent property of the heterojunction i.e. the spatial separation of electrons and holes within different phases, however it could be true in extreme cases [221]. These workers showed that the so-called 'encounter-limited' recombination can only be suppressed to the extent that it results in small reduction factors (< 10) for typical domain sizes (~5 – 10 nm) seen in high efficiency BHJs devices. According to their observations, the bimolecular recombination rate constant approaches the slower-carrier-limited rate as explained by Koster and Blom [58], for very large domain sizes, whilst the rate constant approaches the faster-carrier-limited rate, as explained by Langevin, when the domain size is vanishingly small. Alternatively, within the framework of the Onsager-Braun model for charge generation, the strongly reduced bimolecular recombination may be attributed to an efficient re-dissociation of CT states back to free charges, which are in competition with their decay to the ground state. This results in an equilibrium between the free charges and (a low population of) CT states. This particular scenario has recently been used by Burke et al. to analyse the equilibrium between the CT state and the charge-separated state populations and its implications for the open circuit voltage [31]. We will return to their findings later in the discussion.

Motivated by these debates, and the aforementioned unusual and potentially advantageous thick heterojunction performance of the BTR:$PC_{71}BM$ system, herein we have studied its recombination dynamics. We have used multiple methodologies to determine the bimolecular recombination reduction factor γ_L in optimised, high efficiency solar cells under operational conditions. Despite PCEs >9.5% being maintained for junction thicknesses up to 310 nm, we find nothing remarkable concerning the electron and hole mobilities (μ_e = 3×10^{-4} $cm^2V^{-1}s^{-1}$, μ_h = 4×10^{-3} $cm^2V^{-1}s^{-1}$), which are comparable to many other less efficient organic solar cell blend systems where the recombination rate is diffusion controlled [54, 107, 182]. We do however, observe a Langevin reduction factor of ~150 and this explains why high FF (~0.75) is maintained in thick junctions in this system. Furthermore, we determine that the free charge

generation quantum yield is as high as 90%, implying efficient photogenerated charge transfer (CT) state dissociation. Importantly, by examining the relative rates within a simple Onsager-Braun construct, we also find that there is a high probability of CT state re-dissociation following free carrier encounters at the donor: acceptor interface; this results in an equilibrium between CT states and free carriers. Hence, bulk bimolecular recombination is not limited by the encounter rate. The result is also consistent with the observed high open circuit voltages compared to the blend energy gap E_{DA}.

Results and Discussion

Solar cell performance

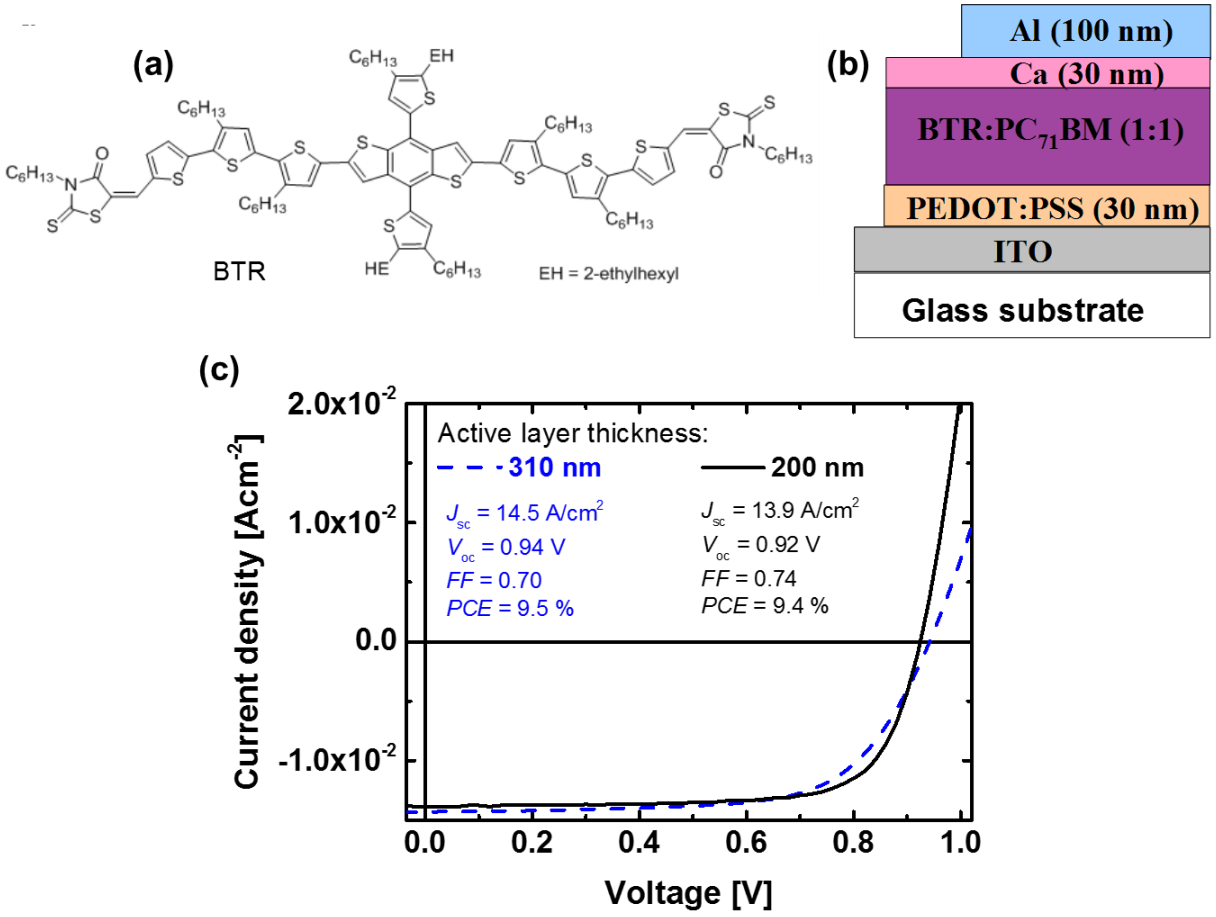

Figure 1. *Device structure and the performance of BTR:$PC_{71}BM$ organic solar cells. (**a**) Molecular structure of BTR. (**b**) Device structure of the solar cell devices made and characterized. (**c**) Current-voltage curves of BTR:$PC_{71}BM$ solar cells with junction thicknesses of 200 nm and 310 nm, respectively, measured under AM1.5G illumination conditions.*

Figure 1 (**a**) shows the molecular structure of the nematic liquid crystal electron donor material, BTR. Bulk heterojunction organic solar cells of BTR:$PC_{71}BM$ with the device structure as shown in **Figure 1** (**b**) were fabricated following the same processing conditions and methodologies as describe by Sun et al. [209] and we confirm the originally reported efficiencies. Typical current density-voltage (*J-V*) curves for two active layer (heterojunction) thicknesses of 200 nm and 310 nm are shown in **Figure 1** (**c**) with PCEs of 9.4% and 9.5%, respectively. As previously indicated, the maintenance of performance in thick junctions is a matter of significant interest, and it has been shown that balanced charge carrier transport [222] and/or suppressed bimolecular recombination [52, 211] can both provide efficient charge extraction under such circumstances.

Electron and hole mobilities

The next phase of the study focused on the charge mobility of the blend film. A space charge limited current (SCLC) hole mobility of $\sim 10^{-3}$ cm^2/Vs has been previously reported for the BTR:$PC_{71}BM$ blend by Sun et al. [209] In the current work, we employ resistance dependent photovoltage (RPV), which is a more direct charge carrier mobility measurement methodology that is based upon extraction of electrons and holes in operational devices [54]. From the measured transit times as a function of the load resistance R_L (shown in **Figure 2**) and heterojunction thickness (310 nm), we obtain a faster carrier mobility of 4×10^{-3} $cm^2V^{-1}S^{-1}$ and slower carrier mobility of 3×10^{-4} $cm^2V^{-1}S^{-1}$. We note that the value we obtain for the faster carrier mobility is close to the SCLC hole mobility reported by Sun et al. [209], and therefore we tentatively assign the faster carriers to the holes. Furthermore, the electron mobility is in agreement with those typically measured in a 50% by weight fullerene blends for multiple systems, which are consistently lower than that typically observed for blends with 80% fullerene loading ($>10^{-3}$ $cm^2V^{-1}S^{-1}$) [107, 222].

This analysis indicates that charge carrier transport in the BTR:$PC_{71}BM$ system is not unusual from the perspective of carrier mobilities – both in terms of their magnitudes and the approximately 10 times imbalanced mobility. Hence, given the rather standard transport characteristics observed, one is led to suspect that favorable recombination is at the heart of the thick junction performance. This is consistent with Bartesaghi et al. [182], who recently pointed out that the overall charge collection efficiency (which determines the FF and the PCE) is a result of the competition between recombination and charge extraction. In what is to follow, we

study the recombination coefficient by applying 4 independent methods in steady state and transient modes, dark and illuminated.

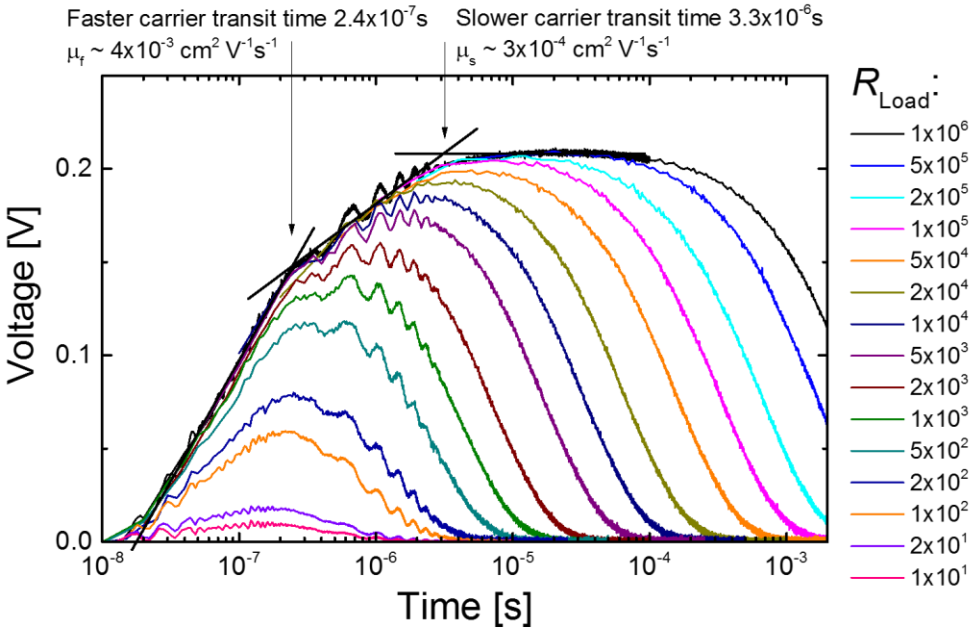

Figure 2. *Resistant dependent photovoltage transients of a BTR:$PC_{71}BM$ solar cell at low laser light intensity. The electron and hole mobilities are quantified from their corresponding transit times marked on the figure.*

Steady state current injection under equilibrium conditions

To quantify the bimolecular recombination reduction factor, we use operational BTR:$PC_{71}BM$ solar cells and analyze their *J-V* curves. In this regard, we assume an insulator (a semiconductor with low equilibrium carrier density) that is sandwiched between an anode and a cathode under forward bias. In the BTR:$PC_{71}BM$ device, the equilibrium charge carrier concentration is negligible compared to the magnitude of the charge on the electrodes at operational voltages. As such, the theory of double injection in insulators is applicable. If the recombination of charges is of Langevin-type, the recombination cross section is so large that the injected electrons and holes from the electrodes recombine as soon as they meet in space. The total current (J_{SCL}) is hence the sum of the space charge limited (SCL) currents from the separated electrons and holes, (J_i^{SCL}) at the cathode and the anode respectively, given by [223]

$$J_{\mathrm{SCL}} = J_n^{\mathrm{SCL}} + J_p^{\mathrm{SCL}} = \frac{9}{8}\epsilon\epsilon_0\left(\mu_n + \mu_p\right)\frac{V^2}{d^3} \qquad \text{(for Langevin case).} \qquad (3)$$

Equation 3 is a generalized Mott-Gurney law and describes the maximum possible injected current into an insulator with the recombination rate limited to that given by the Langevin expression. However, if the recombination is reduced with respect to the diffusion-limited rate, the electron and hole SCL currents do not immediately annihilate each other upon meeting in space, rather allow for the establishment of a plasma in the bulk. In such a case, the current J_{DI} (herein referred to as the double injection current) can be calculated as shown by Mark and Lampert [75]:

$$J_{\mathrm{DI}} = \frac{9}{8}\epsilon\epsilon_0\mu_{\mathrm{eff}}\frac{V^2}{d^3} \tag{4}$$

where

$$\mu_{\mathrm{eff}} = \frac{2}{3}\left(4\pi\mu_f\mu_s\gamma_{\mathrm{L}}\right)^{1/2} \tag{5}$$

and μ_{f} and μ_{s} are respectively the faster and slower carriers. We have taken **Equation 5** from the work of Mark and Lampert (**Equation 11.35**) and modified it to the notation of this work. To mitigate the voltage drop induced by the sheet resistance of the ITO electrode, we reduced the device area to 0.01 cm^2 from the original of 0.2 cm^2. **Figure 3** shows the *J-V* curves of these reduced area devices with fittings to the Parmenter-Ruppel expression using the mobility values of **Figure 2**. The best fit corresponds to a reduction factor of γ_{L} =150. Other fitting values are also shown to demonstrate the sensitivity of the results to the γ_{L} fitting. Note, the built-in voltage V_{bi} was approximated by the open circuit-voltage that matches up with the onset of the dark *J-V* curve as shown in the Supplementary Information. A static dielectric constant of 4 was determined using dark-charge extraction in linearly increasing voltage (dark-CELIV) as previously described [48]. In the next section we employ **Equations 4** and **5** to quantify the reduction factor from the current transients.

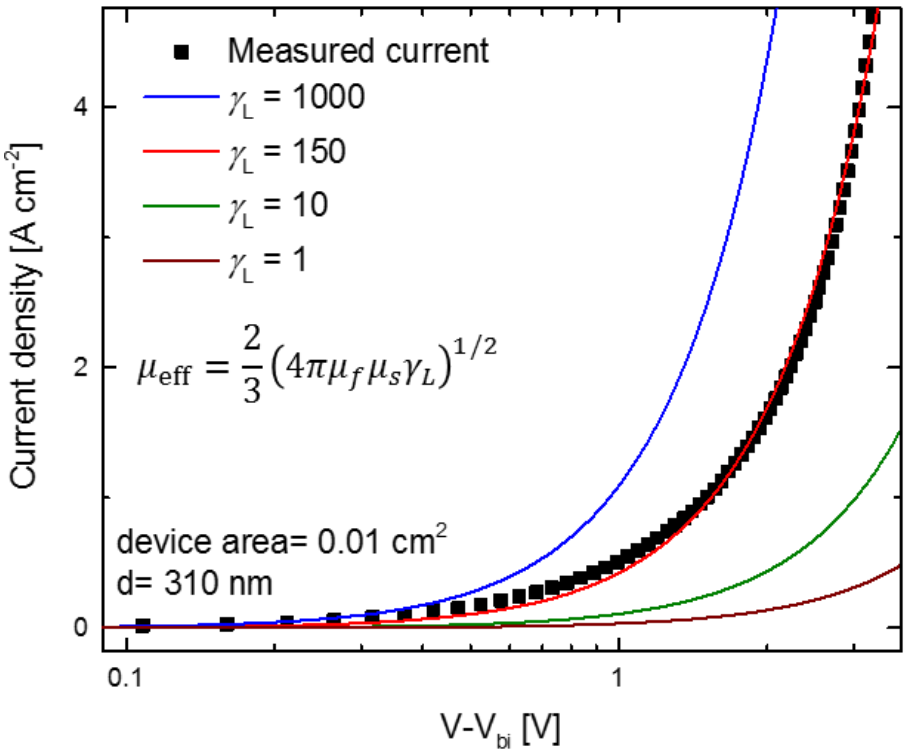

Figure 3. *Current density versus effective voltage for a BTR:PC$_{71}$BM solar cell (310 nm junction thickness, device area 0.01 cm^2 and static dielectric constant of 4). (a) Parmenter-Ruppel current fittings based upon the effective mobility from* ***Equation 5*** *for different values of* γ_L. *The best fit can be achieved with a Langevin reduction factor of* $\gamma_L = 150$.

Transient current injection

The double injection current methodology can also be performed in a transient mode [52]. The transient method benefits from normalization of the currents, implying that any injection barrier due to the imperfect contacts and/or series resistance will have a reduced impact on the analysis. When a forward bias voltage is applied to the solar cell, electrons and holes are injected from the cathode and the anode after an *RC*-decay that first charges the capacitor plates (the electrodes). We note that the *RC*-time must be minimized with respect to the other characteristic times of the system. After the *RC* decay, the total current is expected to be the sum of the two one-carrier SCL currents being injected from each electrode, *i.e.*, **Equation 3**. As indicated above, when the two SCL currents meet in space, two scenarios can emerge: (i) a diffusion-limited recombination regime ($\gamma_L = 1$) in which the recombination cross section is so high that the carriers immediately recombine and no plasma can be formed. In this case, the current does not increase with time and the transient current exhibits a plateau at its SCL value given by the generalized Mott-Gurney law, **Equation 3** [211]; (ii) Alternatively in the case of suppressed

recombination ($\gamma_L > 1$), the current increases further when the carriers meet in space, and electron and hole density increase with time, forming a plasma within the bulk. In this case, the current ultimately increases to the value given by the Parmenter-Ruppel expression, **Equation 4**. The rise of photocurrent is direct and unambiguous evidence of a suppressed recombination rate constant [52]. Note, that the double-injection current transient has been normalized to its initial value immediately after the *RC*-time. Normalizing **Equation 4** by **Equation 3** results in

$$\frac{J_{DI}}{J_{SCL}} = \frac{\mu_{eff}}{\mu_n + \mu_p} \tag{6}$$

which yields the reduction factor together with **Equation 3**

$$\gamma_L = \frac{9}{16\pi}\frac{(\mu_n + \mu_p)^2}{\mu_n \mu_p}\left(\frac{J_{DI}}{J_{SCL}}\right)^2 \tag{7}$$

Figure 4 shows the double injection current transient of an operational BTR:$PC_{71}BM$ solar cell (heterojunction thickness 310 nm) at a bias voltage of 2 V. The current saturates at $\frac{J_{DI}}{J_{SCL}} = 7$. Using the measured electron hole mobilities and **Equation 7** we extract a reduction factor of $\gamma_L = 135$ which is close to the value obtained from steady state *J-V* measurements.

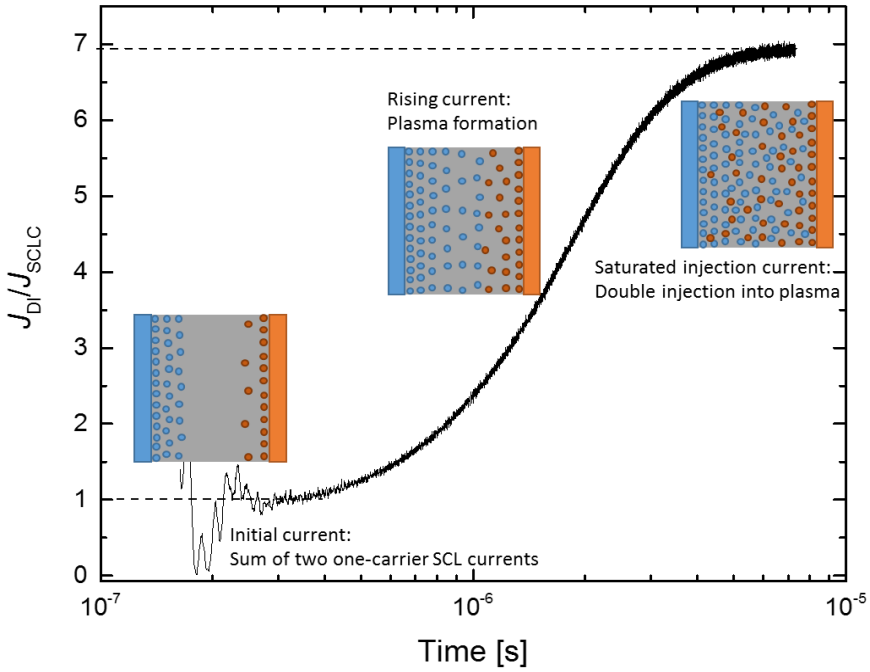

Figure 4. *Injection current transient at forward bias voltage of 2 V normalized to the initial space charge limited (SCL) current. Inset cartoons show the injection of the initial one-carrier SCL currents near the anode and the cathode, rising carrier densities in line with rising current, and ultimately a saturated double injection current into the built-up plasma. The normalized current value of approximately 7 corresponds to a Langevin reduction factors of 135 based upon* ***Equation 7****.*

Resistance dependent photocurrent transient

As discussed previously, systems with reduced bimolecular recombination can sustain higher carrier densities and as a result, a plasma can form during two-carrier injection. The same concept applies to photogenerated charges. To simulate this effect, we use a high fluence incident laser pulse which saturates the photovoltage and immediately screens the electric field inside the film. The photogenerated carriers either recombine due to diffusion, or are collected at the electrodes within the extraction time which can be controlled with a variable load resistance and associated *RC*-time of the circuit. If $\gamma_{\mathrm{L}} \gg 1$, then carriers can survive longer and more charges can be extracted. Integrating the photocurrent transient over time can therefore provide information about the reduction factor. The extracted charge saturates to a value *CV* at the largest load resistances because in this case, the *RC* time is much larger than the photocarrier lifetime, allowing only an amount of charge to be extracted equal to that capable of being stored on the electrodes. Reducing the *RC* time *via* the load resistance allows more charges to be extracted depending on the photocarrier lifetime and the bimolecular recombination coefficient. Using drift-diffusion modeling it has previously been shown that the amount of extracted charges versus the normalized *RC*-time obeys an empirical logarithmic expression [49]

$$\frac{Q_e}{CV} = 1 + c_1 \log\left[1 + c_2 \left(\frac{RC}{t_{\mathrm{tr}}}\right)^{-c_3}\right] \tag{8}$$

where, the fitting coefficients are defined as

$$c_1 = 1.829\left(\gamma_{\mathrm{L}}^{-1} + 0.0159\gamma_{\mathrm{L}}^{-\frac{1}{2}}\right) \tag{9}$$

$$c_2 = 0.63\gamma_{\mathrm{L}}^{0.407} \tag{10}$$

$$c_3 = 0.55\gamma_{\mathrm{L}}^{0.0203} \tag{11}$$

The transit time in **Equation 8** represents an effective transit time for the extraction of both electrons and holes $t_{\mathrm{tr}} = d^2/(\mu_{\mathrm{s}} + \mu_{\mathrm{f}})V$. **Figure 5** shows the experimental results for the integrated photocurrent after a high fluence pulse excitation, *i.e.*, the amount of extracted charges normalized to the number of charges that can be stored on the electrodes (*CV*) plotted against t_{tr} normalized to the *RC*-time of the circuit. The fitting was based upon **Equation 8**. A reduction factor of $\gamma_{\mathrm{L}} = 133$ is obtained which is again close to those values we evaluated based upon the double injection experiments. Non-matching parameters are also shown to highlight the sensitivity of the approach of the fitting parameters.

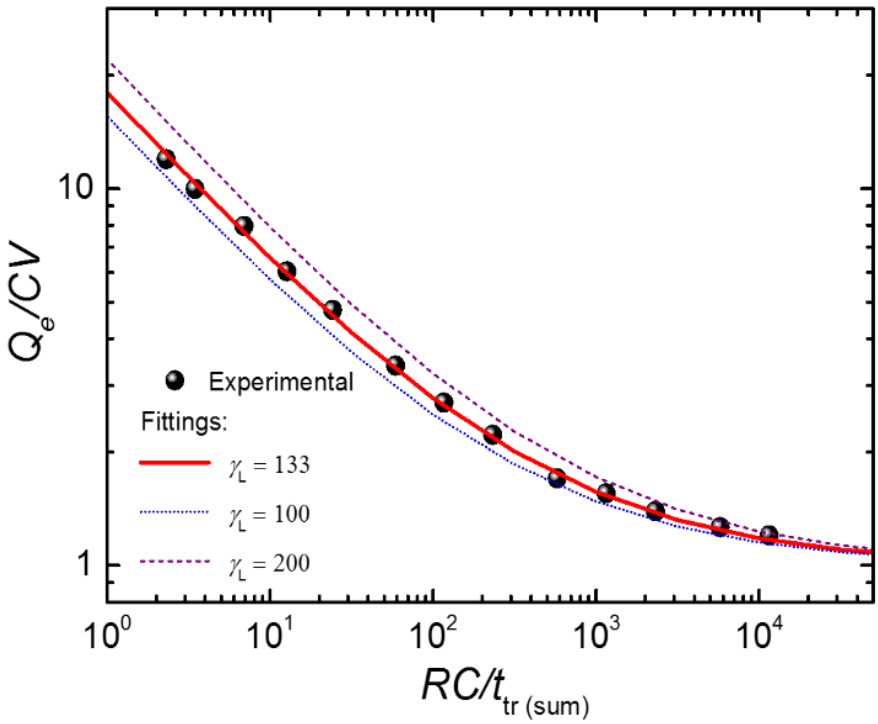

Figure 5. *Extracted charge normalized to the amount of charge on the electrodes (CV) versus the faster carrier transit time normalized to the RC-time. The photovoltage transients (devices similar to* ***Figure 1****) are measured at high laser fluences that saturate the photovoltage (number of photons* $\gg$ *CV/e) and subsequently integrated to obtain the extracted charge. The experimental results are in agreement with the results from injection based methods (****Equation 7****), i.e.,* $\gamma_L = 133$ *. The dashed purple and dotted blue lines correspond to non-matching fittings in order to show the sensitivity of the fittings to the γ value.*

Intensity dependent photocurrent

To investigate the role of suppressed bimolecular recombination under operational conditions we utilized intensity dependent photocurrent (IPC) measurements. We have previously shown [211] that the critical photocurrent at which bimolecular recombination becomes significant is close to the slower carrier space charge current $J_{\mathrm{SCLC\,(slower)}} \approx CV/t_{\mathrm{tr\,(slower)}}$ for systems with Langevin recombination, and where $t_{\mathrm{tr\,(slower)}}$ denotes the transit time of the slower carriers. When the incident light intensity increases, the photocurrent also increases (initially linearly with light intensity) until the current reaches $J_{\mathrm{SCLC\,(slower)}}$. At this point, the charge in the device approaches CV and the average lateral spacing between the charge carriers reduces to a value at which their Coulombic attraction becomes larger than the external electric field that drives carriers to the electrodes. To avoid reaching the bimolecular recombination loss threshold (at the short circuit condition, at least) in Langevin-type systems such as PCDTBT:PC70BM [211, 224], and under 1 sun illumination, the junction thickness must be kept thin enough to avoid the formation of slower carrier space charges. Recently Stolterfoht et al. [172] have extended the use of the IPC methodology to non-Langevin systems and correlated the deviation point to both the slower carrier mobility, and the bimolecular recombination reduction factor. In this case, the current deviates at

$$J_{\mathrm{dev}} \approx \xi \frac{CV}{t_{\mathrm{tr(slower)}}} \gamma_L^{1/2} \tag{12}$$

where, ξ is a prefactor which has been found to be approximately 0.4. Overall, **Equation 12** is in line with double injection current transients in non-Langevin systems. If the recombination is suppressed, the slower carrier space charge limit is effectively increased by a factor of $\sqrt{\gamma_{\mathrm{L}}}$.

Before moving on to the IPC results for BTR:$PC_{71}BM$ operational solar cells, we will further elaborate on the details of **Equation 12** and its implications. As discussed in the double injection current section, non-Langevin recombination can increase the maximum injectable current into insulators. **Equation 6** clearly shows that if $\gamma_{\mathrm{L}} > 1$, the double injection current can be enhanced from j_{SCLC} to j_{DI} whilst it is limited to j_{SCLC} if $\gamma_{\mathrm{L}} = 1$, and no rise in the transient will be expected. **Figure 6** (**a**) shows the drift-diffusion simulation results of the intensity dependent photocurrent for a BTR:$PC_{71}BM$ solar cell (310 nm junction) with different Langevin reduction factors. In **Figure 6** (**b**) simulated double injection transients for the same systems are shown at 2 V bias. It is clear that when $\gamma_{\mathrm{L}} = 1$, the injection current transient

exhibits no rise from J_{SCLC} and as seen from the IPC plot in **Figure 6** (**a**), the photocurrent deviates at approximately $J_{SCLC\,(slower)}$. By increasing the reduction factor ($\gamma_L > 1$) the injection current exhibits a rise towards a maximum value of j_{DI}. Both j_{DI} and the deviation photocurrent (j_{dev}) increase with increasing reduction factor.

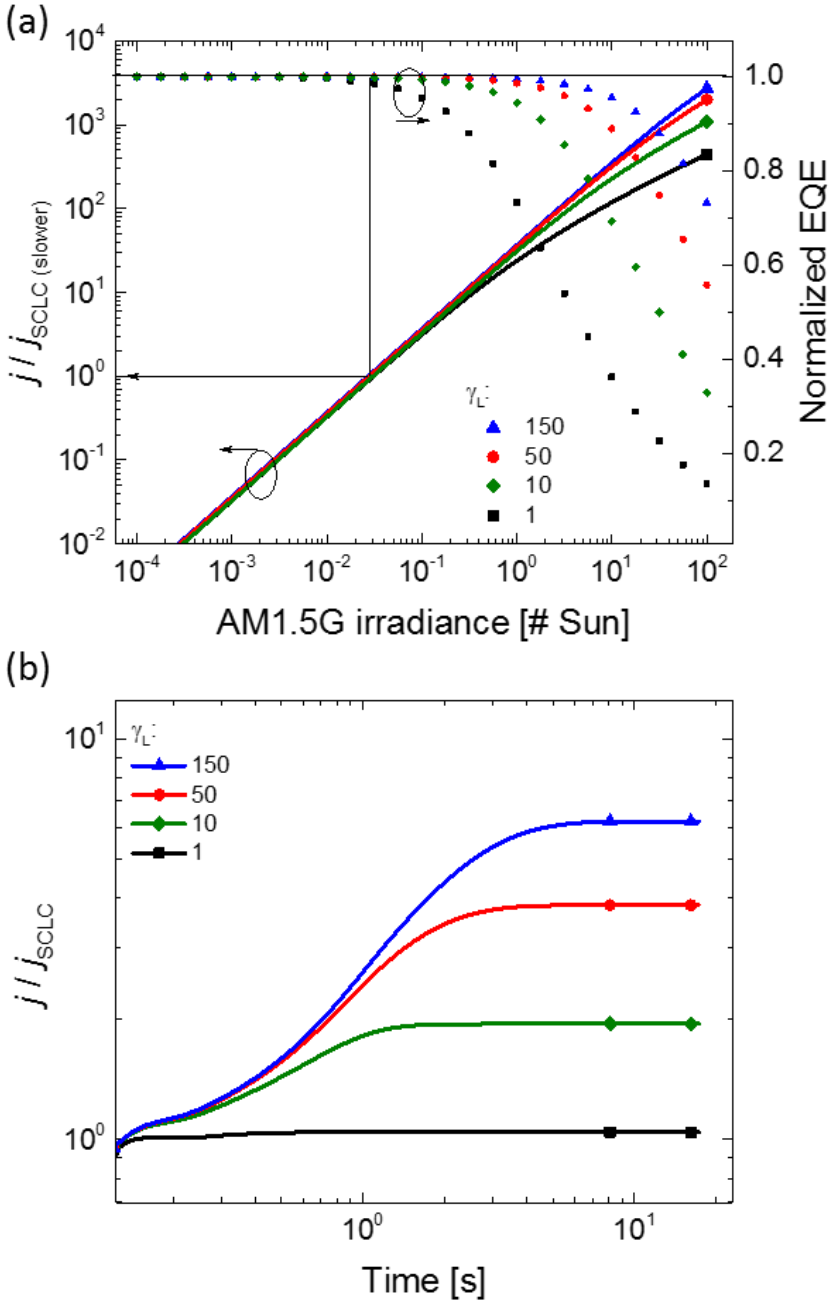

Figure 6. ***(a)*** *Simulated intensity dependent photocurrent for a BTR:$PC_{71}BM$ solar cell with active layer thickness of 310 nm under short circuit condition for different Langevin reduction factors. The current is normalized to the slower carrier space charge current (SCLC). By increasing the reduction factor, the photocurrent deviates at photocurrent values larger than*

*the slower carrier SCLC. The deviation points are more visible from the normalized external quantum efficiencies (EQEs). (**b**) Simulated double injection transients for the same device at a forward bias voltage of 2 V. In all cases the injection current starts from the SCLC limit. For larger reduction factors the current reaches significantly higher values.*

Figure 7 shows the experimental results of intensity dependent photocurrent measurements on a 310 nm thick BTR:$PC_{71}BM$ solar cell device at the short circuit condition. We obtain a deviation current of $J_{\mathrm{dev}} \approx 30\ \mathrm{mAcm^{-2}}$. Qualitatively, this deviation current is far larger than the slower carrier space charge limited current for a 310 nm thick BTR:$PC_{71}BM$ device ($j_{\mathrm{SCLC}}(310\ \mathrm{nm}) \approx 3.5\ \mathrm{mAcm^{-2}}$). We can use **Equation 11** to quantify the reduction factor from J_{dev} and the slower carrier mobility. Using an internal voltage that is approximately the same as the open circuit voltage (~0.9 V) and a dielectric constant of 4, we calculate $\gamma_{\mathrm{L}} \approx 150$. Hence, using four different methodologies to measure the reduction factor we see clearly that the recombination in BTR:$PC_{71}BM$ is approximately 150 times suppressed with respect to that predicted by the Langevin model.

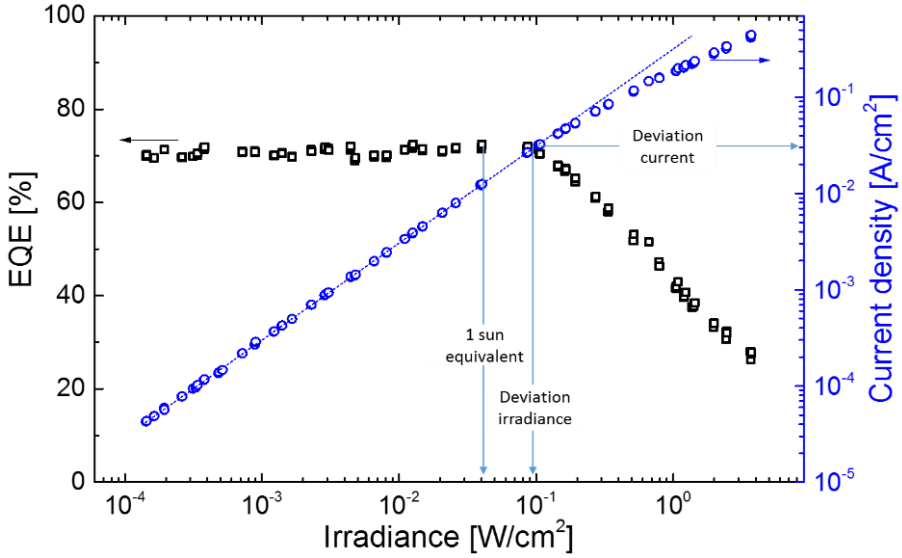

Figure 7. *The photocurrent (right axis) versus continuous light irradiance at an incident wavelength of 532 nm for a BTR:$PC_{71}BM$ solar cell with a junction thickness of 310 nm under short circuit conditions. The EQE is plotted on the left axis versus irradiance to better visualize the irradiance at which the photocurrent deviates from linearity, which also leads to a decrease in the EQE. Due to suppressed bimolecular recombination, the deviation happens at a photocurrent of ~0.03 A/cm^2, which is larger than the space charge current of the slower*

carriers. A reduction factor of $\gamma_{\mathrm{L}} = 150$ *can be estimated from the deviation current and based upon* ***Equation 13****.*

Origin of the suppressed recombination and its implications

We now discuss charge generation in these high efficiency BTR:$PC_{71}BM$ solar cells and its inter-relation with the observed non-Langevin recombination. **Figure 8** (**a**) shows the optical constants; refractive index and extinction coefficient of BTR:$PC_{71}BM$ films on glass. Using these parameters and the optical constants of all the ancillary layers in the solar cell stack, we were able to quantify the parasitic absorptions (i.e. optical losses) in the full device. Subsequently, using the external quantum efficiency (EQE) and near normal incidence reflection we evaluated the internal quantum efficiency (IQE) [35]. The IQE was found to be ~90% [junction thickness 310 nm, **Figure 8** (**b**)] and virtually flat as expected, across the absorption window. We note that the photocurrent does not deviate from linearity in this system until high light irradiances – five orders of magnitude larger than the light irradiance we used to measure the EQE (~ 1 μW/cm^2) in **Figure 6**.

It has recently been shown that under these conditions, the IQE is not limited by non-geminate recombination losses (*i.e.*, bimolecular losses or trap-assisted non-geminate recombination in the bulk) and therefore, it reflects the charge generation quantum yield [35]. Hence, the measurements show that charge generation for the BTR:$PC_{71}BM$ blend is very efficient, and indicate that charge generation and recombination are inter-related. The probability of ionization of CT states is given by the branching ratio $P = k_{\mathrm{d}}/(k_{\mathrm{f}} + k_{\mathrm{d}})$, where k_{d} is the rate constant for dissociation of CT to charge separated (CS) states, and k_f is the decay rate constant of the CT to the ground state (GS). When k_{d} is >> k_{f}, efficient charge generation is expected. Further increasing the ratio of $k_{\mathrm{d}}/k_{\mathrm{f}}$ results in a saturation of the CT state dissociation probability, and will not further increase the charge generation. However, this leads to the formation of an equilibrium between CT and CS states and overall, lowers the CT states density and their recombination rate. The bimolecular recombination involves two independent stages. The first rate, k_{enc}, depends on the probability of the encounter between a free electron and a free hole to form a CT state with a diffusion-limited rate constant. The second stage is the recombination of the CT states to the ground state. The bulk recombination rate constant can therefore be written as

$$k_{\text{bulk}} = (1 - P)k_{\text{enc}} \tag{13}$$

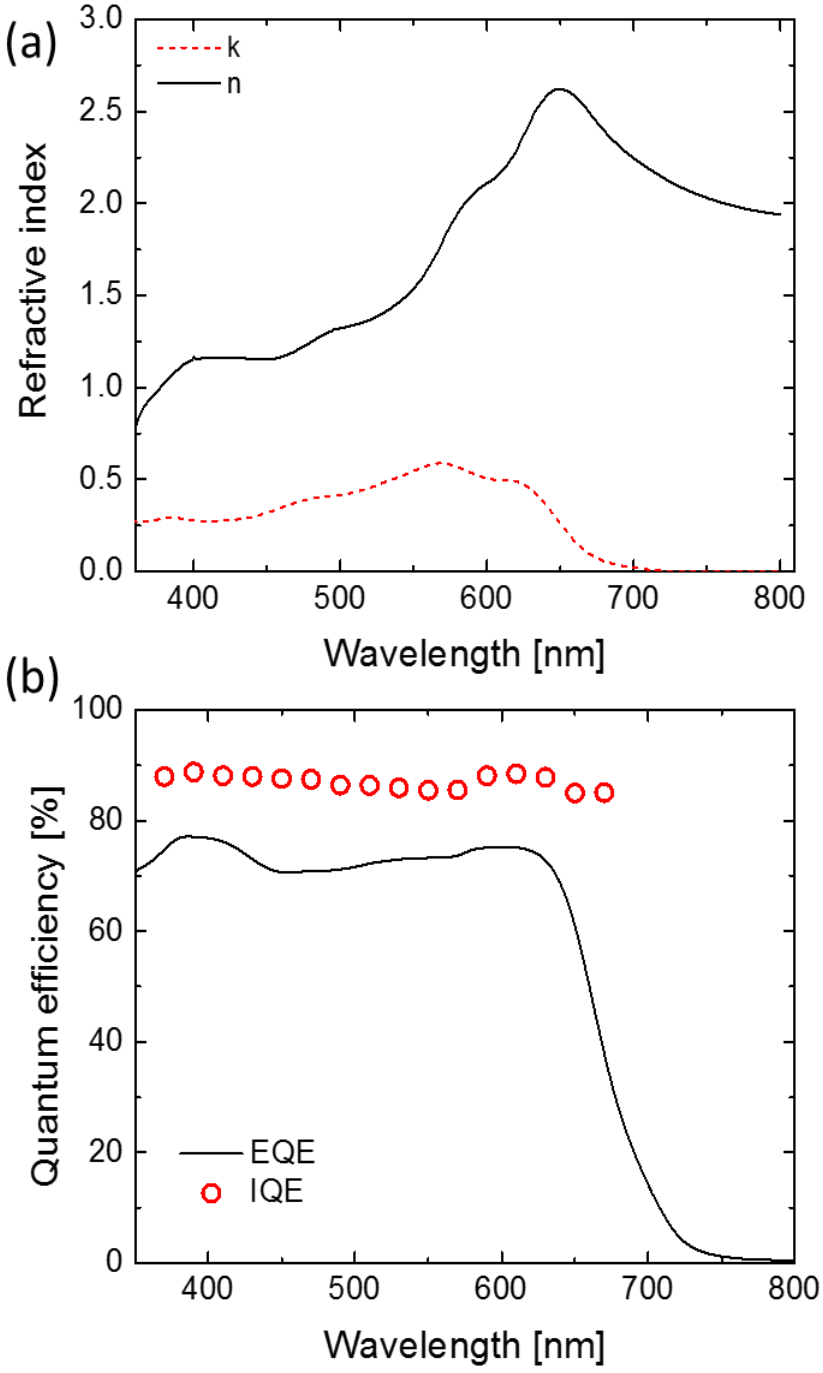

Figure 8. *(**a**) Optical constants (n, k) of a BTR:$PC_{71}BM$ film as determined by spectroscopic ellipsometry and reflectometry. (**b**) Internal and external quantum efficiencies of BTR:$PC_{71}BM$ solar cells. The IQE is measured at low light irradiance where non-geminate recombination is absent. Therefore, the IQE reflects the charge generation quantum yield which is ~ 90%.*

The bulk recombination and Langevin rate constants are related via $\gamma_{\mathrm{L}} = k_{\mathrm{L}}/k_{\mathrm{bulk}}$ and therefore we can write for γ_L

$$\gamma_L = \gamma_{\mathrm{CT}}\gamma_{\mathrm{enc}} \tag{14}$$

where $\gamma_{\mathrm{enc}} = k_{\mathrm{L}}/k_{\mathrm{enc}}$ and $\gamma_{\mathrm{CT}} = \frac{1}{1-P}$. In **Figure 9** we have plotted the predicted diffusion limited reduction factors (γ_{enc}) for different domain sizes – based on the model of Heiber et al. [59] versus the square root of the mobilities product assuming an electron mobility of 3 x 10^{-4} $cm^2V^{-1}s^{-1}$. In addition, we also plot the slower-carrier-limited rate constants according to Koster and Blom [58], as well as the harmonic mean and the geometric mean as suggested by Groves and Greenham [221]. Plotting the measured reduction factor (γ_{L}~150) of the BTR:$PC_{71}BM$ system on the same figure demonstrates that this reduction factor is significantly larger than that predicted by any of these three models, regardless of the domain size or the nano-morphology. This implies that the origin of non-Langevin recombination in this material system is predominantly because of the high probability of CT state dissociation (P ≫1). If we consider a domain size of 10 nm, then γ_{enc}~2, which implies γ_{CT}~75 that approximates the ratio k_d/k_{f}.

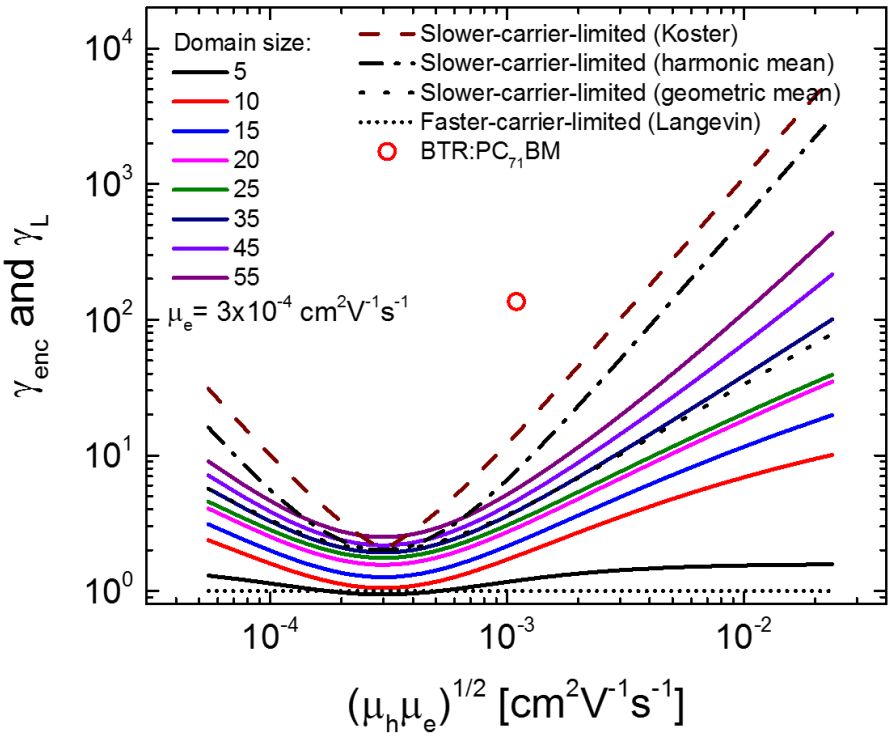

Figure 9. *Predicted diffusion controlled reduction factors of the bimolecular recombination for different domain sizes (colored lines, calculated based on Heiber et al. [59]) as a function of the square root of the mobilities assuming an electron mobility of 3 x 10^{-4} $cm^2V^{-1}s^{-1}$, compared*

to predictions of empirical models such as the slower-carrier-limited rate constant, the harmonic and geometric mean. All these models assume a diffusion (encounter) limited recombination mechanism. The measured Langevin reduction factor of BTR:PC$_{71}$BM (~150) is plotted as a red circle, demonstrating the strongly reduced recombination compared to all of these models.

In addition to these beneficial effects of the strongly reduced recombination rate for the charge generation yield, Burke et al. [31] have demonstrated that a long CT state lifetime (which corresponds to large $k_{\mathrm{d}}\ /k_{\mathrm{f}}$ and reduced recombination) is highly desirable to increase the open-circuit voltage of organic solar cells by the reducing energy losses associated with non-radiative charge recombination. A weak coupling of the CT states to the ground state is key to achieving this condition whereby the radiative V_{OC} loss is reduced logarithmically [31]. It has also been shown that many solar cells lose between 300 to 700 meV in eV_{OC} compared to the CT state energy (or approximately the blend energy gap), as determined by the difference of the ionization potential of the donor and the electron affinity of the acceptor minus the CT state binding energy $\mathrm{E_{b(CT)}}$. We note that the exact energy and binding energy of BTR:PC$_{71}$BM CT states are not known, and therefore we are not able to calculate the exact V_{OC} loss. Nevertheless, a Langevin reduction factor of 150 corresponds to a reduction of the V_{OC} loss (i.e. an increased V_{OC}) of $k_{\mathrm{B}}T\ln(\frac{1}{150}) \approx 120$ meV with respect to a Langevin system with identical energy levels to the BTR:PC$_{71}$BM blend. This is perhaps the reason for the respectable open circuit voltage of 0.94 V with energy levels similar to many other donor/acceptor systems [23, 209] which nevertheless exhibit lower V_{OC}.

Conclusion

Bulk heterojunction organic solar cells based upon the BTR:PC$_{71}$BM blend system exhibit state-of-the-art power conversion efficiencies exceeding 9.5%. These efficiencies are maintained in 'thick' heterojunction devices (> 300 nm). We have found that the electron and hole transport properties in optimized BTR:PC$_{71}$BM operational solar cells do not explain this behaviour – the magnitude and ratio of the mobilities are typical of numerous high and moderate efficiency organic solar cell BHJ combinations. We found a mobility imbalance of ~10 and strongly suppressed bimolecular recombination with respect to the values predicted by Langevin theory that cannot be explained by the carriers existing in separate phases. To quantify the bimolecular recombination reduction factor, we employed four independent methods, which

are based on injection and extraction of charges in both steady state and transient regimes. The results obtained from all four methods are in strong agreement, confirming a reduction factor of ~150 in this intriguing molecular nematic liquid crystal donor: fullerene acceptor system. The simultaneous presence of high free charge generation quantum yield and suppressed bimolecular recombination, suggests a low recombination rate of the CT states compared to the dissociation rate. The suppressed CT state recombination also contributes to the reduction of V_{OC}-loss by 120 meV in this system. Our results explain why this BTR:$PC_{71}BM$ system works so well in organic solar cells, and potentially delivers new design strategies to suppress the CT state recombination, which simultaneously optimises all photovoltaic key parameters of organic solar cells.

Experimental Section

Materials: $PC_{71}BM$ was purchased from American Dye Source and used without purification. BTR was synthesised in house based on the methodology previously described [209].

Solar cell fabrication: Solar cells were fabricated on pre-patterned indium tin oxide (ITO) glass substrates (15 Ω sq^{-1}: Xinyan) in a class 1000 clean room. The substrates were cleaned in a detergent bath (Alconox) at 80 °C for 10 min and mechanically cleaned by a soft cloth, followed by sonication in sequence with Alconox, deionized water, acetone, and 2-propanol for 10 min each. The cleaned substrates were dried with nitrogen before spin-coating the subsequent layers. Substrates were 2.5 cm x 2.5 cm with 6 pixels of 0.2 cm^2 each. The cleaned substrates were coated with a 30±5 nm layer of poly(3,4-ethylenedioxythiophene):poly(styrenesulfonate) (PEDOT:PSS) purchased from Heraeus (Clevios P Al4083), by spin-coating at 5000 rpm for 60 s. The PEDOT:PSS layer was baked for 10 min at 170 °C. After cooling, the substrates were transferred into a nitrogen-filled glove box for device fabrication (O_2 <1 ppm, H_2O <1 ppm). After that, BTR:$PC_{71}BM$ films were deposited from the solutions described above on top of the PEDOT:PSS layer in a nitrogen atmosphere with oxygen and water concentration of <5 ppm. Individual solutions of BTR and $PC_{71}BM$ were prepared in anhydrous chloroform at room temperature and at a concentration of 40 mg/mL. The solutions were then mixed at a volume ratio of 1:1 and spin-coated at 1000 rpm to achieve an active layer thickness of ~310 nm as determined with a Veeco Dektak 150 profilometer. Total concentration of 30 mg/mL was used in order to make 200 nm thick films. The films were then treated with solvent annealing and finished with thermal evaporation of a Ca/Al cathode (20 nm and 80 nm) under a 10^{-6} mbar vacuum.

Solvent annealing: Solvent annealing was performed in a nitrogen glove box with conditions O_2 <1 ppm and H_2O <1 ppm. Tetrahydrofuran (1.5 mL) was injected into a glass Petri dish (volume 40 mL radius 5 cm). The Petri dish was closed for 2 min to let the vapour saturate the inner atmosphere. Then BTR:$PC_{71}BM$ films were attached on the back side of the Petri dish lid, which was quickly swapped with the lid covering the solvent containing Petri dish. The film

was about 1 cm above the solvent level during the annealing. After 15 sec the film was removed from the petri dish.

Solar cell characterization: Current-density–voltage (*J-V*) characteristics were acquired in a nitrogen glove box with conditions O_2 <1 ppm and H_2O <1 ppm using a Keithley 2400 Source Measure Unit under simulated Air Mass 1.5 Global (AM 1.5 G) 1000 W/m^2 illumination (as determined by an NREL-certified photodiode with a KG5 filter) provided by an Abet Sun 2000 Solar Simulator. EQE and near normal incidence reflection spectrum were measured with a QEX7 setup from PV Measurements Inc., using a calibrated photodiode. The integrated EQEs were within ±10% of short circuit current as a self-consistent measure of system calibration.

Internal quantum efficiency: The IQEs was determined using a previously reported methodology [35]. The optical constants of the BTR:$PC_{71}BM$ blends were determined using a combination of spectroscopic ellipsometry (J. A. Woollam VUV-VASE ellipsometer) and reflectometry (QEX7 setup from PV Measurements Inc) based upon a previously reported approach [225]. The optical constants of all the non-active layers have been reported elsewhere [193].

Steady state and transient double injection: Double injection current-voltage curves were recorded in the dark using a Keithley 2400 Source Measure Unit. The double injection current transients were measured using an Agilent 33250A arbitrary waveform generator synchronised by a Stanford Research Systems DG535 delay generated. The signal was recorded using a digital storage oscilloscope (LeCroy Waverunner A6200) via a LabVIEW code.

Resistance dependent photovoltage: Photocurrent and photovoltage transients were recorded using the same setup as explained for double injection transients. A pulsed second-harmonic Nd:YAG laser (Quantel Brio) working at 532 nm was used with pulse duration of 5 ns. The laser beam with ~50 mJ energy output was attenuated with a natural optical-density (OD) filter set. Low laser pulse fluences (~OD 7) were used for the RPV mobility measurements in order to prevent a redistribution (screening) of the internal electric field and maintaining quasi-short-circuit conditions regardless of the load resistance. In contrast, a high laser fluence (~OD 3.5) was used to measure the bimolecular recombination coefficient on the same devices.

Intensity dependent photocurrent: Light intensity dependent photocurrents, EQEs, and *J–V* curves were determined using a second harmonic Nd:YAG laser (Laserver) operating continuously at 532 nm as the illumination source, with a series of neutral density filters purchased from Thorlabs and Holmarc used to vary the light intensity. The light intensity was calibrated using a calibrated photodiode. The photocurrent was recorded by an Agilent B1500A Semiconductor Analyser.

Chapter VI: Conclusions and Outlook

Organic semiconductors continue to be of great interest for photovoltaic energy conversion and light detection applications due to their solution processability, chemical tunability and mechanical flexibility. However, their disordered nature complicates the understanding of the critical mechanisms and pathways from the photoexcitation to free charges, and the subsequent extraction of these charges in a photovoltaic diode. This renders a systematic improvement of their photovoltaic performance difficult, and necessitates more research and the development of new experimental methodologies to understand the underlying physical mechanism which control these processes.

The work described in this thesis is motivated by these considerations. **Chapter I** contains a general introduction to the research topic. **Chapter II** establishes the theoretical and experimental background for the result chapters of this thesis, and highlights in **Section II.9.6** important optimization strategies for future materials design via an increase of the dielectric constant, the charge carrier mobilities, or the CTS lifetime. The work presented in **Chapter III** (**Section III.1**) presents a newly developed transient photovoltage technique that we term "RPV" to quantify the mobility and recombination rate constant of charge carriers moving in the percolated donor/acceptor pathways towards the extracting electrodes. The developed methodology provides key advantages over other conventionally used charge mobility/recombination measurement techniques, notably it is applicable to operational

devices. Inspired by the need to selectively optimize the processes which control the photocurrent output of the cell, such a charge photogeneration and extraction, a technique to quantify and disentangle both efficiencies is developed in a next step, and introduced in **Chapter IV**. The study in **Section IV.1** presents an improved methodology based on the existing light intensity dependent photocurrent measurement technique to quantify bimolecular recombination losses under operating conditions. A model based on the space charge/transport limited photocurrent (I_{SCLC}) has been established to predict and minimize these losses for given solar cell parameters such as thickness, voltage and carrier mobilities. Throughout the work described in this thesis, the model's predictions have been validated for a large number (>25) of BHJ OSC systems under various experimental conditions. **Section IV.2** describes a continuation of charge transport studies using the developed IPC measurement technique. The study shows that the non-geminate recombination of free charges, which impacts the charge collection efficiency, is strictly bimolecular in typical organic solar cells under steady-state and short-circuit conditions, and is therefore distinct in an IPC measurement. Based on these results, a simple but conclusive understanding of the charge transport physics has been reached and was detailed in **Chapter IV**. This understanding leads to simple guidelines to avoid charge transport losses of typical organic semiconductors in thin-film photovoltaic diodes by keeping the photocurrent output of the cell below the I_{SCLC}. The findings also suggest that the issue of free charge carrier extraction is minor compared to the issue of inefficient charge generation.

The next **Chapter V** details three in-depth studies as to how photons are converted into free charges based on the same previously developed IPC technique, corroborated by transient absorption spectroscopy. In contrast to many previous studies, the work presented in **Section V.1** shows that it is the CTS splitting efficiency that significantly limits the photocurrent output under operating solar cell conditions and that the CTS dissociation depends on the slower carrier mobility. The findings indicate that free charge collection and CTS splitting are similar in the sense that both are critically controlled by the slower carrier mobility, which could explain the lasting difficulties to understand the impact of geminate (CTS) and non-geminate recombination (free charges) on the shape of the *JV*-curve. This result was explained in **Section V.2** by the ability of the slower carriers to leave the donor: acceptor interface *via* 1) a high enough mobility, 2) a sufficiently large domain size, and 3) enough conduction pathways (entropy). Lastly, the work introduced in **Section V.3** demonstrates how the finite CTS lifetime and re-dissociation probability can explain the omnipresent "Non-Langevin" recombination in

organic photovoltaic diodes, and highlights the large benefit of re-dissociating CTS for all photovoltaic key parameters. Generally, these studies in **Chapter V** underline the importance of optimizing the photocarrier generation quantum yield *via* a high mobility of both charge carrier types to simultaneously maximize the yield of charge photogeneration and extraction.

Going forward, organic solar cells will likely continue to improve from optimizations in materials design, material processing, device engineering and an ever-increasing fundamental understanding. However, only time will tell whether the challenges associated with their relatively low power conversion efficiencies, long-term stability, and scaling issues can be overcome. The collection of works on charge photogeneration and transport described in this thesis form a simple but powerful model to explain the photovoltaic performance of these systems. The findings offer very direct guidelines for device engineering to minimize the detrimental recombination of free charges and CTS states, and also identified key principles for future materials design, which could potentially bridge the gap to inorganic counterparts in terms of efficiency.

List of Symbols and Abbreviations

Roman Symbols and Abbreviations

a	lattice constant
$A(\lambda)$	device absorption spectra
BHJ	bulk heterojunction
C	capacitance
CELIV	charge extraction using linearly increasing voltage
Channel I	photoinduced electron transfer
Channel II	photoinduced hole transfer
CS	charge-separated state
CT_1	energy of the relaxed charge-transfer state
CTS	charge-transfer state
CU	charge capable of being stored on the electrodes
D	Einstein diffusion coefficient
DPP-DTT	diketopyrrolo-pyrrole-dithiophene-thienothiophene
d	active layer thickness
D*A	excited donor:acceptor state
D^+A^-	charge transferred donor:acceptor state
$d_{\mathrm{f\,(s)}}$	distance of faster (slower) carrier to the interface
e	elementary charge,
E	electric field
EA_A	acceptor electron affinity
EA	electron affinity
EL	Electroluminescence
EQE	external quantum efficiency
E_A	electro-absorption amplitude
E_b^{EX}	exciton binding energy
E_C	Coulombic attractive potential energy
E_{gap}	electrical bandgap
$E_{gap}^{optical}$	optical bandgap
$E_{kin,thermal}$	kinetic thermal energy
FF	fill factor

G	Gibbs free energy
HOMO	highest occupied molecular orbital
$H(r)$	enthalpy as a function of separation distance
IP_D	donor ionization potential
IP	ionization potential
IQE	internal quantum efficiency
ITO	indium tin oxide
I_{MP}	maximum power current
I_{SC}	short-circuit current
J_{MP}	maximum power current density
J_{SC}	short-circuit current density
$J_{SCL(PF)}$	space charge limited current density according to the Poole-Frenkel model
J_{SCL}	Space charge limited current density
JV	current-density vs. voltage
K	equilibrium constant for charge separation
k	absorption coefficient
k_B	Boltzmann constant
k_{bulk}	(actual) bimolecular recombiantion rate coefficient (cm^3s^{-1})
k_d	charge-transfer dissociation rate constant
$k_{diff(EX)}$	exciton diffusion rate constant
k_f	recombination rate coefficient of the charge-transfer state to the ground state
k_L	Langevin recombination rate coefficient
k_m	free carrier encounter rate coefficient
k_r	recombination rate coefficient from the charge-separated to charge-transfer state
k_{slower}	slower carrier dependent recombination rate coefficient
k_{ij}	hopping rate between sites *i* and *j*
LUMO	lowest unoccupied molecular orbital
MDMO-PPV	Poly[2-methoxy-5-(3′,7′-dimethyloctyloxy)-1,4-phenylenevinylene]

L_{D}	exciton diffusion length
n	electron density
$N(E)$	charge-transfer state emission spectra as measured by EL
n_{r}	refractive index
n_{CT} (n_{CS})	population of the charge-transfer (charge-separated) state
OFET	field effect transistors
OLED	organic light emitting diodes
OPD	organic photodetector
OPV	organic photovoltaics
OSC	organic solar cell
p	hole density
PC70BM	[6,6]-phenyl-C_{70}-butyric acid methyl ester
PCDTBT	poly[*N*-9”-heptadecanyl-2,7-carbazole-*alt*-5,5-(4’,7’-di-2-thienyl-2’,1’,3’-benzothiadiazole
PCE	power conversion efficiency
PDS	photothermal deflection spectroscopy
photo-CELIV	photogenerated charge extraction using linearly increasing voltage
PL	Photoluminescence
PV	photovoltaic
P_{light}	power of the incoming light
P_{SC}	electrical power produced by the solar cell
r	carrier distance
R	recombination rate ($cm^{-3}s^{-1}$)
$R(\lambda)$	reflectance spectra
rr-P3HT	regio-regular-Poly(3-hexylthiophene-2,5-diyl
$R_{\mathrm{CS-CT}}$	rate from CS to CT
$R_{\mathrm{CT-CS}}$	rate from CT to CS
r_{c}	Coulomb capture or Onsager radius
r_{ij}	distance between sites *i* and *j*
SCLC	Space charge limited current
S_1	energy of the lowest lying singlet polymer exciton
$S_{\mathrm{A\ (B)}}$	energy of the lowest lying singlet exciton of polymer A (polymer B)

T	temperature.
$T(\lambda)$	transmission spectra
TAS	transient absorption spectroscopy
t_{max}	maximum extraction time in CELIV
ToF	Time of Flight
TRMC	transient Microwave Conductivity
TWy	terrawatt-years
t_{tr}	charge carrier transit time
t_{ij}	hopping time between sites *i* and *j*
U	effective driving voltage
U_{BI}	built-in voltage
v	charge carrier velocity
V_{MP}	maximum power voltage
V_{OC}	open-circuit voltage
v_0	phonon vibration frequency or the jump-attempt rate
v_{ij}	hopping velocity between sites *i* and *j*
ZnOOEP	Zinc octakis (B—octyloxyethyl) porphyrin

Greek symbols and abbreviations

α	light absorption coefficient
γ	the inverse localization radius
γ_{CT}	reduction factor due to finite charge-transfer state recombination probability
γ_{enc}	reduction factor due to encounter limited recombination
γ_{L}	reduction factor of the bimolecular recombination rate coefficient
γ_{PF}	electric field dependence factor of the mobility according to the Poole-Frenkel model
$\Delta E_{\mathrm{CS}}^{\mathrm{A}}$	energetic driving force for separation
ΔG_{B}	Gibbs free energy barrier
ΔE	Coulomb binding energy
ΔG	change in the Gibbs free energy
$\Delta P/P$	relative change in microwave power

δ_{EA}	energy level offset between donor and acceptor electron affinities
ϵ_{ij}	energy between sites *i* and *j*
ε_0	vacuum permittivity
ε_{r}	relative dielectric constant
η_{ABS}	absorption efficiency
η_{COLL}	charge collection efficiency
η_{CT}	charge-transfer state dissociation efficiency
η_{EX}	exciton diffusion and dissociation efficiency
η_{GEN}	charge generation efficiency
λ	reorganization energy
μ	charge carrier mobility
μ_0	zero field mobility
$\mu_{\mathrm{e(h)}}$	electron (hole) mobility
$\mu_{\mathrm{f(s)}}$	faster (slower) carrier mobility
τ	charge carrier lifetime
$\tau_{\mathrm{e\ (h)}}$	electron (hole) lifetime
σ	electrical conductivity
σ_{r}	recombination cross section
$\varphi(\lambda)$	air mass 1.5 global (AM1.5G) solar spectrum with 100 mW/cm^2
$\Omega(r)$	electron-hole configurations as a function of separation distance

Bibliography

[1] Renewables 2015 global status report. Technical report, Renewable Energy Policy Network for the 21st Centruy, 2015. URL: http://www.ren21.net/wp-content/uploads/2015/07/-GSR2015_KeyFindings_lowres.pdf (accessed 22.04.2016).

[2] Key world energy statistics. Technical report, International Energy Agency, 2015. URL: https://www.iea.org/publications/freepublications/publication/KeyWorld_Statistics_2015.pdf (accessed 22.04.2016).

[3] Tsao, N. Lewis, and G. Crabtree. Solar faqs. Technical report, U.S. Department of Energy, Office of Basic Energy Science, 2006. URL: http://www.sandia.gov/~jytsao/-Solar%20FAQs.pdf (accessed 22.04.2016).

[4] Lang, M. and Lang, A., The 2014 german renewable energy sources act revision - from feed-in tariffs to direct marketing to competitive bidding. *Journal of Energy & Natural Resources Law* **33**, (2015), 131–146.

[5] BP statistical review of world energy. Technical report, British Petroleum Company, 2015. URL: https://www.bp.com/content/dam/bp/pdf/energy-economics/statistical-review-2015/bp-statistical-review-of-world-energy-2015-full-report.pdf (accessed 22.04.2016).

[6] Perez, R. and Perez, M., A fundamental look at supply side energy reserves for the planet. *The International Energy Agency SHC Programme Solar Update* **62**, (2015), 4–6.

[7] Masuko, K., et al., Achievement of more than 25%; conversion efficiency with crystalline silicon heterojunction solar cell. *IEEE Journal of Photovoltaics* **4**, (2014), 1433–1435.

[8] Zhao, J., Wang, A., and Green, M. A., 24.5% Efficiency silicon PERT cells on MCZ substrates and 24.7% efficiency PERL cells on FZ substrates. *Progress in Photovoltaics: Research and Applications* **7**, (1999), 471–474.

[9] Silicon fabrication processing techniques. URL: http://www.sumcosi.com/english/-products/process/step_01.html (accessed 22.04.2016).

[10] Photovoltaics report. Technical report, Fraunhofer Institute for Solar Energy Systems, ISE, 2016. URL: https://www.ise.fraunhofer.de/de/downloads/pdf-files/aktuelles/-photovoltaics-report-in-englischer-sprache.pdf (accessed 22.04.2016).

[11] Tiedje, T., Yablonovitch, E., Cody, G., and Brooks, B., Limiting efficiency of silicon solar cells. *IEEE Transactions on Electron Devices* **31**, (1984), 711–716.

[12] Richter, A., Hermle, M., and Glunz, S., Reassessment of the limiting efficiency for crystalline silicon solar cells. *IEEE Journal of Photovoltaics* **3**, (2013), 1184–1191.

[13] Green, M. A., Emery, K., Hishikawa, Y., Warta, W., and Dunlop, E. D., Solar cell efficiency tables (version 46). *Progress in Photovoltaics: Research and Applications* **23**, (2015), 805–812.

[14] Sariciftci, N. S., Smilowitz, L., Heeger, A. J., and Wudl, F., Photoinduced electron transfer from a conducting polymer to buckminsterfullerene. *Science* **258**, (1992), 1474–1476.

[15] Jingbo Zhao, et al., Efficient organic solar cells processed from hydrocarbon solvents. *Nature Energy* **1**, (2016), 1–7.

[16] Konstantatos, G. and Sargent, E. H., Nanostructured materials for photon detection. *Nature Nanotechnology* **5**, (2010), 391–400.

[17] Lin, Q., Burn, P. L., Armin A., and Meredith, P., Filterless narrowband visible photodetectors. *Nature Photonics* **9**, (2015), 687–694.

[18] Li, S. S. and Thurber, W. R., The dopant density and temperature dependence of electron mobility and resistivity in n-type silicon. *Solid-State Electronics* **20**, (1977), 609 – 616.

[19] Gao, F. and Inganäs, O., Charge generation in polymer-fullerene bulk-heterojunction solar cells. *Physical Chemistry Chemical Physics* **16**, (2014), 20291–20304.

[20] Sze, S. (1985) *Semiconductor devices, physics and technology*. Wiley.

[21] Thompson, B. C. and Frechet, J. M. J., Polymer-fullerene composite solar cells. *Angewandte Chemie International Edition* **47**, (2008), 58–77.

[22] Koster, L. J. A., Shaheen, S. E., and Hummelen, J. C., Pathways to a new efficiency regime for organic solar cells. *Advanced Energy Materials* **2**, (2012), 1246–1253.

[23] Armin, A., Kassal, I., Shaw, P. E., Hambsch, M., Stolterfoht, M., Lyons, D. M., Li, J., Shi, Z., Burn, P. L., and Meredith, P., Spectral dependence of the internal quantum efficiency of organic solar cells: Effect of charge generation pathways. *Journal of the American Chemical Society* **136**, (2014), 11465–11472.

[24] Dang, M. T., Hirsch, L., and Wantz, G., P3HT:PCBM, best seller in polymer photovoltaic research. *Advanced Materials* **23**, (2011), 3597–3602.

[25] Moon, J. S., Jo, J., and Heeger, A. J., Nanomorphology of PCDTBT:PC70BM bulk heterojunction solar cells. *Advanced Energy Materials* **2**, (2012), 304–308.

[26] He, Z., Zhong, C., Su, S., Xu, M., Wu, H., and Cao, Y., Enhanced power-conversion efficiency in polymer solar cells using an inverted device structure. *Nature Photonics* **6**, (2012), 591 – 595.

[27] Shockley, W. and Queisser, H. J., Detailed balance limit of efficiency of p-n junction solar cells. *Journal of Applied Physics* **32**, (1961), 510–519.

[28] Byrnes, S. (2012). The shockley-queisser limit. http://sjbyrnes.com/sq.pdf (accessed: 31.03.2016).

[29] Byrnes, S. (2015). The shockley-queisser limit and its discontents. http://sjbyrnes.com/-shockley_queisser_talk.pdf (accessed: 31.03.2016).

[30] Li, S.-B., Duan, Y.-A., Geng, Y., Li, H.-B., Zhang, J.-Z., Xu, H.-L., Zhang, M., and Su, Z.-M., A designed bithiopheneimide-based conjugated polymer for organic photovoltaic with ultrafast charge transfer at donor/PC71BM interface: theoretical study and characterization. *Physical Chemistry Chemical Physics* **16**, (2014), 25799–25808.

[31] Burke, T. M., Sweetnam, S., Vandewal, K., and McGehee, M. D., Beyond langevin recombination: How equilibrium between free carriers and charge transfer states determines the open-circuit voltage of organic solar cells. *Advanced Energy Materials* **5**, (2015), 1500123.

[32] Reinhardt, J., Grein, M., Bühler, C., Schubert, M., and Würfel, U., Identifying the impact of surface recombination at electrodes in organic solar cells by means of electroluminescence and modeling. *Advanced Energy Materials* **4**, (2014), 1400081.

[33] Sandberg, O. J., Nyman, M., and Österbacka, R., Effect of contacts in organic bulk heterojunction solar cells. *Physical Review Applied* **1**, (2014), 024003.

[34] Palik, E. D. (1985) *Handbook of Optical Constants of Solids*. Academic Press, NY.

[35] Armin, A., Velusamy, M., Wolfer, P., Zhang, Y., Burn, P. L., Meredith, P., and Pivrikas, A., Quantum efficiency of organic solar cells: Electro-optical cavity considerations. *ACS Photonics* **1**, (2014), 173–181.

[36] Peumans, P., Yakimov, A., and Forrest, S. R., Small molecular weight organic thin-film photodetectors and solar cells. *Journal of Applied Physics* **93**, (2003), 3693–3723.

[37] Miller, A. and Abrahams, E., Impurity conduction at low concentrations. *Physical Review* **120**, (1960), 745–755.

[38] Tessler, N., Preezant, Y., Rappaport, N., and Roichman, Y., Charge transport in disordered organic materials and its relevance to thin-film devices: A tutorial review. *Advanced Materials* **21**, (2009), 2741–2761.

[39] Rauh, D., Deibel, C., and Dyakonov, V., Charge density dependent nongeminate recombination in organic bulk heterojunction solar cells. *Advanced Functional Materials* **22**, (2012), 3371–3377.

[40] Cowan, S. R., Leong, W. L., Banerji, N., Dennler, G., and Heeger, A. J., Identifying a threshold impurity level for organic solar cells: Enhanced first-order recombination via well-

defined PC84BM traps in organic bulk heterojunction solar cells. *Advanced Functional Materials* **21**, (2011), 3083–3092.

[41] Credgington, D. and Durrant, J. R., Insights from transient optoelectronic analyses on the open-circuit voltage of organic solar cells. *The Journal of Physical Chemistry Letters* **3**, (2012), 1465–1478.

[42] Onsager, L., Initial recombination of ions. *Physical Review* **54**, (1938), 554–557.

[43] Langevin, P., Recombinaison et mobilités des ions dans les gaz. *Ann. Chim. Phys.* **28**, (1903), 433.

[44] Wolf, K., Bartczak, W., and Lodz Technical University (2001) *Dynamics of Diffusion-Controlled Recombination of Ions in Ionic Solutions. Limits of Validity of the Debye - Smoluchowski Equation*. Defense Technical Information Center.

[45] Smoluchowski, M., Versuch einer mathematischen theorie der koagulationskinetik kolloider loeschungen. *Zeitschrift für physikalische Chemie* **92**, (1917), 92–129.

[46] Debye, P., Reaction rates in ionic solution. *Journal of the Electrochemical Society* **72**, (1942), 265-272.

[47] Agarwal, A. (2014) *Simulation Studies of Recombination Kinetics and Spin Dynamics in Radiation Chemistry*, chap. Theory of Scavenging and Recombination Kinetics, 23–59. Springer International Publishing.

[48] Armin, A., Velusamy, M., Burn, P. L., Meredith, P., and Pivrikas, A., Injected charge extraction by linearly increasing voltage for bimolecular recombination studies in organic solar cells. *Applied Physics Letters* **101**, (2012), 083306.

[49] Philippa, B., Stolterfoht, M., White, R. D., Velusamy, M., Burn, P. L., Meredith, P., and Pivrikas, A., Molecular weight dependent bimolecular recombination in organic solar cells. *The Journal of Chemical Physics* **141**, (2014), 054903.

[50] Wetzelaer, G.-J. A. H., Van der Kaap, N. J., Koster, L. J. A., and Blom, P. W. M., Quantifying Bimolecular Recombination in Organic Solar Cells in Steady State. *Advanced Energy Materials* **3**, (2013), 1130–1134.

[51] Pope, M. and Swenberg, C. (1999) *Electronic processes in organic crystals and polymers* 2nd ed., Oxford University Press.

[52] Armin, A., Juška, G., Philippa, B. W., Burn, P. L., Meredith, P., White, R. D., and Pivrikas, A., Doping-induced screening of the built-in-field in organic solar cells: Effect on charge transport and recombination. *Advanced Energy Materials* **3**, (2013), 321–327.

[53] Pivrikas, A., Sariciftci, N. S., Juška, G., and Österbacka, R., A review of charge transport and recombination in polymer/fullerene organic solar cells. *Progress in Photovoltaics: Research and Applications* **15**, (2007), 677–696.

[54] Stolterfoht, M., Philippa, B., Armin, A., Pandey, A. K., White, R. D., Burn, P. L., Meredith, P., and Pivrikas, A., Advantage of suppressed non-langevin recombination in low mobility organic solar cells. *Applied Physics Letters* **105**, (2014), 013302.

[55] Nyman, M., Sandberg, O. J., and Österbacka, R., 2d and trap-assisted 2d langevin recombination in polymer:fullerene blends. *Advanced Energy Materials* **5**, (2015), 1400890.

[56] Obarowska, M. and Godlewski, J., Electric field dependence of the bimolecular recombination rate of the charge carriers. *Synthetic Metals* **109**, (2000), 219 – 222.

[57] Koster, L. J. A., Mihailetchi, V. D., and Blom, P. W. M., Bimolecular recombination in polymer/fullerene bulk heterojunction solar cells. *Applied Physics Letters* **88**, (2006), 052104.

[58] Koster, L. J. A., Mihailetchi, V. D., and Blom, P. W. M., Bimolecular recombination in polymer/fullerene bulk heterojunction solar cells. *Applied Physics Letters* **88**, (2006), 052104.

[59] Heiber, M. C., Baumbach, C., Dyakonov, V., and Deibel, C., Encounter-limited charge-carrier recombination in phase-separated organic semiconductor blends. *Physical Review Letters* **114**, (2015), 136602.

[60] Gélinas, S., Rao, A., Kumar, A., Smith, S. L., Chin, A. W., Clark, J., van der Poll, T. S., Bazan, G. C., and Friend, R. H., Ultrafast long-range charge separation in organic semiconductor photovoltaic diodes. *Science* **343**, (2014), 512–516.

[61] Marcus, R. A., On the theory of oxidation-reduction reactions involving electron transfer. 1. *The Journal of Chemical Physics* **24**, (1956), 966–978.

[62] Hush, N. S., Adiabatic theory of outer sphere electron-transfer reactions in solution. *Transactions of the Faraday Society* **57**, (1961), 557–580.

[63] Marcus, R. A., Electron transfer reactions in chemistry. Theory and experiment. *Reviews of Modern Physics* **65**, (1993), 599–610.

[64] Coffey, D. C., Larson, B. W., Hains, A. W., Whitaker, J. B., Kopidakis, N., Boltalina, O. V., Strauss, S. H., and Rumbles, G., An optimal driving force for converting excitons into free carriers in excitonic solar cells. *The Journal of Physical Chemistry C* **116**, (2012), 8916–8923.

[65] Bakulin, A. A., Rao, A., Pavelyev, V. G., van Loosdrecht, P. H. M., Pshenichnikov, M. S., Niedzialek, D., Cornil, J., Beljonne, D., and Friend, R. H., The role of driving energy

and delocalized states for charge separation in organic semiconductors. *Science* **335**, (2012), 1340–1344.

[66] Braun, C. L., Electric field assisted dissociation of charge transfer states as a mechanism of photocarrier production. *The Journal of Chemical Physics* **80**, (1984), 4157–4161.

[67] Etzold, F., Howard, I. A., Mauer, R., Meister, M., Kim, T.-D., Lee, K.-S., Baek, N. S., and Laquai, F., Ultrafast exciton dissociation followed by nongeminate charge recombination in pcdtbt:pcbm photovoltaic blends. *Journal of the American Chemical Society* **133**, (2011), 9469–9479.

[68] Vithanage, D. A., et al., Visualizing charge separation in bulk heterojunction organic solar cells. *Nat. Commun.* **4**, (2013), 2334.

[69] Savenije, T. J., Ferguson, A. J., Kopidakis, N., and Rumbles, G., Revealing the dynamics of charge carriers in polymer:fullerene blends using photoinduced time-resolved microwave conductivity. *The Journal of Physical Chemistry C* **117**, (2013), 24085–24103.

[70] Juška, G., Arlauskas, K., Viliunas, M., Genevius, K., Österbacka, R., and Stubb, H., Charge transport in pi-conjugated polymers from extraction current transients. *Physical Review B - Condensed Matter and Materials Physics* **62**, (2000), R16235–R16238.

[71] Goh, C., Kline, R. J., McGehee, M. D., Kadnikova, E. N., and Fréchet, J. M. J., Molecular-weight-dependent mobilities in regioregular poly(3-hexyl-thiophene) diodes. *Applied Physics Letters* **86**, (2005), 122110.

[72] Malliaras, G. G., Salem, J. R., Brock, P. J., and Scott, C., Electrical characteristics and efficiency of single-layer organic light-emitting diodes. *Physical Review B* **58**, (1998), R13411–R13414.

[73] Mihailetchi, V., Xie, H., de Boer, B., Koster, L., and Blom, P., Charge transport and photocurrent generation in poly(3-hexylthiophene): Methanofullerene bulk-heterojunction solar cells. *Advanced Functional Materials* **16**, (2006), 699–708.

[74] Mott, N. F. and Gurney, R. W. (1948) Oxford University Press, London.

[75] Lampert, M. A. and Mark, P. (1970) *Current Injection in Solids*. Academic Press, New York and London.

[76] Blakesley, J. C., Castro, F. A., Kylberg, W., Dibb, G. F., Arantes, C., Valaski, R., Cremona, M., Kim, J. S., and Kim, J.-S., Towards reliable charge-mobility benchmark measurements for organic semiconductors. *Organic Electronics* **15**, (2014), 1263 – 1272.

[77] Frenkel, J., On pre-breakdown phenomena in insulators and electronic semi-conductors. *Physical Review* **54**, (1938), 647–648.

[78] Clarke, T. M., Peet, J., Nattestad, A., Drolet, N., Dennler, G., Lungenschmied, C., Leclerc, M., and Mozer, A. J., Charge carrier mobility, bimolecular recombination and trapping in polycarbazole copolymer:fullerene (PCDTBT:PCBM) bulk heterojunction solar cells. *Organic Electronics* **13**, (2012), 2639 – 2646.

[79] Kim, Y., Cook, S., Choulis, S. A., Nelson, J., Durrant, J. R., and Bradley, D. D. C., Organic photovoltaic devices based on blends of regioregular poly(3-hexylthiophene) and poly(9,9-dioctylfluorene-co-benzothiadiazole). *Chemistry of Materials* **16**, (2004), 4812–4818.

[80] Kline, R. J. and McGehee, M. D., Morphology and charge transport in conjugated polymers. *Journal of Macromolecular Science, Part C: Polymer Reviews* **46**, (2006), 27–45.

[81] Campoy-Quiles, M., Ferenczi, T., Agostinelli, T., Etchegoin, P. G., Kim, Y., Anthopoulos, T. D., Stavrinou, P. N., Bradley, D. D. C., and Nelson, J., Morphology evolution via self-organization and lateral and vertical diffusion in polymer:fullerene solar cell blends. *Nature Materials* **7**, (2008), 158–164.

[82] Kline, R., McGehee, M., Kadnikova, E., Liu, J., and Fréchet, J., Controlling the field-effect mobility of regioregular polythiophene by changing the molecular weight. *Advanced Materials* **15**, (2003), 1519–1522.

[83] Nekrašas, N., Genevicius, K., Viliunas, M., and Juška, G., Features of current transients of photogenerated charge carriers, extracted by linearly increased voltage. *Chemical Physics* **404**, (2012), 56 – 59.

[84] Juška, G., Nekrašas, N., Valentinavicius, V., Meredith, P., and Pivrikas, A., Extraction of photogenerated charge carriers by linearly increasing voltage in the case of langevin recombination. *Physical Review B* **84**, (2011), 155202.

[85] Baran, D., Li, N., Breton, A.-C., Osvet, A., Ameri, T., Leclerc, M., and Brabec, C. J., Qualitative analysis of bulk-heterojunction solar cells without device fabrication: An elegant and contactless method. *Journal of the American Chemical Society* **136**, (2014), 10949–10955.

[86] Scharber, M. C., Lungenschmied, C., Egelhaaf, H.-J., Matt, G., Bednorz, M., Fromherz, T., Gao, J., Jarzab, D., and Loi, M. A., Charge transfer excitons in low band gap polymer based solar cells and the role of processing additives. *Energy & Environmental Science* **4**, (2011), 5077–5083.

[87] Tvingstedt, K., Vandewal, K., Gadisa, A., Zhang, F., Manca, J., and Inganäs, O., Electroluminescence from charge transfer states in polymer solar cells. *Journal of the American Chemical Society* **131**, (2009), 11819–11824.

[88] Dimitrov, S. D. and Durrant, J. R., Materials design considerations for charge generation in organic solar cells. *Chemistry of Materials* **26**, (2014), 616–630.

[89] Vandewal, K., et al., Efficient charge generation by relaxed charge-transfer states at organic interfaces. *Nature Materials* **13**, (2014), 63–68.

[90] Albrecht, S., Vandewal, K., Tumbleston, J. R., Fischer, F. S. U., Douglas, J. D., Fréchet, J. M. J., Ludwigs, S., Ade, H., Salleo, A., and Neher, D., On the efficiency of charge transfer state splitting in polymer:fullerene solar cells. *Advanced Materials* **26**, (2014), 2533–2539.

[91] Kniepert, J., Schubert, M., Blakesley, J. C., and Neher, D., Photogeneration and recombination in P3HT/PCBM solar cells probed by time-delayed collection field experiments. *The Journal of Physical Chemistry Letters* **2**, (2011), 700–705.

[92] Mauer, R., Howard, I. A., and Laquai, F., Effect of external bias on nongeminate recombination in polythiophene/methanofullerene organic solar cells. *The Journal of Physical Chemistry Letters* **2**, (2011), 1736–1741.

[93] Foertig, A., Kniepert, J., Gluecker, M., Brenner, T., Dyakonov, V., Neher, D., and Deibel, C., Nongeminate and geminate recombination in PTB7:PCBM solar cells. *Advanced Functional Materials* **24**, (2014), 1306.

[94] Dibb, G. F. A., Jamieson, F. C., Maurano, A., Nelson, J., and Durrant, J. R., Limits on the fill factor in organic photovoltaics: Distinguishing nongeminate and geminate recombination mechanisms. *The Journal of Physical Chemistry Letters* **4**, (2013), 803–808.

[95] Devižis, A., Jonghe-Risse, J. D., Hany, R., NÃ¼esch, F., Jenatsch, S., Gulbinas, V., and Moser, J.-E., Dissociation of charge transfer states and carrier separation in bilayer organic solar cells: A time-resolved electroabsorption spectroscopy study. *Journal of the American Chemical Society* **137**, (2015), 8192–8198.

[96] Bernardo, B., Cheyns, D., Verreet, B., Schaller, R., Rand, B., and Giebink, N., Delocalization and dielectric screening of charge transfer states in organic photovoltaic cells. *Nature Communications* **5**, (2014), 3245.

[97] Shoaee, S., An, Z., Zhang, X., Barlow, S., Marder, S. R., Duffy, W., Heeney, M., McCulloch, I., and Durrant, J. R., Charge photogeneration in polythiophene-perylene diimide blend films. *Chemical Communications* **26**, (2009), 5445–5447.

[98] Gregg, B. A., Entropy of charge separation in organic photovoltaic cells: The benefit of higher dimensionality. *The Journal of Physical Chemistry Letters* **2**, (2011), 3013–3015.

[99] Monahan, N. R., Williams, K. W., Kumar, B., Nuckolls, C., and Zhu, X.-Y., Direct observation of entropy-driven electron-hole pair separation at an organic semiconductor interface. *Physical Review Letters* **114**, (2015), 247003.

[100] Clarke, T. M. and Durrant, J. R., Charge photogeneration in organic solar cells. *Chemical Reviews* **110**, (2010), 6736 – 6767.

[101] van der Horst, J.-W., Bobbert, P. A., Michels, M. A. J., and Bässler, H., Calculation of excitonic properties of conjugated polymers using the bethe-salpeter equation. *The Journal of Chemical Physics* **114**, (2001), 6950–6957.

[102] Donaghey, J. E., Armin, A., Burn, P. L., and Meredith, P., Dielectric constant enhancement of non-fullerene acceptors via side-chain modification. *Chemical Communications* **51**, (2015), 14115–14118.

[103] Li, J., et al., A stable solution-processed polymer semiconductor with record high-mobility for printed transistors. *Scientific Reports* **2**, (2012), 754.

[104] Philippa, B., Stolterfoht, M., Burn, P. L., Juska, G., Meredith, P., White, R. D., and Pivrikas, A., The impact of hot charge carrier mobility on photocurrent losses in polymer-based solar cells. *Scientific Reports* **4**, (2014), 1–8.

[105] Armin, A., et al., Simultaneous enhancement of charge generation quantum yield and carrier transport in organic solar cells. *Journal of Materials Chemistry C* **3**, (2015), 10799–10812.

[106] Tandy, K., Dutta, G. K., Zhang, Y., Venkatramaiah, N., Aljada, M., Burn, P. L., Meredith, P., Namdas, E. B., and Patil, S., A new diketopyrrolopyrrole-based co-polymer for ambipolar field-effect transistors and solar cells. *Organic Electronics* **13**, (2012), 1981 – 1988.

[107] Armin, A., Juska, G., Ullah, M., Velusamy, M., Burn, P. L., Meredith, P., and Pivrikas, A., Balanced carrier mobilities: Not a necessary condition for high-efficiency thin organic solar cells as determined by mis-celiv. *Advanced Energy Materials* **4**, (2014), 1300954.

[108] Jailaubekov, A. E., et al., Hot charge-transfer excitons set the time limit for charge separation at donor/acceptor interfaces in organic photovoltaics. *Nature Materials* **12**, (2013), 66–73.

[109] Grancini, G., Maiuri, M., Fazzi, D., Petrozza, A., Egelhaaf, H.-J., Brida, D., Cerullo, G., and Lanzani, G., Hot exciton dissociation in polymer solar cells. *Nature Materials* **12**, (2013), 29–33.

[110] Heeger, A. J., 25th anniversary article: Bulk heterojunction solar cells: understanding the mechanism of operation. *Advanced Materials* **26**, (2014), 10–27.

[111] Blom, P. and Vissenberg, M., Charge transport in poly(p-phenylene vinylene) light-emitting diodes. *Materials Science and Engineering: R: Reports* **27**, (2000), 53–94.

[112] Bässler, H., Charge Transport in Disordered Organic Photoconductors a Monte Carlo Simulation Study. *Physica Status Solidi (B)* **175**, (1993), 15–56.

[113] Howard, I. A., Etzold, F., Laquai, F., and Kemerink, M., Nonequilibrium Charge Dynamics in Organic Solar Cells. *Advanced Energy Materials* **4**, (2014), 1301743.

[114] Melianas, A., Pranculis, V., Devižis, A., Gulbinas, V., Inganäs, O., and Kemerink, M., Dispersion-Dominated Photocurrent in Polymer:Fullerene Solar Cells. *Advanced Functional Materials* **24**, (2014), 4507–4514.

[115] Street, R., Song, K., Northrup, J., and Cowan, S., Photoconductivity measurements of the electronic structure of organic solar cells. *Physical Review B* **83**, (2011), 1–13.

[116] Seifter, J., Sun, Y., and Heeger, A. J., Transient photocurrent response of small-molecule bulk heterojunction solar cells. *Advanced Materials* **26**, (2014), 2486.

[117] Scher, H. and Montroll, E., Anomalous transit-time dispersion in amorphous solids. *Physical Review B* **12**, (1975), 2455–2477.

[118] Baranovskii, S., Cordes, H., Hensel, F., and Leising, G., Charge-carrier transport in disordered organic solids. *Physical Review B* **62**, (2000), 7934–7938.

[119] Schönherr, G., Bässler, H., and Silver, M., Dispersive hopping transport via sites having a Gaussian distribution of energies. *Philosophical Magazine Part B* **44**, (1981), 47–61.

[120] Österbacka, R., Pivrikas, A., Juška, G., Genevicius, K., Arlauskas, K., and Stubb, H., Mobility and density relaxation of photogenerated charge carriers in organic materials. *Current Applied Physics* **4**, (2004), 534–538.

[121] Novikov, S., Dunlap, D., Kenkre, V., Parris, P., and Vannikov, A., Essential role of correlations in governing charge transport in disordered organic materials. *Physical Review Letters* **81**, (1998), 4472–4475.

[122] Pasveer, W., Cottaar, J., Tanase, C., Coehoorn, R., Bobbert, P., Blom, P., de Leeuw, D., and Michels, M., Unified description of charge-carrier mobilities in disordered semiconducting polymers. *Physical Review Letters* **94**, (2005), 206601.

[123] Fishchuk, I. I., Kadashchuk, A., Hoffmann, S. T., Athanasopoulos, S., Genoe, J., Bässler, H., and Köhler, A., Unified description for hopping transport in organic semiconductors including both energetic disorder and polaronic contributions. *Physical Review B* **88**, (2013), 125202.

[124] Tiedje, T. and Rose, A., A physical interpretation of dispersive transport in disordered semiconductors. *Solid State Communications* **37**, (1980), 49–52.

[125] Jakobs, A. and Kehr, K. W., Theory and simulation of multiple-trapping transport through a finite slab. *Physical Review B* **48**, (1993), 8780–8789.

[126] Schubert, M., Preis, E., Blakesley, J. C., Pingel, P., Scherf, U., and Neher, D., Mobility relaxation and electron trapping in a donor/acceptor copolymer. *Physical Review B* **87**, (2013), 024203.

[127] Street, R. A., Krakaris, A., and Cowan, S. R., Recombination through different types of localized states in organic solar cells. *Advanced Functional Materials* **22**, (2012), 4608–4619.

[128] Shuttle, C. G., Hamilton, R., Nelson, J., O'Regan, B. C., and Durrant, J. R., Measurement of charge-density dependence of carrier mobility in an organic semiconductor blend. *Advanced Functional Materials* **20**, (2010), 698–702.

[129] Park, S. H., Roy, A., Beaupre, S., Cho, S., Coates, N., Moon, J. S., Moses, D., Leclerc, M., Lee, K., and Heeger, A. J., Bulk heterojunction solar cells with internal quantum efficiency approaching 100%. *Nature Photonics* **3**, (2009), 297–302.

[130] Baumann, A., Lorrmann, J., Rauh, D., Deibel, C., and Dyakonov, V., A new approach for probing the mobility and lifetime of photogenerated charge carriers in organic solar cells under real operating conditions. *Advanced Materials* **24**, (2012), 4381–4386.

[131] Liang, Y., Xu, Z., Xia, J., Tsai, S.-T., Wu, Y., Li, G., Ray, C., and Yu, L., For the bright future - bulk heterojunction polymer solar cells with power conversion efficiency of 7.4%. *Adv. Mater.* **22**, (2010), E135–E138.

[132] Li, Z., Lakhwani, G., Greenham, N. C., and McNeill, C. R., Voltage-dependent photocurrent transients of PTB7:PC70BM solar cells: Experiment and numerical simulation. *J. Appl. Phys.* **114**, (2013), 034502.

[133] Wakim, S., Beaupre, S., Blouin, N., Aich, B.-R., Rodman, S., Gaudiana, R., Tao, Y., and Leclerc, M., Highly efficient organic solar cells based on a poly(2,7-carbazole) derivative. *J. Mater. Chem.* **19**, (2009), 5351–5358.

[134] Nicolai, H. T., Kuik, M., Wetzelaer, G. A. H., de Boer, B., Campbell, C., Risko, C., Brédas, J. L., and Blom, P. W. M., Unification of trap-limited electron transport in semiconducting polymers. *Nature Materials* **11**, (2012), 882–887.

[135] Armin, A., Zhang, Y., Burn, P. L., Meredith, P., and Pivrikas, A., Measuring internal quantum efficiency to demonstrate hot exciton dissociation. *Nat. Mater.* **12**, (2013), 593–593.

[136] Cunningham, P. D. and Hayden, L. M., Carrier Dynamics Resulting from Above and Below Gap Excitation of P3HT and P3HT/PCBM Investigated by Optical-Pump Terahertz-Probe Spectroscopy. *The Journal of Physical Chemistry C* **112**, (2008), 7928–7935.

[137] Chan, K. K., Tsang, S., Lee, H. K., So, F., and So, S., Charge injection and transport studies of poly(2,7-carbazole) copolymer PCDTBT and their relationship to solar cell performance. *Organic Electronics* **13**, (2012), 850–855.

[138] Koster, L. J. A., Smits, E. C. P., Mihailetchi, V. D., and Blom, P. W. M., Device model for the operation of polymer/fullerene bulk heterojunction solar cells. *Physical Review B* **72**, (2005), 085205.

[139] Neukom, M., Reinke, N., and Ruhstaller, B., Charge extraction with linearly increasing voltage: A numerical model for parameter extraction. *Solar Energy* **85**, (2011), 1250–1256.

[140] Orenstein, J. and Kastner, M., Photocurrent Transient Spectroscopy: Measurement of the Density of Localized States in a-As2Se3. *Physical Review Letters* **46**, (1981), 1421–1424.

[141] Staniec, P. A., et al., The Nanoscale Morphology of a PCDTBT:PCBM Photovoltaic Blend. *Advanced Energy Materials* **1**, (2011), 499–504.

[142] Pettersson, L. A. A., Roman, L. S., and Inganäs, O., Modeling photocurrent action spectra of photovoltaic devices based on organic thin films. *Journal of Applied Physics* **86**, (1999), 487.

[143] Sun, Y., Takacs, C. J., Cowan, S. R., Seo, J. H., Gong, X., Roy, A., and Heeger, A. J., Efficient, air-stable bulk heterojunction polymer solar cells using MoO(x) as the anode interfacial layer. *Advanced Materials* **23**, (2011), 2226.

[144] Hecht, K., Zum mechanismus des lichtelektrischen primaerstromes in isolierenden kristallen. *Zeitschrift fuer Physik* **77**, (1932), 235–245.

[145] Schubert, E. (2006) *Light-Emitting Diodes*. Proceedings of SPIE - The International Society for Optical Engineering, Cambridge University Press.

[146] Vijila, C., et al., Relation between charge carrier mobility and lifetime in organic photovoltaics. *Journal of Applied Physics* **114**, (2013), 184503.

[147] Poortmans, J. and Arkhipov, V. (2006) *Thin film solar cells: fabrication, characterization and applications*, vol. 5. John Wiley & Sons.

[148] Klauk, H. (2006) *Organic Electronics: Materials, Manufacturing, and Applications*. Wiley.

[149] Zang, L. (2011) *Energy Efficiency and Renewable Energy Through Nanotechnology*. Springer.

[150] Kirchartz, T., Agostinelli, T., Campoy-Quiles, M., Gong, W., and Nelson, J., Understanding the thickness-dependent performance of organic bulk heterojunction solar cells: The influence of mobility, lifetime, and space charge. *The Journal of Physical Chemistry Letters* **3**, (2012), 3470–3475.

[151] Tumbleston, J. R., Liu, Y., Samulski, E. T., and Lopez, R., Interplay between bimolecular recombination and carrier transport distances in bulk heterojunction organic solar cells. *Advanced Energy Materials* **2**, (2012), 477–486.

[152] Blouin, N., Michaud, A., and Leclerc, M., A low-bandgap poly(2,7-carbazole) derivative for use in high-performance solar cells. *Advanced Materials* **19**, (2007), 2295–2300.

[153] Huynh, W. U., Dittmer, J. J., Teclemariam, N., Milliron, D. J., Alivisatos, A. P., and Barnham, K. W. J., Charge transport in hybrid nanorod-polymer composite photovoltaic cells. *Physical Review B* **67**, (2003), 115326.

[154] He, Z., Zhong, C., Huang, X., Wong, W.-Y., Wu, H., Chen, L., Su, S., and Cao, Y., Simultaneous enhancement of open-circuit voltage, short-circuit current density, and fill factor in polymer solar cells. *Advanced Materials* **23**, (2011), 4636–4643.

[155] Lenes, M., Morana, M., Brabec, C. J., and Blom, P. W. M., Recombination-limited photocurrents in low bandgap polymer/fullerene solar cells. *Advanced Functional Materials* **19**, (2009), 1106–1111.

[156] Koster, L. J. A., Kemerink, M., Wienk, M. M., KlarÃ¡, M., and Janssen, R. A. J., Quantifying bimolecular recombination losses in organic bulk heterojunction solar cells. *Advanced Materials* **23**, (2011), 1670–1674.

[157] Verreet, B., Cnops, K., Cheyns, D., Heremans, P., Stesmans, A., Zango, G., Claessens, C. G., Torres, T., and Rand, B. P., Decreased recombination through the use of a non-fullerene acceptor in a 6.4% efficient organic planar heterojunction solar cell. *Advanced Energy Materials* **4**, (2014), 1301413.

[158] Wu, S.-h., Li, W.-l., Chu, B., Lee, C. S., Su, Z.-s., Wang, J.-b., Yan, F., Zhang, G., Hu, Z.-z., and Zhang, Z.-q., High response deep ultraviolet organic photodetector with spectrum peak focused on 280 nm. *Applied Physics Letters* **96**, (2010), 093302.

[159] Gong, X., Tong, M., Xia, Y., Cai, W., Moon, J. S., Cao, Y., Yu, G., Shieh, C.-L., Nilsson, B., and Heeger, A. J., High-detectivity polymer photodetectors with spectral response from 300 nm to 1450 nm. *Science* **325**, (2009), 1665–1667.

[160] Street, R. A., Schoendorf, M., Roy, A., and Lee, J. H., Interface state recombination in organic solar cells. *Physical Review B* **81**, (2010), 205307.

[161] Cowan, S. R., Roy, A., and Heeger, A. J., Recombination in polymer-fullerene bulk heterojunction solar cells. *Physical Review B* **82**, (2010), 245207.

[162] Cowan, S., Banerji, N., Leong, W., and Heeger, A., Charge formation, recombination, and sweep-out dynamics in organic solar cells. *Advanced Functioanl Materials* **22**, (2012), 1116–1128.

[163] Leong, W. L., Cowan, S. R., and Heeger, A. J., Differential resistance analysis of charge carrier losses in organic bulk heterojunction solar cells: Observing the transition from bimolecular to trap-assisted recombination and quantifying the order of recombination. *Advanced Energy Materials* **1**, (2011), 517–522.

[164] Mihailetchi, V. D., Wildeman, J., and Blom, P. W. M., Space-charge limited photocurrent. *Physical Review Letters* **94**, (2005), 126602.

[165] Pivrikas, A., Neugebauer, H., and Sariciftci, N., Charge carrier lifetime and recombination in bulk heterojunction solar cells. *IEEE Journal of Selected Topics in Quantum Electronics* **16**, (2010), 1746–1758.

[166] Vandewal, K., Tvingstedt, K., Gadisa, A., Inganas, O., and Manca, J. V., On the origin of the open-circuit voltage of polymer-fullerene solar cells. *Nature Materials* **8**, (2009), 904–909.

[167] Wolfer, P., Armin, A., Pivrikas, A., Velusamy, M., Burn, P. L., and Meredith, P., Solution structure: defining polymer film morphology and optoelectronic device performance. *Journal of Materials Chemistry C* **2**, (2014), 71–77.

[168] Kaur, N., Singh, M., Pathak, D., Wagner, T., and Nunzi, J., Organic materials for photovoltaic applications: Review and mechanism. *Synthetic Metals* **190**, (2014), 20–26.

[169] Heeger, A. J., Bulk heterojunction solar cells: Understanding the mechanism of operation. *Advanced Materials* **26**, (2014), 10–28.

[170] He, Z., Xiao, B., Liu, F., Wu, H., Yang, Y., Xiao, S., Wang, C., Russell, T. P., and Cao, Y., Single-junction polymer solar cells with high efficiency and photovoltage. *Nature Photonics* **9**, (2015), 174–179.

[171] Liu, Y., Zhao, J., Li, Z., Mu, C., Ma, W., Hu, H., Jiang, K., Lin, H., Ade, H., and Yan, H., Aggregation and morphology control enables multiple cases of high-efficiency polymer solar cells. *Nature Communications* **5**, (2014), 1–8.

[172] Stolterfoht, M., Armin, A., Philippa, B., White, R. D., Burn, P. L., Meredith, P., Juska, G., and Pivrikas, A., Photocarrier drift distance in organic solar cells and photodetectors. *Scientific Reports* **5**, (2015), 1–7.

[173] Credgington, D., Jamieson, F. C., Walker, B., Nguyen, T.-Q., and Durrant, J. R., Quantification of geminate and non-geminate recombination losses within a solution-processed small-molecule bulk heterojunction solar cell. *Advanced Materials* **24**, (2012), 2135–2141.

[174] Shoaee, S., Deledalle, F., Shakya Tuladhar, P., Shivanna, R., Rajaram, S., Narayan, K. S., and Durrant, J. R., A comparison of charge separation dynamics in organic blend films employing fullerene and perylene diimide electron acceptors. *Journal of Physical Chemistry Letters* **6**, (2015), 201–205.

[175] Li, Z. and McNeill, C. R., Transient photocurrent measurements of PCDTBT:PC70BM and PCPDTBT:PC70BM solar cells: Evidence for charge trapping in efficient polymer/fullerene blends. *Journal of Applied Physics* **109**, (2011), 074513.

[176] Shuttle, C. G., Maurano, A., Hamilton, R., O'Regan, B., de Mello, J. C., and Durrant, J. R., Charge extraction analysis of charge carrier densities in a polythiophene/fullerene solar cell: Analysis of the origin of the device dark current. *Applied Physics Letters* **93**, (2008), –.

[177] Balderrama, V. S., Albero, J., Granero, P., Ferre-Borrull, J., Pallares, J., Palomares, E., and Marsal, L. F., Design, fabrication and charge recombination analysis of an interdigitated heterojunction nanomorphology in P3Ht/PC70BM solar cells. *Nanoscale* **7**, (2015), 13848–13859.

[178] Guerrero, A., Fernandez-Montcada, N., Ajuria, J., Etxebarria, I., Pacios, R., Garcia-Belmonte, G., and Palomares, E. J., Charge carrier transport and contact selectivity limit the operation of ptb7-based organic solar cells of varying active layer thickness. *Journal of Materials Chemistry A* **1**, (2013), 12345–12354.

[179] Lai, T.-H., Tsang, S.-W., Manders, J. R., Chen, S., and So, F., Properties of interlayer for organic photovoltaics. *Materials Today* **16**, (2013), 424–432.

[180] Bruno, A., Reynolds, L. X., Dyer-Smith, C., Nelson, J., and Haque, S. A., Determining the exciton diffusion length in a polyfluorene from ultrafast fluorescence measurements of polymer/fullerene blend films. *The Journal of Physical Chemistry C* **117**, (2013), 19832–19838.

[181] Qi, B. and Wang, J., Fill factor in organic solar cells. *Physical Chemistry Chemical Physics* **15**, (2013), 8972–8982.

[182] Bartesaghi, D., Perez, I. d. C., Kniepert, J., Roland, S., Turbiez, M., Neher, D., and Koster, L. J. A., Competition between recombination and extraction of free charges determines the fill factor of organic solar cells. *Nature Communications* **6**, (2015), 7083.

[183] Street, R., Cowan, S., and Heeger, A., Experimental test for geminate recombination applied to organic solar cells. *Physical Review B* **82**, (2010), 11–13.

[184] Dibb, G. F. A., Kirchartz, T., Credgington, D., Durrant, J. R., and Nelson, J., Analysis of the relationship between linearity of corrected photocurrent and the order of recombination in organic solar cells. *The Journal of Physical Chemistry Letters* **2**, (2011), 2407–2411.

[185] Morteani, A. C., Sreearunothai, P., Herz, L. M., Friend, R. H., and Silva, C., Exciton regeneration at polymeric semiconductor heterojunctions. *Phys. Rev. Lett.* **92**, (2004), 247402.

[186] Offermans, T., van Hal, P. A., Meskers, S. C. J., Koetse, M. M., and Janssen, R. A. J., Exciplex dynamics in a blend of π-conjugated polymers with electron donating and accepting properties: Mdmo-ppv and pcnepv. *Physical Review B* **72**, (2005), 045213.

[187] Mihailetchi, V. D., Koster, L. J. A., Hummelen, J. C., and Blom, P. W. M., Photocurrent generation in polymer-fullerene bulk heterojunctions. *Physical Review Letters* **93**, (2004), 216601.

[188] Veldman, D., Ipek, Ö., Meskers, S. C. J., Sweelssen, J., Koetse, M. M., Veenstra, S. C., Kroon, J. M., van Bavel, S. S., Loos, J., and Janssen, R. A. J., Compositional and electric field dependence of the dissociation of charge transfer excitons in alternating polyfluorene copolymer/fullerene blends. *Journal of the American Chemical Society* **130**, (2008), 7721–7735.

[189] Li, W., Hendriks, K. H., Roelofs, W. S. C., Kim, Y., Wienk, M. M., and Janssen, R. A. J., Efficient small bandgap polymer solar cells with high fill factors for 300 nm thick films. *Advanced Materials* **25**, (2013), 3182–3186.

[190] Stickley, K. R. and Blackstock, S. C., Cation radicals of 1,3,5-tris(diarylamino)benzenes. *Tetrahedron Letters* **36**, (1995), 1585 – 1588.

[191] Stickley, K. R. and Blackstock, S. C., Triplet dication and quartet trication of a triaminobenzene. *Journal of the American Chemical Society* **116**, (1994), 11576–11577.

[192] Stolterfoht, M., Philippa, B., Shoaee, S., Jin, H., Jiang, W., White, R. D., Burn, P. L., Meredith, P., and Pivrikas, A., Charge transport without recombination in organic solar cells and photodiodes. *The Journal of Physical Chemistry C* **119**, (2015), 26866–26874.

[193] Lyons, D. M., Armin, A., Stolterfoht, M., Nagiri, R. C., van Vuuren, R. D. J., Pal, B. N., Burn, P. L., Lo, S.-C., and Meredith, P., Narrow band green organic photodiodes for imaging. *Organic Electronics* **15**, (2014), 2903 – 2911.

[194] Stolterfoht, M., Armin, A., Shoaee, S., Kassal, I., Burn, P., and Meredith, P., Slower carriers limit charge generation in organic solar cells. *Nature Communications* ***7****, (2016), 11944*.

[195] Few, S., Frost, J., and Nelson, J., Models of charge pair generation in organic solar cells. *Physical Chemistry Chemical Physics* **17**, (2015), 2311–2325.

[196] Brabec, C. J., Gowrisanker, S., Halls, J. J. M., Laird, D., Jia, S., and Williams, S. P., Polymer-fullerene bulk-heterojunction solar cells. *Advanced Materials* **22**, (2010), 3839–3856.

[197] Deotare, P. B., et al., Nanoscale transport of charge-transfer states in organic donor-acceptor blends. *Nature Materials* **14**, (2015), 1130–1134.

[198] Deibel, C., Strobel, T., and Dyakonov, V., Role of the charge transfer state in organic donor-acceptor solar cells. *Advanced Materials* **22**, (2010), 4097–4111.

[199] Mandoc, M. M., Koster, L. J. A., and Blom, P. W. M., Optimum charge carrier mobility in organic solar cells. *Applied Physics Letters* **90**, (2007), 133504.

[200] Wetzelaer, G.-J. A. H., Van der Kaap, N. J., Koster, L. J. A., and Blom, P. W. M., Quantifying bimolecular recombination in organic solar cells in steady state. *Advanced Energy Materials* **3**, (2013), 1130–1134.

[201] Shoaee, S., Clarke, T. M., Huang, C., Barlow, S., Marder, S. R., Heeney, M., McCulloch, I., and Durrant, J. R., Acceptor energy level control of charge photogeneration in organic donor/acceptor blends. *Journal of the American Chemical Society* **132**, (2010), 12919–12926.

[202] Collins, B. A., Li, Z., Tumbleston, J. R., Gann, E., McNeill, C. R., and Ade, H., Absolute measurement of domain composition and nanoscale size distribution explains performance in PTB7:PC71BM solar cells. *Advanced Energy Materials* **3**, (2013), 65–74.

[203] Jamieson, F. C., Domingo, E. B., McCarthy-Ward, T., Heeney, M., Stingelin, N., and Durrant, J. R., Fullerene crystallisation as a key driver of charge separation in polymer/fullerene bulk heterojunction solar cells. *Chemical Science* **3**, (2012), 485–492.

[204] Miller, N. C., Sweetnam, S., Hoke, E. T., Gysel, R., Miller, C. E., Bartelt, J. A., Xie, X., Toney, M. F., and McGehee, M. D., Molecular packing and solar cell performance in blends of polymers with a bisadduct fullerene. *Nano Letters* **12**, (2012), 1566–1570.

[205] Sharenko, A., Gehrig, D., Laquai, F., and Nguyen, T.-Q., The effect of solvent additive on the charge generation and photovoltaic performance of a solution-processed small molecule:perylene diimide bulk heterojunction solar cell. *Chemistry of Materials* **26**, (2014), 4109–4118.

[206] Keivanidis, P. E., Clarke, T. M., Lilliu, S., Agostinelli, T., Macdonald, J. E., Durrant, J. R., Bradley, D. D. C., and Nelson, J., Dependence of charge separation efficiency on film microstructure in poly(3-hexylthiophene-2,5-diyl):[6,6]-phenyl-c61 butyric acid methyl ester blend films. *The Journal of Physical Chemistry Letters* **1**, (2010), 734–738.

[207] Mihailetchi, V., Koster, L., Blom, P., Melzer, C., de Boer, B., van-Duren, J., and Janssen, R., Compositional dependence of the performance of poly(p-phenylene vinylene):methanofullerene bulk-heterojunction solar cells. *Advanced Functional Materials* **15**, (2005), 795–801.

[208] Zhang, Q., et al., Small-molecule solar cells with efficiency over 9%. *Nature Photonics* **9**, (2015), 35–41.

[209] Sun, K., Xiao, Z., Lu, S., Zajaczkowski, W., Pisula, W., Hanssen, E., White, J. M., Williamson, R. M., Subbiah, J., and Ouyang, J., A molecular nematic liquid crystalline material for high-performance organic photovoltaics. *Nature communications* **6**, (2015).

[210] Armin, A., Yazmaciyan, A., Hambsch, M., Burn, P. L., and Mederdith, P., Electro-optics of conventional and inverted thick junction organic solar cells. *ACS Photonics* **2**, (2015), 1745–1754.

[211] Jin, H., Armin, A., Hambsch, M., Lin, Q., Burn, P. L., and Meredith, P., Bulk heterojunction thickness uniformity -a limiting factor in large area organic solar cells? *physica status solidi (a)* **212**, (2015), 2246-2254.

[212] Arkhipov, V. and Perova, I., Non-langevin recombination in disordered dielectrics. *Journal of Physics D: Applied Physics* **26**, (1993), 1301.

[213] Reis, B., Bassler, H., Schonherr, G., Silver, M., and Snow, E., Geminate recombination and mobility in a-si alloys. *Journal of Non-Crystalline Solids* **66**, (1984), 243–248.

[214] McGhie, A., Blum, H., and Labes, M., Radical recombination in anthracene single crystals. *Molecular Crystals and Liquid Crystals* **5**, (1969), 245–255.

[215] Hughes, R., Bulk recombination of charge carriers in polymer films: Poly-n-vinylcarbazole complexed with trinitrofluorenone. *The Journal of Chemical Physics* **58**, (1973), 2212–2219.

[216] Arkhipov, V., Perova, I. A., and Rudenko, A., Sign-alternating kinetics of radiation-induced current in disordered dielectrics. *International journal of electronics* **72**, (1992), 99–102.

[217] Tyutnev, A., Karpechin, A., Boev, S., Saenko, V., and Pozhidaev, E., Current overshoot in polymers under continuous irradiation. *physica status solidi (a)* **132**, (1992), 163–170.

[218] Adriaenssens, G. and Arkhipov, V., Non-langevin recombination in disordered materials with random potential distributions. *Solid state communications* **103**, (1997), 541–543.

[219] Juška, G., Arlauskas, K., Stuchlik, J., and Ã–sterbacka, R., Non-langevin bimolecular recombination in low-mobility materials. *Journal of non-crystalline solids* **352**, (2006), 1167–1171.

[220] Hilczer, M. and Tachiya, M., Unified theory of geminate and bulk electron-hole recombination in organic solar cells. *The Journal of Physical Chemistry C* **114**, (2010), 6808–6813.

[221] Groves, C. and Greenham, N. C., Bimolecular recombination in polymer electronic devices. *Physical Review B* **78**, (2008), 155205.

[222] Armin, A., Hambsch, M., Wolfer, P., Jin, H., Li, J., Shi, Z., Burn, P. L., and Meredith, P., Efficient, large area, and thick junction polymer solar cells with balanced mobilities and low defect densities. *Advanced Energy Materials* , (2014).

[223] Parmenter, R. H. and Ruppel, W., Two-carrier space-charge-limited current in a trap-free insulator. *Journal of Applied Physics* **30**, (1959), 1548–1558.

[224] Clarke, T. M., Peet, J., Nattestad, A., Drolet, N., Dennler, G., Lungenschmied, C., Leclerc, M., and Mozer, A. J., Charge carrier mobility, bimolecular recombination and trapping in polycarbazole copolymer: fullerene (PCDTBT:PCBM) bulk heterojunction solar cells. *Organic Electronics* **13**, (2012), 2639–2646.

[225] Lin, Q., Armin, A., Nagiri, R. C. R., Burn, P. L., and Meredith, P., Electro-optics of perovskite solar cells. *Nature Photonics* **9**, (2014).